Sustainable insulating lightweight materials for enhancing indoor building performance

MISCANTHUS, AEROGEL AND NANO-SILICA

Yuxuan Chen

Bouwstenen 322

Sustainable insulating lightweight materials for enhancing indoor building performance

Miscanthus, aerogel and nano-silica

PROEFSCHRIFT

ter verkrijging van de graad van doctor
aan de Technische Universiteit Eindhoven,
op gezag van de rector magnificus prof.dr.ir. F.P.T. Baaijens,
voor een commissie aangewezen door het College voor Promoties,
in het openbaar te verdedigen op vrijdag 5 november 2021 om 16:00 uur

door

Yuxuan Chen

geboren te Wuhan, China

CIP-DATA LIBRARY TECHNISCHE UNIVERSITEIT EINDHOVEN

Sustainable insulating lightweight materials for enhancing indoor building performance: Miscanthus, aerogel and nano-silica/ by Yuxuan Chen

A catalogue record is available from the Eindhoven University of Technology Library

ISBN: 978-90-386-5366-2

Bouwstenen 322

NUR 955

Cover design: Yuxuan Chen & Xuan Ling

Ph.D. thesis, Eindhoven University of Technology, the Netherlands

Dit proefschrift is goedgekeurd door de promotoren en de samenstelling van de promotiecommissie is als volgt:

Voorzitter:	prof. dr. ir. T.A.M. Salet
1e Promotor:	prof. dr. ir. H.J.H. Brouwers
2e Promotor:	prof. dr. ir. Q.L. Yu
Co-promotor:	dr. K.Schollbach
Promotiecommissieleden:	prof. dr. S. Amziane (Université Clermont Auvergne)
	prof. dr. W. Chen (Wuhan University of Technology)
	prof. dr. B. P. Jelle (Norwegian University of Science and Technology)
	prof. dr. ir. M.C.J. Hornikx

Het onderzoek of ontwerp dat in dit proefschrift wordt beschreven is uitgevoerd in overeenstemming met de TU/e Gedragscode Wetenschapsbeoefening.

Dedicated to my wife and parents

Preface

I started my research on 9st, November 2017 in the group of Building Materials, Department of Built Environment, Eindhoven University of Technology (TU/e), in the Netherlands under the leadership of Prof. H.J.H. (Jos) Brouwers. This research is supported by China Scholarship Council and Eindhoven University of Technology. Since my PhD research is going to the end, I would like to express my sincere gratitude to people who helped and supported me on my 4 years' study.

First of all, I would like to express my sincere appreciation to my promotor and supervisor Prof. H.J.H. Brouwers. 4 years ago, you provided me such a great opportunity to be a member of the Building Materials group. New research fields, biomaterials and aerogel, were open for me by your guidance and support. During my PhD study, you offered me all the necessary conditions for my investigation, as well as enough trust. The suggestions and experiences from you always provided me new insights to improve my work and life. I have lots of chance to learn from knowledgeable experts from many other fields, from which I improved and benefited a lot.

In addition, I am grateful to my daily supervisor and co-promotor Dr. K. (Katrin) Schollbach. You helped me a lot with the revision of my many manuscripts and provide professional insight. You gave me enough freedom and trust to finish my research during my 4 years PhD study. You always encouraged and inspired me when I was in trouble with my research, especially for the aerogel project. Optimism is such a great trait for a researcher and I really learned it from you. The gratitude also goes to Prof. Q.L. Yu, I cannot finish my PhD study and thesis without your help. You supported me with your professional knowledge and suggestions. You contributed a lot to my scientific papers in terms of writing and revision. I'm very grateful to have you in the group.

Furthermore, I sincerely thank my master supervisors Prof. Zhonghe Shui and Prof. Wei Chen, who guided me in the field of building materials at the very beginning in Wuhan. You taught me how to do research independently and gave me a lot of help with my master thesis.

I also would like to extend my appreciation to my promotion committee, Prof. dr. Sofiane Amziane (Université Clermont Auvergne), Prof. dr. Wei Chen (Wuhan University of Technology), Prof. dr. ir. Maarten Hornikx (Eindhoven University of Technology) and Prof. dr. Bjørn Petter Jelle (Norwegian University of Science and Technology) for accepting to be a member. Thanks for your reading and evaluation of my thesis.

Furthermore, the thesis cannot be finished without the efforts and help from my current and former colleagues. Thanks for the contributions from Ing. A.C.A Delsing and Mr. H.L.W Smulders for the tests and technical support during my research. Xu Gao and Bo Yuan, thanks for your help and guidance for my daily life at the beginning of my study, I still remember the days when we spent together. Alberto Lazaro and Yuri Hendrix, thanks for leading me into this olivine project, which I learned a lot from you. Gang Liu, my roommate during my stay here, I really thank you for helping me in research and life. You taught me lots of life skills and sports, among which the most unforgettable thing was jogging with you, which increased my stamina and reduced the pressure from work. Luyang, thanks for the times we spent together to cook

delicious food and taste different beers on weekends. Florent, thanks for the guidance in SEM and other technical help from you. Roman Dalessi and Polle Huijsse, my two internship students from Fontys, thanks for your effort in doing lots of experiments and writing the reports. Yanjie, thanks for the sports organized in the evening, which helped me a lot in adjusting the pressure from work. Together with Peipeng, Yueye, Perry, Qadeer, Anna, Jawad, Winnie, Kinga, Kate, Katerina, Hoss, Zhengyao, Xiaoxiao, Tao, Yan, Zixiao, Fan, Xuan, Daoru, Helong, Zhihan, Shaohua, Xinglong, Ricardo, Iris, Charles, Jonathan, Naomi, Felix, Marc, Marina, Alex and Samuel. I wish you all the best in the future and have a wonderful life.

Moreover, I give my thank from the bottom of my heart to my Mum (Xiuping Jia) and Dad (Bin Chen). Thanks for your support and encouragement on my every choice and decision. Also, I would like to thank my aunt (Ling Chen) and grandmother (Haimei Zhong) to support me and understand me during my PhD study. Finally, I would like to give the sincerest appreciation to my wife (Yudi Xie). Thanks for the 4 years you accompanied me to obtain this degree while waiting in China. We experienced happiness, excitement, loneliness and sadness during these 4 years, but finally we made it.

Eindhoven, 8th August 2021

Yuxuan Chen

Summary

The insulation properties of buildings regarding thermal and acoustic are becoming a major concern as the energy savings and healthy living environments of buildings are increasingly important for human life. Moreover, sustainability plays an important role in recent developed building materials as the society and industry are striving to reduce the CO_2 emissions and energy consumption worldwide. In this thesis, bio-based materials and super insulating materials, especially miscanthus fibers (MF) and silica aerogels, are used as a natural lightweight aggregate in concrete, and as high-performance insulating materials in the built environment.

The first section (Chapter 2, Chapter 3 and Chapter 4) of this thesis verifies that the insulation properties of bio-lightweight concrete can be improved with miscanthus fibers by utilizing its porous structure. Thermal insulation and acoustic absorption of miscanthus lightweight concrete are investigated and the interaction between cement and miscanthus are revealed. The main contribution of miscanthus fibers in ultra-lightweight concrete is to improve the open porosity and internal defects by introducing more air voids. Optimization of the concrete can be achieved by using different parts of miscanthus and suitable concentration in concrete. Further, with the incorporation of expanded waste glass and the substitution of MF, an ultra-lightweight miscanthus concrete (ULMC) is developed. Results show ULMC with 30% 2–4 mm MF obtained an ultra-low density (554 kg/m^3), thermal conductivity (0.09 W/(m · K)) and high acoustic absorption coefficient (0.9) at low frequencies, with relatively low strength (3.99 MPa at 28d). It is discovered that the acoustic absorption of ULMC can be improved by optimizing the dosage and shape of miscanthus fibers. Lastly, the finely ground miscanthus fibers is found to be effective in reducing the density and thermal conductivity of artificial steel slag based lightweight aggregates produced with a cold bonding process. The finely ground miscanthus fiber is applied as an accelerator for carbonation of steel slag based artificial lightweight aggregate and proved to be a promising aggregate to prepare insulating and sustainable lightweight concrete.

The second section (Chapter 5, Chapter 6, Chapter 7 and Chapter 8) of this thesis explores the possibility of producing silica aerogel from olivine at ambient pressure and temperature, showing the advantage of sustainable, cost-effective and competitive thermal insulating performance. The produced silica aerogel features a high specific surface area (694 m^2/g) and pore volume (2.99 cm^3/g), with a uniform pore size distribution and mesoporous structure. The produced silica aerogel is also successfully applied as a photocatalytic support to increase the efficiency of titania catalyst. In order to further enhance the integrity of aerogel, a nano-fibrillated cellulose is applied as the reinforcement in silica aerogel to increase the mechanical performance and thermal stability. Moreover, a methyltrimethoxysilane-based silica aerogel is prepared with a co-precursor method to increase the production efficiency and mechanical performance of the aerogel. Furthermore, the application of silica aerogel in geopolymer foam concrete is investigated, focusing on influence of silica aerogel with different particle size on the performance of foam concrete. The results show that silica aerogel can enhance the hydrothermal performance and acoustic absorption effectively by using large fraction of silica aerogel.

For the last section (Chapter 9 and Chapter 10), different kinds of mesoporous silica from olivine are produced at low temperatures directly via acid extraction, by using different non-ionic surfactant. The pore size of mesoporous silica can be tailored, and the sustainable silica can be utilized as photocatalytic support and the potential to be nano-insulation materials. Finally, a highly dispersed colloidal silica from olivine is produced via colloidal milling and is applied in ultrahigh performance concrete (UHPC) to enhance the early age performance, including rheology and early age strength of UHPC from 1d to 7d. The mechanism of the improved performance contributed by olivine colloidal silica is explained in detail.

Contents

Chapter 1 Introduction

1.1 Background

As the energy use in the building sector accounts for a significant part of the world's total energy use and greenhouse gas emissions, there is a demand to improve the energy efficiency of buildings [1]. Therefore, for the sake of constructing environmentally friendly and energy efficient buildings, it is of great interest to design sustainable and high-performance thermal insulation building materials to reduce the energy consumption [2]. Furthermore, the healthy living environment is also an important aspect in today's building design. Therefore, it is also important to design and develop acoustic absorption and air-purifying materials used in a building environment.

Fig. 1.1 shows the thermal conductivity versus the density of different materials used in constructions and buildings. Thermal conductivity (*k*-value or lambda value (λ)) is a measure of the rate at which temperature differences transmit through a material. The lower the thermal conductivity of a material, the slower the heat rate through it for a given temperature, and so the more effective it is as an insulator. Generally, the lower the thermal conductivity of a building's fabric, the less energy is required to maintain comfortable conditions inside.

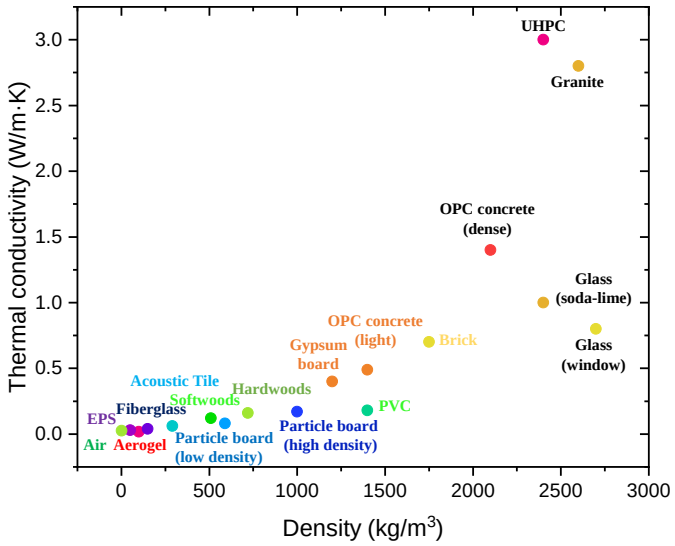

Fig. 1.1 Thermal conductivity vs density of different building materials.

It is observed that the highest thermal conductivity is achieved with ultrahigh performance concrete, reaching around 3.0 (W/m·K) [3]. While the lowest thermal conductivity can be achieved by aerogel, whose thermal conductivity reaches 0.010~0.023 (W/m·K) [4]. In between, there exists many other kinds of building material, possessing different thermal conductivities. The density and thermal conductivity generally have a positive correlation, i.e. the higher the density, the higher the thermal conductivity. Normally, due to the use of aggregates, conductive inorganic powder and/or reinforced steel fibers, concrete has a higher conductivity. While other non-structural materials have lower thermal conductivities, for example, gypsum board, soft/hard wood, low/high density particle board, fiber glass and expanded polystyrene. This is

because they possess high porosity and low solid conductivity, which makes the total effective thermal conductivity lower.

Therefore, in order to make the most used materials (i.e. concrete) in the building sector more insulating, a sustainable method should be explored to increase the insulating performance. Generally, the simplest way is to incorporate lightweight (hollow) aggregates in concretes. Another method is to introduce more air or voids in the concrete, mainly by using air-entraining agents or foaming techniques to create the porous structures [5,6]. Recent research shows the substitution of natural aggregate by bio-aggregate could be a promising choice [7]. The utilization of plant fibers instead of porous aggregates requiring high temperature processing in cement and concrete, features green and environmentally friendly. However, more investigations are still needed to assess the performance of plant fibers in lightweight concrete.

In order to achieve the lowest thermal insulation and highest fire safety of buildings, silica aerogel is the best suited material. As discussed above, it reaches the lowest thermal conductivity among all building materials [4]. Besides, silica aerogel has an excellent resistance to high temperatures and even fire, which make construction and building safer [8]. The overall insulation performance for aerogel is better than biobased materials. However, the main limitations for the practical use in buildings are its high embodied energy, expensiveness, the low fracture energy and the ultralow strength [9]. Therefore, more efforts are still needed to make the aerogel more suitable to be applied in buildings.

Fig. 1.2 shows the noise reduction efficiency versus the density of different materials that can be used in building sector. Sound absorption is the capability of a surface, or building material, to absorb sound instead of reflecting it. Surfaces that absorb sound better will not allow for reflections to bounce around and will deaden the sound wave more quickly. Many common building materials, such as gypsum board, concrete, brick and tile, are fairly reflective and do not absorb much sound. Softer materials, such as cellulose fibers, carpet, foam padding, and fiberglass, are better at absorbing sound. Optimal control of noise in buildings can be achieved by understanding the basics of how sound moves through solid objects and air. Building materials will have the most impact on controlling sound in interiors, but strategic placement of absorptive materials in finished areas can also be very effective [10].

Bio-materials such as porous plant fibers can be a promising choice as sound absorptive aggregate in concrete [11]. As cement-based materials are the most available materials in buildings, the improvement of sound absorption is very important. Hence, the introduction of bio-materials in lightweight concrete is hypothesized to improve the sound absorption. Silica aerogel also possess excellent sound absorption due to the interconnected nanopores inside the 3D-network of silica primary particles [12]. Therefore, in this thesis, these two materials are investigated in terms of both sound and thermal properties.

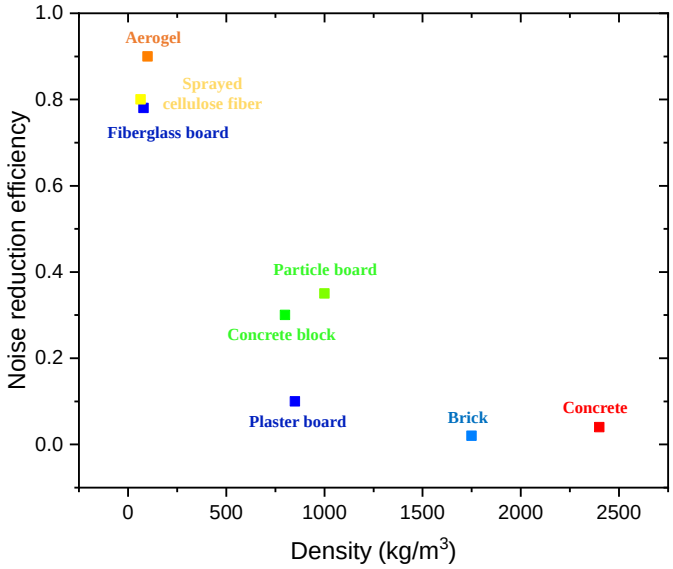

Fig. 1.2 Noise reduction efficiency vs density of different building materials.

1.1.1 Bio-based natural fibers in building materials: Miscanthus fibers

The rising agricultural output and the rapid expansion of bio-based manufactures have recently produced great amounts of agricultural wastes. While the majority of bio-wastes cannot be efficiently handled and applied, bio-based insulating materials made from waste and recyclable plant fibers are interesting alternatives to those obtained from fossil carbon, which are also sustainable and eco-friendly to the environment. For the sake of constructing environmentally friendly and cost-effective buildings, it is of great interest to design green and low-cost building materials to reduce the environmental impact, particularly related to CO_2-emissions. Miscanthus is a kind of this material and can be worked as a sustainable material.

1.1.1.1 Miscanthus fibers as sustainable lightweight aggregate in lightweight concrete

Lightweight concrete (LWC), similar to normal weight concrete, is a mixture of water, ordinary Portland cement (OPC), and aggregates. It is classified as structural or nonstructural concrete depending on strength and compression rating, generally determined by the type of aggregate material used in the concrete mix. Lightweight aggregate concrete uses a variety of aggregates with lower density than normal weight concrete.

The use of renewable materials as construction material opens up an enormous scope of possibilities for farmers and industrial enterprises. Among other possible dedicated crops, the use of miscanthus has received considerable attention due to its widespread availability and lack of competition with food and animal feed. Miscanthus features many favorable agronomic characteristics and leads to tremendous biomass yields [13].

Miscanthus contains other fiber compounds which are considerably stronger than e.g. straw, and contains chemical constituents like silicon, so it could represent a suitable basic material in building and construction. Miscanthus shows two major advantages as compared to common renewable materials like conifers. These are the thermal insulating qualities [14] and in addition the very high firmness of the plant material [15]. A cross-section of the miscanthus shoot shows, that there is the parenchyma which provides the thermal insulation and around the parenchyma

there are three rings with relevance to firmness: the epidermis, the thick sclerenchyma characteristics and the radial allocation of vascular bundles with its own firmness texture [16].

The basic advantage of miscanthus is that it is a low cost and widely available resource in many agricultural areas, especially in Europe. The lightweight cement–organic composite is a completely recyclable material. The material can be ground and later used to produce new lightweight composites [17,18]. Furthermore, it has a better compatibility with cement and concrete, as the polysaccharides leached from miscanthus is lesser than that of other plant fibers, such as coconut fibers.

Despite all the aforementioned advantages, there are some serious concerns for successful application of natural fibers as concrete reinforcement. These are the high variation of fiber properties, high moisture absorption capacity, and the main concern is the durability of fibers in the alkaline environment of a cement matrix. The degradation of fibers in a cement matrix occurs as a consequence of lignin and the hemicellulose dissolution in the middle lamellae of the fibers through the alkaline pore water. In order to overcome the problem associated with natural fibers in cement-based composites, a proper understanding of the deterioration mechanisms of the fibers in the matrix is required [19].

1.1.1.2 Miscanthus powder as carbonation accelerator in CBLAs

The rising waste quantities and the excessive use of natural resources are becoming the major concern worldwide. In order to address these problems, more and more studies have been carried out to focus on the production of artificial aggregates, as a kind of substitution to natural aggregates [20]. Cold bonded lightweight aggregates (CBLAs) are a kind of lightweight aggregates that were recently developed to decrease the CO_2 emission and lower the investment requirement by using waste and by-product materials. Normally, artificial aggregate is produced through the agglomeration of powdered waste materials into fresh pellets with a certain range of sizes [21]. The fresh pellets are then hardened by a cold bonding process and suitable curing process to attain the strength needed to meet the requirement of applications.

Most common used materials in CBLA are cement (CEM), fly ash (FA) and ground granulated blast furnace slag (GGBS) [22]. Cement is used as a binder in artificial aggregates, while FA and GGBS are used to decrease the usage of cement and embodied energy and lower the density. In addition, other waste materials such as waste treatment sludge and rice husk ash, municipal solid waste incineration fly ash, cement kiln dust and washing aggregate sludge have been used in BCLAs [23–27].

Miscanthus powder is a kind of finely ground short natural fiber. Because the surface area of miscanthus powder is higher than of normal miscanthus fibers, the direct application of miscanthus powder in lightweight concrete is very difficult. This is due to the higher water absorption and quicker release of polysaccharides that influence the cement hydration and performance of composite concrete, leading to a much lower strength of concrete. However, it is interesting to find a way to incorporate miscanthus powder in CBLAs to make artificial lightweight aggregate, due to less use of cement as a binder, or with other kinds of binders.

Steel slag is a by-product in steel making industry, which has a high CO_2 reactivity [28].

The carbonation of steel slag can result in the formation of calcite and silica gel. They can function as binders in cold bonded lightweight aggregate. However, the density of steel slag is very high and thus the motivation to decrease the density of stee slag is also strong. Hence, the combination of steel slag and miscanthus powder become a promising method to produce novel artificial lightweight aggregates. Miscanthus powder has a large amount of internal pores and can help to increase the carbonation rate of steel slag. Therefore, miscanthus powder not only decrease the density of CBLAs but also increase the formation of calcite and silica gel in the aggregate.

1.1.2 Advanced silicate materials in building materials: Silica aerogel

Silica aerogel is a super insulating lightweight material created in the 1920's by Samuel Kistler and published in *Nature* in 1931 [29]. Aerogel is derived from a specific gel, in which the liquid component for the gel is replaced with air without significant collapse of the gel structure. Due to its unique properties, such as high porosity, extremely low density and a large specific surface area, it can be applied to a large variety of applications [30]. Aerogel is now mostly used in specific fields such as aerospace applications, insulation for shipping container, transportation device (plane/automobile), high-energy physics, insulation for buildings and catalytic support [31,32].

In order to achieve the goal of sustainable production of silica aerogel, a cost-effective and environmentally friendly synthesis route is an important task [33,34]. The commercialized silica aerogel is mainly produced from organic silica sources, for instance, tetrathoxysilane (TEOS) or tetramethyl orthosilicate (TMOS), which are mostly expensive and difficult for large scale production of silica aerogel. For large scale production, abundant waste minerals like dunite or olivine and other waste silicate minerals are recently believed to be easily available and inexpensive silica sources [35].

Nano-silica can be produced by dissolving the mineral olivine in sulfuric acid according to the exothermic reaction:

$$(Mg,Fe)_2SiO_4 + 4H^+ = Si(OH)_4 + 2(Fe,Mg)^{2+}, 223KJ/mol \quad (1.1)$$

Using this reaction nano-silica can be obtained at much lower temperatures (50-90 ^{O}C) and more environmentally friendly than with conventional methods. A detailed description of this process and the properties of this nano-silica can be found in a previous PhD thesis [36].

1.1.2.1 Silica aerogel prepared at ambient pressure from olivine and its application

Olivine is a silicate mineral that contains the magnesium rich end-member forsterite (Mg_2SiO_4) and the iron rich end-member fayalite (Fe_2SiO_4). Olivine is the fastest weathering silicate due to the inosilicate in its structure. In addition, olivine is the most common mineral in the upper mantle and a common mineral in the earth's crust, which makes it a low-price commodity.

The dissolution of olivine in sulfuric acid yields a slurry consisting of a mixture of magnesium/iron salts, amorphous silica, unreacted olivine and inert minerals. Once the reaction is complete, the unreacted olivine and inert minerals are removed from the final suspension by

sedimentation. Subsequently, the silica can be cleaned from the resulting mixture by washing and filtering. After the filtration, a cake with around 20 wt.% solid content of nano-silica is obtained. A flow chart of this process is presented in **Fig. 1.3**.

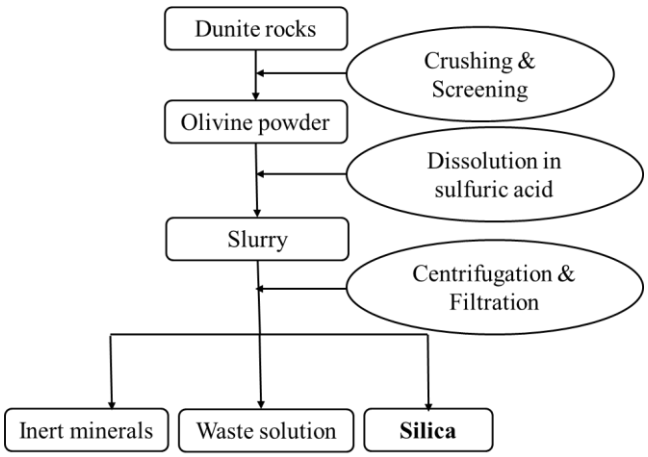

Fig. 1.3. Chart flow of the olivine nano-silica production.

In this work, water glass was prepared from olivine as a cheap and sustainable silica source to compensate the cost of additional solvent exchange in the aerogel synthesis. Water glass is conventionally manufactured by reacting sodium carbonate with silicon dioxide in the molten state. Because of the high temperature involved in this process, conventional water glass is unattractive as a precursor [37]. Thus, using dunite rocks as the precursor to synthesize aerogel can substitute the use of expensive raw materials, and help to reduce environmental pollution.

Water glass is prepared by dissolving olivine silica in a sodium hydroxide (NaOH) solution, resulting in a sodium silicate solution containing small amounts of impurities. The resulting solution is filtrated by vacuum filtration and a sodium silicate solution is obtained. The silica content of water glass is fixed at 8 wt.% [38], because water glass containing 4 wt.% to 8 wt.% silica is the best suited to prepare silica aerogel.

Similar to alkoxide precursor-based silica gels, gelation of water glass can be induced directly in a single step process by a simple neutralization or in a more elaborate two-step process (acidification/ion exchange followed by base addition). **Fig. 1.4** summarizes these similarities between water glass and alkoxide chemistry.

During the neutralization of water glass, gelation occurs typically rather quickly (seconds to minutes, depending on the solution pH and the type of acid used). However, the residual sodium ions from the water glass render the processing rather difficult, due to the increased surface tension of the gel pore solution. Therefore, the two-step route is a more promising synthesis method that eliminates sodium ions in gels via ion exchange, and hence applied here.

In a two-step water glass process, the sol used to prepare the gels consists of silicic acid (H_2SiO_3) and its oligomers polysilicic acids, which are produced by exchanging Na^+ ions from the sodium silicate with H^+. To remove sodium ions in the sodium silicate solution, the as-prepared sodium silicate solution is passed through a strongly acidic, cationic ion-exchange resin (e.g. Amberlyst 15). The pH of as-prepared sodium silicate solution is around 11.9~12.1 and once passed through the ion exchange resin, drops into the acidic range with typical values

around 2.5~3.0. Following the ion exchange step, catalytic amounts of a base (e.g. ammonium hydroxide (NH_4OH)) are added to induce gelation. The obtained gels are then typically aged overnight and exchanged into ethanol twice and then into hexane twice. Afterwards, the solvent exchanged gels are surface modified by silylating agent (e.g. hexamethyldisilazane (HMDS), hexamethyldisiloxane (HMDSO) or trimethylsilyl chloride (TMCS)) and then dried at room temperature and then in an oven at 230°C. The silica aerogel from olivine should be prepared successfully.

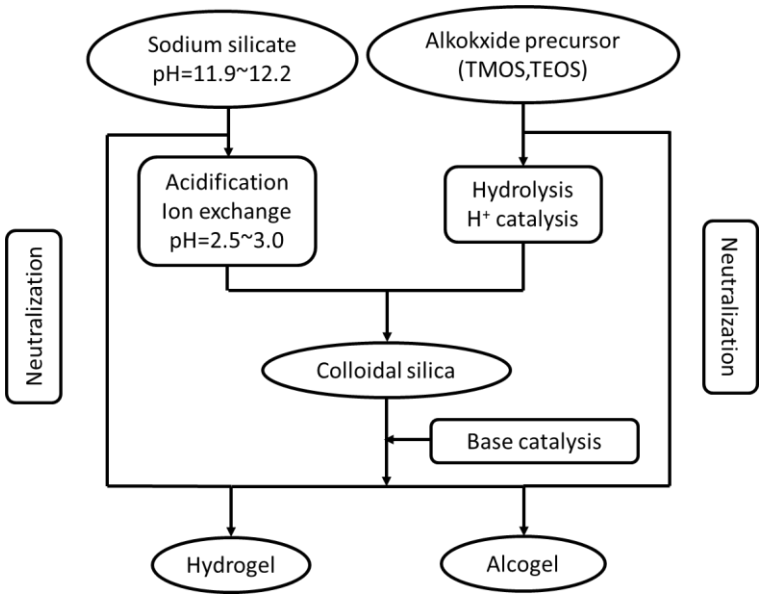

Fig. 1.4. Schematic illustration describing the chemical mechanisms by which gel networks are formed from sodium silicate and alkoxide precursors.

1.1.2.2 Development of silica-cellulose composite aerogel

It is well known that classical silica and some organic synthetic aerogels are thermal super-insulating materials, with a thermal conductivity (0.003-0.020 (W/m·K)) lower than that of air (0.026 W/(m·K)) in room conditions [39]. These aerogels are in majority mesoporous which allows decreasing the thermal conductivity of gaseous phase below that of air due to the Knudsen effect, without needing vacuum technology [4]. However, silica aerogels are very brittle which hinders their applications, and synthesis of organic aerogels that are resorcinol-formaldehyde based, leads to mechanically strong materials, but uses toxic components [40]. It would thus be extremely attractive to develop aerogels that could perform like classical silica aerogels in terms of thermal conductivity/sound absorption and like synthetic organic ones regarding mechanical strength.

Cellulose nano-fibrils can be used as enhancement in classical silica aerogel. In fact, cellulose nano-fibers themselves can be used as the precursor to produce cellulose aerogel [41]. Cellulose, being the most abundant natural polymer on earth, is of low cost and easily available, and therefore attracts a lot of interest for making new materials. Aside of classical films, sponges and fibres, functional materials with high added value, such as cellulose nanocrystals, nano-fibres and aerogels can be made from cellulose [42]. The latter are highly porous materials with large specific surface areas. Their potential applications are very wide, ranging from

scaffolds and matrices for controlled drug release to gas absorbers and thermal insulating materials as well as for batteries and fuel cell electrodes when pyrolyzed [43–46]. However, the thermal insulation of cellulose aerogel cannot be comparable to classic silica aerogel. This is because the macropores present in cellulose aerogel are beyond the mesoporous range and cannot restrict the air movement in the pores.

One of the potential ways to decrease the thermal conductivity of bio-aerogels could be "filling" their pores with a super-insulating material which can be silica aerogel. Theoretically, it is then expected that the conductivity of the gaseous phase, which represents about 60% of the total conductivity would be significantly decreased due to the presence of nanostructured and super-insulating silica aerogel in the pores of the cellulose aerogel network.

1.1.2.3 MTMS aerogel reinforced with PDMS and NFC

The production of aerogel is fairly complex due to the lengthy preparation time with a complex sol-gel synthesis, with multiple steps of solvent exchange and supercritical drying or freeze drying. The required expensive technology is also an issue, where the drying process comes with the additional dangers of extremely high temperature and pressure [47]. So further development and advancement in commercial use of these kinds of aerogels are highly restricted. Due to these downsides, researchers have invented a new method, i.e. ambient pressure drying (APD), which enables the ability to dry aerogels at ambient pressures at different temperatures [48].

Methyltrimethoxysilane (MTMS) aerogel has been invented recently and can be used as precursor to prepare monolithic aerogel via ambient pressure drying [49]. MTMS aerogel features low density, monolithic, rapid processing and without solvent exchange. Some researchers have investigated the rapid synthesis of silica aerogel from MTMS within 1-day, and other have invented very flexible silica aerogel from MTMS with a maximum strain of 50% [50]. However, the MTMS aerogel needs to be further optimized to increase the strength and strain or the hydrophobicity to possess a better performance during application.

Therefore, it is of interest to develop a co-precursor silica aerogel with modified-nano-fibrillated cellulose (NFC) in a one-step drying method at ambient temperature and pressure to find optimal processing conditions, suitable agents and materials. Together with the two co-precursors, methyltrimethoxysilane (MTMS) and polydimethylsiloxane (PDMS), the modified cellulose should give a positive increase in mechanical properties, such as a more springy, compressible and hydrophobic aerogel compared to the normal MTMS-aerogel.

1.1.2.4 Application of silica aerogel in geopolymer foam rendering

The rising building energy demands together with the concerns for the rising greenhouse gas emissions are driving the demand for energy saving materials and systems. Worldwide countries are promoting policies aiming to support the retrofit of existing buildings, as these provide energy savings, lower maintenance costs, and higher comfort levels [51]. The most important part of a building from an insulation perspective is the building envelope. One way to decrease the energy consumption in buildings and thus increase the energetic efficiency of

the building envelopes is by improving the thermal insulation. Better insulation materials in terms of performance, durability and embodied energy are therefore required. This concerns both new buildings as well as refurbishment applications.

Geopolymer foam render (GFR) is a recently developed novel thermal insulating concrete [52]. Geopolymer is principally manufactured through alkali hydroxide and/or silicate activation of a reactive aluminosilicate, in particular calcined clays (metakaolin) or fly ash [53]. The advantage of using geopolymer as binder is the reduced energy consumption and CO_2 emissions compared to ordinary Portland cement. Current applications of alkali-activated materials include the production of precast structural members, different types of grout, masonry bricks, aerated concrete, heat-resistant concrete and matrixes for the solidification and immobilization of extremely hazardous or radioactive waste [54].

The porous structure of GFR is currently developed by introducing foam through a chemical foaming agents (Al powder) or mechanical pre-foaming techniques [55]. However, the porous structure of GFR is randomly distributed and cannot have an even lower thermal insulating performance or acoustic absorption performance. Hence, it is interesting to find a solution to effectively increase the insulation performance of GFR.

Silica aerogel is a siliceous substance that consists of a network of interconnected nanostructures. More than 90% of a typical silica aerogel consists of air voids. These particles lead to the formation of a high surface area and mesoporous structure, offering this material low solid conductivity and thermal energy diffusivity [56]. These inherent properties allow the aerogel to exhibit various useful characteristics, such as outstanding thermal insulation (thermal conductivity as low as 0.012–0.022 W/m·K), high hydrophobicity with a water contact angle value exceeding 150 degree, a high surface area (600–800 m^2/g) and high porosity (>90%) [30]. It is hypothesized that the incorporation of silica aerogel in GFR could increase the thermal insulation in high humidity condition and also increase the acoustic absorption.

1.1.3 Advanced silicate materials in building materials: Nano-silica

1.1.3.1 Ordered mesoporous silica from olivine and its applications

The formation of ordered mesoporous silica by the use of surfactants has been achieved since the early 1990's [57]. This creates silica materials that contain very large surface areas of up to 1000 m^2/g and a porous network of silica with pore widths between 2 to 50 nm [58]. The most commonly used silica precursors are sodium silicate and tetraethoxysilane (TEOS). However, it is often associated with high production energy, which makes it a costly precursor for the syntheses of silica. Just recently a low-energy silica precursor has been introduced for the formation of the mesoporous silica. Namely, from the silicate mineral olivine which is abundantly present on earth and can often be found as an industrial waste as well [59].

The olivine crystal structure consists of individual SiO_4 tetrahedra, ionically linked by Mg/Fe atoms, with no interconnected Si-O-Si bonds between the tetrahedra. When olivine is dissolved in sulphuric acid, the following reaction occurs, releasing silica monomers into the environment. Silicas with surface areas up to 500 m^2/g have been synthesised by this method [60]. However, the pore size distribution of olivine silica is random and cover a wide range

from a few to hundreds of nanometers. If a narrower pore size distribution is required (as for catalysis or drug delivery) this olivine nano-silica in its current state cannot be used. Therefore, a great demand is to optimize the pore size distribution of silica.

With the use of different surfactants and production conditions, finding the optimal processing conditions, surfactants, additives and swelling agents are key objectives. Comparing the quality of the mesoporous silica to industrial reference materials gives an indication if the silica could serve as a catalytic support and other commercial purposes.

1.1.3.2 Application of colloidal olivine nano-silica in UHPC

Nano-silica is an important cement additives in high performance concrete thanks to its high pozzolanic reactivity and seeding effect compared to other supplementary cementitious materials (SCMs) [61]. The effects of nano silica on the performance of cement and concrete have already been widely investigated in the last few decades [62,63]. It is acknowledged that nano silica can improve the mechanical properties and optimize the microstructure of concrete when added in a proper amount [64,65]. Furthermore, nano-silica can perform more effectively at early age in cement than micro-silica because of the higher specific surface area (50 to at least 500 m^2/g) and nano-seeding effects [66,67]. However, currently applied silicas in the cement industry are mainly silica fume or micro-silica, that are mainly used in special concrete for instance, oil well cement, due to the high price [68].

Ultrahigh performance concrete (UHPC) is a type of cementitious materials with a low w/b (water to binder ratio, typically 0.20-0.30) and reinforced with steel fibers, showing high strength (normally exceeding 150 MPa), durability and self-compacting properties. UHPC normally contains Portland cement, silica fume, ultrafine sand, fine aggregate, steel fibers and large amounts of superplasticizer. However, the low w/b ratio and high dosage of superplasticizer result in the slow cement hydration of UHPC at early ages. Therefore, the addition of nano-silica to accelerate the early age cement hydration is of significant interest. However, limitations of nano-silica applied in UHPC in practice are mainly its high embedded energy and the tendency to agglomerate, making it difficult to disperse in cement paste during mixing.

Recently developed olivine nano silica has been a promising choice for the application in UHPC. Compared to commercial nano-silica products, the nano-silica can be produced in a one-step process at low temperatures (50~90 °C). A few researchers have investigated the application of the green olivine nano-silica in concrete to improve the overall performance and lower the carbon footprint of concrete [59,69].

However, none of these studies have investigated the agglomeration of olivine nano-silica that may cause severe dispersion problem in cement and concrete and the way to tackle this issue. It is shown the nanoparticles can influence the rheology of paste and increase the viscosity. It is widely acknowledged that a very low water to binder ratios ranging from 0.18 to 0.25 are required in designing UHPC [10,37]. Therefore, finding a way to break up the agglomerate and decrease the water demand of silica is of significantly importance, especially in the low w/b ratio system.

A few technologies are found to be effective in reducing the particle size of nanomaterials. For instance, ultrasonic is a way to reducing the particle size by generating alternating low-pressure and high-pressure waves in liquids, leading to the formation and violent collapse of small vacuum bubble. Another way is to use high shear mixing for better dispersion of nano-materials. However, the methods mentioned above have no obvious effect on particle size reduction of nanomaterials that was bonded by hydrogen bonding, which is a very strong chemical bonding in nano silica. In this study, it was found that by using a colloidal mill, the nano silica can be deagglomerated by using grinding media at micrometer size, specifically, the 300 and 100 μm ZrO_2 microparticles. The colloidal mill can be used to grind the olivine silica cake into a silica suspension, thus avoiding the heat treatment process and applying it is effectively and better dispersed in UHPC.

Commercially available colloidal silica is mainly made from sol-gel methods. This kind of silica is widely used in high strength concrete and show good performance in enhancing the properties of UHPC. However, the olivine colloidal silica is a kind of novel colloidal silica. Therefore, it is interesting to make a comparative study on the two kinds of silica and their early age performance on UHPC. The mechanism of using nano silica in cement is mainly for two effects, one is the pozzolanic effect, the other is the filling effect. The filler effect can densify the cementitious materials and optimize the packing of the materials. In terms of pozzolanic effect, the commercial silica can consume the portlandite formed during cement hydration and thus generate more C-S-H, which is a phase that provide extra strength to hardened cement paste. Hence, the mechanism of the influence of this novel O-CnS on cement paste and UHPC is investigated in detail.

1.2 Motivation and objectives

In recent years, sustainable concretes have been widely investigated in order to meet the requirement of CO_2 emission reduction and energy saving. By introducing bio-based materials and aerogel in building materials, the amount of traditional Portland cement can be effectively reduced and lower the embodied energy. As mentioned above, miscanthus is one of the bio-materials, a natural fiber in agriculture and widely available around the world, can be smartly utilized in lightweight concrete and increase the thermal insulation and acoustic absorption of bio-concrete. Another material is silica aerogel from olivine, whose thermal insulating and acoustic absorption property are the best among all the building materials. By developing silica aerogel from olivine at ambient temperature and pressure, the ecological aspect of aerogel is improved. Lastly, nano-silica from olivine can be used to apply as functional materials in photocatalytic support and as a cement accelerator in ultrahigh performance concrete. Therefore, the objectives of this study are as follows:

- Investigating the effect of miscanthus fibers as lightweight aggregates on hydration kinetics, reaction products, microstructure, and insulating performance of cement-based lightweight concrete, which provide a comprehensive understanding of sustainable lightweight building materials containing miscanthus fibers.
- Evaluating the performance and insulation behaviour of ultralightweight concrete containing expanded waste glass and miscanthus fibers as lightweight aggregates.

- Proposition of a cement-free cold-bonded method for producing biobased artificial lightweight aggregate using carbonated steel slag as a binder and miscanthus powder and its application in lightweight concrete.
- Investigating the development of silica aerogel from olivine at ambient pressure and its application as photocatalytic support and its thermal properties.
- Investigating the cellulose-silica composite aerogel and the effects of cellulose nano-fibrils on the performance.
- Development of Methyltrimethoxysilane (MTMS) aerogel without solvent exchange and via ambient drying. The co-precursor method using MTMS and polydimethylsiloxane (PDMS) is investigated to produce a more robust silica aerogel. The performance evaluation on insulation is further investigated.
- Evaluating the microstructure and insulation behaviour of geopolymer foam concrete containing silica aerogel as insulative additives to improve the hygrothermal and acoustic absorption performance.
- Application of colloidal nano-silica in ultrahigh performance concrete and its further influence on early age cement hydration and rheology behaviour.

1.3 Outline of the thesis

The research framework is shown in **Fig. 1.5.** The contents of chapters are briefly introduced in the following paragraphs.

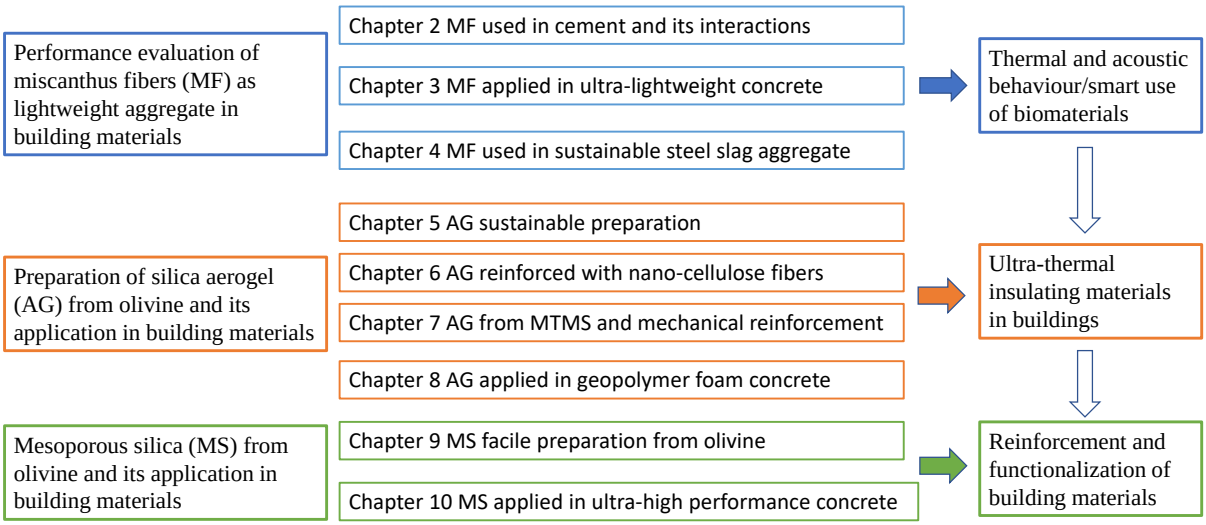

Fig. 1.5 Outline of the thesis.

In **Chapter 2**, novel miscanthus fibers (MF) are applied as lightweight aggregates in ordinary Portland cement-based lightweight concrete. Miscanthus lightweight concrete (MLC) was prepared and systematically studied, focusing on the acoustic absorption property and interaction between miscanthus and Portland cement. The effect of miscanthus on cement hydration is analysed by isothermal calorimetry, X-ray diffraction (XRD), thermogravimetry (TG), and scanning electron microscopy (SEM).

In **Chapter 3**, the acoustic absorption and thermal insulation of ultra-lightweight miscanthus concrete (ULMC) containing miscanthus fibers and expanded waste glass are investigated. Mechanical properties were characterized, including bulk density and flexural and compressive strengths. Results showed ULMC with 30% 2-4 mm MF obtained an ultra-low density (554 kg/m^3), thermal conductivity (0.09 W/(m·K)) and high acoustic absorption coefficient (0.9) at low frequencies. It is found that the acoustic performance of ULMC can be improved by optimizing the dosage and shape of miscanthus fibers.

In **Chapter 4**, a novel type of bio-based cold-bonded lightweight aggregate (BCBLWAs) is developed with the use of miscanthus powder and steel slag via CO_2 curing. The artificial aggregates using steel slag as a binder show relatively high strength and low density with the use of miscanthus. The reaction products and microstructure of BCBLWAs after carbonation curing are characterized by TGA, XRD, SEM and nitrogen physisorption. The CO_2 uptake capacity of BCBLWAs is also evaluated. Furthermore, the prepared BCBLWAs are utilized to prepare a lightweight concrete. The effect of BCBLWAs on the hydration of cement is also evaluated to be minor.

Chapter 5 investigates the development of silica aerogel from olivine silica and its application as thermal insulating materials and photocatalytic support. In this research, it was discovered sodium silicate derived from olivine, an abundant mineral in earth crust, can be used as the silica precursor to produce silica aerogel. The hydrophobic silica aerogel from olivine is developed with a low temperature synthesis route via ambient pressure drying. Moreover, this chapter investigates the performance of a silica aerogel-based air purifying coating to functionalize building materials. Titania is loaded onto the prepared silica aerogel through a precipitation method. The resulting samples were characterized by measuring the conversion efficiency to oxidize nitric oxide under ultraviolet (UV) radiation, nitrogen physisorption and Fourier-transform infrared spectroscopy (FTIR).

Chapter 6 studies a composite aerogel with silica and nano-cellulose fibers. The silica aerogel nanoparticles are formed inside the cellulose nanofibrils by using sol-gel method and freeze-drying. The developed silica-cellulose composite aerogel has a lowered thermal conductivity and is significantly stronger compared to plain cellulose aerogel. The microstructure of silica-cellulose aerogel was characterized by SEM, TGA, FTIR and N_2 physisorption tests. The developed silica-cellulose aerogel has a bulk density of 0.055~0.06 g/cm^3, compressive strength of 95.4 kPa, surface area of 900 m^2/g and thermal conductivity of 0.023 W/(m·K). The thermal stability of the composite aerogel is also improved and showed the higher cellulose decomposition temperature. Furthermore, the composite aerogel is modified by trimethylchlorosilane making it hydrophobic, reaching a water contact angle of ~140°, enhancing its volumetric and thermo-physical stability when applied in a humid environment.

In **Chapter 7**, MTMS aerogel with the addition of PDMS and modified NFC is investigated. The first step of this research is to modify the surface properties of the cellulose fibres. This chemical modification of nano-fibrillated cellulose with maleic anhydride provides the nano-fibrillated cellulose with a much higher hydrophobicity. The second part consists of the optimisation-process of the synthesis for the basic MTMS silica-aerogel at ambient pressure and temperature. Furthermore, the silica aerogel receives modification in its overall properties

due to the addition of hydrolysed PDMS as a co-precursor. After the optimization of the aerogel preparation, modified nano-fibrillated cellulose fibres are added in different amounts to optimize the concentration needed to achieve the required compression, thermal conductivity, surface area, density, hydrophobicity and appearance.

In **Chapter 8**, geopolymer foam render (GFR) with addition of silica aerogel is developed as a novel high performance insulating mortar, obtaining high porosity, insulation properties and fire resistance. Four kinds of silica aerogels with different particle sizes are applied in GFR as an insulative additive to improve the hygrothermal and acoustic absorption. The effect of the dosage and particles size of silica aerogel on the insulation performance is systematically studied. The microstructure of geopolymer foam aerogel render (GFAR) was investigated in depth with the use of micro-CT, scanning electron microscope, optical microscope and ultrasonic pulse velocity (UPV) test. The mechanism of the improved performance of GFAR with silica aerogel is explained.

Chapter 9 investigates the possibility of developing ordered mesoporous silica from olivine using surfactant and acid extraction. The nitrogen physisorption results show the produced mesoporous silica using poly(propylene glycol)-poly(ethylene glycol)-poly(propylene glycol) (PEG-PPG-PEG) symmetric triblock copolymer contains the microstructure with average pore size of 12 to14 nm. Moreover, the average pore size can be further increased to 15 nm when using n-heptane as the swelling agent. Furthermore, these produced mesoporous silicas are tested as catalytic support by loading anatase for the photocatalytic oxidation of NO_x pollutants. The results show the produced olivine derived mesoporous silica can be applied as excellent catalytic substrate. The enlargement and uniformity of the pore size have positive effects on its application as photocatalytic support.

In **Chapter 10**, a novel colloidal nano-silica is produced from olivine via acid extraction at low temperatures (50~90 ℃) and further grinded with a colloidal mill to break up the agglomerates. The properties of olivine colloidal nano-silica (C-OnS) are characterized with laser light scattering (LLS), nuclear magnetic resonance (NMR), zeta-potential and X-ray florescence (XRF). The highly dispersed C-OnS is applied as an admixture to enhance the cement hydration of UHPC thanks to its strong pozzolanic reactivity at early age compared to commercial colloidal nano-silica (C-nS). The effect of C-OnS and C-nS on UHPC is systematically compared by calorimetry, thermal gravimetry (TG), nuclear magnetic resonance (NMR), nitrogen physisorption and mercury intrusion porosimeter (MIP). The results show that the performance of UHPC is enhanced by substituting cement with the novel C-OnS and is even better than that with CnS at early ages (1, 3, 7 days).

In **Chapter 11**, overall conclusions of the presented work are drawn, and recommendations for the future study are proposed.

Chapter 2 Acoustic performance and microstructural analysis of bio-based lightweight concrete containing miscanthus

This chapter aims at a fundamental research of a bio-based lightweight concrete containing miscanthus (MLC), with the special focus on the acoustic absorption property and interaction between miscanthus and cement hydration. Miscanthus Giganteus (i.e. Elephant Grass) is a cost-effective and extensively available ecological resource in many agricultural regions. The effects of the content, particle size and treatment of fibers on the performance of MLC, including the flowability, strength and acoustic properties, are investigated. Furthermore, the effect of miscanthus on cement hydration is analysed by isothermal calorimetry, X-ray diffraction, thermogravimetry, and scanning electron microscopy. It is demonstrated that the sound absorption of MLC is dramatically strengthened with the increasing content of miscanthus. The results show that there is a certain amount of interconnected pores in the composites, which contribute to this enhanced acoustic absorption performance.

This chapter is partially published elsewhere:

Y. Chen, Q.L. Yu, H.J.H. Brouwers, Acoustic performance and microstructural analysis of bio-based lightweight concrete containing miscanthus, Construction and Building Materials 157 (2017) 839-851.

2.1. Introduction

Recently, natural plant fibers as building materials in construction are of great demand because sustainable development has become a global major concern, in both developed and developing countries. Bio-based insulating materials made from recyclable plant fibers are interesting alternatives to those obtained from fossil carbon. For the sake of constructing environmentally friendly and cost-effective buildings, it is of great interest to design green and low-cost building materials to reduce the environmental impact, particularly related to CO_2-emission.

Natural fibers as lightweight aggregate of building materials are developing fast and are widely used now, for instance hemp, straw, flax and miscanthus [70]. Among other plant-based natural fibres, the adoption of miscanthus has drawn great attention attributed to its widespread availability and lack of competition with food and animal feed [71]. Miscanthus is a perennial plant, located for several years, which reduces costs of crop establishment. Compared to wood, miscanthus has a high content of parenchyma, surrounded by a tough fibrous structure. It therefore combines a high rigidity with a low density [72]. The modulus of elasticity of Miscanthus Giganteus and Miscanthus Sinensis varies between 2 and 8 GPa. Miscanthus has other structural component and is considerably stronger than straw, besides it contains chemical composition like silicon, it could represent a suitable basic material in construction materials.

Therefore, it is promising to develop miscanthus lightweight concrete, which is expected to have a good performance in acoustic absorption because of its lightweight and porous structure. Miscanthus has a significantly lower density than normal weight aggregates and its porosity has a significant effect on its acoustic properties [11]. Constructions built with miscanthus concrete can lower the environmental impact dramatically compared with cellular concrete. Moreover, the lightweight cement-miscanthus composite is a completely recyclable material, which can be ground and later used to produce new lightweight composites [17][73].

Many researchers have studied the acoustic absorption performance of plant-based construction materials. Sound absorption coefficients, ranging from 0-1, are often rather low for normal Portland cement concrete. Various kinds of other construction materials have been studied for obtaining an enhanced sound absorption property, for instance cellular [74] and autoclaved [75] concretes, and concretes incorporating plant materials like hemp. These construction materials all have porous structures which are beneficial for sound absorption. Because sound waves will convert to heat through the pores inside the matrix. Miscanthus-cement concrete can also be characterized as a high porosity material. The existence of pores of different scales, which consist of inter-particle pores (between the miscanthus fibers) and intra-particle pores (inside the miscanthus fibers), enables the dissipation of sound waves. A profound study by Glé et al. has demonstrated the good sound absorption of plant fiber-based concrete by experimental [11] and modelling [76] approaches. Cezero et al. [77] studied the influence of binder to fibers proportion, observing a dramatic decrease of acoustic absorption property with an increased cement content. Therefore, it is reasonable to expect that MLC can possess the same acoustic properties, but further investigation is needed.

Despite all the promising benefits of miscanthus fibers, there exists severe concerns for the practical application of natural plant fibers in cement and concrete. Like other natural plant fibers, the miscanthus fibers have a large differentiation of fiber qualities, high water absorption ability, and issues of compatibility with cement paste, which is an alkali environment [78]. The dissolution of lignin and hemicellulose in the middle lamellae of fibers delays the cement hydration process and in return alkali degrades fibers as well [79]. Therefore, in order to overcome the aforementioned durability problem, a proper understanding of the interaction mechanism of miscanthus is required [19]. Many researchers explored the methods to enhance the durability of concrete containing natural fibers. Romildo et al. [80] demonstrated that the methods comprise carbonation of the cement paste in a carbon dioxide atmosphere and pre-treatment of fibers with immersion in silica fume slurry before mixing with cement paste. Mármol et al. [81] suggested that the use of low alkalinity cement paste incorporated with supplementary cementitious materials could be an approach to relieve the severe damage on cellulose fibers.

The chapter aims at investigation of an environmentally friendly bio-based lightweight concrete with the addition of miscanthus fibers, with the special focus on acoustic absorption property and the interaction between cement hydration and miscanthus. Pre-treated miscanthus fibers with different sizes and percentages are adopted to prepare the miscanthus based lightweight composites. Furthermore, the mechanical and acoustic properties are studied. Moreover, the interaction mechanism between miscanthus and cement paste is investigated through advanced test technologies, including X-ray diffractometry, thermogravimetry and isothermal calorimetry. This work will contribute to a deeper understanding of miscanthus usage in construction materials, especially for non-structural walls and ceilings, indoor furniture or some other outdoor structures like noise barriers.

2.2 Materials and experiments

2.2.1 Raw materials

2.2.1.1 Miscanthus

Miscanthus is provided by Vibers (the Netherlands). The miscanthus is harvested in winter and further treated by the company. The morphology of the raw miscanthus fibers is shown in **Fig. 2.1**. The size and shape of miscanthus fibers are varied, so sieving is required for producing a regular size of the fibers. 2 mm and 4 mm size sieves were adopted in this study and fibers were sieved in a sieving machine. **Fig. 2.1 (a)** and **(b)** show the 0-2 mm and 2-4 mm size fibers in bulk, respectively. Meanwhile miscanthus powder is another type of product from the company, which is shown in **Fig. 2.1 (c)**. The lengths of the fibers are about 2 to 20 mm long while the diameters are classified by the sieving process. Therefore, the sieving process is a sorting of diameter rather than of length.

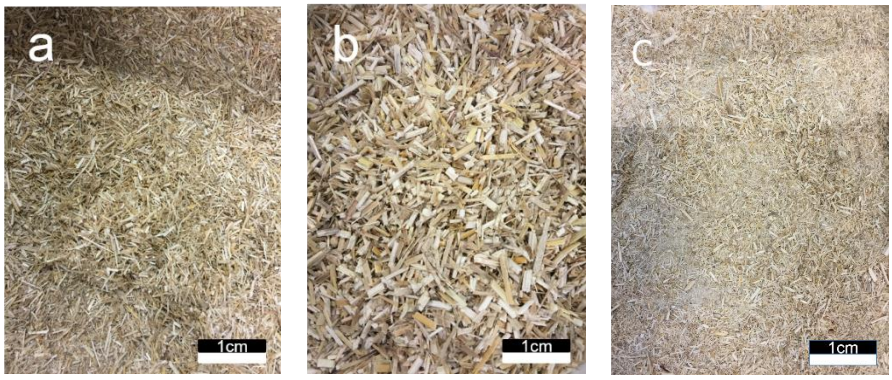

Fig. 2.1. Pictures of the raw miscanthus.

The chemical composition of miscanthus is analyzed via acid hydrolysis method. Monomeric sugars after H_2SO_4 hydrolysis measured with HPAEC (High-Performance Anion-Exchange Chromatography) is presented in **Table 2.1**. The leachate was prepared by boiling the fibers for 2 h in water with a water to fiber ratio of 5.

Table 2.1. Concentration of sugar leached from miscanthus.

Monomeric Sugar (mg/ml)	Arabinose	Galactose	Glucose	Xylose	Mannose
Concentration	0.06	0.09	0.19	0.16	0.05

2.2.1.2 Cementitious materials

The cement used in this research is Portland Cement CEM I 52.5 R, provided by ENCI, Heidelberg Cement (the Netherlands). The supplementary cementitious material is ground granulated blast furnace slag (GGBS), provided by ENCI as well. The chemical composition of cement and GGBS were analyzed by X-ray fluorescence as shown in **Table 2.2**. The used slag has a median particle size (d50) of 12.43 μm and a specific density of 2.93 g/cm^3, which are measured by Mastersizer 2000 and Helium pycnometer, respectively. A polycarboxylic ether-based superplasticizer (SP) is adopted to modify the flowability of the designed MLC.

Table 2.2. Oxides composition of the used cement and GGBS (wt.%).

Oxides	CaO	SiO_2	Al_2O_3	Fe_2O_3	SO_3	MgO	K_2O	Na_2O	LOI
Cement	64.60	20.08	4.98	3.24	3.13	1.98	0.53	0.27	0.4
GGBS	4.44	54.62	24.42	7.21	0.46	1.43	1.75	0.73	4.5

2.2.2 Experimental

2.2.2.1 Characterization of miscanthus

2.2.2.1.1 Density and porosity

The bulk density of miscanthus fibers is determined according to the fixed volume method. In brief, fibers are filled in a 1 liter graduated iron cup and the mass of the cup before and after filling is measured. No vibration or compaction is adopted in the filling process. Then the bulk density is calculated according to

$$\rho_b = \frac{(M - M_0)}{V_0} \tag{2.1}$$

where ρ_b is the bulk density, M_0 and M are the mass of graduated cup before and after filling, V_0 is the volume of the cup, which equals to 1 litre.

The particle density of miscanthus fibers is determined according to the water displacement method. In brief, 20 gram of dry fibers is immersed in water for 6 hrs and then the excess water is removed by filtration. Water remaining on the surface of saturated fibers is wiped out by carefully clapping using a filter paper. Then the mass of water saturated fibers is determined. The particle volume is then determined through immersing the saturated fibers in a specific volume of water. Then the increased volume of water is the particle volume Vp. The particle density is calculated according to

$$\rho_p = \frac{M_d}{V_p} \tag{2.2}$$

where ρ_p is particle density, M_d is the dry mass of fibers, V_p is the particle volume of fibers.

The skeleton density of miscanthus is measured by a Helium pycnometer (AccuPyc II 1340 Micromeritics). This density is closely related to the volume of the particles without intra-particle pores and the mass of the skeleton [82].

The total connected porosity of miscanthus fibers is noted as Φ in this research. Miscanthus fiber is a granular aggregate, therefore it can be represented by two kinds of porosities, the intra-particle porosity Φ_{intra} and the inter-particle porosity Φ_{inter}. Inter-particle porosity, which is determined according to

$$\Phi_{Inter} = 1 - (\frac{\rho_b}{\rho_p}) \tag{2.3}$$

where Φ_{inter} is the inter-particle porosity of miscanthus fibers, ρ_b and ρ_p are bulk density and particle density, respectively. Intra-particle porosity is determined according to

$$\Phi_{Intra} = \frac{(M_s - M_d)/\rho_0}{V_p} \tag{2.4}$$

where Φ_{intra} is the intra-particle porosity of miscanthus fibers, M_d and M_s are the mass of dry fibers and water saturated fibers, ρ_0 is the density of water, V_p is the particle volume.

2.2.2.1.2 Water absorption

Water absorption is measured by immersing the miscanthus fibers in tap water and measuring the soaked miscanthus mass after 5, 10, 30 60, 120, 360, 720 and 2880 min, respectively. The water absorption capability is represented by the ratio of water soaked miscanthus weight and dry miscanthus weight. In brief, 20 g dry miscanthus fibers are immersed in water in a beaker. After specific period of time, the soaked fibers are filtrated, so the water is removed while fibers remain on the filter paper. The fibers surface is then carefully clapped with another dry filter paper to remove the surface water. Finally, the water-saturated fibers are weighed so the water absorption can be determined.

2.2.2.2 Pre-treatment of miscanthus

Miscanthus is pre-treated with two approaches, i.e. water saturated and cement impregnated. For the pre-wetting treatment, the dry miscanthus is immersed in water in a container for 6 h and then the excess water is removed using a 200 μm sieve. Then the miscanthus surface is carefully clapped with dry paper to remove the surface water and the miscanthus is ready for use. For the cement impregnation treatment, 200 g of dry miscanthus is placed in a mixing bowl and then mixed with cement slurry with a cement and water usage of 400 g and 400 g, respectively. Then the mixture is mixed for 2 min and then cured in room temperature for 3 days and the cement impregnated miscanthus is ready for use.

2.2.2.3 Design of miscanthus lightweight concrete

The mix design of miscanthus lightweight concrete is presented in **Table 2.3**. Firstly, the cement and GGBS are blended in the mixer for about 1 min. Afterwards, water is added and mixed with the cement and GGBS for another 2 min. Subsequently the pre-treated miscanthus is added into the mixer and mixed for an additional 2 min. Later the superplasticizer is slowly added into the mixer until the end of the mixing procedures. The mixing process takes about 7 minutes. The preparation process is under laboratory conditions. The room temperature during the mixing and measuring is constant, around 20 ±2 ^{o}C.

Table 2.3. Mix design of miscanthus cement composite.

Mixture	Cement (kg/m^3)	GGBS (kg/m^3)	Water (kg/m^3)	SP (%)[a]	Pre-treated[b] Miscanthus (Liters/m^3)		
					Powder	0-2 mm	2-4 mm
Mix A	1020.7	255.2	572.5	0.1%	-	-	-
Mix B	918.6	283.6	515.3	0.1%	-	-	100
Mix C	816.6	204.2	458.0	0.1%	-	-	200
Mix D	714.5	178.6	400.8	0.1%	-	-	300
Mix E	918.6	283.6	515.3	0.1%	-	100	-
Mix F	816.6	204.2	458.0	0.1%	-	200	-
Mix G	714.5	178.6	400.8	0.1%	-	300	-
Mix H	918.6	283.6	515.3	0.1%	100	-	-
Mix I	816.6	204.2	458.0	0.1%	200	-	-
Mix J	714.5	178.6	400.8	0.1%	300	-	-

*a: SP is used to adjust the flow of the composite the dosage should be adjusted in practical experiment. *b: Pre-treatment include water saturated and cement impregnated so every mix includes two kinds of miscanthus.

2.2.2.4 Mechanical properties of miscanthus lightweight concrete

Workability of MLC was measured by the mini spread-flow test, following EN 1015-3 [83]. Fresh MLC was placed into a normal conical ring and followed by a 15-times jolting. The diameter of cement paste was measured 4 times after jolting and the average value was noted as the slump flow.

After mixing, the fresh MLC was cast into 40 mm×40 mm×160 mm moulds and vibrated on a jolting table. After 1d from casting, samples are stripped from the moulds and placed in a climate chamber with a relative humidity of above 95% and temperature of about 20 ^{o}C, according to EN 12390-2 [84]. Then after 28 days curing, the density of MLC samples were measured according to EN 12390-7 [85].

The compressive and flexural strength measurements were proceeded following EN 196-1 [86]. The compressive and flexural strength value for each sample were obtained from the average of six and three specimens, respectively.

2.2.2.5 Acoustic property of miscanthus lightweight concrete

To determine the sound absorption coefficient, the impedance tube (see **Fig. 2.2**) at the Acoustic Lab at Eindhoven University of Technology was used. In this research, the impedance tube measures both the normal incidence absorption coefficient and surface impedance under well-defined and controlled conditions. In brief, the measurement principle is through generating a plane wave by a loudspeaker on the one side of the tube that is then spreading through the tube before reflecting by the MLC. The MLC changes the reflected wave and by collecting the generated standing wave, the sound absorption coefficient of the samples can be determined. The wave was measured at six different locations in the tube. This was done to increase the accuracy as described in the measurement protocol for the impedance tube. MLC samples were inserted at the end of the impedance tube and backed by a rigid surface.

Fig. 2.2 Pictures of the used impedance tube.

2.2.2.6 Interaction between miscanthus and cement hydration

Qualification and semi-quantification of hydration products of pure cement paste and MLC were assessed by X-ray diffraction, which were carried out by an X-ray diffractometer D5000 Siemens. The X-ray diffraction (Cu tube, 40 kV, 30 mA, 3-75^{o}, 0.02^{o}/step, 0.2^{o}/ min, variable divergence slits V20) was adopted to detect the crystal structure present in MLC.

Thermogravimetric curves of cement pastes with addition of miscanthus were assessed by a thermogravimeter and differential scanning calorimeter (TG/DSC), which were conducted by a NETZSCH STA449-F1 instrument in the range of room temperature to 1000 °C with a heating rate of 5 ^{o}C·min^{-1} under nitrogen atmosphere.

The cement hydration process was monitored by an isothermal calorimeter (TAM Air, Thermometric). The cement paste and miscanthus were blended with de-ionized water externally for about 1 min and vibrated with an electrical vibrator, then the mixed paste was injected into a sealed glass ampoule and loaded into the calorimeter. All measurements were conducted for 72 h under a constant temperature of 20 °C. The heat release and heat flow results were normalized by mass of binder, miscanthus and de-ionized water.

The microstructure of miscanthus fibers was observed by scanning electron microscopy (SEM), which was conducted by JOEL JSM-5600 instrument with an accelerating voltage of 15kv.

The element concentration of cement paste mixtures adopting a constant water to cement mass ratio (W/C = 2) was examined by HPLC (High Performance Liquid Chromatography). In brief, cement paste was incorporated with different fiber contents (3%, 5% and 10% based on mass). Afterwards, the plastic bottle that contains the paste was placed in a shaker machine to keep the paste fluid for 1d with a rate of 250 r/min. Then the mixtures were filtrated and the calcium, sodium and potassium ion concentration of extracted aqueous phase were measured by HPLC.

2.3. Results and discussion

2.3.1 Characterization of miscanthus

2.3.1.1 Density and porosity

The bulk density, particle density, skeleton density, inter-particle and intra-particle porosity are shown in **Table 2.4.** The particle density is important for the volume calculation of miscanthus used in mix design. The skeleton densities of all fibers are almost the same, which is due to all miscanthus fibers are made up of cellulose, hemicellulose and lignin and the density of those are 1559 kg/m^3, 1520 kg/m^3 and 1260 kg/m^3, respectively. Inter-particle porosity is a significant factor that influences the acoustic property of biomass. The primary concern is that cement paste may interact with miscanthus fibers. However, the number of affected inter and intra particle pores are difficult to calculate. Cement paste not only has a dramatic impact on the inter-particle pores, but also forms a mineralized coating on the fibers and blocks the intra-particle pores.

Table 2.4. Density and porosity of different types of miscanthus.

Miscanthus	Bulk density(kg/m^3)	Particle density (kg/m^3)	Skeleton density (kg/m^3)	Inter-particle porosity (%)	Intra-particle porosity (%)
powder	155.6 ± 3.1	173.9 ± 2.2	1410 ± 10	10.5 ± 0.9	77.2 ± 0.5
0-2 mm	77.6 ± 1.3	222.2 ± 3.6	1406 ± 16	65.1 ± 1.2	58.1 ± 1.5
2-4 mm	119.4 ± 2.6	250.0 ± 1.5	1400 ± 21	52.2 ± 1.6	38.3 ± 2.1

2.3.1.2 Morphology

The scanning electron microscopic images of 2-4 mm miscanthus fibers are shown in **Fig. 2.3**. The miscanthus fibers possess very porous structures. From **Fig. 2.3 (a)** one can see that

the surface of the stem has two paralleled linear structures, one is relatively smooth while the other one has regular nodes positioning on the surface of stem. The nodes increase the roughness of the fiber. **Fig. 2.3 (b)** shows that the internal structure of the stem has a rather rough surface due to shredding process. Lots of cavities and walls can be observed and the size of pores are about 30-50 μm in average, which is smaller than that of hemp [11]. **Fig. 2.3 (c)** shows the cross section of the fiber. A great number of pores is shown inside the stem, while the outside of the stem has a denser structure, indicating fibers are more porous from outside to inside. It can be concluded that miscanthus fiber is a very porous structure with many cavities and pores, which is beneficial when applied as a lightweight aggregate.

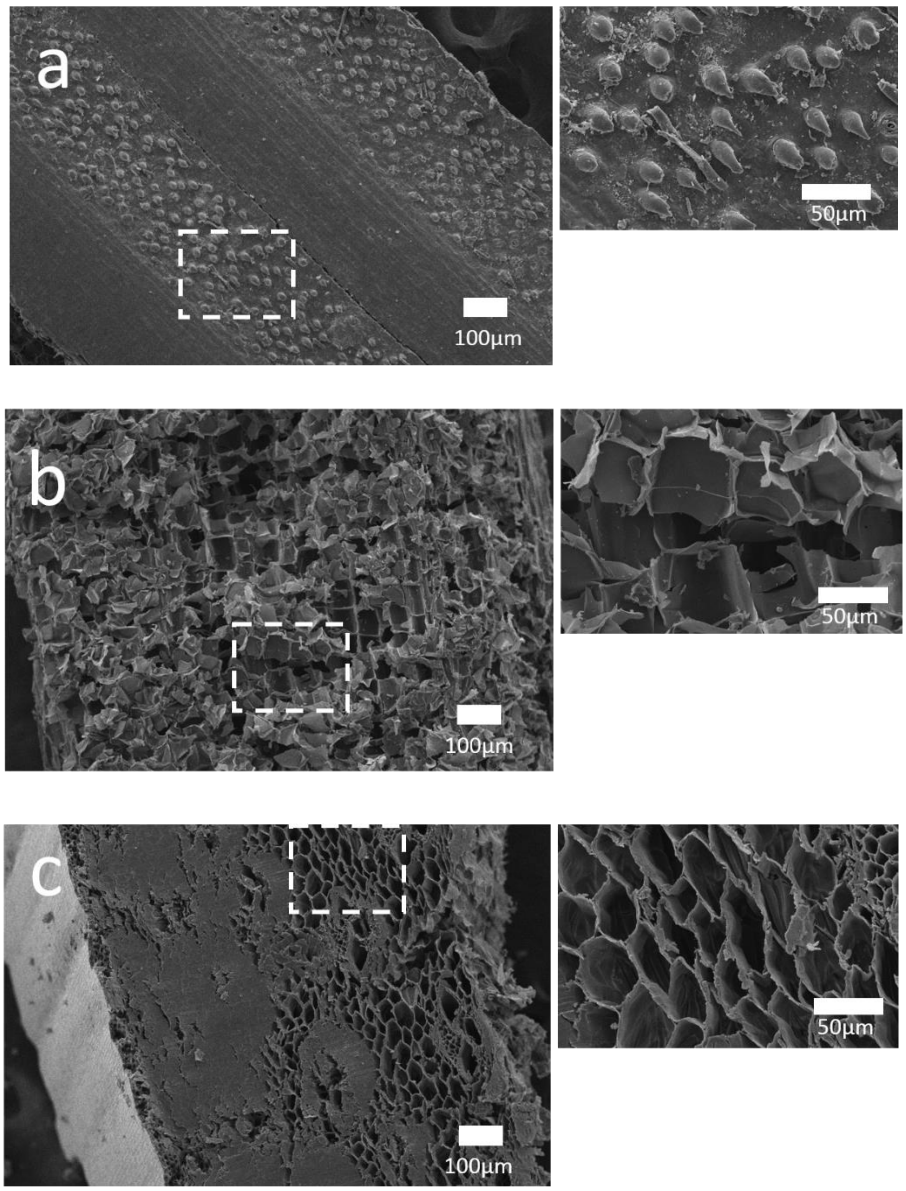

Fig. 2.3 SEM images of 2-4 mm miscanthus fibers: (a) surface (b) inside (c) cross section.

However, 0-2 mm miscanthus fibers possess smaller and closed pores, as shown in **Fig. 2.4** (a). The internal stem that is exposed outside shows more closed pores. Therefore, this type of fiber is not beneficial for acoustic property of lightweight concrete. Although this kind of fine

green aggregate can act as filler in cement system, acoustic absorption property is not expected to be significantly improved by adding this type of aggregate.

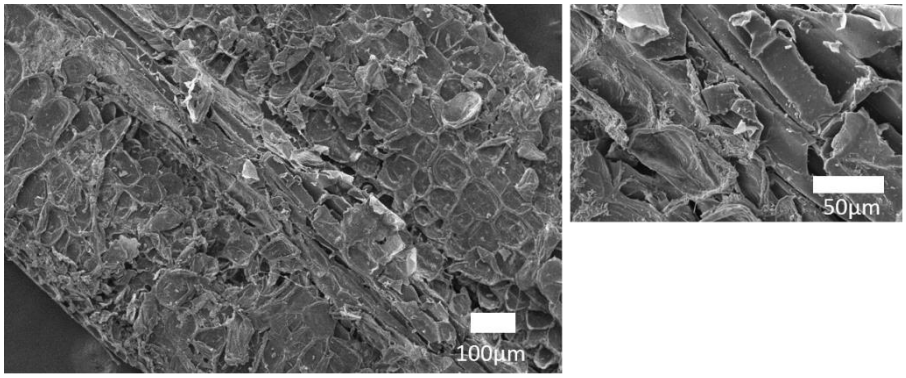

Fig. 2.4 SEM images of miscanthus: 0-2 mm fibers.

2.3.1.3 Water absorption

The water absorptivity of different sizes of miscanthus is shown in **Fig. 2.5**. The miscanthus powder and 0-2 mm fibers have larger water adsorption capability compared to 2-4 mm fibers, reaching 524% and 396% at 2880 min, respectively. The finer fibers can absorb water more quickly at early age and reach equilibrium much sooner than larger fibers. For instance, the miscanthus powder reached an absorptivity of 440% only 5 min, and increase constantly for another 60 min to 490%. Meanwhile the absorptivity of 0-2 mm fibers also increases sharply, reaching 330% at 5 min and 380% at 60 min. The finer the miscanthus, the larger amount of water it absorbs; the observations under microscope indicates that the quality of the interpenetration is directly influenced by the porosity of the external wall of the vegetal, mainly by the degree of fragmentation [72]. The water absorption of 2-4 mm fibers reached 180% at 5min and 290% at 2880 min. Obviously the time to reach equilibrium is longer and the slope of the absorption curve at early age is much lower than those of powder and 0-2 mm fibers. Large fibers contain the intact plant stem and consequently the ability of stem to absorb water becomes a key factor. However, the specific surface area of 0-2 mm fibers and miscanthus powder are much larger than 2-4 mm fibers, resulting in higher water absorptivity.

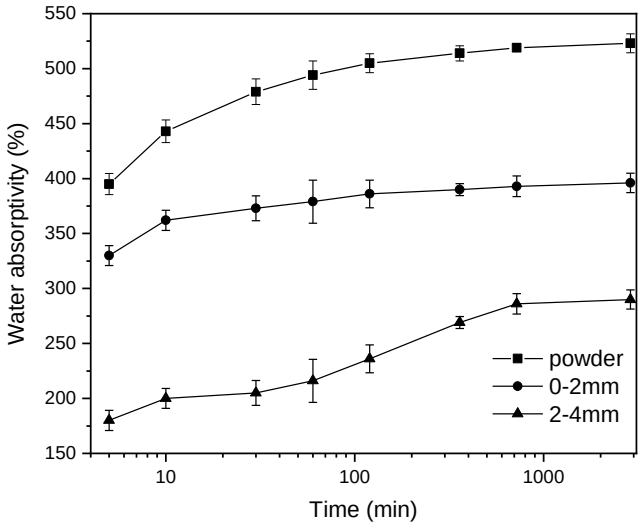

Fig. 2.5. Water absorptivity of miscanthus with different sizes.

2.3.2 Mechanical properties

2.3.2.1 Flowability

The slump flow of the different miscanthus-cement mortars with a w/b ratio of 0.45 is presented in **Fig. 2.6**. M0, M10, M20 and M30 represent 0, 10%, 20% and 30% miscanthus volume dosages, respectively. Miscanthus decreases the flowablility of MLC as the content of miscanthus fibres increases. For 2-4 mm and 0-2 mm fibers, the samples show similar slump flow results; while for miscanthus powder, the slump flow is better but also slightly decreases. Due to the pre-treatment of fibers, reduction in flowability is not attributed to the water absorption of miscanthus fibers, but closely related to the fiber aspect ratio and volume fraction in cement paste, which is in agreement with other literatures [87]. Mansur and Aziz concluded the workability of jute fiber cement composite decreased with the increasing length and volume fraction of the fibres [88]. Hence, in order to obtain a better slump flow for a high miscanthus dosage, more superplasticizer should be applied but in an appropriate amount to prevent segregation.

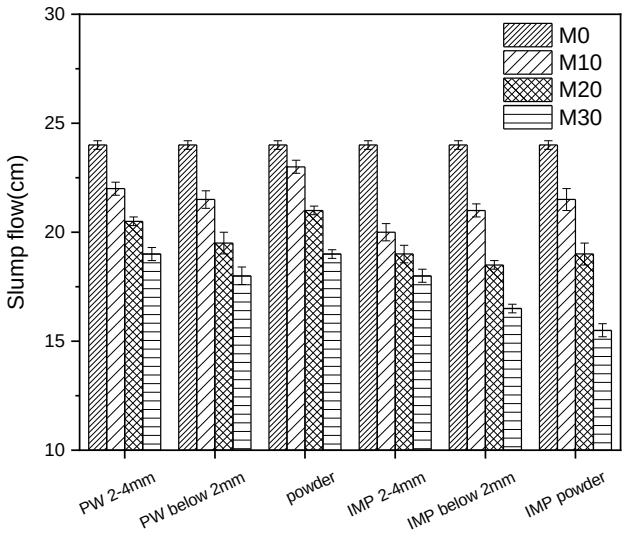

Fig. 2.6. Slump flow of different cement-miscanthus composite mortars with a w/b ratio of 0.45.

2.3.2.2 Strength and density

In general, the density and compressive strength of all samples dramatically decrease with the increasing content of miscanthus fibers. This is attributed to more voids and pores in the hardened cement paste introduced by the fibers, and the compressive strength of miscanthus itself is rather weak as well. The incorporation of miscanthus has less negative effect on the flexural strength, attributed to the crack bridging effect of fibers and its good tensile strength (180~260 N/mm^2) [78].

The dry densities of miscanthus concrete with different sizes of pre-wetted and cement impregnated miscanthus is presented in **Table 2.5.** The dry density of concrete decreases dramatically from 1540 kg/m^3 to 1160 kg/m^3 with 30 vol.% pre-soaked 2-4 mm miscanthus fibers. The obvious reduction in dry density is mainly due to the low density of the used miscanthus fibers. While for cement impregnated fibers, the dry density of MLC only reduces to 1440 kg/m^3, which is due to the increase of fibers particle density. The trend is also observed

for 0-2 mm fibers-cement composite. However, for the powdered miscanthus concrete, the apparent dry density only reduced to 1255 kg/cm^3, which is due to the altered porous structure caused by the grinding process.

Table 2.5. Dry density of miscanthus lightweight concrete.

Dry density (kg/m^3)	Reference	Pre-soaked			Cement Impregnated		
		2-4 mm	0-2 mm	Powder	2-4 mm	0-2 mm	Powder
10%	1540	1504	1479	1488	1520	1510	1520
20%	1540	1406	1333	1356	1436	1475	1487
30%	1540	1160	1129	1255	1340	1415	1460

The compressive strength of miscanthus concrete with different sizes of pre-wetted and cement impregnated miscanthus at 28d are presented in **Table 2.6**. The compressive strength of composites containing pre-soaked miscanthus decreases by 60~80% in comparison with the pure cement paste. Though several factors might contribute to the loss of mechanical strength, the decrease in composite bulk density and pores and voids introduced by fibers would mainly be responsible for such behavior [71]. In fact, the fibers can act as voids in hardened cement paste because of their super lightweight property, so more fibers equal to more pores in cement. However, all cement impregnated samples show better performance than pre-soaked samples. Cement impregnated fibers possess a better mechanical strength and a higher density, the surface of fibers is much rougher as well. Moreover, the retarding effect of sugar leached from fibers has disappeared after the pre-treatment. Therefore the only problem is the defect bond between aggregates and cement paste, which can decreases the compressive strength dramatically [89].

Table 2.6. Compressive strength of miscanthus lightweight concrete at 28 days.

Compressive strength (MPa)	Reference	Pre-soaked			Cement Impregnated		
		2-4 mm	0-2 mm	Powder	2-4 mm	0-2 mm	Powder
10%	55.4	14.8	13.4	17.58	23.14	23.69	28.21
20%	55.4	11.0	6.8	11.02	15.97	21.17	24.12
30%	55.4	5.21	2.26	3.59	10.78	14.59	16.87

The cross-link comparison between oven dry density and compressive strength of various types of LWC is presented in **Fig. 2.7**. An obvious increasing tendency of the compressive strength can be noticed when the oven dry density of lightweight concretes increases from around 300 kg/m^3 to about 2100 kg/m^3 [71,78,97–99,87,90–96]. Furthermore, it can be noticed that the compressive strength of miscanthus lightweight concrete is lower than those of other LWCs at the same density range, especially at low densities, but slightly higher than those of other bio-based LWCs, which implies that the developed miscanthus lightweight concrete obtain moderate mechanical performance between these two kinds of LWCs.

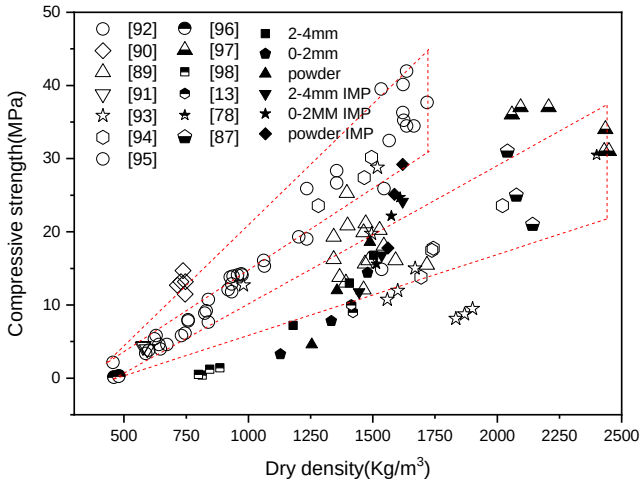

Fig. 2.7. Relationship between the compressive strength and dry density for different types of lightweight concrete at 28 days.

The flexural strength of miscanthus concrete at 28d is presented in **Table 2.7.** The flexural strengths of all composites manufactured with miscanthus do not dramatically change compared to the pure cement paste. For 2-4 mm fibers, the flexural strength slightly decreases with the increasing amount of fibers and cement impregnated samples have a better performance. For 0-2 mm fibers, the flexural strength dramatically decreases, especially for 30% pre-soaked miscanthus sample. However, when the fiber is cement impregnated, the flexural strength of 30% content sample is much higher, even exceeding the reference sample at 28 days. For miscanthus powder, the flexural strength is comparable with the reference at low miscanthus dosages but becomes very low at 30%. When powder is cement impregnated, the strength becomes higher than pure cement paste, indicating cement impregnated miscanthus powder can reinforce the flexural strength of cement mortar. Overall, the smooth flat surface of the pre-soaked fibers leads to a poor bonding with the cement paste and a fiber pull-out failure without any stress transfer [78]. Hence the adoption of pre-wetted fibers as reinforcement in concrete is limited. However, cement impregnated fibers can have a positive effect on flexural strength of cement composite.

Table 2.7. Flexural strength of miscanthus lightweight concrete at 28 days.

Flexural strength (MPa)	Reference	Pre-soaked			Cement Impregnated		
		2-4 mm	0-2 mm	Powder	2-4 mm	0-2 mm	Powder
10%	4.53	3.7	2.96	3.36	2.88	3.17	5.89
20%	4.53	2.14	1.98	3.2	2.9	3.56	5.98
30%	4.53	1.93	1.12	1.29	3.21	4.57	5.78

2.3.3 Acoustic absorption

In this research, acoustic characterization was carried out on MLC incorporated with 2-4 mm miscanthus fibers, due to its different pore structure compared with 0-2 mm fibers and powder. Concretes prepared with 2-4 mm miscanthus fibers pre-treated with pre-wetting treatment, were tested with 40 mm diameter impedance tube.

The acoustic absorption of MLC incorporated with 2-4 mm fibers for various contents of miscanthus is presented in **Fig. 2.8**. **Fig. 2.8 (a)** shows that the pure cement paste has a rather weak sound absorption capability, which is due to the dense structure and less porosity of cement paste. However, when miscanthus fibers are incorporated, the absorption coefficient increases significantly with increasing the content of miscanthus, from 0.28 to 0.63. For 10% replacement of miscanthus, the frequency of absorption peak remains the same at about 700Hz as that of pure cement. While for 20% and 30% replacement the sound absorption peak frequency is shifted to higher value at about 1200 Hz and 1300 Hz, respectively. It is due to the increased content of miscanthus fibers which means more interconnected pores with different scales inside the cement paste [11]. Porous materials have a better sound absorption among high frequency range. Miscanthus fiber is a porous material with a great amount of open pores and cement paste porosity can increase with the incorporation of miscanthus. All these factors lead to a better performance in acoustic absorption.

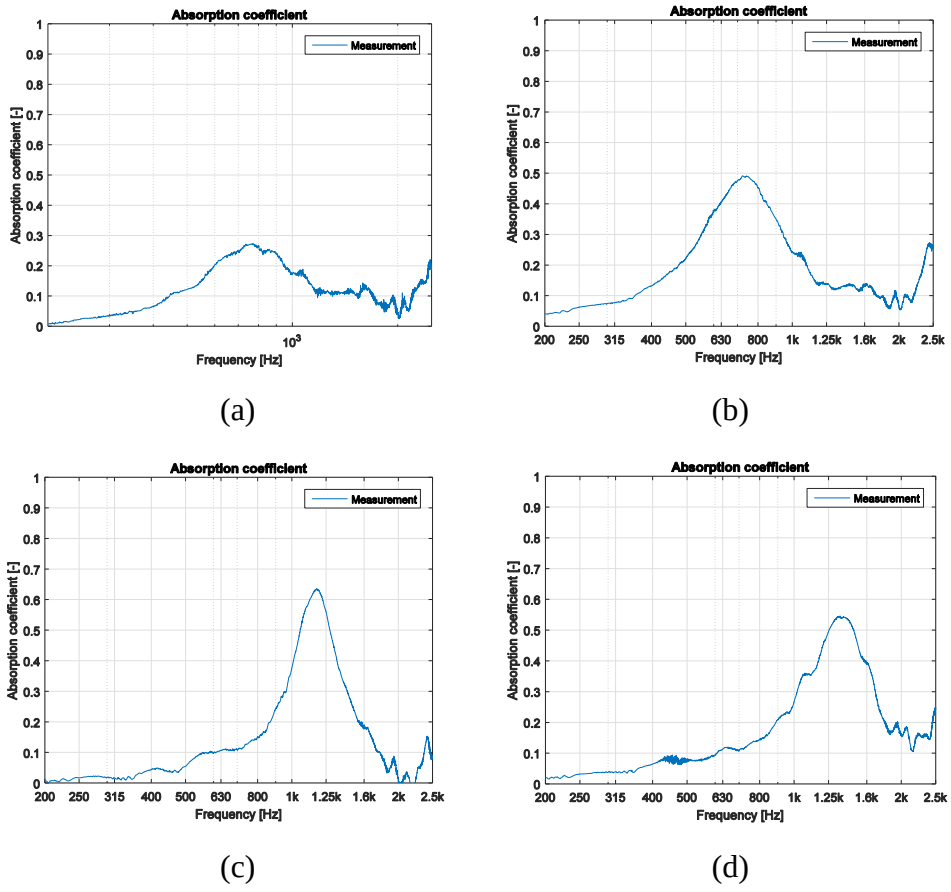

Fig. 2.8. Sound absorption of miscanthus cement composites for various content of 2-4mm fibers: (a) Ref (b) M10 (c) M20 (d) M30.

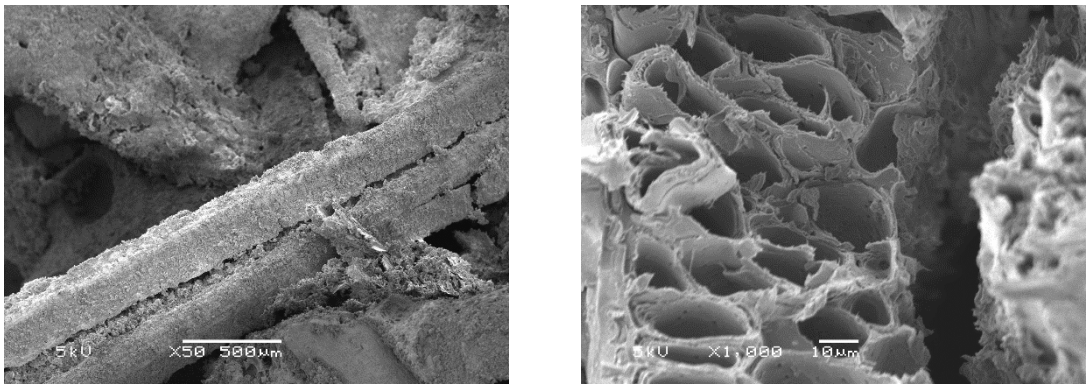

(a) (b)

Fig. 2.9 SEM images of fracture surface of MLC.

The SEM images of MLC matrix showing the microstructures is presented in **Fig. 2.9**. As can be observed in **Fig. 2.9 (a)**, inter-particle pores are obviously present between the miscanthus fibers, which is an advantageous feature for sound absorption property. The 2-4 mm fibers can lower the workability of cement paste and consequently the porosity of matrix increases. Furthermore, the microstructure shown in **Fig. 2.9 (b)** exhibits a clear structure of fibers intra-particle pores. The dense distribution of pores in the straw of miscanthus can also have a positive influence on the acoustic property of MLC.

There exist also other types of green lightweight concrete used as acoustic absorber, especially for hemp shiv, which is similar as miscanthus concrete. Starch-hemp composite designed by [99] can reach a sound absorption coefficient of 0.7 at frequency of 1250Hz. Hemp concrete [11] prepared with lime binder can reach a sound absorption coefficient of 0.6 but at low frequency of about 150Hz, which may be due to the larger impedance tube adopted (a length of 5.5 m and a square section of 60×60 cm^2, samples are 10 cm in thickness). Other types of green aggregate such as sunflower stalks and corn stalks were also investigated [100,101], but the results are not that good compared with the hemp and miscanthus fibers, which may be explained by the fabrication method and the nature of vegetables. Gle [11] demonstrated acoustic properties are influenced by the pores of plant-based aggregate concrete, which is mainly combined with micro grade pores of cement paste and granularity of plant particle, and larger pores among the plant aggregates. Therefore, the acoustic absorption of MLC falls in between the perfect acoustic absorption of vegetable fibers, and the variation of the sound absorption of cement paste.

2.3.4 Interaction between miscanthus and cement paste

The influence of miscanthus fibers on the hydration of cement was analysed by advanced testing technologies. The X-ray diffraction patterns of pure cement paste and cement paste with 10% miscanthus fibers cured for 3 days are presented in **Fig. 2.10**. It is evident that the hydration products are primarily C-S-H gel, portlandite and ettringite. The characteristic peaks of portlandite of pure cement paste are much higher than those of M10, indicating a higher hydration degree of cement. Meanwhile the amount of C-S-H gel generated is also much larger than that of M10, which is due to the retarding effect of sugars dissolved from miscanthus. The C-S-H gel is the primary phase for strength of hardened cement paste, which explains when 10%

miscanthus fibers is incorporated, a much lower strength is obtained. Similar XRD results are obtained by other researchers studying the interaction of plant fibers and cement. Fan [102] demonstrated that the intensity of portlandite peaks decreased dramatically for the plant-cement composites. It is attributed to poisonous organic extracted from wood that leads to a reduction of portlandite formed.

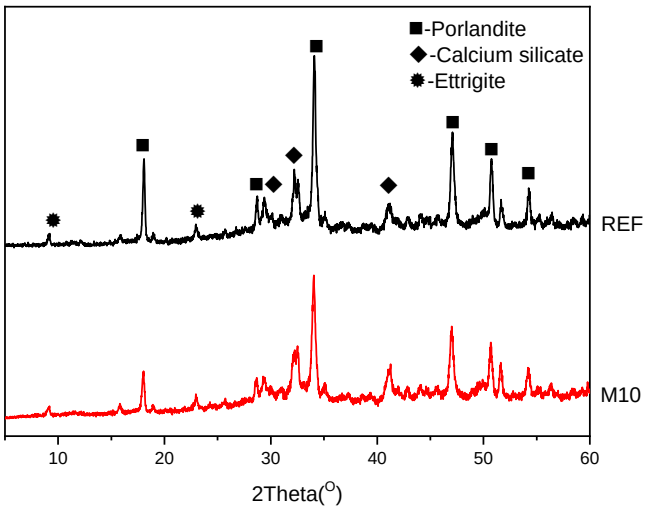

Fig. 2.10. XRD patterns of pure cement paste and cement paste with 10% miscanthus fibers cured for 3d.

Thermogravimetric curves of pure cement paste and cement paste with 3%, 5% and 10% mass percent miscanthus fibers cured for 3,7 and 28 days are shown in **Fig. 2.11**. All test specimens present a significant mass reduction before about 100 ºC due to the evaporation of water, which is physically bound in the cement paste. With the increasing temperature, the gradual and continuous mass loss ranging from around 180 °C to 420 °C is attributed to the breakdown of calcium silicate hydrate gels. It can be noticed that with the rising percentage of miscanthus fibers the C-S-H gels formation is decreased significantly for all the ages, indicating a slower hydration process.

The significant reduction of thermal gravity curve between 420 °C and 480 °C is attributed to the decomposition of calcium hydroxide, which is a direct indicator of cement hydration degree. It can be monitored that 3.0% mass loss is detected for pure cement paste at 3 days while for 10% miscanthus fibers only 1.3% mass loss is detected. Hence the cement hydration process is delayed since the very initial age.

Because the used cement is a rapid cement, the hydration is very quick during the first 7 days while for miscanthus cement the hydration degree is much slower, which can be evidenced by **Fig. 2.11 (b)**. However, when it approaches 28 days, the hydration degree of 3% miscanthus cement is largely increased, indicating the retarding effect is gradually disappeared while for 5% and 10% miscanthus cement the increase of cement hydration degree is negligible. This may be due to the retarding effect of high concentration of leached sugars from miscanthus fibers, which poisoned the cement severely.

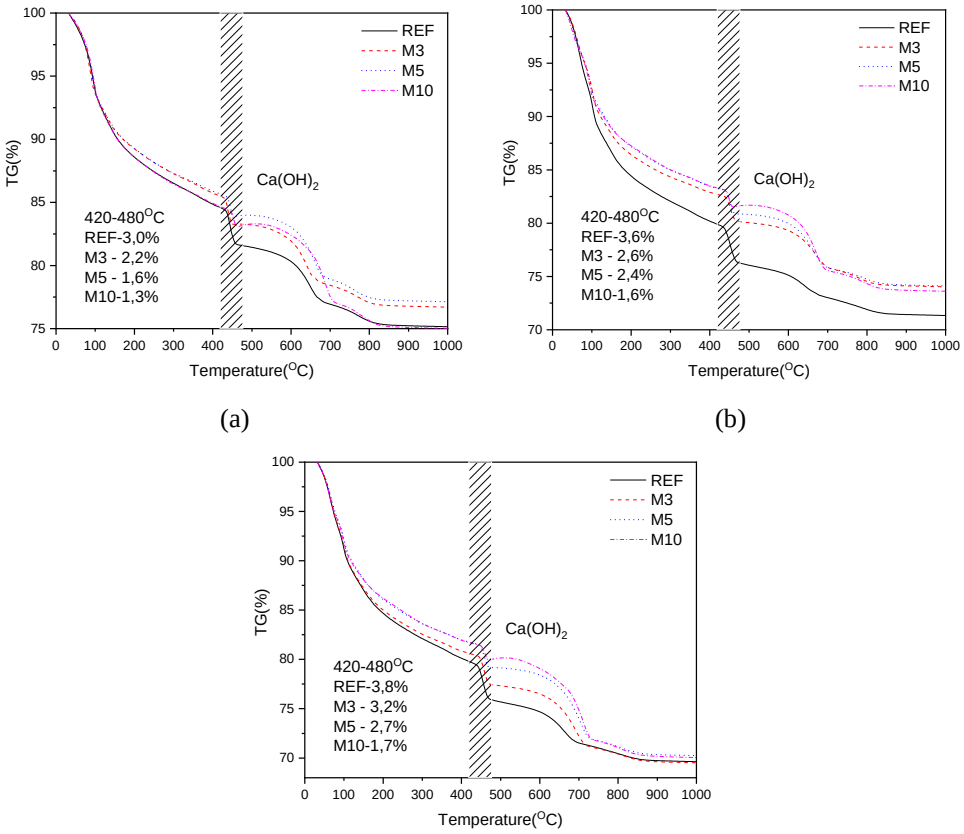

Fig. 2.11. Thermogravimetric curves of pure cement paste and cement paste with 3%, 5% and 10% miscanthus fibers cured for (a) 3d, (b) 7d and (c) 28 days.

The normalized heat flows of pure cement pastes and pastes with the addition of different types of miscanthus fibers are presented in **Fig. 2.12** (left). The characteristic peak of the acceleration period is situated at about 12 hours after the beginning of the test, indicating the formation of reaction products. It can be noticed that as the miscanthus fibers are added, the peak of the acceleration period significantly transfers to later times and exhibits lower intensities, suggesting the reaction process of cement hydration is dramatically delayed with the addition of miscanthus. The results are in accordance to previous studies on the influence of miscanthus or other plant fibers on cement hydration [103]. Miscanthus dissolute organics in cement matrix, which poison cement and prevent the generation and growth of cement hydration products [104]. However, the most severely poisoned sample is the one incorporated with 0-2 mm fibers, the intensity of the heat flow is the lowest while the time delayed is the longest as well. For 2-4 mm and the powder samples, they show similar trend and powder sample is slightly delayed longer while with more heat released.

Fig. 2.12 (right) shows the cumulative heat evolution of the pure cement paste and paste with the addition of different types of miscanthus fibers. For a fixed miscanthus content, test specimens with 0-2 mm fibers show the lowest total heat release, suggesting the existence of 0-2 mm fibers strongly delayed the cement hydration during the test period; however, for specimens with 2-4 mm and powder miscanthus, they show dramatically larger total heat release, which indicates a less harmful impact on cement hydration. It is noteworthy that 0-2

mm fibers show darker extracted solution when immersed in water, indicating more organic materials dissolved in water, which is detrimental to cement hydration.

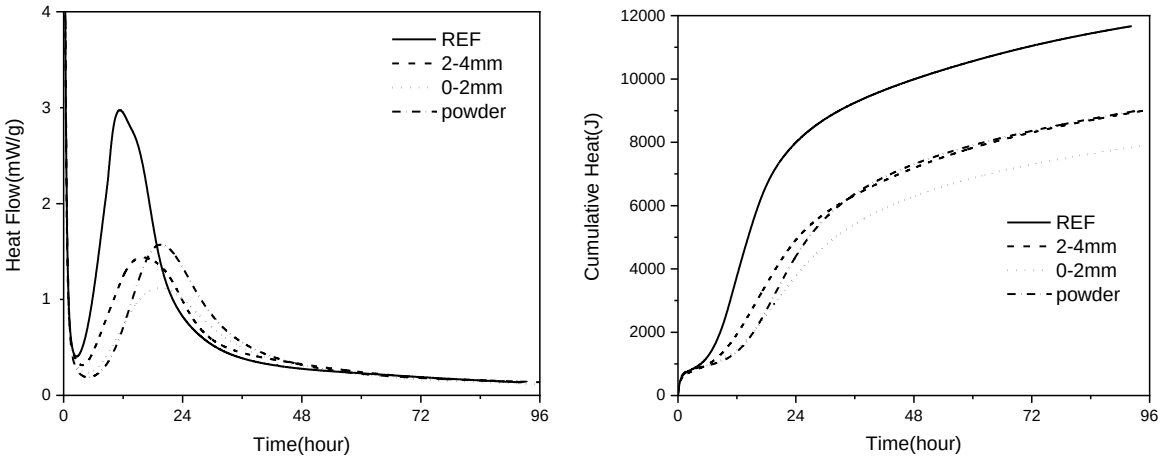

Fig. 2.12. (Left) Normalized heat flow by weight of cement, (Right) Cumulative heat release of pure cement pastes and with addition of different types of 5% miscanthus.

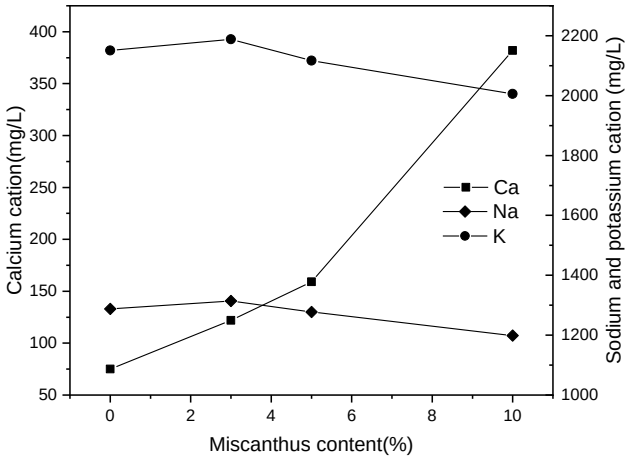

Fig. 2.13 Element concentration of cement pore solution with different miscanthus dosages.

The element concentration in the pore solution with different miscanthus dosages is shown in **Fig. 2.13**. First of all, it supports the previous conclusion that cement hydration is delayed significantly with the increasing content of miscanthus. The calcium concentration in the cement filtrated solution increased from 75 to 382 mg/L when the miscanthus content raised from 0 to 10%, indicating that calcium is dissolved in cement solution, but it can only form a limited quantity of hydration product like C-S-H gel and calcium hydroxide. In fact, Biblis demonstrated that organic extractives like glucose and cellulose severely interrupt the cement reaction. The negative effect of organic materials is attributed to the ability of sugar to be bound onto the hydration product containing Ca^{2+}, hence interrupting the C_3S hydration and the formation of C-S-H gel. However, no calcium absorption is observed, which is in disagreement with Sedan [105], who discovered and described a reduction in calcium ion concentration of cement pore solution. The sodium and potassium concentration showed minor fluctuations, indicating the dissolution of cement in water is not influenced by the incorporation of miscanthus.

2.4. Conclusions

This chapter investigates the properties of a bio-based lightweight concrete containing miscanthus, including workability, strength, acoustic absorption, reaction kinetics and microstructure. Furthermore, the role of miscanthus in blended cement systems is discussed. Based on the current results, the following conclusions can be drawn:

- Miscanthus fiber is a porous material with very low density, which can be used as lightweight aggregate in cement and concrete. 2-4 mm fibers obtain intact and large pore structure and perform better with regard to acoustic properties.
- Organic sugar leached from miscanthus delays the cement hydration. The high absorptivity of miscanthus fibers can be the obstacle for concrete mix design. Therefore, pre-treatment such as pre-wetting or cement impregnation is necessary to prepare miscanthus lightweight concrete.
- Workability of miscanthus lightweight concrete is closely related to aspect ratio of fibre and volume percentage in cement paste.
- The compressive strength decreases significantly with the addition of miscanthus, e.g. from 56 MPa to 15 MPa for 2-4 mm fibers (20% volume replacement) at 28 days. Nevertheless, flexural strength remains stable and for samples with cement impregnated fibers the strength is slightly enhanced, from 2.88 MPa to 3.21 MPa for 2-4 mm miscanthus fibers at 28 days. Cement mortar with pre-wetted miscanthus particles gains a lower strength than those of cement impregnated, but the density is lower as well. This is mainly caused by the denser aggregate resulted from cement impregnation.
- Acoustic absorption properties are significantly enhanced by incorporation of miscanthus fibers. More miscanthus represents more open pores and voids inside the cement paste and consequently more energy can be absorbed by the miscanthus cement composite.
- The interaction between miscanthus and cement starts at the initial age. All fibers show retarding effect on cement hydration, but 0-2 mm fibers have the worst effect on the cement hydration. The XRD evidence indicates the low strength of cement composite is also attributed to a less C-S-H gel formation. A high dosage of miscanthus can poison the cement paste, resulting in a lower hydration degree. The negative effect of sugar is attributed to the ability of organic to be bound onto the hydration product containing Ca^{2+}, hence interrupting the C_3S hydration and the formation of C-S-H gel

Chapter 3 Bio-based ultra-lightweight concrete applying miscanthus fibers: Acoustic absorption and thermal insulation

Acoustic and thermal comfort play an important role in the building environment. This chapter investigates the application of miscanthus fibers in ultra-lightweight concrete as replacement for lightweight aggregates to improve sound absorption and thermal insulation properties. Miscanthus fibers (MF) is a kind of sound absorption biomass that can dissipate sound noise thanks to its porous and flexible inner structures and fibrous shape. Therefore, the acoustic absorption and thermal insulation of ultra-lightweight miscanthus concrete (ULMC) is investigated using two different kinds of miscanthus fibers to substitute the lightweight aggregate-expanded waste glass. Meanwhile other mechanical properties were characterized, including bulk density and flexural strength. Results showed ULMC with 30% 2-4 mm MF obtained an ultra-low density (554 kg/m^3), thermal conductivity (0.09 W/(m·K)) and relatively high acoustic absorption coefficient (0.9) at 870 Hz. It is found that the acoustic performance of ULMC can be improved by optimizing the dosage and shape of miscanthus fibers. The developed green and sustainable bio-based ULMC possesses an excellent acoustic absorption and thermal insulation and is very suitable to use as indoor ceiling boards and in non-structural walls to make indoor living environment comfortable and energy-saving.

This chapter is partially published elsewhere:

Y.X. Chen, F. Wu, Q. Yu, H.J.H. Brouwers, Bio-based ultra-lightweight concrete applying miscanthus fibers: Acoustic absorption and thermal insulation, Cement and Concrete Composites 114 (2020) 103829.

3.1. Introduction

As governments and industries are striving to save energy and reduce environmental burden, concrete with low carbon footprints and unique functions are attractive and promising for a sustainable society [106–110]. Lightweight concrete (LWC) is a type of cementitious material with a density from 800 kg/m^3 to 2000 kg/m^3 and has the potential to obtain good thermal insulation and acoustic absorption properties [111,112]. Due to the large variations in aggregates, admixtures and preparation processes, LWCs can possess different properties in terms of density, thermal and acoustic properties, mechanical property and sustainability. Therefore, proper selections of lightweight aggregates and production procedures are the keys to prepare LWC with low environmental impact and improved functionalities.

One type of ultra-lightweight concrete (ULWC) previously investigated [90,113,114] showed excellent thermal insulation and ultra-low density. The applied lightweight aggregate (LWA) was produced from waste glass with a special procedure. Reuse of this unrecyclable waste glass to tackle the problems of over landfilling and contamination of environment is a promising recycling method [115,116]. According to the previous studies, this expanded waste glass can be applied in cementitious mixtures to produce ULWC, with drying density lower than water (~800 kg/m^3) and thermal conductivity around 0.12 W/(m·K) [113]. However, the acoustic absorption property of ULWC is rarely investigated, which is an important aspect that is associated with the quality of indoor living environment. Recent research has shown bio-based lightweight aggregates like hemp and miscanthus fibers can function as sound absorption materials in cement and concrete [117]. Glé et al. [11,76] investigated the acoustic absorption of hemp fiber reinforced concrete by experimental and modelling methods. The results show the hemp fibers itself can greatly absorb sounds and also can increase the acoustic performance of bio-concrete. Therefore, it is promising to hybridize expanded waste glass and plant fibers as lightweight aggregates in LWC to increase the acoustic absorption performance and thus improve the quietness in indoor environment.

In this chapter, miscanthus fibers are adopted to improve the unique functions of ULWC. Miscanthus fiber has received much attention due to its environmentally friendliness and wide spread availability, especially in Europe [13]. Miscanthus can also act as a kind of lightweight aggregate in cementitious materials to prepare lightweight concrete [70,73,97]. Miscanthus has low particle density and its porous structure has a positive effect on acoustic absorption like hemp [76,117]. The inter-particle pores and intra-particle pores all contribute to the dissipation of sound waves. Moreover, the high porosity of miscanthus fibers can further contribute to a lower thermal conductivity of miscanthus lightweight concrete [118–122]. It is noteworthy that the structure of miscanthus fibers is a complex core-shell structure, as shown in **Fig. 3.1**. One single miscanthus particle consists of the outer shell called epidermis structure, while the middle and inner structures are sclerenchyma and parenchyma, respectively. Thus, the contribution of different parts of miscanthus fibers to acoustic performance is hypothesized to be different, which should be investigated. Therefore, the hybridization uses of different parts of miscanthus fibers and expanded waste glass to prepare ULWC with low density, high thermal insulation and excellent acoustic absorption is interesting and needs detailed investigation.

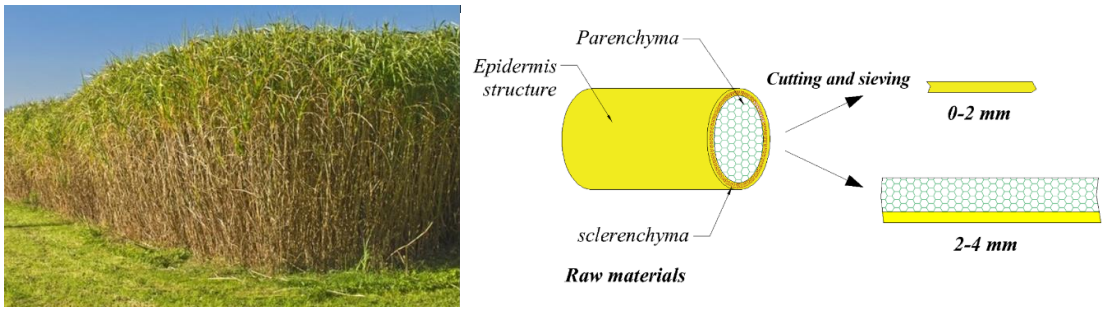

Fig. 3.1 Schematic diagram of the microstructure of two different kinds of miscanthus fibers: 0-2 mm and 2-4 mm.

From the above perspectives, the objective of this chapter is to investigate the acoustic absorption and thermal insulation properties of ultra-lightweight concrete by incorporating miscanthus fibers and expanded waste glass. Two kinds of miscanthus fibers are used, which are 0-2 mm and 2-4 mm fibers. A performance evaluation of the developed ULMC is carried out, including the mechanical properties, acoustic absorption coefficient and thermal conductivity. The mechanism of the improvement in insulation properties of ULMC are explored by scanning electron microscopy.

3.2. Materials and experiments

3.2.1. Starting Materials

3.2.1.1. Raw miscanthus fibers

Miscanthus fibers (MF) adopted was provided and further treated by Vibers (the Netherlands). The raw granules of MF were different in size and shape, hence sieving was carried out to produce a uniform granules of the fibers. Sieves with 2 and 4 mm diameter were applied to classify MF with the use of a sieving machine. The length of the two kinds of MF was approximately 2 to 20 mm. **Fig. 3.2** exhibits the morphology of 0-2 mm and 2-4 mm MF, respectively. **Fig. 3.3** presents the scanning electron microscopy (SEM) images of the utilized 0-2 mm and 2-4 mm MF, whose surface were sputtered with gold and were observed by JOEL JSM-5600 with an accelerating voltage of 10 kV. The used 2-4 mm MF possesses porous structures. Large amounts of mesopores and stem walls are existed in the fibers. The pore size is in the range of 20 to 50 μm. However, for 0-2 mm MF, it shows a more compacted porous structure, where the pore size is much smaller and tighter than those of 2-4 mm MF. The water absorptivity of the two MFs are shown in **Table. 3.1**. The 0–2 mm MF has a higher water adsorption capability (396% at 48 hours) compared to 2–4 mm MF (290%), The finer fibers can absorb water more quickly at early age and reach equilibrium much sooner than larger fibers. The types of sugar leached from miscanthus are mainly arabinose, galactose, glucose, xylose and mannose, with a concentration of 0.06 mg/ml, 0.09 mg/ml, 0.19 mg/ml, 0.16 mg/ml and 0.05 mg/ml, respectively [117].

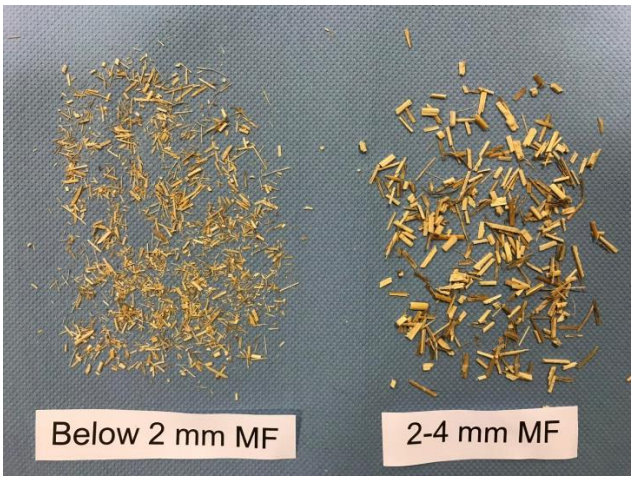

Fig. 3.2. Morphology of the 0-2 mm MF and 2-4 mm MF.

Table 3.1. Water absorptivity of miscanthus fibers with different sizes.

Water absorptivity (%)	10 min	30 min	1 h	6 h	12 h	24 h	48 h
0-2 mm MF	330	361	372	384	391	394	396
2-4 mm MF	180	210	224	271	281	289	290

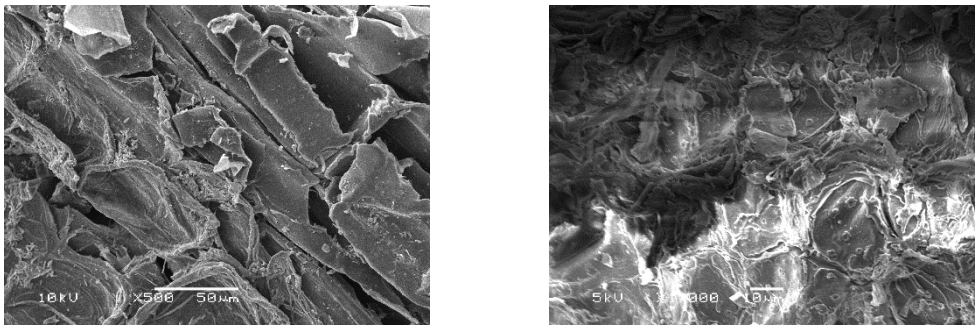

(a)

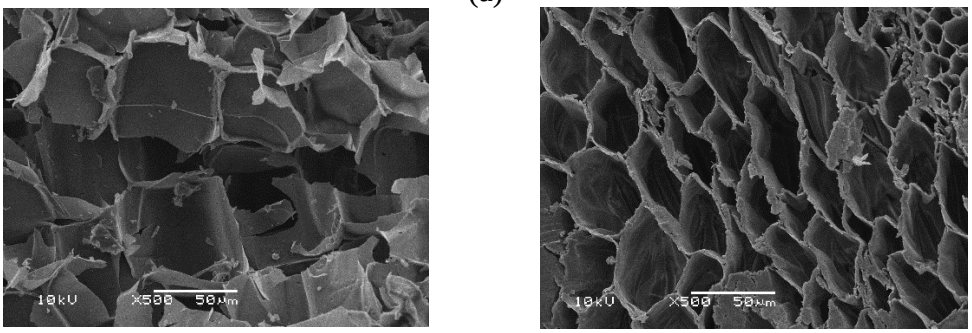

(b)

Fig. 3.3. SEM of the utilized miscanthus fibers (a) 0-2 mm and (b) 2-4 mm (Magnification: ×500).

3.2.1.2. Expanded waste glass

The expanded waste glass (EWG) was produced from recycled glass through a special procedure, which was adopted as lightweight aggregate to produce ULMC in this study [113]. Five different sizes of EWG were adopted in this research, with a particle size distribution of EWG from 0.25~8.0 mm, which are detailed exhibited in **Fig. 3.4 (a).** The SEM of the adopted EWG is presented in **Fig. 3.4 (b),** which was observed using the same instrument as that of MF. The physical properties and oxides composition of EWG are shown in **Table 3.2** and **Table 3.3**. The water absorption is quite low compared to other kinds of commercial LWAs [113], especially in the first hour of soaking, reaching around 1.0% by mass. This is attributed to the closed external surface observed from **Fig. 3.4 (b)**. Therefore, the adopted EWG had little influence on the workability of ULMC, and in turn slightly reduced the w/c ratio at the beginning of cement hydration, preventing micro-bleeding at the interface of LWA. Hence the Liaver EWG can be blended in the cementitious mixtures directly without pre-soaking.

Table 3.2. Densities, water absorption and mechanical properties of the used EWG.

EWG *D* (mm)	Bulk density (kg/m^3)	Specific density (kg/m^3)	Crushing resistance (N/mm^2)	1 h water absorption (wt.%)	24 h water absorption (wt.%)
EWG 0.25-0.5	300	540	＞2.9	0.88	3.90
EWG 0.5-1.0	250	450	＞2.6	1.59	8.50
EWG 1.0-2.0	220	350	＞2.4	1.71	7.63
EWG 2.0-4.0	190	310	＞2.2	0.55	7.80
EWG 4.0-8.0	170	300	＞2.0	1.30	9.11

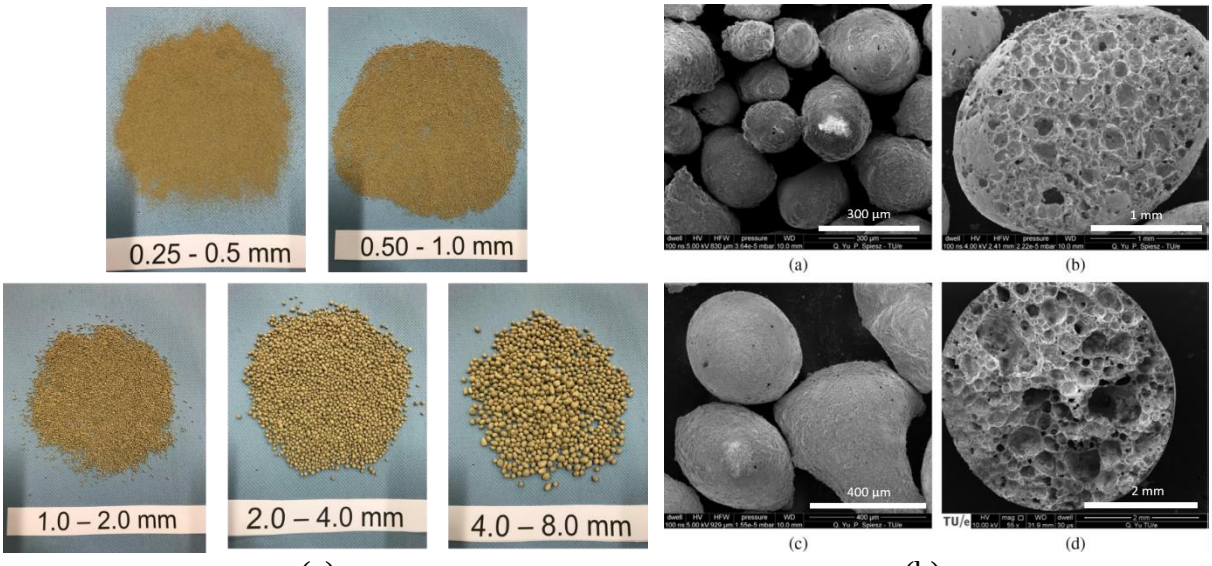

Fig. 3.4. (a) Morphology of expanded waste glass with different sizes and (b) SEM image.

3.2.1.3. Cement matrix of ULMC

The cementitious material used for ULMC was CEM III 52.5 N cement, which was provided by ENCI, Heidelberg Cement (the Netherlands). The oxides composition of the cement was analyzed by X-ray fluorescence (XRF), as shown in **Table 3.3**. Superplasticizer (SP) was used to optimize the flowability of the fresh ULMC paste. Air entraining agent (AE) was used to introduce extra air voids to further decrease the density of ULMC.

Table 3.3. Oxides composition of the used cement and EWG.

Oxides composition	CaO	SiO_2	Al_2O_3	Fe_2O_3	K_2O	Na_2O	SO_3	MgO	LOI*
Cement	47.20	30.10	9.41	1.38	0.38	0.27	3.3	0.96	0.4
EWG	6.4	71.0	2.0	0.5	1.0	13.0	-	2.0	0.9

*Loss on ignition

3.2.2. Experimental design

3.2.2.1. Mix design of ULMC

The mix design methodology of the ULMC applied a modified A&A model, as reported in previous studies [123,124]. The miscanthus fibers were used to replace EGW with each particle size by 10 %, 20% and 30 % by volume, which were marked as M10, M20 and M30, respectively. The water to cement ratio was fixed as 0.45. SP was used to increase the workability of the fresh concrete paste, which was determined to be 1 wt.% as the optimum. The designed recipes of ULMC mixtures are presented in **Table 3.4**.

3.2.2.2. Mixing procedures

Miscanthus fibers should be pre-soaked in water before mixing with cementitious materials to keep water to binder ratio constant during the mixing. In brief, 50 g of MF was weighed and placed in a 500 ml beaker filled with distilled water. Then MF was filtrated through an 80 μm sieve to remove water. Afterwards, the surface water remaining on MF was dried by carefully clapping the MF with paper. Then water-saturated MF was ready for use.

In terms of preparation of ULMC, the cement and EWG were firstly mixed for 1 min without water. Afterwards, 70% of distilled water was added and mixed with the cement and EWG for 2 min. Then, the superplasticizer and 30% of distilled water were added and mixed for another 2 min. Finally, miscanthus fibers was added and mixed for 3 min with the above mixture. The temperature during production of ULMC was approximately 20 ℃.

After mixing, the fresh ULMC paste was cast into moulds and vibrated on a jolting table. Workability of ULMC was measured by the mini spread-flow test [125]. Fresh ULMC paste was placed into a normal conical ring and followed by 15 times jolting. The diameter of cement paste was measured perpendicularly 4 times after jolting and the average value was noted as the slump flow. After 1 day from casting, samples were stripped from the moulds and placed in a climate chamber with a relative humidity of above 95% and temperature of around 20 ℃. After 7- and 28-days curing, respectively, the properties and performances of ULMC samples were measured.

Table 3.4. Mix design of ULMC.

ULMC	CEM 52.5 N (kg/m^3)	EWG (kg/m^3)					Water (kg/m^3)	SP (%)	AE agent (kg/m^3)	0-2 MF (vol %)	2-4 MF (vol %)
		0.25-0.5 mm	0.5-1 mm	1-2 mm	2-4 mm	4-8 mm					
Reference	403	23.70	35.60	27.30	47.10	57.30	184	1.0	2.25	0	0
M1-10	403	21.33	32.00	24.57	42.39	51.60	184	1.0	2.25	10%	0
M1-20	403	18.96	28.48	21.84	37.68	45.84	184	1.0	2.25	20%	0
M1-30	403	16.59	24.92	19.11	32.97	40.11	184	1.0	2.25	30%	0
M2-10	403	21.33	32.00	24.57	42.39	51.60	184	1.0	2.25	0	10%
M2-20	403	18.96	28.48	21.84	37.68	45.84	184	1.0	2.25	0	20%
M2-30	403	16.59	24.92	19.11	32.97	40.11	184	1.0	2.25	0	30%

3.2.3. Performance evaluation of ULMC

3.2.3.1. Densities

The fresh density of the reference sample, M10, M20 and M30 was determined following EN 12350-6 (2009) [85]. After mixing, the fresh ULMC paste was first placed in a 1 litre graduate cup to determine the fresh density. Afterwards, the ULMC samples were cast in the moulds of two sizes, i.e. 100 mm × 100 mm × 100 mm and 150 mm × 150 mm × 150 mm. After 1 day curing in a climate chamber, the specimens were stripped from the moulds and continued curing for 7 and 28 days at 20 °C, following EN 12390-2 (2009) [83]. Cubic samples with the size of 100 mm × 100 mm × 100 mm were used to determine the dry density of ULMC (Standard EN 12390-7 (2009)). The average density of three test specimens was calculated as the final density of the concrete.

3.2.3.2. Compressive and flexural strength

The reference sample, M10, M20 and M30 cubes with the size of 150 mm × 150 mm × 150 mm were used to determine the compressive strength at 7 and 28 days (Standard EN12390-3) [84]. The ULMC concrete bars with the size of 40 mm × 40 mm ×160 mm were used to test the flexural strength at 7 and 28 days (Standard EN 196-1) [86]. The average strength of three test specimens was calculated as the final strength of the concrete.

3.2.3.3. Acoustic absorption

Acoustic absorption efficiency of ULMC was determined with the impedance tube method**.** Specifically, the fresh ULMC paste was cast in the cylindrical mould with the size of 40 mm in diameter and 80 mm in thickness. After 28 days curing, the reference sample, M10, M20 and M30 for sound absorption test were ready for use. The mechanism of sound absorption test is briefly described as follows. The sound generator emits a plane wave and spread through the tube before reflecting by the ULMC. The ULMC reflects, absorbs and transmits the wave and by detecting the generated sound wave, the sound absorption coefficient of ULMC can be calculated. Every sample was tested twice to ensure the reliability of the results.

3.2.3.4. Thermal conductivity of ULMC

The ULMC cubes with the size of 100 mm × 100 mm × 100 mm were first dried at 105 ℃ overnight to a constant mass (Standard EN12390-7) [85]. The heat transfer analyzer modelled ISOMET model 2104 was used to determine the thermal properties of the reference sample, M10, M20 and M30. Both the volumetric heat capacity (J/(m^3·K)) and the thermal conductivity (W/(m·K)) of materials can be tested. The temperature during test is constant at 20 ℃. The average thermal conductivity of three test specimens was calculated as the final thermal conductivity of the concrete.

3.2.3.5 Water permeable porosity

The porosity test for the reference sample, M10, M20 and M30 was carried out with the vacuum saturation approach, following ASTM C642-13 (2013) [126]. The porosity can be calculated with:

$$\varphi_{v,\,water} = \frac{m_s - m_d}{m_s - m_w} \times 100 \tag{3.1}$$

where φ_v, water is the water-permeable porosity (%), m_s is the mass of saturated sample in surface dry condition (g), m_w is the hydrostatic mass of the water-saturated sample (g) and m_d is the mass of oven dried sample (g).

3.2.3.6 UPV test

Ultrasonic pulse velocity (UPV) test was used to test the strength and voids of the reference sample, M10, M20 and M30, following ASTM C597-09 [127]. It measures the velocity of an ultrasonic pulse passing through a concrete structure. Direct method was used during the whole test, which requires access to two surfaces of the concrete cubes. Each specimen was tested thrice, and the average value was determined as the final velocity of the concrete.

3.2.3.7 Scanning electron microscopy

The microstructure of ULMC was observed by scanning electron microscopy (SEM), which was conducted by JOELJSM-5600 instrument with an accelerating voltage of 10 kV. The surfaces of the tested ULMC samples were pre-treated with sputtered gold before the SEM test.

3.3. Results and discussion

3.3.1 Physical Properties

The spread flow of ULMC is presented in **Fig. 3.5 (a).** Both 0-2 mm and 2-4 mm MFs decrease the flowability of ULMC as the replacement of MF amount increases. Due to the pre-treatment of fibers, reduction in flowability is not attributed to the water absorption of miscanthus fibers, but closely related to the aspect ratio and volume fraction of MF in cement paste. The fresh density and dry density of ULMC are presented in **Fig. 3.5 (b)**. The fresh densities of all ULMC mixtures are around 700 kg/m^3, suggesting the pre-soaked MF has only slight influence on the fresh densities of ULMC mixtures. The reason behind this phenomenon is the high porosity and water absorption of MF. The dry densities of all ULMC samples are

less than 800 kg/m^3, which is lower than the minimum density of LWC defined by standard – EN 206-1 (2001) [128]. Hence the designed miscanthus concrete is an ultra-lightweight concrete. It can be observed from **Fig. 3.5** that the dry density of ULMC decreased with the increasing dosage of MF. This phenomenon should be attributed to two reasons. Firstly, the MF is a porous material with inter-particle porosity of 52.2% and intra-particle porosity of 38.3% and particle density around 250 kg/m^3 [117], which means the dried MF is more porous and lightweight than expanded waste glass. Secondly, the high percentage of MF can have an impact on the internal packing of ULMC. The long and stiff MF can push the surrounding expanded waste glass apart and change the packing of the granule structure. Hence, the ULMC becomes more porous due to the additional of MF and also more air is entrapped in the ULMC mixtures.

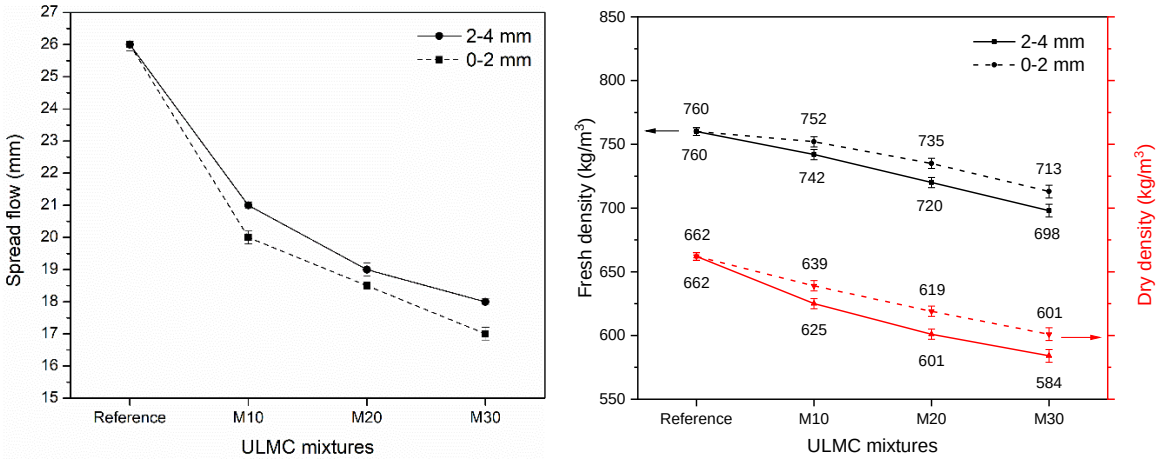

Fig. 3.5. Spread flow (a) and fresh/dry density (b) of the designed ULMC.

The compressive strength and flexural strength of ULMC at the age of 7 days and 28 days are presented in **Fig. 3.6**. All the groups of ULMC show decreased strengths with the increasing dosages of MF. The compressive strength of reference mixture at 28 days reduces from 8.42 MPa to 3.99 MPa with 30% 2-4 mm MF replacement of EWG. Meanwhile, ULMC with 0-2 mm MF show slightly lower compressive strength than those of 2-4 mm samples, reaching 3.8 MPa with 30% MF substitution. 0-2 mm MF possesses a lower mechanical strength and a lower particle density, and the surface is smoother than 2-4 mm MF, indicating a weak bonding between fibers and hardened cement paste. Therefore, miscanthus fibers have a negative effect on compressive strength of ULMC. This phenomenon is probably attributed to two reasons. Firstly, the crushing resistance of MF is much lower than that of expanded waste glass, which means the average strength of lightweight aggregates applied in ULMC decreased dramatically. In general, the compressive strength of lightweight concrete is much dependent on the strength of lightweight aggregates used in the cement matrix. This can also explain the relatively slow rate (20%) of strengths development of ULMC from 7 days to 28 days. Secondly, the organic materials leached from the MF retard the hydration process of cement, which is detailed investigated in a previous research [117]. The C-S-H formation is much slower because of the retarding effect of sugar in the MF. However, the late age strength of ULMC needs further investigation since the retardation effect may have positive effect on the later strength.

However, flexural strengths of ULMC only slightly decease with the addition of 2-4 mm MF, ranging from 1.09 MPa to 1.59 MPa. This phenomena is probably due to the bridging

effect of MF demonstrated by many researchers [70,78,129]. With the increased load on ULMC, the 2-4 mm MF will become active and resist part of the load. However, the retarding effect of leached sugar on cement hydration as mentioned above can compromise the positive bridging effect. Therefore, the two opposite effects resulted in a slight decrease in the flexural strength of ULMC with the incorporation of 2-4 mm MF. However, the flexural strength dramatically decreases to 0.95 MPa at 28 days for ULMC with addition of 30% 0–2 mm MF. The smooth flat surface of the 0-2 mm MF leads to a poor bonding with the cement paste and a fiber pull-out failure without any stress transfer.

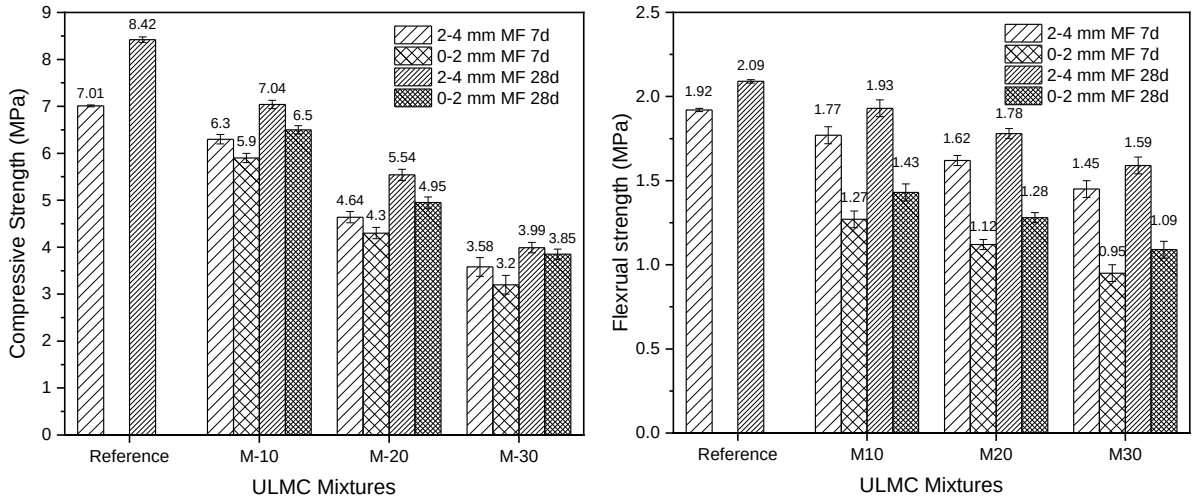

Fig. 3.6. Compressive (a) and flexural (b) strength of the designed ULMC at 7 and 28 days.

3.3.2 Acoustic absorption of ULMC

The acoustic absorption coefficient of ULMC with different dosages of 2-4 mm MF are presented in **Fig. 3.7**. It can be observed that the M10 sample reaches a moderate sound absorption coefficient of approximately 0.58 at the frequency of 712 Hz. However, the sound band width that exceeded absorption efficiency of 0.5 is relatively low, reaching only 142 Hz showing a poor absorption in low frequencies. However, when 20% 2-4 mm MF replaced EWG in the ULMC, the peak of sound absorption coefficient increased to 0.73 and the sound frequency also shifted to higher value of 784 Hz. The band width of frequencies above the efficiency of 0.5 also increased to 247 Hz, indicating the sound that can be effectively absorbed increased. Furthermore, the sample with 30% MF shows the highest sound absorption efficiency. The sound absorption efficiency reached 0.89 at the frequency of 841 Hz. The band width of the sound absorption efficiency higher than 0.5 is 333 Hz ranging from 712~1050 Hz. Therefore, it can be concluded more 2-4 mm MF incorporated in lightweight concrete can result in higher sound absorption and cover more range of sound frequencies, meaning more sound can be effectively absorbed by ULMC.

The phenomena may be attributed to two reasons. Firstly, porous and lightweight materials possess a higher acoustic absorption compared to dense materials. 2-4 mm MF is a kind of lightweight biomaterial with large amounts of open interconnected pores which is rather different from expanded waste glass (closed shell structure that prevent pores connected to outer

space). Researches [11] show that compacted long hemp fibers can have a sound absorption coefficient of 0.9 at frequencies from 400 to 1000 Hz, which obtains the similar physical properties to miscanthus fibers. Secondly, porosity of ULMC could increase with the incorporation of 2-4 mm MF, which can be further evidenced by the porosity test. Therefore, both factors contribute to the improved acoustic absorption of ULMC.

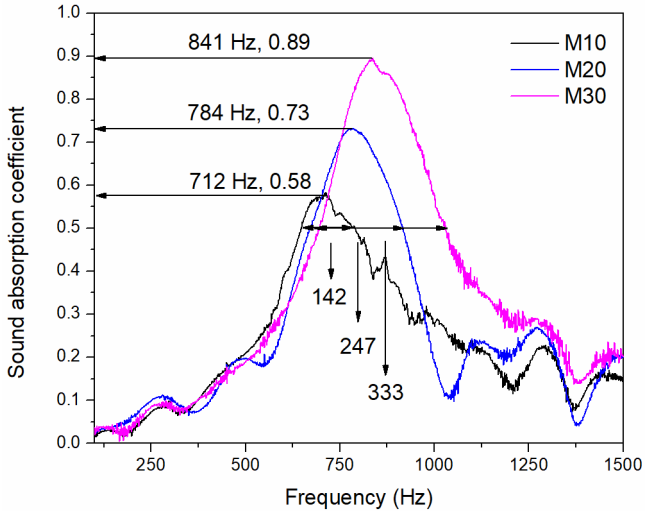

Fig. 3.7. Acoustic absorption coefficient of ULMC with different dosages of 2-4 mm MF.

The sound absorption of ULMC incorporating 0-2 mm MF is presented in **Fig. 3.8.** Generally, the acoustic absorption of pure cement paste is pretty low, with the sound absorption coefficient ranging from nearly 0 to 0.2 depending on different processing conditions [74]. The reference sample only reaches a sound absorption coefficient of 0.25 at the frequency of 800 Hz. With the increasing content of 0-2 mm MF, the sound insulation of ULMC increased slightly, reaching only 0.39 at the same frequency. As MF content increased to 20% and 30%, the sound absorption of ULMC remains relatively stable, indicating a limited rise in sound insulation performance. This phenomenon can be explained by the different microstructure of different shapes of miscanthus fibers. 0-2 mm MF has a morphology of smooth outer shell of the straw, resulting in a less porous microstructure as shown in **Fig. 3.3**. Therefore, in this study 2-4 mm MF is the optimal biomaterial for the enhancement of sound insulation property.

The schematic diagram of the sound insulation of ULMC is shown in **Fig. 3.9**. As the sound is generated from the loudspeaker, three kinds of sound can be generated: 1) the reflected sound, 2) the absorbed sound and 3) the transmittance sound. More 2-4 mm MF in ULMC can improve the amount of the inter-particle and intra-particle pores and contact areas with air molecules, thus considerably having a beneficial effect to dissipate sound energy. Moreover, acoustic waves can propagate through the 2-4 mm MF better than 0-2 mm MF because of the increasing amount of intra-particle porosity. Hence the sound absorption performance of ULMC with 2-4 mm MF is improved in low frequency. It is noteworthy that the intra-particle pores in 2-4 mm miscanthus fibers further improve the connectivity between the inter-particle pores, thus increasing the consumption of acoustic energy by converting into thermal energy. However, for 0-2 mm MF, the shape is mainly outer shell with rigid surface, showing negligible function as an insulation material.

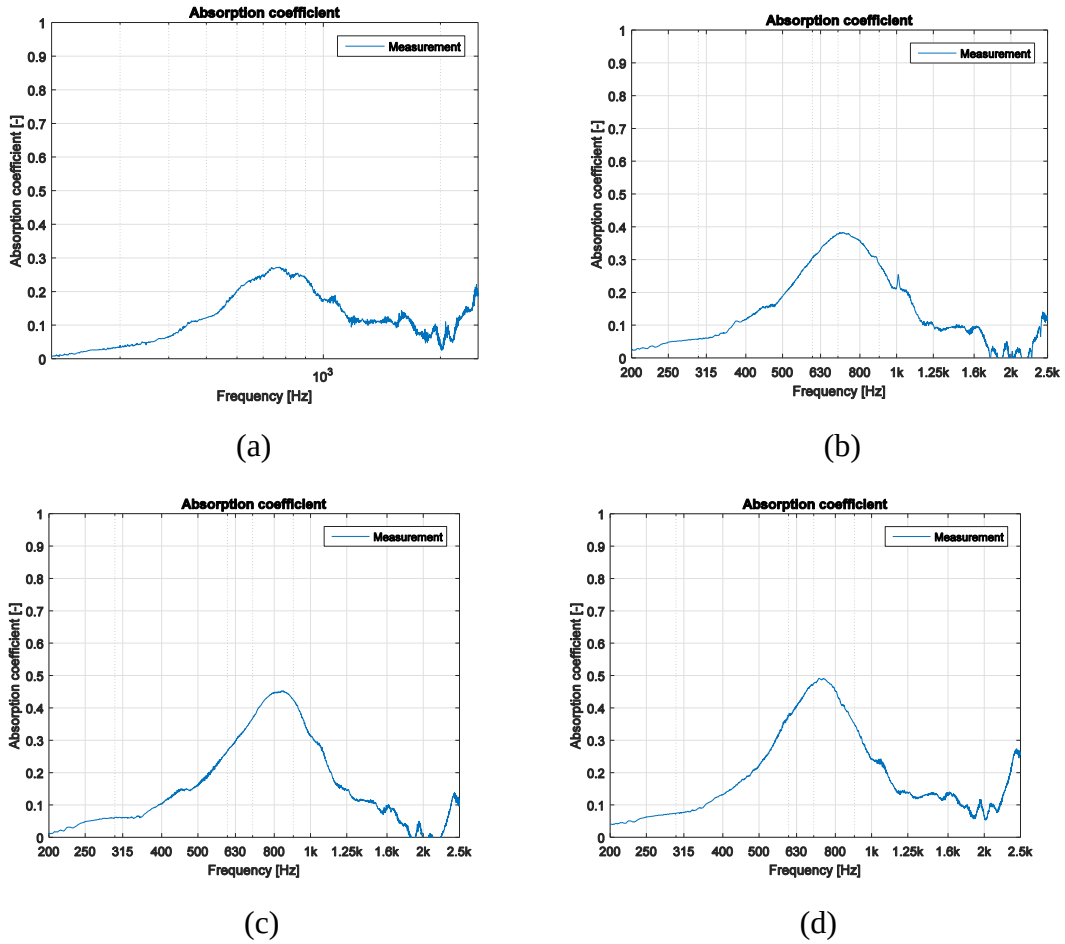

Fig. 3.8. Sound absorption coefficient of ULMC with 0-2 mm MF (a) Ref (b) 10% MF (c) 20% MF (d) 30% MF.

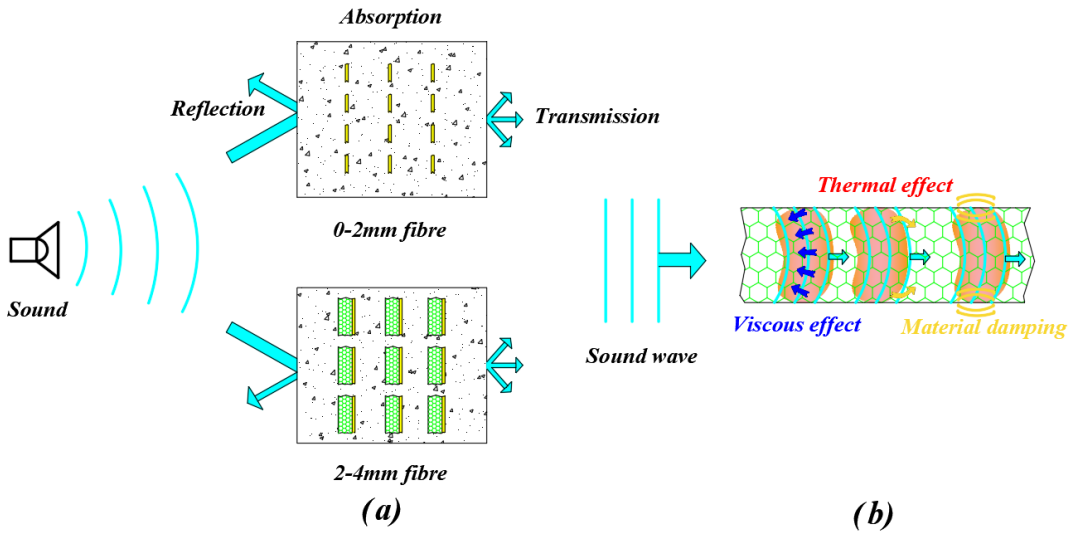

Fig. 3.9. Schematic diagram of mechanism of (a) sound absorption by ULMC (b) sound absorption by a single 2-4 mm MF.

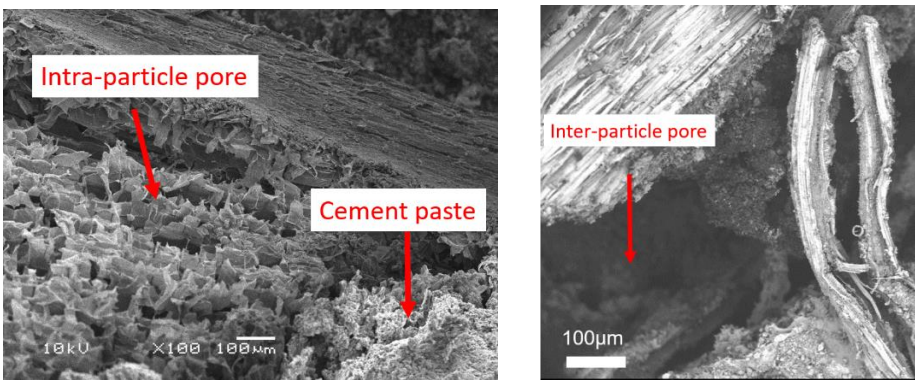

(a)

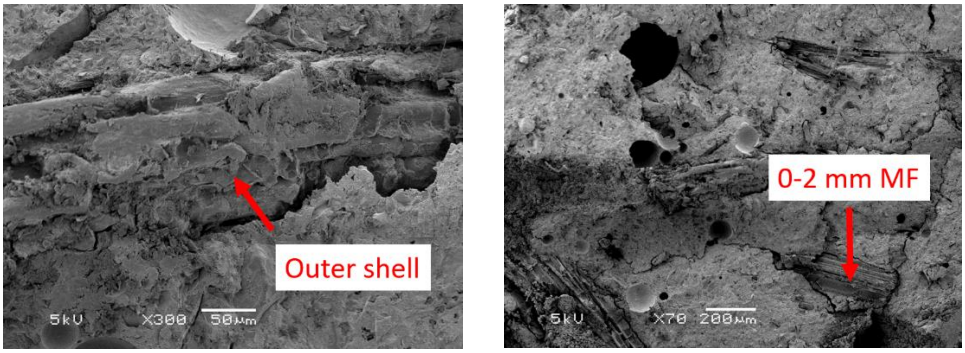

(b)

Fig. 3.10. SEM of fracture surface of ULMC (a) 2-4 mm MF (b) 0-2 mm MF.

The scanning electron microscopy of ULMC fracture surface is shown in **Fig. 3.10**. It can be observed that the inter-particle pores and intra-particle pores both exist in the ULMC matrix containing 2-4 mm MF, which is beneficial for the sound absorption of ULMC. The pores in the straw of miscanthus are concentrated and also positively influence the acoustic absorption property of ULMC. However, for 0-2 mm MF shown in **Fig. 3.10 (b)**, the smooth surface of the fibers has negative effect on the sound insulation properties of ULMC. The dense surface structure of 0-2 mm MF plays a significant role on reflecting the sound wave by the rigid surface.

Table 3.5. Porosity and 24 hours water absorption of ULMC.

ULMC	Reference	M10	M20	M30
24 hours water absorption (%)	13.2±0.1	16.2±0.2	19.4±0.1	20.7±0.3
Porosity (%)	21.8±0.2	24.6±0.3	26.1±0.2	28.0±0.3

The porosity of ULMC tested by vacuum saturation approach is presented in **Table 3.5**. It is obvious that the porosity increases with the incorporation of more 2-4 mm MF. The reference samples obtained the lowest porosity as 21.8% while the M30 reached the highest porosity of 28.0%. The increase in porosity is mainly attributed to the random distribution of miscanthus fibers in cement matrix. The pores created in the mixing of the cement paste and fibers can increase thanks to the long and stiff miscanthus fibers, and thus form voids between them. The

pores are mainly in the size of millimeter and in combination with the intra-particle pores (micrometer sized), improving the sound absorption efficiency of ULMC.

Table 3.6. Sound absorption, compressive strength and density of several bio-based materials.

Bio-based materials	Sound absorption coefficient at a frequency (Hz)	Compressive Strength (MPa)	Density (kg/m^3)	Sample thickness (mm)	Literature
M30-ULMC	0.9 at 800	2.99	554	80	This study
Hemp-Starch	0.7 at 1250	0.55	168	35	[99]
Sunflower-Chitosan	0.1~0.2 at 1000-2000	2.0	150~200	13	[101]
Hemp-GGBS	0.5 at 400-2000	NM	522	300	[130]
Hemp-lime[1]	0.5 at 600	NM	573	300	[131]
Hemp-lime[2]	0.9 at 1000	NM	180~300	40-50	[132]
Hemp-lime[3]	0.9 at 800	1.2	415	40	[133]
Hemp particles	1.0 at 800	0	120	50	[76]

GGBS: Ground granulated blast-furnace slag; NM: Not mentioned.

Other lightweight concretes incorporated with plant fibers were also investigated by other researchers, for instance, hemp concrete, which is similar as miscanthus concrete. **Table 3.6** shows the sound properties of different kinds of bio-based sound insulation materials to make a comparison with the ULMC in this study. Hemp concrete made with starch binder can obtain sound absorption of 0.7 at 1250 Hz [99]. However, the strength of this material is very low (0.55 MPa). Lightweight concrete with sunflower stalk and corn stalks were also investigated but reaching a relatively low sound absorption coefficient compared to ULMC. The reason may be due to the different production approaches, properties of plant fibers and the thickness of the samples. Gle's research indicated that sound absorption is affected by the pores of bio-based LWC, which is mainly a combination of micro pores in cement paste and intra-particle pores in plant fibers, and larger inter-particle pores between the fibers. Hence, the acoustic absorption of ULMC located among the high sound absorption of miscanthus fibers, and the variation of the reference hardened concrete.

3.3.3 Thermal conductivity of ULMC

Thermal insulation property is a critical parameter in designing and applying lightweight concrete. The thermal properties of all the designed ULMC with different additions of MF are presented in **Fig. 3.11**. The thermal conductivity is decreased considerably with the increasing dosage of both kinds of MF. However, 2-4 mm MF shows more reduction on thermal conductivity of ULMC than 0-2 mm MF. The M2-30 ULMC reaches a thermal conductivity of 0.09 W/(m·K), decreasing 24.5% compared with the reference ULMC. However, for the sample M1-30, the reduction percentage is only 15.0%.

The reasons for the reduction in thermal conductivity are attributed to the porous structure and fibrous shape of miscanthus fibers and also their influence on the packing of cement paste.

When 30% MF substituted EWG in cement, it means the large amount of fibers will influence the internal packing of the ULMC. Generally, a less dense granular packing leads to better thermal insulation due to more air voids entrapped in the cement matrix. Therefore, more MF in mixtures indicates more air voids and less density of ULMC and consequently reduced thermal conductivity. Previous researches on thermal properties of lightweight concrete indicated that thermal conductivity is closely related to density and porosity of the concrete [134,135]. Secondly, the porous structure of 2-4 mm MF can introduce more voids in cement paste and act as a heat insulator, making the thermal conductivity of ULMC even lower.

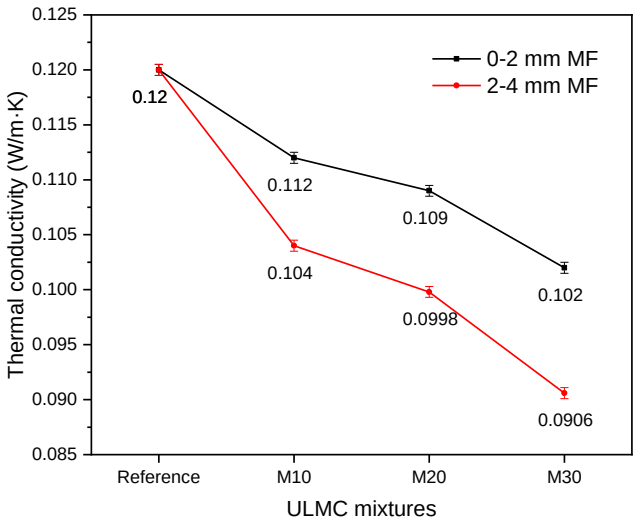

Fig. 3.11. Thermal conductivities of ULMC with the incorporation of MF.

The UPV test can show the inner voids and inhomogeneity of concrete without destroying the sample. The results of UPV test of ULMC are shown in **Table 3.7**. The UPV decreases significantly with the incorporation of 10% MF (2857 to 2490 m/s). This phenomenon is in accordance with the results from the porosity test. It is obvious that the more MF incorporated in concrete, the more air voids and inhomogeneity of concrete exist. Generally, UPV is the essential method to detect large pores in the aggregate and mortar interface. The 30% MF dosage ULMC obtained the largest number of pores as the UPV reaches the lowest value to 2142 m/s. Therefore, M30 obtains the best thermal insulation performance (0.09 W/m·K).

Table 3.7. UPV test of ULMC with 2-4 mm MF.

ULMC	Reference	M2-10	M2-20	M2-30
UPV (m/s)	2857±8	2490±15	2320±6	2142±32

The schematic diagram of heat transfer in ULMC is illustrated in **Fig. 3.14**. Heat transfer analyzer produces heat that is transferred by ULMC through three media: (1) cement matrix (2) expanded waste glass and (3) miscanthus fibers. The thermal conductivities of a single particle of MF and expanded waste glass are 0.10 W/(m·K) and 0.07 W/(m·K), respectively [136]. However, the thermal conductivity of hardened cement paste is around 1.70 W/(m·K). Therefore, the reference sample already obtained a relatively low thermal conductivity than normal concrete since all the lightweight aggregates were EWG (0.12 W/(m·K)). However, miscanthus fibers can further lower the thermal conductivity of ULMC even with a slightly

higher intrinsic thermal conductivity. If it is assumed that the MF is a spherical shape similar to EWG, the thermal conductivity of ULMC should be slightly higher than the reference sample according to [137]:

$$K = \frac{k_0 v_0 + k_1 v_1 \dfrac{3k_0}{(2k_0 + k_1)} + k_2 v_2 \dfrac{3k_0}{(2k_0 + k_2)}}{v_0 + v_1 \dfrac{3k_0}{(2k_0 + k_1)} + v_2 \dfrac{3k_0}{(2k_0 + k_2)}} \tag{3.2}$$

This equation describes the heat transfer through composite materials including one continuous phase and two dispersed phases. K is the effective thermal conductivity of ULMC, k_0 is the conductivity of cement matrix, k_1 is the conductivity of EWG, k_2 is the conductivity of MF and v is the volume fraction of each phase respectively. However, there is a difference between the theoretical conductivity and experiment result. This is attributed to the fibrous shape of MF, leading to an interfacial thermal resistance (ITR) that can increase the thermal resistance of MF, thus reduce the thermal conductivity of ULMC [138]. As can be seen from the SEM shown in **Fig. 3.10**, the interface between cement matrix and miscanthus fibers is not perfectly attached. Also, the aspect ratio of MF is much higher than EWG, indicating a larger contact area than EWG. Thus, the fibrous shape of MF can increase the interface thermal resistance (ITR) and function as a thermal barrier in cement paste, making the diffusion of heat more difficult. However, the contribution to thermal insulation from MF is quite small compared to its contribution to acoustic absorption of ULMC. The reason is the EWG obtains an internal core-shell structure that contributes to better thermal insulation for ULMC. Meanwhile, MF introduces the air voids and further increases the thermal resistance in ULMC, resulting in slight increase in thermal insulation.

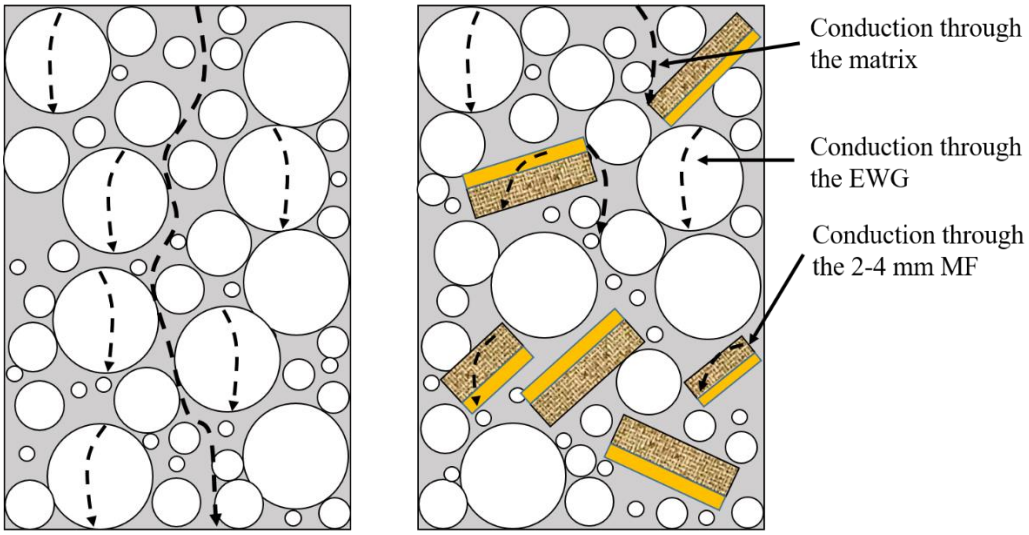

(a) Reference (b) M2-30

Fig. 3.12. Schematic illustration of mechanism of heat transfer by conduction in ULMC.

The following equation relates the relationship between thermal conductivity and density:

$$\lambda = a_0 \times e^{b_0 \times \rho} \tag{3.3}$$

Where λ is the thermal conductivity (W/(m·K)), ρ is the density (kg/m^3), and a_0 and b_0 are constant parameters. For instance, ACI committee suggest 0.072 W/(m·K) and 0.00125 m^3/kg for a_0 and b_0. In this study, the a_0 and b_0 are 0.022 W/(m·K) and 0.00258 m^3/kg respectively according to the thermal conductivities and dry densities of ULMC calculated from **Table 3.5** and **Fig. 3.5.** The results are plotted in **Fig. 3.13**.

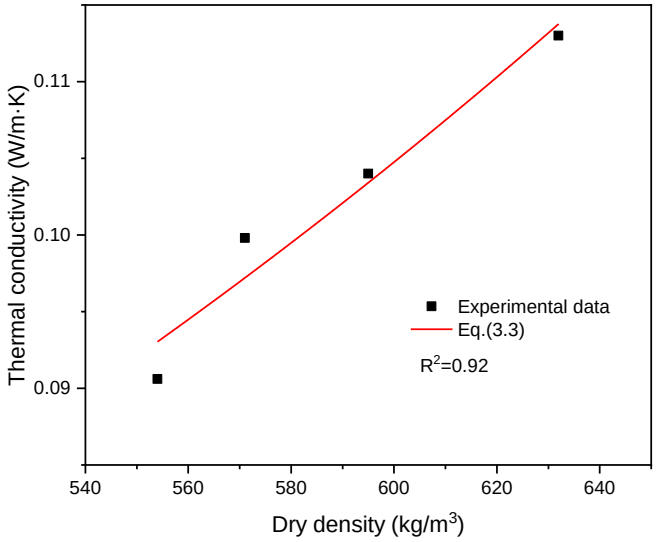

Fig. 3.13. The thermal conductivity versus dry density of ULMC.

The relationship between thermal conductivity and compressive strength of different types of lightweight concrete is shown in **Fig. 3.14**. Almost all the LWC presented here, a positive relationship between thermal conductivity and compressive strength is observed. The ULMC presented in red obtain higher compressive strength than other kinds of lightweight concrete having the similar thermal conductivity, for instance, foam concrete and porous concrete [95]. Other lightweight concrete with the use of pumice, tuff and diatomite, since the production method is quite different, thus the density is beyond the upper limit of ULWC (800 kg/m^3) [139]. It is important to choose the suitable lightweight aggregate and mix design to produce ultra-lightweight concrete. Therefore, it can be concluded the developed ULMC has a better performance in thermal insulation, while possesses moderate compressive strength at the same time.

3.3.4 Comparison with other lightweight insulation panels

There exist different kinds of insulation panels on the market, in which the most popular materials are gypsum, glass wool and foam for drop-ceiling boards or non-structural walls. In some scenarios, these materials are used to produce layered structures, for example, a sandwich structure consisting of glass wool and gypsum board. These materials possess low thermal conductivity and high sound absorption, however, with a high CO_2 footprint during production and sometimes harmful to health. For instance, high temperature involved during glass wool preparation. Specifically, natural sand and recycled glass are mixed and heated to 1450 ℃ to produce glass. Moreover, complex production method like connection of each fibers by using resin and further heated at 200 ℃ and calendared to provide strength are needed. For the harmful aspect, glass wool used for insulating appliances appears to produce human disease that is similar to asbestosis, which can cause respiratory problem or irritation to the eyes [140].

The bio-based ULMC possesses comparable or better thermal insulation and acoustic absorption capability to the traditional insulation boards. Moreover, it has better ecological advantages by using waste miscanthus fibers as lightweight aggregate. Since miscanthus fiber itself is a widely available natural resource in Europe, so the cost and energy consumption are much lower than commercial lightweight materials. Moreover, thanks to the CO_2 sequestration during miscanthus growth, this results in a carbon dioxide equivalent mitigation potential of 117% [141]. Furthermore, the porous structure in the stem can function as insulating cells in the ULMC. Therefore, applying MF in ULMC shows much better ecological potential than traditional insulation boards.

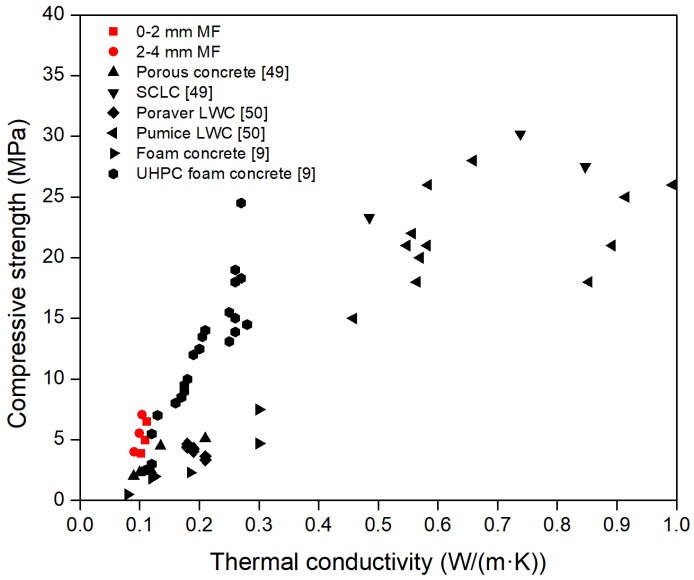

Fig. 3.14. Thermal conductivity versus compressive strength of different kinds of LWC.

3.4. Conclusions

This chapter presents the research of developing ultra-lightweight miscanthus concrete (ULMC) incorporating miscanthus fibers (MF) and expanded waste glass (EWG), with the extra efforts on the effects of different format of MF on acoustic absorption. Acoustic absorption coefficient of ULMC is greatly improved to 0.9 at low frequencies by the incorporation of 2-4 mm miscanthus fibers. Moreover, the thermal conductivity of ULMC decreases to 0.09 W/(m·K) by the contribution of both EWG and MF. Overall, the developed ultra-lightweight miscanthus concrete (ULMC) can help to reduce environmental impact and functions as indoor heat insulation and as lightweight material for noise insulation. According to the current results, the following conclusions can be drawn:

- The addition of miscanthus fibers in cement matrix decreases the density and compressive strength of ULMC, while the flexural strength remains stable. 2-4 mm MF has a better performance than 0-2 mm MF in terms of enhancement of the flexural strength.
- An increasing percentage of 2-4 mm MF leads to a higher acoustic absorption coefficient of ULMC with a wider frequency band. To obtain a high sound absorption above 0.5 at frequencies of 600~1200 Hz, the incorporated MF percentage in the ULMC mixture should

be more than 20% 2-4 mm MF. However, 0-2 mm MF has negligible effect on acoustic absorption of ULMC due to the dense surface structure.

- The thermal insulation performance of ULMC slightly improves because more air voids and interfacial thermal gaps are introduced by the fibrous miscanthus particles. UPV test shows the large pores exist in the interface of fibers and cement matrix. The lowest thermal conductivity of ULMC reaches 0.09 W/(m·K).
- The main LWAs adopted to prepare ULMC are the miscanthus fibers and expanded waste glass, indicating a novel approach to efficiently recycle the waste biomass and waste glass, contributing to the sustainable development of cement and concrete industry.

Chapter 4 Development of cement-free bio-based cold-bonded lightweight aggregates (BCBLWAs) using steel slag and miscanthus powder via CO_2 curing

This chapter explains the development of a novel type of bio-based artificial lightweight aggregate. The use of plant-based aggregates in concrete effectively decreases its bulk density, the environmental impact and improve the insulation properties. However, the application of plant-based aggregate in ordinary cement-based concrete still faces critical problems, for instance, the polysaccharide leached from the plant retards the hydration of clinker and lead to degradation of concrete strength. In this study, a novel bio-based cold-bonded lightweight aggregates (BCBLWAs) was developed with the use of converter steel slag and miscanthus powder via CO_2 curing. The aggregates using steel slag as a binder show relatively high strength and low density with the use of miscanthus. The polysaccharide leached from miscanthus powder, which negatively influences the cement-based aggregates, has no influence on the artificial carbonated steel slag aggregate. The developed BCBLWAs obtained compressive strengths from 0.58 MPa to 5.3 MPa and loose bulk densities from 550 kg/m^3 to 1300 kg/m^3. The reaction products and microstructure of BCBLWAs after carbonation curing were characterized by TGA, XRD, SEM and nitrogen physisorption. The CO_2 uptake capacity of BCBLWAs was also evaluated. Furthermore, the prepared BCBLWAs were utilized to prepare a lightweight concrete, which obtained optimal compressive strength (28.5 MPa), dry bulk density (1630 kg/m^3) and thermal conductivity (0.439 W/(m·K)). The effect of BCBLWAs on the hydration of cement was also evaluated to be minor and only showed a slight retardation effect. The lowest thermal insulation of BCBLWAs incorporated lightweight concrete reached 0.255 W/(m·K).

This chapter is partially published elsewhere:

Y.X. Chen, G. Liu, K. Schollbach, H.J.H. Brouwers, Development of cement-free bio-based cold-bonded lightweight aggregates (BCBLWAs) using steel slag and miscanthus powder via CO_2 curing, Journal of Cleaner Production 322 (2021) 129105.

4.1. Introduction

Lightweight concrete is widely used in construction and buildings. It can effectively reduce the mass and show superior thermal insulation and sound absorption properties, while maintaining adequate strength [142]. The combination of cementitious materials and different lightweight aggregates (LWAs) can be utilized to produce various kinds of lightweight aggregate concretes, for instance, ultralightweight concrete incorporated with expanded glass or expanded polystyrene foam [3–6]. The properties of LWA, such as density, strength and thermal conductivity, are the key factors influence the performance of lightweight concrete. Furthermore, the LWA accounts for the main cost and energy consumption of lightweight concrete.

Generally, the sintering process contributes to a high CO_2 emission of commercial LWAs production, which is indispensable to produce the porous structure of aggregates. For example, expanded glass derived lightweight aggregate, where the raw glass is crushed, ground and mixed with blowing agents before granulation. After that the formed granules are heated in a rotary kiln to more than 1400 °C [144]. This mechanism of high temperatures to produce porous structure is also applied to lightweight expanded clay aggregate (LECA) and perlite. The LECA is heated to around 1200 °C in a rotary kiln to yield gases, expand the clay and produce a honeycomb structure [145]. Perlite needs to be heated to 760–1100 °C, and the moisture is converted to gas and resulting in a lightweight high porosity material [146]. Therefore, a lowered embedded energy of lightweight aggregate is in dire needed.

Recently, more studies have focused on the production of economic LWAs, using the cold-bonding process to produce sustainable lightweight aggregates by various industrial by-products [147–149]. Normally, ordinary Portland cement (OPC) is a necessary binder during the pelletizing process to provide adequate strength of cold-bonded LWAs (CBLWAs), which plays as an adhesive agent. For instance, cement slurry and fine incineration bottom ash were used to produce lightweight aggregates that show strengths from 0.3–2.0 MPa [25]. In another study, the application of 10-15% of CEM I 42.5 N cement in CBLWA provides a compressive strength of 5.7 MPa after 28 days normal curing [147]. **Table 4.1** shows the summary of the studies using CBLAs in lightweight concrete. Using this method, the artificial lightweight aggregates produced at room temperatures, while still showing considerable strength [21,23,149].

However, Portland cement accounts for a high amount of CO_2 emission. Therefore, alternative binder system like geopolymer or alkali-activated materials are also utilized in cold-bonded lightweight aggregates. For instance, GGBS and FA utilized as binders have been investigated [22,150–152]. Alkaline activator, including Na_2SiO_3 and NaOH, have been incorporated in the production of geopolymer CBLAs [153,154]. However, FA and GGBS are not regarded as solid waste in recent years and become more valuable in concrete production. Hence, it is interesting to find a solid waste to be utilized as a binder to produce CBLWAs. To the authors' knowledge, industrial by-product such as converter steel slag has never been reported to be used as a binder in the production of CBLAs.

Table 4.1. CBLAs in recent studies, showing most of the CBLAs components contain cement.

Components	Curing method	LBD (kg/m^3)	WAB (wt-%)	WC (wt-%)	BS (MPa)	Literatures
Cement, class-F FA	RH 70% at 20℃	1460	21.15	22	-	[24]
Waste concrete powder, cement, slag, $Ca(OH)_2$	CO_2 curing; RH 60%	926-972	9.30-36.30	-	0.75-2.98	[26]
Cement, Class-F FA, EPP	RH 65%-99%	510-650	30-52	-	0.20-3.55	[155]
Cement, lime, class-F FA, $Ca(OH)_2$, Na_2SO_4	In water	750-980	19-23	30-33	-	[156]
Class-F FA, GGBS, CEM I 42.5	RH 70% at 21 ℃		4-20	18-20	-	[157]
Class-F FA, quarry dust, cement	In water	950-1100	16-21	-	6.15-8.32	[27]
MSWI FA, CEM II 42.5R, lime, coal fly ash	Seal curing	980	14.9	-	7.5	[21]

*LBD: loose bulk density; WAB: water absorption; WC: water content; BS: bulk crushing strength; FA: fly ash; EPP: expanded perlite powder; MSWI FA: municipal solid waste incineration fly ash; GGBS: granulated ground blast slag

Converter steel slag is a by-product of the steel making process [158]. In the European Union, there is more than 100 million tons of steel slag currently landfilled and will continue to produce millions of tons of steel slag every year [159]. The main crystalline phases in CSS are larnite, wüstite, brownmillerite, free lime and magnetite [160]. Although C_2S can provide some hydraulic properties of CSS, the large amount of other inert phases and the presence of free lime make it difficult to use as a binder or aggregate in concrete [161,162]. However, carbonation of steel slag can transform free lime and C_2S to calcite and solve the volumetric instability issue. The main carbonation reaction happens as follows:

$$Ca_2SiO_4 + CO_2 + H_2O \rightarrow CaCO_3 + SiO_2 + H_2O \quad (4.1)$$

$$CaO + CO_2 + H_2O \rightarrow CaCO_3 + H_2O \quad (4.2)$$

The C_2S and free lime react with CO_2 and in presence of water, forming calcite and amorphous silica. In this process, the carbonation products can bond particles together and contribute to the development of the strength, for example, carbonated steel slag mortars [28]. Therefore, the carbonation process of converter steel slag is predicted to replace the hydrated cement as an adhesive agent in the production of CBLWAs. However, the density of converter steel slag is very high (around 3.9 kg/m^3) which makes it difficult to be applied in the manufacture of lightweight aggregate [163]. Furthermore, the thermal conductivity of steel slag is relatively high, reaching 0.85 to 1.2 W/(m·K) or even higher. The insulation property is closely related to the density of the materials. Therefore, finding a sustainable and renewable

lightweight additive for the sake of reducing the density of carbonated steel slag, and further to prepare novel lightweight aggregate is very important.

On the other hand, biomaterials are recently investigated as interesting substitution of fossil fuel materials like polymers, which can be applied in construction materials. Natural fibers is an ultralow density and high porosity biomaterial and can be used as a kind of LWA in lightweight concrete, for instance, jute, hemp and miscanthus [117,143]. The incorporation of finely grounded natural fibers in LWA production can effectively reduce the density, while contributing to the improvement of thermal insulation and acoustic absorption [117,143]. Miscanthus shows two major advantages as compared to common renewable materials like conifers. These are the thermal insulating qualities and in addition the very high firmness of the plant material. A cross-section of the miscanthus shoot shows, that there is the parenchyma which provides the thermal insulation and around the parenchyma there are three rings with relevance to firmness: the epidermis, the thick sclerenchyma characteristics and the radial allocation of vascular bundles with its own firmness texture. However, miscanthus powders have very high water absorption and are difficult to be used in concrete directly [117]. This is due to the high surface area of miscanthus powder. Preliminary results also showed that miscanthus powders severely delay clinker hydration which makes it difficult to form cement-based pellets [102,117]. In summary, combining miscanthus powder and converter steel slag for LWA production by using carbonation curing could solve above incompatibilities, such as retardation effect and high density. In this way, the LWA could be produced without cement. This makes it possible to produce sustainable LWA that are not affected by the polysaccharide leached from natural fibers and also significantly reduce the density of steel slag pellets. It is also expected that the moderate amount of miscanthus powder (MP) in aggregates could accelerate the carbonation of steel slag, resulting in a higher strength of the CBLAs, thanks to the high porosity and water retention of MP.

In this chapter, lightweight aggregates are produced by the carbonation of cold-bonded steel slag and miscanthus powder. The miscanthus plays a role as lightweight biofibres and accelerates the carbonation reaction. The microstructure and carbonation products of the produced bio-based cold-bonded lightweight aggregates (BCBLWAs) are characterized by SEM, TGA, XRD and nitrogen physisorption. The CO_2 uptake capacity of BCBLWAs is also calculated. The mechanical properties of BCBLWAs are measured by individual pellet strength and bulk crushing resistance. Moreover, a lightweight concrete with the incorporation of BCBLWAs is prepared. The developed novel lightweight concrete is characterized by dry density, compressive strength, and thermal insulation properties. The result of this study shows promising application of steel slag and miscanthus powder as the raw materials in the production of sustainable and negative CO_2 footprint CBLAs.

4.2. Materials and experiments

4.2.1 Raw materials

Converter steel slag was provided by Tata steel, IJmuiden, the Netherlands (specific density is 3.9 kg/m^3). Miscanthus powder (below 1 mm) was provided by Vibers, the Netherlands. These two materials are the ingredients to prepare BCBLWAs.

Ordinary Portland cement (CEM I 52.5 R) was used to prepare BCBLWAs lightweight aggregate concrete, which was provided by ENCI. The oxide composition of steel slag and CEM I 52.5 R are shown in **Table 4.2**. The mineral composition was determined using X-ray diffraction (XRD) analysis, which is shown in **Fig. 4.1 (a).** The converter steel slag mainly consists of brownmillerite, C_2S, wüstite and magnetite. Minor amounts of free lime and C_3S are also possible. The MgO mainly exists in the mineral phase of wuestite, which is a solid solution between MgO and FeO. The content of free lime in the converter slag from Tata Steel is very low (<2%). The particle size distribution of finely grounded steel slag using a disc mill is presented in **Fig. 4.1 (b)**. The specific surface area of steel slag and cement is 0.42 m^2/g and 1.00 m^2/g, respectively. The specific density of steel slag and cement is 3.9 g/m^3 and 3.15 g/m^3, respectively.

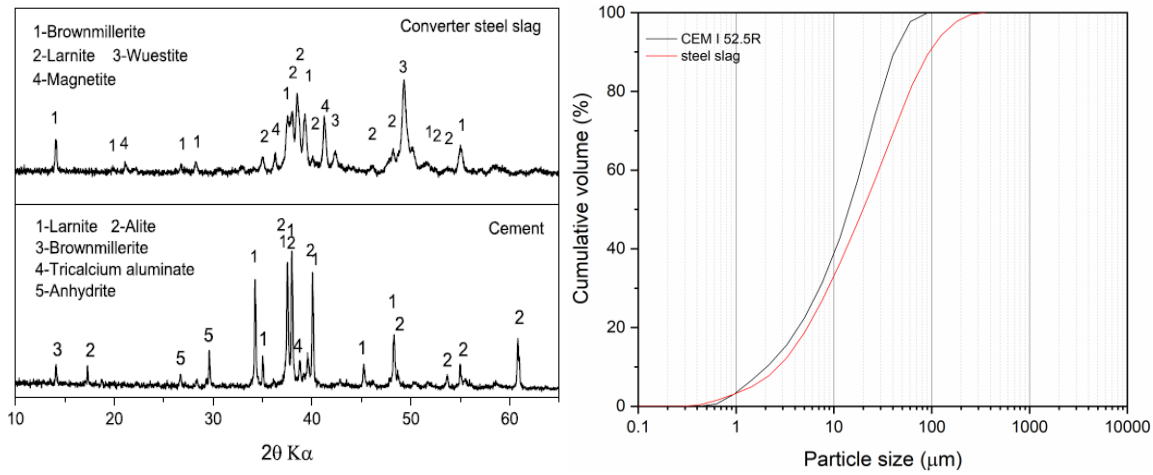

(a) (b)

Fig. 4.1. XRD (a) and PSD (b) of the used converter steel slag and cement.

Table 4.2. The oxides composition of raw materials used.

Materials (wt%)	CaO	SiO_2	Al_2O_3	Fe_2O_3	TiO_2	P_2O_5	MgO	MnO	V_2O_5	SO_3	LOI
Steel slag	41.55	11.47	2.24	31.35	1.56	1.30	3.78	4.78	1.14	-	0.72
Cement	64.64	20.08	4.98	3.24	0.30	0.42	1.98	0.10	-	3.13	0.51

The monomeric polysaccharides' concentration of miscanthus powder was tested by using High-Performance Anion-Exchange Chromatography (HPAEC) after H_2SO_4 hydrolysis in mg/ml were: For example, Arabinose 0.06, Galactose 0.09, Glucose 0.19, Xylose 0.16 and Mannose 0.05. The component of miscanthus are mainly cellulose, hemicellulose and lignin, which account for 40.21%, 43.24% and 17.93% of the total mass, respectively [117]. The SEM images of the miscanthus powders (**Fig. 4.2**) show a porous structure with pore sizes of around tens of micrometres. The particle shape of miscanthus powder is quite heterogeneous, with particle size ranging from 50 um to 1 mm. The water absorption of MP is quite high according to previous research, showing a water absorption capability of above 300% [117]. The density of the MP is around 300 kg/m^3, which is quite low compared to converter steel slag.

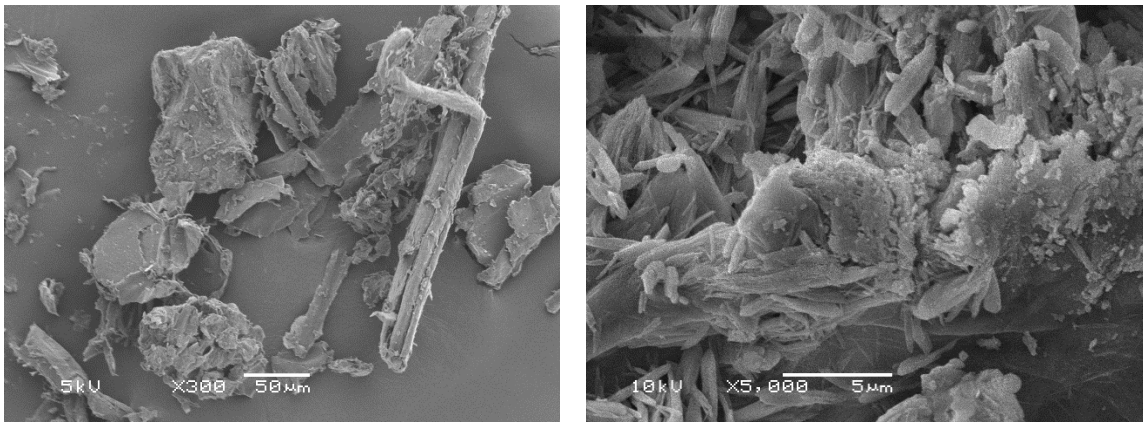

Fig. 4.2. SEM images of the used miscanthus powder (a) magnification ×300 (b) magnification ×5000.

4.2.2 Pelletizing procedure

Fig. 4.3 shows the pelletizing process of BCBLWAs manufactured with miscanthus powders and steel slag. The disc pelletizer was used to produce the artificial aggregates. The model was D-7736, Maschinenfabrik Gustav Eirich, Germany. The size of the pelletizer was 40 cm in diameter and 10 cm in collar height. The vertical angle of the pan was 75° and the rotating speed was 60 rpm during the production. The starting mixtures of steel slag and miscanthus powders used for BCBLWAs were first mixed via a planetary mixer. Then around 500 grams of the mixed powders were placed on the rotating pan. After about 3 min rotating, around 50 grams of distilled water was sprayed slowly onto the mixed powder in the pan using a spray bottle in 10 min. After small balls formed in the pan, the pan continued running for 5 min to make the aggregate grow. Afterwards, the first round as-prepared aggregate would drop off simultaneously from the bottom of the pan. The next batch was prepared with the addition of another 500 gram of dry mixed powder and followed the same procedure again. The freshly prepared BCBLWAs were placed in a sealed plastic box for further CO_2 curing.

For the CO_2 curing process, the BCBLWAs were placed in a CO_2 chamber and carbonated for 3 days to complete the carbonation process. The CO_2 concentration and the humidity were set at 20% and 75%, respectively. The temperature during curing was constant, around 20 ℃. The pressure used is atmospheric pressure, i.e. 101.3 kPa.

In order to determine the optimal volume ratio of steel slag and miscanthus powders, 5 batches of artificial aggregates were pelletized (SS:MP = 100:0, 90:10, 80:20, 65:35 and 50:50 in volume percent). The recipe for BCBLWAs in this study is shown in **Table 4.4**.

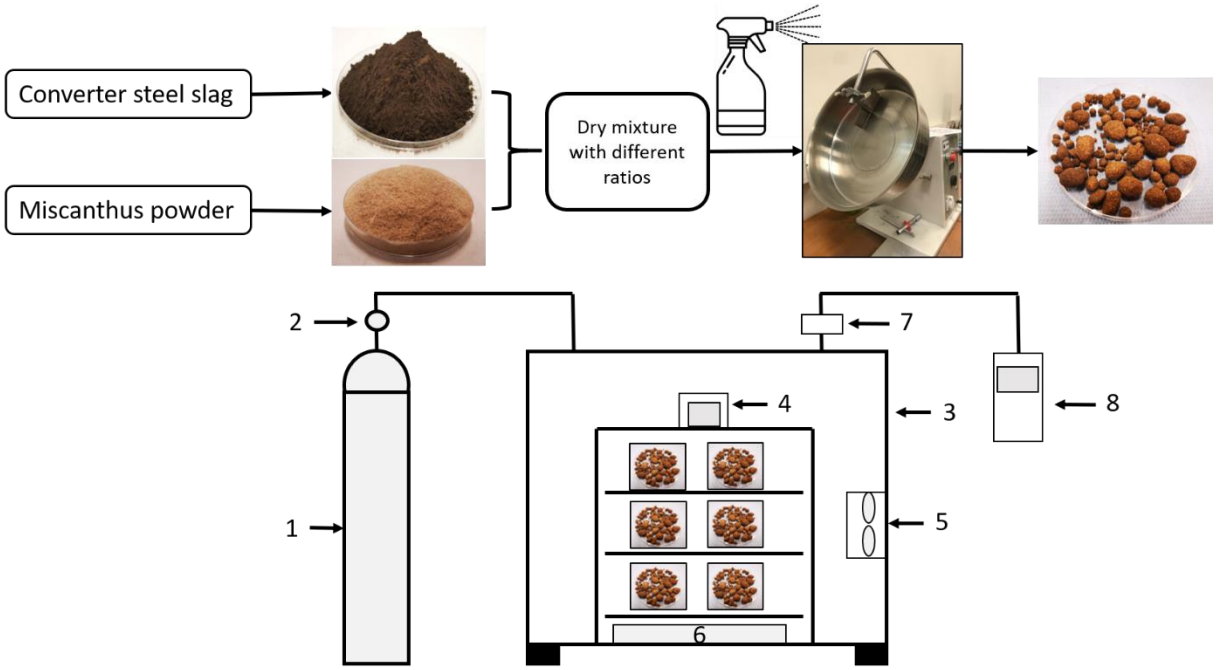

Fig. 4.3 Schematic process of the production of BCBLWAs with steel slag and miscanthus powder. (1. CO_2 2. Regulator 3. Carbonation chamber 4. Humidity and temperature meter 5. Fan 6. NaCl solution 7. CO_2 probe 8. CO_2 meter)

Table 4.4. Recipe for BCBLWAs with different volume ratio of steel slag and miscanthus powder.

Groups / Materials	SS100	SS90MP10	SS80MP20	SS65MP35	SS50MP50
Steel slag (g/vol.%)	1000/(100%)	960/(90%)	919/(80%)	838/(65%)	735/(50%)
Miscanthus powder (g/vol%)	0/0	41/(10%)	82/(20%)	162/(35%)	264/(50%)

4.2.3. Lightweight concrete (LWC) preparation

The mix design for LWC-BCBLWAs is shown in **Table 4.5**. The preparation of lightweight concrete with the incorporation of BCBLWAs is described as follows: (1) CEM I 52.5 R was dry mixed in the planetary mixer for 1 min. (2) Tap water was added into the mixer with a w/b ratio of 0.5 and continued mixing for 3 min. (3) The as-prepared BCBLWAs was added into the cement paste and continued mixing for 5 min. (4). After the fresh grout was homogeneous, the fresh grout was poured into the mould without compaction. The grout showed self-compacting property due to the spherical shape of BCBLWAs. (5) The mould was sealed with plastic film for 1 day and demoulded the next day. Seal curing was applied to cure the samples until the age of 7 and 28 days.

Table 4.5. The mix design of lightweight concrete incorporated with 50 vol.% BCBLWAs (kg/m^3).

Groups	CEM I 52.5 R (kg/m^3)	Water (kg/m^3)	BCBLWAs (kg/m^3)	BCBLWAs (vol.%)
LWC-SS100	608	304	1400	50
LWC-SS90MP10	608	304	1050	50
LWC-SS80MP20	608	304	900	50
LWC-SS65MP35	608	304	750	50
LWC-SS50MP50	608	304	500	50

4.2.4 Characterization methods

4.2.4.1 Physical and mechanical properties of BCBLWAs

The loose bulk density test was carried out according to EN 1097-3 [164]. The water absorption test was carried out according to EN 1097-6 [165]. The particle size of the tested pellets was around 4-8 mm. The water content of BCBLWAs was determined by heating the pellets in the oven at 110 ℃ for 24 hours and then measuring the remaining mass of the pellets. Hence, the water content was the weight difference before and after heating divided by the original mass of the pellets. The mechanical property of the individual pellet of BCBLWAs with different sizes were tested in an MTS Criterion equipped with a load cell of 5000 N at a speed of 0.6 mm/min until collapse. The maximum force was used to calculate the individual crushing strength according to [22].

$$\sigma = \frac{2.8P}{\pi d^2} \tag{4.3}$$

where σ (MPa) is the crushing strength of each pellets tested, P (N) is the maximum force each pellet can withstand, d (mm) is the approximate diameter of the round pellet produced. Around 20 pellets were used as representatives for every batch of BCBLWAs prepared.

The bulk crushing resistance (CR) of the BCBLWAs aggregates was measured according to EN 13055-1 (Annex Procedure 1) [166]. The proper amount of sample pellets was filled in the cylinder and then compressed to a height of 20 mm. The following equation was used to calculate the CR:

$$C = \frac{L + F}{A} \tag{4.4}$$

where C is the crushing resistance of (MPa), L is the force generated by the load cell (N), F is the compression force (N), and A is the compressed area (mm^2), equals to $\pi d^2/4$.

4.2.4.2 Reaction products and microstructure analysis of BCBLWAs

The microstructure of the BCBLWAs was observed with scanning electron microscopy (SEM), by using a JOEL JSM-5600 instrument at an accelerating voltage of 15 kV. The specific surface area and pore size distribution of BCBLWAs were measured after grinding and sieving using a 68 μm sieve to remove most of the miscanthus powder. It was measured by nitrogen

physisorption using a Micromeritics Tristar 2000 with BET and BJH method, respectively. The CO_2 uptake capacity of the BCBLWAs was measured by using thermogravimetric analysis (TGA) with a NETZSCH STA449-F1 instrument at a heating rate of 10 ℃/min under nitrogen atmosphere. The quantification of the CO_2 uptake per gram BCBLWAs was determined by the mass loss from 600 to 800 °C, which is the temperature where decomposition of calcite takes place. The following equation was used to calculate the CO_2 uptake capability of BCBLWAs per unit [28].

$$CO_{2\,(uptake)} = \frac{M_{600} - M_{800}}{M_{800} + M_{fiber}} \times 100\% \quad (4.5)$$

The crystalline phases of carbonated BCBLWAs were detected by X-ray diffraction analysis. The parameters chosen were as follows: Co tube, 40KV, 30 mA, 0.02°/ step, 0.2°/min, with variable divergence slits V20. The BCBLWAs samples were first ground and passed through a 68 μm sieve to remove most of the miscanthus powders. The remaining material was used to prepare the XRD samples.

4.2.4.3 Characterization of LWC-BCBLWAs

The fresh density of LWC incorporated with BCBLWAs was measured following EN 12350-6 (2009) [41]. After mixing, the LWC-BCBLWAs was cast into moulds of 100 mm × 100 mm × 100 mm and 40 mm × 40 mm × 160 mm. The samples were demoulded after 1d and the dry density was determined following EN 12390-7 (2009) [42]. The compressive and flexural strength of the LWC-BCBLWAs were tested at the age of 7 and 28 days. After 28 days curing, the LWC-BCBLWAs cubes were first dried at 105 ℃ overnight to a constant mass. The heat transfer analyser ISOMET model 2104 was used to determine the thermal conductivity of the LWC-BCBLWAs. The isothermal calorimeter (TAM Air, Thermometric) with three channels was used to test the influence of BCBLWAs on the hydration of Portland cement CEM 52.5 R using calorimeter pots with a volume of 100 ml. The volumetric ratio of BCBLWAs to the volume of cement paste was 1:1. All measurements were conducted for 72 h under a constant temperature of 20 °C. The heat release and heat flow results were normalized by mass of binder, miscanthus and de- ionized water.

4.3. Results and discussion

4.3.1 Physical properties of the produced BCBLWAs

The water content and water absorption of the prepared BCBLWAs are shown in **Table 4.6**. The water content of BCBLWAs is influenced by the percentage of miscanthus powder in the LWA mix because the miscanthus powder has a much larger intra-particle porosity than the carbonated steel slag, thus absorbs more water during pelletization. As indicated in [117], the intra-particle porosity of MP is around 77%, As seen from **Table 4.6**, the water content of BCBLWAs increases with the increasing content of MP from 1.14% to 18.1%. However, according to literatures, many cold-bonded lightweight aggregates have a water content ranging from 12% to 50% depending on the binder used, for instance cement and lime, with the addition of fly ash and other additives [155,156,167]. Therefore, the prepared BCBLWAs have an even lower water content than other CBLAs. This is mainly due to the different microstructure and

binder used. In cement-based pellets, the hydration products like C-S-H contain water. However, for carbonated steel slag, it contains a dense surface structure after calcite formation and also much compacted, that contains less water.

The water absorption of the prepared BCBLWAs is relatively low for SS100 to SS65MP35, reaching only 5.86% to 18.83%. However, SS50MP50 has a much higher value of 41.06%. The interesting finding here is that with the 10 vol.% MP in the BCBLWAs, the water absorption of prepared aggregate deceases from 5.86% to 5.09% compared to plain steel slag pellets. The reason may be that the formed calcite spreads on the surface of the MP and mitigates the water absorption of MP. However, for the last three mixes with more than 20 vol.% MP, the water absorption increases very fast, and finally reaches 41.06%, which is higher than other CBLAs. For the cement-based binder aggregate with fly ash addition, the water absorption of CBLAs is from 10% to 30% as shown in **Table 4.1** [24,27,168,169]. For the water content and absorption of this study, it is found that solely steel slag based aggregate has a much lower water content (1.14%) and water absorption (5.86%) than cement or lime based lightweight aggregate. High water adsorption of LWAs in concrete can be problematic, because the aggregate competes with the cement for water and thus increases the water demand of the whole concrete. On the other hand, using pre-saturated LWA can increase the time and cost of the preparation process and reduce the strength of the interface between aggregate and cement. Hence, carbonated steel slag incorporated with up to 35 vol.% MP can be a good alternative.

Lightweight aggregate is defined in BS EN 13055 as any aggregate with a particle density of less than 2000 kg/m^3 or a dry loose bulk density of less than 1200 kg/m^3. Therefore, SS80MF20, SS65MF35, and SS50MP50 qualify as lightweight aggregates. SS100 and SS90MP10 do not meet the criterion but will be referred to with the same abbreviation BCBLWA for convenience. Overall, the density of BCBLWAs falls significantly with increased content of MP, the loose bulk density of SS80MP20, SS65MP35 and SS50MP50 are 1050 kg/m^3, 760 kg/m^3 and 550 kg/m^3, respectively.

Table 4.6. Water content, water absorption and densities of BCBLWAs.

Groups	SS100	SS90MF10	SS80MF20	SS65MF35	SS50MF50
Water content (%)	1.14±0.12	2.98±0.25	4.20±0.31	6.80±0.29	18.1±0.98
Water absorption (%)	5.86±0.22	5.09±0.16	7.77±0.27	18.83±0.55	41.06±1.23
Loose bulk density (kg/m^3)	1630±12	1300±10	1050±11	760±9	550±7
Particle density (kg/m^3)	2800±26	2130±15	1760±19	1390±20	1080±32

The compressive strength of the individual BCBLWAs for each group is shown in **Fig. 4.4**. As can be seen in **Fig. 4.4 (a),** the maximum strength of BCBLWAs increases with the rising size of the aggregate. And this trend is more obvious for the groups containing less than 20% MP. This is due to the size effect on the stress of the aggregates and is in agreement with other researches [149]. It is interesting that SS90MP10 shows a steeper linear fit than other groups, indicating a higher strength or better carbonation effect and optimized MP content.

From **Fig. 4.4 (b),** it is obvious the calculated compressive strength is quite variable for each mix. Most of the aggregates show an evenly distributed strength regardless of their particle size. The strength development shows the sequence of SS90MP10 (4.18MPa), SS100 (3.4MPa), SS80MP20 (1.8MPa), SS65MP35 (0.58MPa) and SS50MP50 (0.12MPa) as described in **Table 4.7.** However, the standard deviation is high. Therefore, bulk crushing resistance was used to further determine the strength of the BCBLWAs as shown in **Table 4.7**. As can be seen, the crushing resistance follows the same trend as the individual pellet strength. With the addition of 10% MP, the crushing resistance went up from 4.0 MPa to 4.8 MPa, while with increasing MP content the crushing resistance decreases to lower value, and the worst performance is shown by sample SS50MP50. This indicates a proper amount of MP can contribute to higher strength of BCBLWA, while excessive dosage of MP can lower the strength of BCBLWAs. Compared with other cold-bonded lightweight aggregates, the strength of the prepared BCBLWAs is similar [27,168,170,171]. Therefore, the strength mainly provided by the formation of calcite in the aggregate can offer similar strength to cement or lime based lightweight aggregate.

Table 4.7. Individual pellet strength and bulk crushing resistance of BCBLWAs.

Groups	SS100	SS90MP10	SS80MP20	SS65MP35	SS50MP50
Individual pellet strength (MPa)	3.4±1.2	4.2±1.5	1.8±1.0	0.58±0.29	0.12±0.01
Bulk crushing resistance (MPa)	4.0±0.3	4.8±0.4	2.0±0.2	0.99±0.11	0.32±0.06

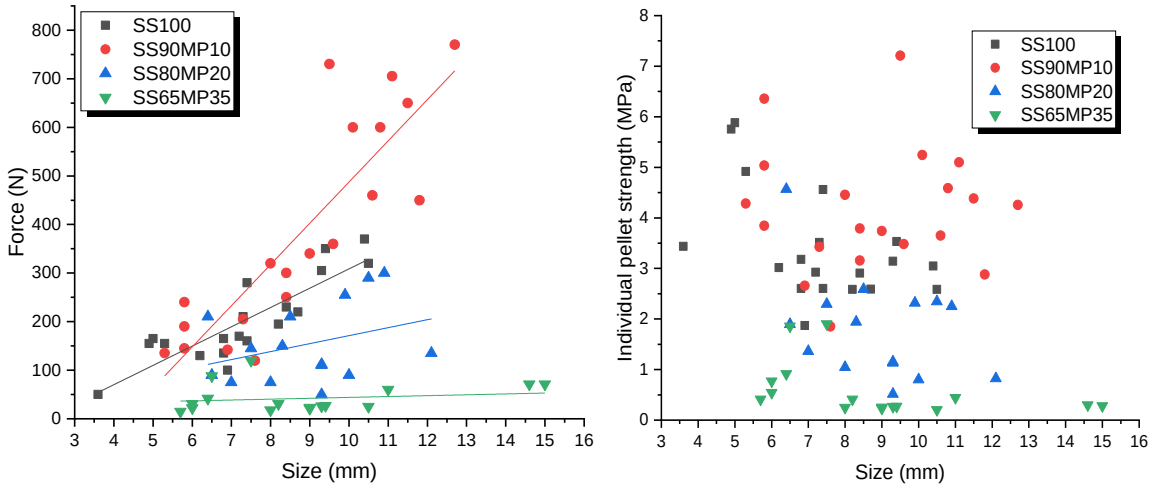

(a) (b)

Fig. 4.7. Individual pellet stress (a) and strength (b) of different groups of BCBLWAs.

4.3.2 Reaction products and microstructure of BCBLWAs

4.3.2.1 XRD analysis

The X-ray diffraction pattern of the BCBLWAs with different amounts of miscanthus powder are shown in **Fig. 4.5.** The SS100 sample shows a very similar pattern as the raw steel slag shown in **Fig. 4.2**. The carbonation of the steel slag aggregate is very slow during the 3

days CO_2 curing. The main phases are wüstite, larnite and brownmillerite. Small amounts of magnetite are also present. The tiny peak emerging at 34.4° is the typical peak of calcite. However, the peak intensity of calcite is relatively low compared to other mixes with MP, showing that the SS100 aggregate is only partially carbonated and that the strength mainly comes from the compactness of the finely grounded steel slag.

After the addition of miscanthus powders, the XRD pattern changed and the calcite intensity increased with the increasing amount of MP. This trend is more obvious when 20% of MP was added. It can be seen from the peak at 34.4° that the calcite concentration increased significantly for the last three groups, which is in agreement with the TGA analysis in Section 3.2.2. And the peak of larnite and brownmillerite decreased and even hardly observed for group SS50MP50. This may be due to the dilution effect because there is still some MP in the sample regardless of the pre-treatment. However, it still can be inferred that the carbonation could transform the minerals larnite C_2S and partially brownmillerite C_4AF into calcite. The XRDs show that small amount of unreacted C_2S is still present so the carbonation could continue with longer CO_2 curing. The intensity of the wüstite (FeO) and magnetite (Fe_3O_4) peaks (49.1° and 35.1°) remains unchanged. Meanwhile, the silica that formed during carbonation is not visible in the XRD pattern, because it is amorphous.

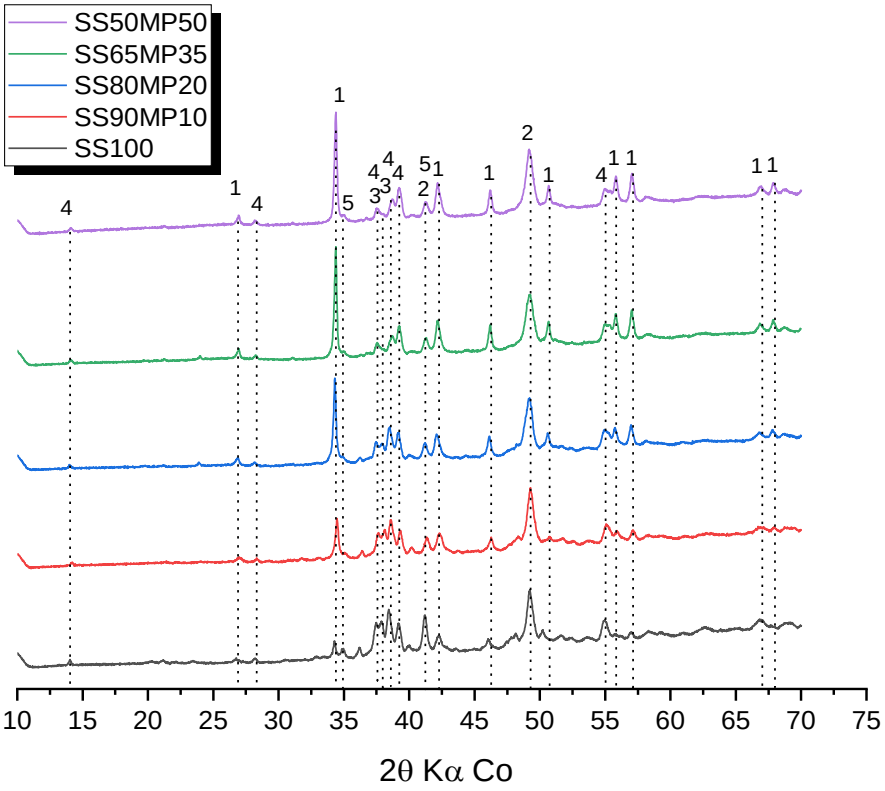

Fig. 4.5. XRD of the different kinds of BCBLWAs: 1- calcite 2- wüstite 3- larnite 4- brownmillerite 5- magnetite.

4.3.2.2 TGA

The thermal gravimetry analysis of the produced BCBLWAs are presented in **Fig. 4.6**. There exist a few stages during the decomposition of the BCBLWAs. At the first stage, ranging from 40 to 105 °C, the loss of physical bonded water in the aggregates occurs. The second stage

is the decomposition of miscanthus powder, ranging from 220 to 380 °C, due to the loss of organic component like cellulose and lignin [172]. The third stage is the decomposition of calcite, ranging from 650 to 800 °C, where the calcite formed in the aggregate during CO_2 curing decomposes to CaO and CO_2. It seems there is a fourth stage up until 1000 °C, this result may be due to the decomposition of lignin in the BCBLWAs, which needs further investigation [173].

As can be seen in **Fig. 4.6**, the BCBLWA produced with 100% steel slag shows the least amount of calcite present, reaching only 7.1wt% in the artificial aggregates. While the 50SS50MP sample shows the largest calcite concentration among all the groups, reaching 27.7%. The calcite concentration of SS90MP10, SS80MP20 and SS65MP35 reached 7.6%, 16.4% and 24.5%, respectively, forming a clear trend.

Moreover, the CO_2 uptake of the BCBLWA aggregates is shown in **Table 4.8**. It is obvious the CO_2 uptake increases significantly with the rising MP content in the aggregate. The reference SS100 only adsorbs 4.17 wt.%/g $_{(pellet)}$ CO_2, while for SS50MP50, this value increase to 16.43%/g. This can be interpreted as follows. Firstly, the CO_2 uptake in the aggregate is determined by the humidity, temperature and pore structure. More MP in the aggregate increases the porosity, thus providing more paths for CO_2 into the aggregate. Secondly, the water retained by the MP can provide more humidity than plain steel slag aggregate, creating a necessary water film on the slag surface accelerating carbonation. The phenolphthalein showed no color after spraying onto the surface of a fractured SS65MP35 aggregate, further indicating the complete formation of calcite and consumption of $Ca(OH)_2$. In the SS100 sample the phenolphthalein still showed a red color inside the aggregate. Therefore, it is confirmed that MP contributes to faster carbonation of steel slag in the aggregate and a higher CO_2 uptake of the artificial aggregates.

Table 4.8. CO_2 uptake capacity of each BCBLWA mix based on TG.

Group	SS100	SS90MP10	SS80MP20	SS65MP35	SS50MP50
CO_2 uptake (wt%/g pellets)	4.17	4.37	9.26	14.13	16.43

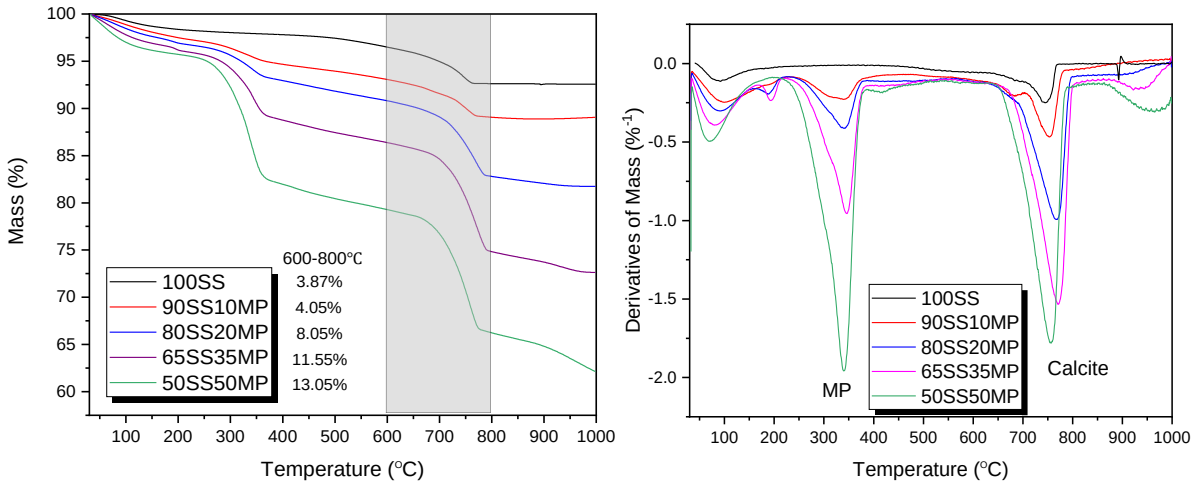

Fig. 4.6 Thermal gravimetric analysis of the synthesized BCBLWAs.

4.3.2.3 Nitrogen physisorption analysis

The nitrogen sorption isotherm and the pore size distribution of the prepared BCBLWAs are shown in **Fig. 4.7**. The reference SS100 sample and all other samples with miscanthus powder present the same type of physisorption isotherm. According to IUPAC definition, the isotherm is a type IV isotherm, meaning the aggregates have a mesoporous structure. The SS100 sample adsorbed a very low nitrogen quantity, while SS65MP35 shows a much higher amount of nitrogen absorbed. Consequently, the specific surface area of SS100 and SS65MP35 are 4.25 m^2/g and 20.64 m^2/g, respectively. This difference in surface area and absorbed nitrogen is due to the different microstructure of steel slag before and after carbonation. Firstly, the steel slag itself has very low intra-particle porosity hence the surface area is low. Also, the reference plain steel slag-based aggregate is so compacted that the carbonation effect on steel slag is very limited, leading to less carbonation products. Therefore, the surface area of SS100 is only slightly increased compared to uncarbonated steel slag (~2.0 m^2/g). While the addition of miscanthus powders contributes a route for CO_2 and moisture to get into the core of the aggregate and majority of the steel slag was carbonated. The carbonation of steel slag accelerates the formation of amorphous silica and calcite due to the reaction with C_2S in steel slag. The fact is the amorphous silica formed during carbonation shows a much higher surface area, normally from 50 m^2/g to 200 m^2/g according to literature [28]. The calcite formed is also in the form of very fine particles, which can also increase the specific surface area. Therefore, this is another indirect evidence that mesoporous silica with high surface area formed after carbonation. Also, this result is in agreement with the XRD and TGA analysis.

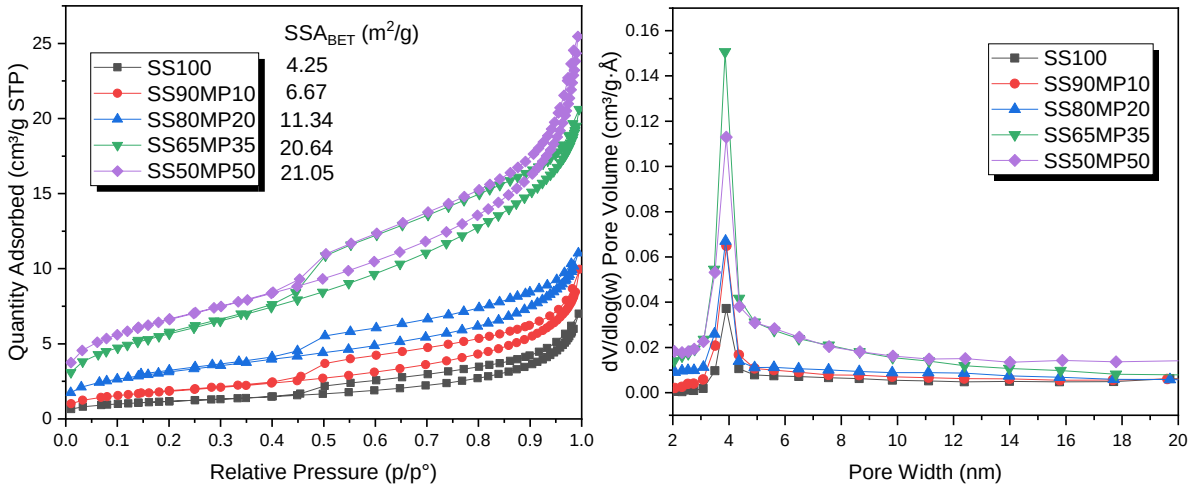

Fig. 4.7. Nitrogen isotherm and pore size distribution of different BCBLWAs.

4.3.2.4 SEM

SEM pictures of fracture surface of BCBLWAs are presented in **Fig. 4.8.** As can be seen from **Fig. 4.8 (a)**, the reference SS100 (plain carbonated steel slag aggregates) shows the morphology of discrete steel slag particles. The bonding between each particle is weak compared to other aggregates. The strength of the SS100 is mainly contributed by the compactness of steel slag and the thin carbonated outer surface of the aggregate. The inner structure is barely carbonated because the CO_2 cannot penetrate deep into the inner structure.

However, with the addition of miscanthus powder, it is obvious that the bonding between steel slag particles is greatly enhanced by the formation of more calcite and amorphous silica. The phenomena are even more obvious when the MP content reaches a volume of 35%. As can be seen from **Fig. 4.8 (d),** more small and bright particles with a size below 10 μm are observed on the surface of MP, which indicates the formation of carbonation products from steel slag. Much more carbonation products are formed with a high surface area, resulting from a higher CO_2 absorption than the pure SS100 sample.

Therefore, it can be inferred from the SEM of BCBLWAs that with the incorporation of miscanthus powders, the porous structure of the MP provides the pores for CO_2 penetration, as a consequence, increasing the carbonation degree of steel slag inside the aggregate and also improving the bonding between particles by forming smaller size carbonation products that are below 10 μm in size.

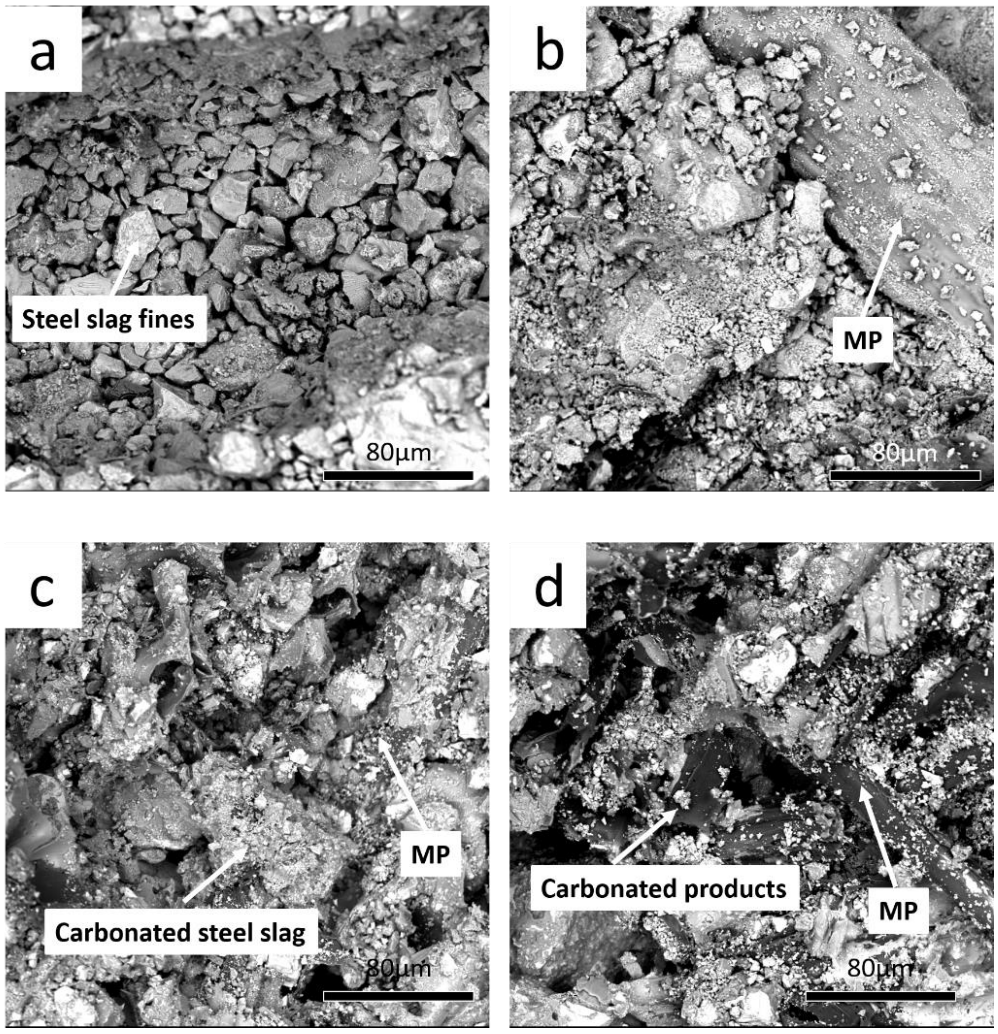

Fig. 4.8. SEM of BCBLWAs from different groups: (a) SS100 (b) SS90MP10 (c) SS80MP20 (d) SS65MP35.

4.3.2.5 Mechanism of carbonation reaction

The purpose of using MP in carbonated steel slag is to decrease the particle density and induce the carbonation reaction in the inner structure of BCBLWAs. As illustrated in **Fig. 4.9**

(a), the surface of the aggregate SS100 is carbonated after 3 days, forming a dense shell structure composed of calcite. The main CO_2 reactive component in converter steel slag is C_2S. C_2S can react with carbon dioxide and water to form calcite and silica gel as discussed above. The density of calcite (2.71 g/cm^3) and silica gel (2.65 g/cm^3) are smaller than C_2S (3.28 g/cm^3), thus the total volume of carbonation products will increase and fill in the inter-particle pores of steel slag, finally generate a much denser and ultralow porosity carbonation layer over the course of the 3-day CO_2 curing. However, the inner structure of the aggregate is barely carbonated, and are mainly compacted raw steel slag particles. Hence, the strength of the aggregate is primarily provided by the outer thinner shell structure of the aggregate. The dense calcite surface prevents the further CO_2 activation of the steel slag inside the aggregate, which means the transportation of CO_2 into the core of aggregate is limited.

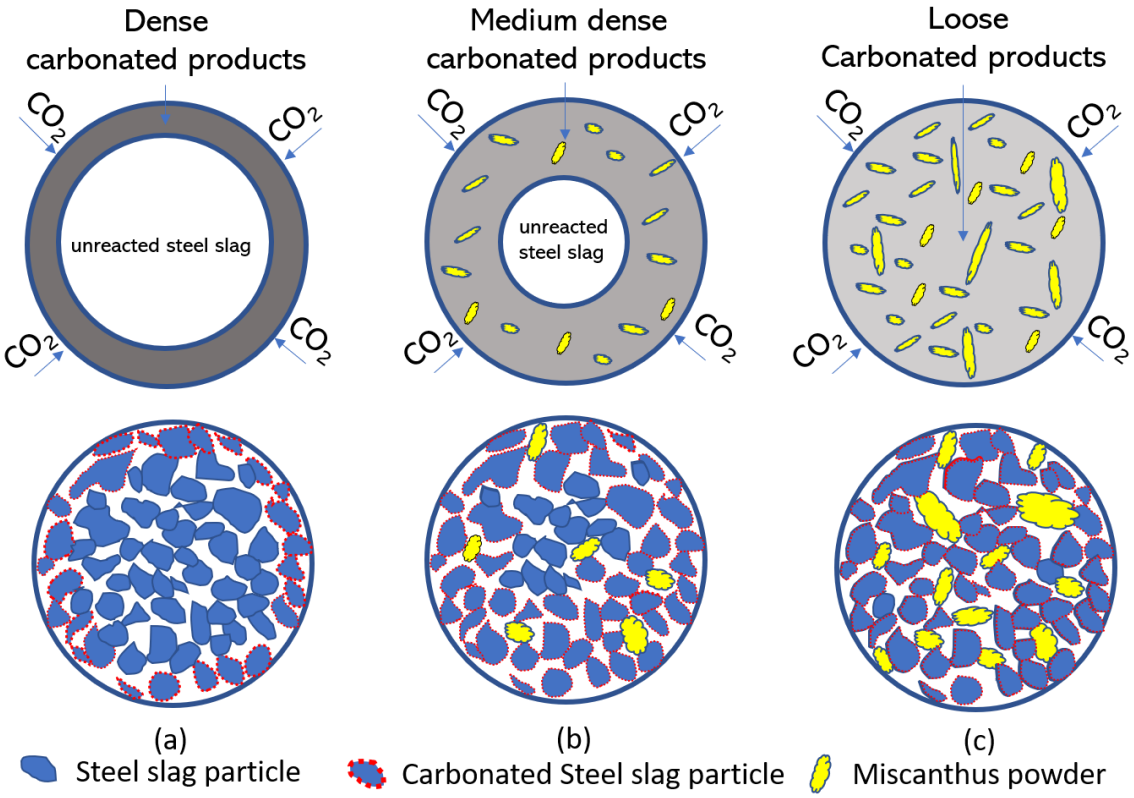

Fig. 4.9. Schematic illustration of inner structure of BCBLWAs: (a) SS100 (b) SS90MP10 (c) SS65MP35. The red dashed outline represents the carbonated steel slag, the blue shape outline represents the water film on the surface of miscanthus powder.

Fig. 4.9 (b) shows the 10% MP addition in the aggregate can provide a 'shortcut' for the CO_2 to permeate deeper inside the compacted steel slag. The surface of the aggregate still first gets carbonated and form a medium dense shell structure. However, the MP change the packing of steel slag and allow more CO_2 pass through the intra-particle pores in the MP. Hence, the steel slag near MP can be carbonated faster and forms more calcite than steel slag located further. The water retained in the MP could also provide more intermedia for CO_2 activation, as the water film on the surface of steel slag particles accelerates the carbonation reaction [174,175]. This is because CO_2 has to first dissolve into the water to form CO_3^{2-} and then react with steel

slag. Therefore, proper amount of MP benefits the mechanical performance of aggregate, regardless of the weak mechanical property of MP itself, which could be compromised.

The increase of MP dosage in the aggregate could induce more CO_2 reaction with steel slag, as illustrated in **Fig. 4.9 (c)**. The MP provides more 'shortcuts' for CO2 and moisture for transport into the cold-bonded particles, resulting in a complete carbonation of the aggregate, as evidenced by XRD result, showing most of the larnite are consumed by carbonation and forming calcite. This inference is also in accordance with the results of N2 physisorption, as the surface area and gel pore volume of BCBLWA is the highest, indicating more carbonation products formed. However, due to the low mechanical performance of MP, the MP become the weak point or defect of the aggregate, thus decrease the strength. Therefore, excessive amount of MP degrades the strength of BCBLWAs. Hence, an optimal amount of MP is suggested in the production of BCBLWAs.

4.3.3 Lightweight concrete prepared with BCBLWAs

4.3.3.1 Density and strength of LWC-BCBLWAs

The density and strength of LWC-BCBLWAs with 50 vol% BCBLWAs at 7 and 28 days are presented in **Fig. 4.10.** Lightweight concrete is defined by BS EN 206-1 [176] as having an oven-dry density of not less than 800 kg/m^3 and not more than 2000 kg/m^3 by replacing dense natural aggregates either wholly or partially with lightweight aggregates. According to BS EN 206-1, all the LWC-BCBLWAs meet the criterial of lightweight concrete except for LWC-SS100 (2110 kg/m^3). The density of LWC-BCBLWAs ranges from 1852 to 1111 kg/m^3. The interesting finding here is the addition of SS90MP10 and SS80MP20 can not only lower the density of LWC-BCBLWAs, but also increase the compressive and flexural strength compared to concrete containing SS100. The reason is already explained and is owing to the optimal amount of MP allowing more calcite formation which compensates for the low strength of the MP themselves.

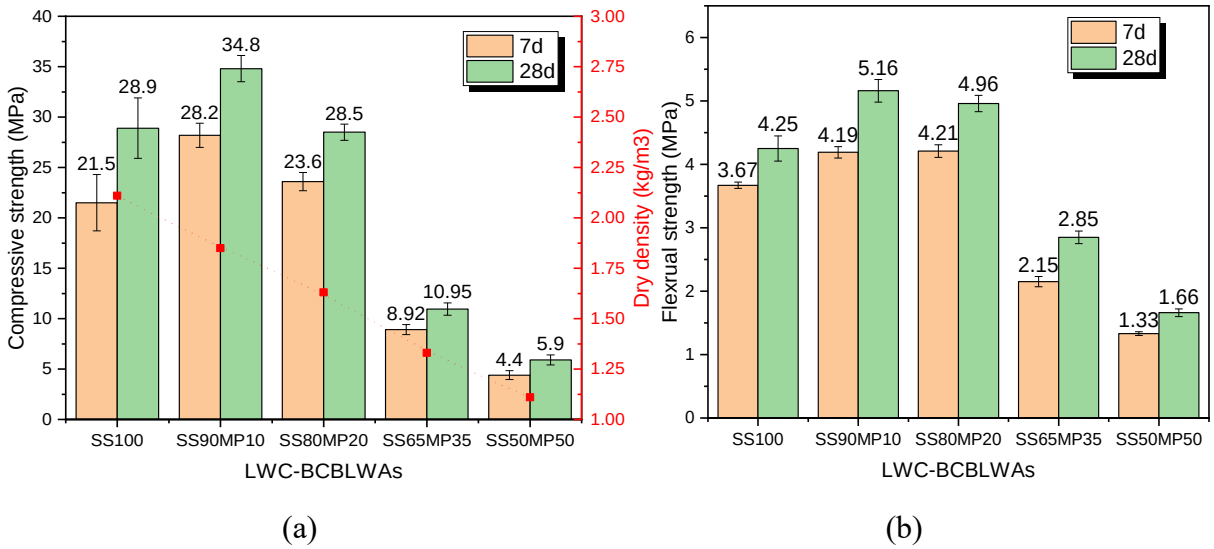

(a) (b)

Fig. 4.10. Compressive (a) and flexural (b) strength of LWC-BCBLWAs at 7 and 28 days.

For the groups with more MP incorporated in the aggregates, the strength of the lightweight concrete decreased significantly, and the dry density also reduced. This is expected if much lighter artificial aggregates are mixed in a cement matrix. For the LWC-SS50MP50, the compressive strength and flexural strength was 5.9 MPa and 1.66 MPa, respectively, while the dry density decreased to only 1111 kg/m^3. The sequence of strength is as follows: LWC-SS90MP10, LWC-SS80MP20, LWC-SS100, LWC-SS655MP35 and LWC-SS50MP50. According to literatures [90,113], a linear relationship exists between strength and density. However, in this study, the lower density of lightweight concrete not always indicates lower strength. Therefore, it is evidenced that 10% and 20% of MP in the BCBLWAs can increase the strength of the aggregate and consequently increase the strength of the lightweight concrete.

The facture surface after the flexural strength test is shown in **Fig. 4.11**. It is observed that all the BCBLWAs in the cement matrix are split due to the compression, much like the split of normal quartz aggregates. This is because of the strong interfacial bonding between BCBLWAs and hardened cement paste. Hence, the route of breaking was through BCBLWAs rather than through the interfacial transition zone (ITZ). Another reason is that the mechanical strength of BCBLWAs is much lower than that of hardened cement paste. Therefore, the strength of LWC-BCBLWAs is mainly dependent on the mechanical properties of BCBLWAs. However, it can be observed that the bonding between the cement paste and BCBLWAs is relatively weak for sample LWC-SS50MP50. It is possible that these aggregates take up a lot of water from the cement and then release it later, which creates a very porous low strength ITZ around the BCBLWAs, which is indicated by the spalling of aggregate from the hardened cement paste.

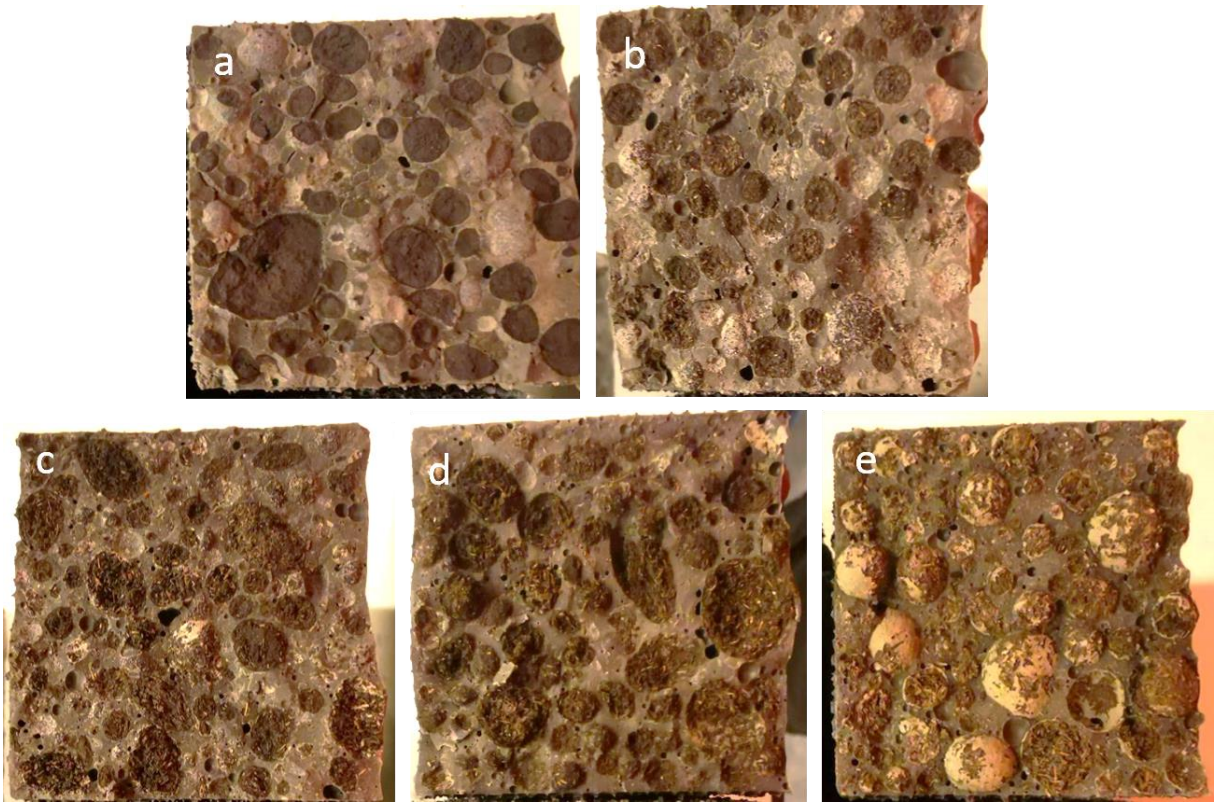

Fig. 4.11. Fracture surface of (a) LWC-SS100 (b) LWC-SS90MP10 (c) LWC-SS80MP20 (d) LWC-SS65MP35 (e) LWC-SS50MP50 (Table 4.5).

4.3.3.2 Thermal conductivity of the LWC-BCBLWAs

The thermal conductivity of plain SS100 lightweight concrete is 0.674 W/(m · K). While the thermal conductivity of other BCBLWAs is much lower as can be seen from **Table 4.9**. The SS90MP10, SS80MP20, SS65MP35 and SS50MP50 possess thermal conductivities of 0.545, 0.439, 0.369 and 0.255 W/(m · K), respectively. The higher MP content in the aggregates means more air voids are presented in the lightweight concrete. This also means that the LWC-BCBLWA is more porous and has a lower thermal conductivity than normal lightweight aggregates. The more porous a concrete, the more entrapped air is inside the concrete and consequently the heat conduction can be lowered. As widely acknowledged, air has a thermal conductivity of 0.026 W/(m · K) at room temperature, which is much lower than hardened cement paste and miscanthus. The plain cement paste (w/b = 0.5) and miscanthus powder have very different thermal conductivity, reaching around 1.2 and 0.1 W/(m·K), respectively. Thus, by applying miscanthus powder in the aggregate, it is possible to lower the thermal conductivity and consequently increase the overall thermal insulation of LWC-BCBLWAs. Other lightweight concrete with cold-bonded lightweight aggregate shows similar or higher thermal conductivity. Frankovic et al. [177] have found that cold-bonded aggregate concrete (CBAC) made with 100% CBLAs has a dry density of 1490 kg/m^3 and a thermal conductivity of 0.73 W/(m·K). Tajra et al. have also reported that the use of core-shell CBA allows the production of CBAC with a thermal conductivity of 0.6364 W/(m·K) [178].

The thermal conductivity versus the density of different kinds of lightweight concrete is shown in **Fig. 4.12**. The LWC-BCBLWAs have a slightly better compressive strength than other conventional lightweight concrete, for instance, pumice concrete and foam concrete [95,113,139]. The slope of the linear correlation between strength and thermal conductivity is significantly higher than for other LWCs. Therefore, the prepared LWC-BCBLWAs could obtain a good performance regarding thermal insulation and while still possessing sufficient strength at the same time. However, there is still potential to further lower the thermal conductivity of LWC-BCBLWAs, since the cement matrix used in this study is pure cement paste with w/b of 0.5. If the cement matrix can be further optimized by using an air-entraining agent and a hollow fly ash [33], the thermal conductivity could be lowered even further.

Table 4.9. Thermal conductivity of the developed LWC-BCBLWAs.

Groups	LWC-SS100	LWC-SS90MP10	LWC-SS80MP20	LWC-SS65MP35	LWC-SS50MP50
Thermal conductivity (W/(m · K))	0.674±0.003	0.545±0.002	0.439±0.002	0.369±0.004	0.255±0.003

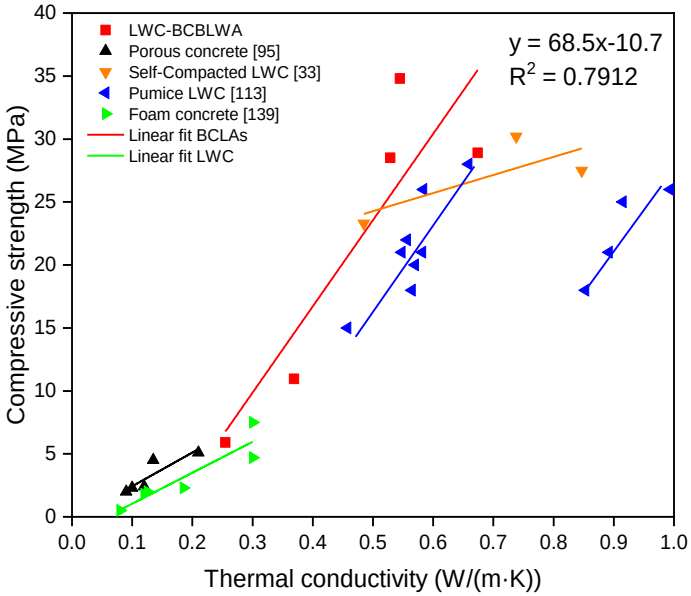

Fig. 4.12. Thermal conductivity versus compressive strength of different kinds of LWC.

4.3.3.3 The influence of BCBLWAs on the hydration of LWC-BCBLWA

The effect of BCBLWAs on the hydration of Portland cement is interpreted using the calorimeter test. The hydration heat of three different groups of LWC-BCBLWAs is shown in **Fig. 4.13**. The hydration peak of the SS100 sample is the highest among all the groups, reaching the maximum heat release at 11 hours. The SS100 sample shows almost the same time to reach the hydration peak as plain cement paste (10 hours), according to literature [117], indicating carbonated steel slag itself has no retardation effect on cement paste. With rising content of MP in BCBLWAs, the time to reach hydration peak maximum increases which could be due to released polysaccharide by miscanthus. The SS80MP20 samples shows the hydration peak at 12 hours. Meanwhile, SS65MP35 takes 12.5 hours to reach the peak. MP by itself has a severe retardation effect on the cement hydration. If Miscanthus powder is added directly into the cement paste, the hydration peak maxima occurs only after 20 h [117]. Hence, the delay of cement hydration is greatly mitigated by incorporating natural fibers into BCBLWAs. Therefore, the MP incorporated in steel slag-based binder shows less influence on the cement hydration. The steel slag fines surround the MP can contribute to the delay of the polysaccharide release from MP, resulting in less negative effect on the cement paste. Furthermore, the miscanthus is granulated which significantly reduces the surface area and amount of miscanthus that can leach polysaccharide. It is partially covered by carbonated slag and the miscanthus in the middle of the aggregate is probably not leach directly to the outer surface of the BCBLWAs. Therefore, it is a promising method to mitigate the retardation effect of miscanthus powders on the hydration of cement. Another reason should be the formation of amorphous silica, which can accelerate the hydration of cement and compensate the delay of cement hydration by polysaccharides. Overall, the cement hydration is only slightly delayed. The cumulative heat release also follows the same trend as the normalized heat release as shown in **Fig. 4.13 (b).**

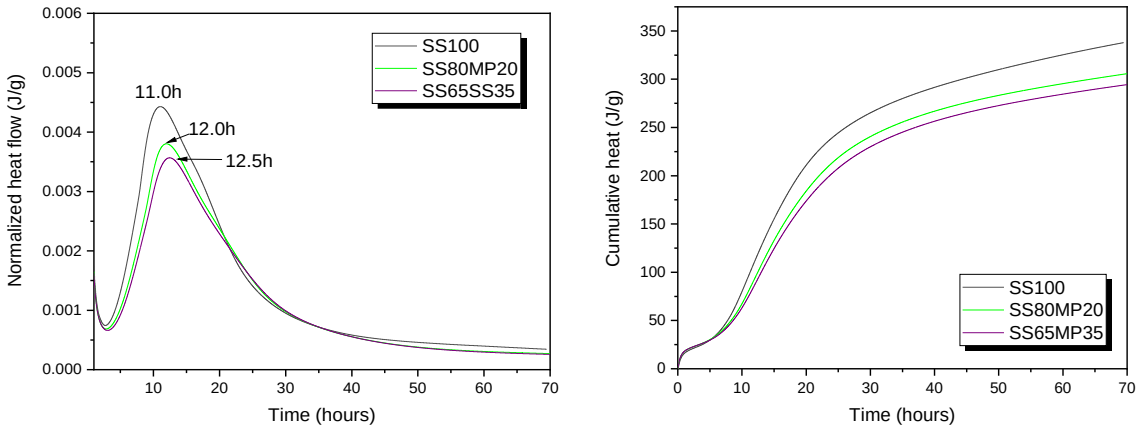

(a) (b)

Fig. 4.13. The calorimeter test of BCBLWAs incorporated cement paste with an aggregate volume ratio of 0.5: (a) Normalized heat release (b) Cumulative heat.

4.3.4 CO_2 emission of lightweight concrete with BCBLWAs

One of the significant motivations of using carbonated steel slag and miscanthus is the high CO_2 uptake of BCBLWA aggregates and the low CO_2 emission of prepared lightweight concrete. The quantified CO_2 emissions of BCBLWAs and LWC-BCBLWAs are shown in **Table 4.10** and **Table 4.11**. The CO_2 emission of finely grounded steel slag and miscanthus using disc mill are included, which is inferred as 0.1 kg CO_2/kg steel slag or miscanthus [28]. The milling of steel slag and miscanthus increases CO_2 emission, however, the CO_2 uptake of milled steel slag can compensate for this, leading to a negative CO_2 emission in total. For miscanthus itself, thanks to the CO_2 sequestration during growth, the carbon dioxide equivalent mitigation potential is 117%/gram [141]. Therefore, for the aggregates containing higher amounts of MP, the total CO_2 emission is much lower. As observed in **Table 4.10**, for 1 m^3 BCBLWAs, the increasing dosage of MP in the aggregate decreases the total CO_2 emission significantly. Firstly, the CO_2 uptake capacity of the BCBLWAs is much higher than plain steel slag, as calculated from TGA in **Table 4.8**. Secondly, the MP itself have a high CO_2 absorption capacity than steel slag. Therefore, the artificial aggregate containing 20 vol.% MP starts to obtain a negative CO_2 emission of -92.8 kg/m^3.

Table 4.11 shows the lightweight concrete incorporated with BCBLWAs also features low CO_2 emission than plain steel slag aggregate concrete. For LWC-SS100, the CO_2 emission is 574.2 kg/m^3, due to the cement and finely grounded steel slag produce large amount of CO_2, while the CO_2 uptake of plain SS100 aggregate is the lowest among the five groups. With the utilization of BCBLWAs in the lightweight concrete, the CO_2 uptake capacity of bio-aggregate rises significantly as presented in **Table 4.10**, thus compensates the high CO_2 emission of cement and the usage of disc mill. The lowest CO_2 emission reaches 305.0 kg/m^3 for LWC-SS50MP50. Therefore, the utilization of BCBLWAs in LWC significantly reduce the embedded CO_2 footprint and thus more sustainable. These results demonstrate that the optimal combination of carbonated steel slag and miscanthus powder can result in a much lower CO_2 emission than normal lightweight concrete.

Table 4.10. CO_2 emission of BCBLWAs (1 m^3).

CO_2 emission ($kgCO_2/kg$)	SS100	SS90MP10	SS80MP20	SS65MP35	SS50MP50
Steel slag (milling)	163.0	124.7	96.4	63.7	40.5
Miscanthus (milling)	0	5.3	8.6	12.3	14.5
CO_2 uptake (BCBLWAs)	-67.9	-56.8	-97.2	-107.3	-90.3
CO_2 absorption (Miscanthus)	0	-62.01	-100.6	-143.9	-169.6
CO_2 curing	0.025	0.025	0.025	0.025	0.025
Total CO_2 emission for BCBLWAs	95.1	11.2	-92.8	-175.2	-204.9

Table 4.11. CO_2 emission of prepared lightweight concrete with 50 vol% BCBLWAs for 1 m^3.

CO_2 emission ($kgCO_2/kg$)	LWC-SS100	LWC-SS90MP10	LWC-SS80MP20	LWC-SS65MP35	LWC-SS50MP50
Cement	492.5	492.5	492.5	492.5	492.5
Steel slag (milling)	140.5	100.7	82.6	62.8	36.7
Miscanthus(milling)	0	4.3	7.4	12.5	13.3
Water	0.04	0.04	0.04	0.04	0.04
CO_2 uptake (BCBLWAs)	-58.8	-46.2	-83.3	-106.0	-82.15
CO_2 absorption (Miscanthus)	0	-50.3	-86.6	-142.2	-155
CO_2 for curing	0.025	0.025	0.025	0.025	0.025
Total CO_2 emission of LWC-BCBLWAs	574.2	501.0	412.6	319.6	305.0

4.4. Conclusions

In this chapter, a cement-free bio-based cold-bonded lightweight aggregate (BCBLWAs) using steel slag and miscanthus powders via CO_2 curing was developed and investigated. The prepared BCBLWAs features a low density, low water absorption and high CO_2 uptake capacity. Lightweight concrete utilizing as-prepared BCBLWAs shows low density, relatively high strength and superior thermal insulation properties. The following conclusions can be drawn:

- The miscanthus powders can provide additional routes for CO_2 transportation in prepared aggregate, thus contributing to a more rapid carbonation process of steel slag particles. However, high content of miscanthus powder can result in a porous structure of BCBLWAs, as well as low strength. Samples with 10 vol% miscanthus powder show the best strength performance, which is 20% higher compared to plain carbonated steel slag.
- The carbonation products of BCBLWAs are mainly calcite and amorphous silica. The calcite acts as a binding agent and increases the mechanical properties of BCBLWAs. Contrary to cement hydration, carbonation was not affected by the presence of

polysaccharides leaching from the miscanthus powder, which makes it an effective strategy for producing cold bonded aggregates containing natural fibers. The pelletization also covers the miscanthus powder in carbonation products and reduces their water adsorption, which makes it possible to use them in OPC based concrete.

- Concrete incorporating BCBLWAs meets the standard of lightweight concrete and the strength is relatively high for concrete using BCBLWAs with 10 vol% miscanthus powder, reaching a strength of 34.8 MPa at 28 d. The bonding between BCBLWAs and cement paste is negatively impacted if very high amounts of miscanthus powder are used in the aggregate as the fracture happens at the surface of BCBLWAs rather than at the interface. This also results in lower mechanical strength of the concrete. More work is needed to investigate this and find a method to enhance the interface when high amounts of miscanthus are incorporated into BCBLWAs.
- The thermal conductivity of LWC-BCBLWAs deceased to 0.255 W/(m·K) when 50% SS50MP50 used in lightweight concrete. Furthermore, the density dropped to 1100 kg/m^3. The thermal insulation property of LWC-BCBLWAs is projected to have a better performance than other non-plant based lightweight concrete.

This chapter shows that the use of carbonation makes it possible to avoid the problem of cement and bio-fibers incompatibility without additional treatment of the bio-fibers. This method could be applied to other biomaterials that leach even more polysaccharide than miscanthus, for instance, coconut fibers or hemp fibers as well saw dust.

Chapter 5 Sustainable silica aerogel made from olivine and its usage as thermal insulation and photocatalytic support

This chapter investigates the development of silica aerogel from olivine and its application as thermal insulating materials and photocatalytic support. It was discovered sodium silicate derived from olivine, an abundant mineral in earth's crust, can be used as the silica precursor to produce silica aerogel. The hydrophobic silica aerogel from olivine is developed with a low temperature synthesis route via ambient pressure drying. The produced silica aerogel obtained a high specific surface area (694 m^2/g) and pore volume (2.99 cm^3/g), with a uniform pore size distribution and mesoporous structure. Moreover, this chapter investigates the performance of a silica aerogel-based air purifying coating to functionalize building materials. It has been shown that the photocatalytic activity increases when the photocatalyst is supported on a silica network with a large surface area like silica aerogels. Titania was loaded onto the prepared silica aerogel through a precipitation method. Titanium (IV) isopropoxide was used to slowly form titania monomers in ethanol with the silica aerogel. This method was used to precipitate titania inside the mesopores of the silica aerogel to obtain a good spread of the titania around and inside the aerogel for a higher photocatalytic activity. The resulting samples were characterized by measuring the conversion efficiency to oxidize nitric oxide under UV-light irradiation, nitrogen physisorption and FTIR. The silica aerogel coating with titania crystals showed a photocatalytic activity of 99.6%, showing to be a promising photocatalysts for air purification for building environment.

This chapter is partially published elsewhere:

Y.X. Chen, Y. Hendrix, K. Schollbach, H.J.H. Brouwers, A silica aerogel synthesized from olivine and its application as a photocatalytic support, Construction and Building Materials 248 (2020) 118709.

5.1. Introduction

5.1.1 Development of silica aerogel from olivine

Silica aerogel is an ultralight material consisting of a silica network with mesoporous structures [29]. Silica aerogel possesses ultra-low density (0.03-0.2 g/cm^3), high specific surface area (600-1000 m^2/g) and ultra-high porosity (95-99%) [179–181]. Due to these properties, silica aerogel has been applied in thermal insulation [4,182–184], catalytic supports [185,186], absorbent of pollutants [187–190] and drug carrier materials [191]. Currently available silica aerogel is mainly produced from organic silica sources and via supercritical drying, for instance, tetrathoxysilane (TEOS) and methyltrimethoxysilane (MTMS), which are relatively expensive and difficult for continuous production [192]. Therefore, exploring a cost-effective and environmentally friendly synthesis route for production of silica aerogel is of great interest [180,193].

Sodium silicate, also called water glass, is an alternative silica source to produce silica aerogel. It is conventionally manufactured by reacting sodium carbonate (Na_2CO_3) with quartz sand in the molten state at 1300~1600 ℃ [194]. Because of the high temperatures involved, the large carbon footprint of commercial water glass makes it unattractive as the precursor to synthesize silica aerogel. Recently, silica aerogels produced from industrial byproducts or silicate minerals were investigated, for instance, fly ash, kaolin and trona ore [34,195–197]. It was demonstrated by researchers that sodium silicate derived from alternative silica sources could produce silica aerogels with properties similar to commercial silica aerogel. However, the above preparation processes still involves a relatively high temperature (600~850 ℃) calcination process that requires a high energy input [198].

Therefore, a low temperature and sustainable synthesis of a silica-based precursor would be desirable. Abundant mineral olivine with the chemical formula $(Mg,Fe)_2SiO_4$ was recently investigated as an easily available and low-cost silica sources to produce nano-silica at low temperatures (50-90 ℃) [60,199]. Currently, large quantities of waste olivine are disposed as a by-product from magnesite mining in Europe, which could be used for high-quality silica products [35]. The nano-silica produced by dissolving the mineral olivine in sulfuric acid has lower energy requirements than conventional methods that include a spray pyrolysis (1200-1600 ℃) process. In previous research [59,200,201], it was shown that silica produced from olivine at 50-90 ℃ had a purity higher than 99% and a specific surface area between 100 to 400 m^2/g. Thus, the obtained nano-silica can react easily with sodium hydroxide (NaOH) to produce sodium silicate at ambient pressure and low temperatures, thanks to its high surface area and the non-crystalline. Thus, applying olivine-derived sodium silicate as a precursor instead of organic silica source or commercial water glass can reduce the energy consumption of silica aerogel.

The supercritical drying (SCD) generally used for commercial silica aerogel is also energy intensive. Although SCD eliminates the interface between liquid and gas phase to avoid pore collapsing during extraction of the solvent, the high temperature and pressure make it difficult for a continuous production and may cause operation risk. In this regard, ambient pressure drying (APD) has the advantages of a lower energy consumption and continuous production

which is a more promising drying method [202,203]. This method includes a surface modification of silica aerogel, making it possible to dry aerogel at atmospheric condition.

In this chapter, hydrophobic silica aerogel was produced from olivine at low temperatures via ambient pressure drying. The schematic diagram of silica aerogel synthesis is shown in **Fig. 5.1.** First of all, olivine silica was produced via acid leaching at 50 ℃. Secondly, the sodium silicate solution was prepared by reacting olivine silica with sodium hydroxide (NaOH) at 80 ℃. The as-prepared sodium silicate was used for silica aerogel preparation at ambient pressure. The effects of pH, aging time and TMCS dosage on the properties of olivine silica aerogel were investigated. This research aims to develop a sustainable and environmentally friendly method for recycling of waste olivine towards advanced materials.

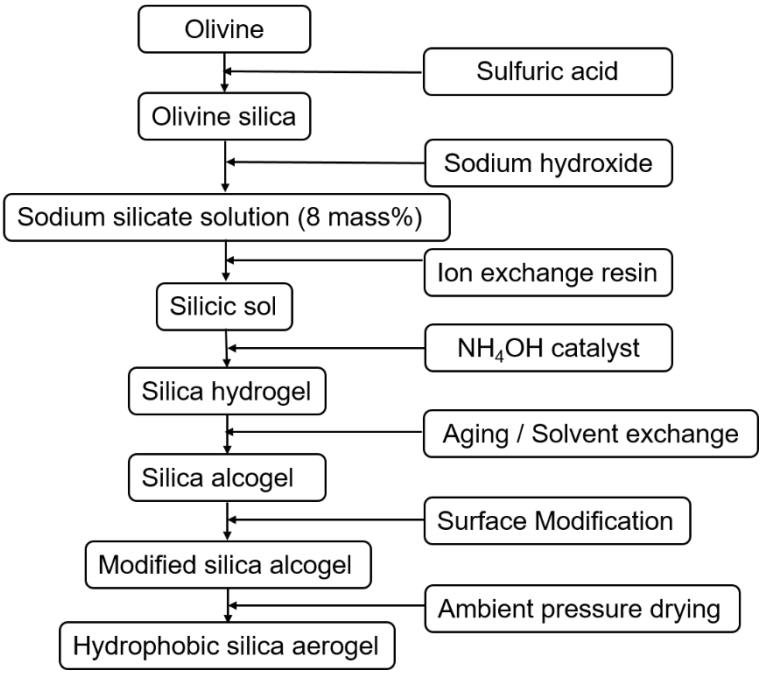

Fig. 5.1. Schematic process of silica aerogel production from olivine silica.

5.1.2 Application of silica aerogel as photocatalytic support

Air pollution in large urban cities is becoming a big threat to human health, especially for the harmful gases such as nitrogen oxides (NO_x). The reduction of the concentration of these pollutants with the use of photocatalyst coatings in roads and buildings has been paid much attention [204–207]. Generally, semiconductors like titanium oxide (TiO_2) are used as an effective photocatalyst in air purification. Recently it has been shown that the titania with the combination of silica substrate obtained higher photocatalytic efficiency and cost-effective [208,209]. However, the silica applied is normally random porous silica that can limit the performance of titania since they cannot spread evenly on the silica substrate.

Thanks to the large pore volume and porosity of silica aerogel, it is promising to apply silica aerogel as a catalyst support to load a catalyst like photocatalytic titania. Several researchers have investigated the possibility of applying TiO_2-SiO_2 composite for a better catalytic efficiency during the last decade. Zhang et al. [210] have studied the TiO_2-SiO_2 aerogel nanocomposite absorbent using sol-gel method investigating the photocatalytic degradation on

automobile exhaust. It is demonstrated the composite is promising in environmental treatment due to the high surface area and big average pore size. Wang et al. [211] have investigated the photocatalytic activity of TiO_2 supported SiO_2-Al_2O_3 aerogels from fly ash. It is shown that the composite had higher photocatalytic activity for DNBP degradation than that of pure TiO_2. Liu et al. [212] have studied the $WxTiO_2$ nanoparticles on silica aerogel with a high absorptivity and photocatalytic activity. The nanocomposite had high efficiency for removing the RhB from water and can be recycled for many times. Zu et al. [213] have invented a chemical liquid deposition method to prepare a silica-titania composite aerogel as a photocatalyst. It is demonstrated the small particle size, high surface area, and enhanced crystallinity after heat treatment at 600 ℃ together contribute to the excellent photocatalytic property of the silica-titania composite aerogel. Cheng et al. [214] have prepared SiO_2-TiO_2 composite aerogel via ambient pressure drying and test the photocatalytic performance. The photocatalytic performance was evaluated by degradation of MB and showed promising results. Therefore, silica aerogel is an emerging candidate of photocatalytic support for many nano-sized catalysts. However, most of the study mentioned above rarely mentioned the thermal treatment of the silica aerogel that can increase the pore size and pore volume significantly. In this chapter, it is found that with a thermal treatment at 500 ℃, the pore size increased to 15-20 nm and pore volume nearly doubled. As former research suggested, the crystal size of well-prepared anatase crystals (ranging from 10-14 nm) can be smaller than the majority of the pore sizes in the thermal treated silica aerogel (15~20 nm) [208]. Therefore, it is possible to apply the aerogel as a catalyst support to make a great spread of the titania on and inside the aerogel for a high photocatalytic activity.

Therefore, in this research, silica aerogel was first synthesized from olivine via ambient pressure drying. The modified silica aerogel is thermal treated at 500 ℃ for 3 hours. Then the modified silica aerogel was applied as a photocatalytic support to load titania and the photocatalytic efficiency of the silica aerogel-TiO_2 coating was measured. Furthermore, Fourier-transform infrared spectroscopy (FTIR) and nitrogen physisorption were used to analyze the microstructure of the resulting silica aerogel-TiO_2 composite coating.

5.2. Experiments and methodology

5.2.1 Raw materials

Olivine used for aerogel preparation was provided by Eurogrit from Norway. **Table 5.1** lists the oxide composition and the loss on ignition of olivine measured by X-ray fluorescence (XRF). The particle size of olivine was around 0.10~0.50 mm.

Table 5.1. Oxide composition of olivine (wt.%).

Composition	MgO	Fe_2O_3	SiO_2	Cr_2O_3	Al_2O_3	NiO	MnO	CaO	LOI*
Olivine	49.3	7.32	41.4	0.31	0.46	0.32	0.09	0.15	0.59

*Loss on ignition

Sulfuric acid (H_2SO_4, 50%, VWR), sodium hydroxide pellets (NaOH, VWR), ethanol absolute (CH_3CH_2OH, 100%, VWR), n-heptane (C_7H_{16}, Analytic grade, Biosolve), ammonia solution ($NH_3 \cdot H_2O$, 5M, Sigma-Aldrich), trimethychlorosilane (C_3H_9SiCl, ＞99%, Sigma-Aldrich) and Amberlyst 15 hydrogen form (cation exchange resin, Sigma-Aldrich) were adopted to prepare silica aerogel from olivine. Titanium (IV) isopropoxide 97% (Sigma-Aldrich) was used as the precursor to produce the titania monomer. Commercial titania P25 was used as a reference to compare the performance of titania-aerogel composite sample.

5.2.2 Experimental procedure

5.2.2.1 Pre-treatment of olivine and preparation of sodium silicate

For lab scale production of olivine silica, olivine particles were first added in 3M sulfuric acid at 50 ℃ in a thermostat reactor as shown in **Fig. 5.2 (a).**

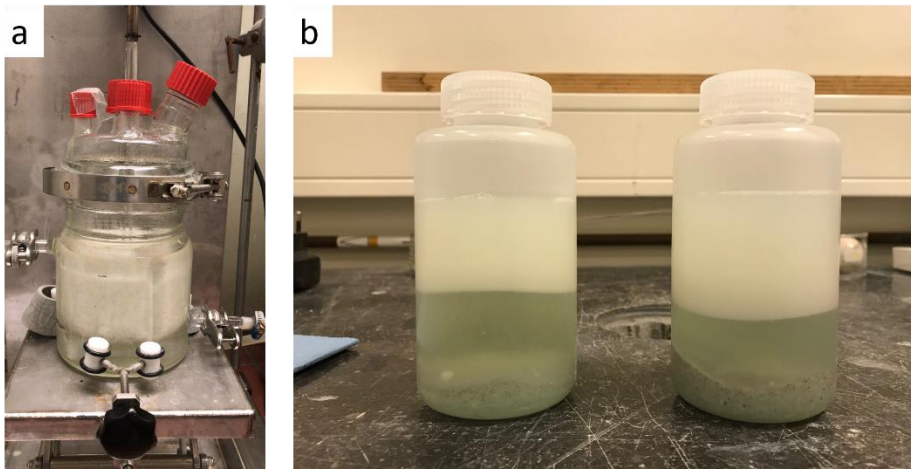

Fig. 5.2. The end mixture of olivine dissolved sulfuric acid solution (a) before and (b) after centrifugation at 4800 rpm for 5 min.

The silica monomers would release into the solution through the following reaction:

$$(Mg,Fe)_2SiO_4 + 4H^+ = Si(OH)_4 + 2(Fe,Mg)^{2+}, 223KJ/mol \quad (5.1)$$

The dissolution of olivine yields a mixture solution, which includes high concentrations of magnesium, iron and sulfate, precipitated silica and inert minerals. The end mixture of this suspension can be centrifuged at 4800 rpm and resulted in a three-layer composite. The upper layer was the silica that released from olivine. The final silica can be obtained by vacuum filtration and washing with distilled water until no impurities left.

A pilot scale production for olivine silica was also carried out in Hellas Gold (Greece) as shown in **Fig. 5.3**. The resulting silica filter cake can directly be used to produce olivine-derived sodium silicate in this study. The silica yield in this case was around 60%~80%, indicating an efficient silica extraction.

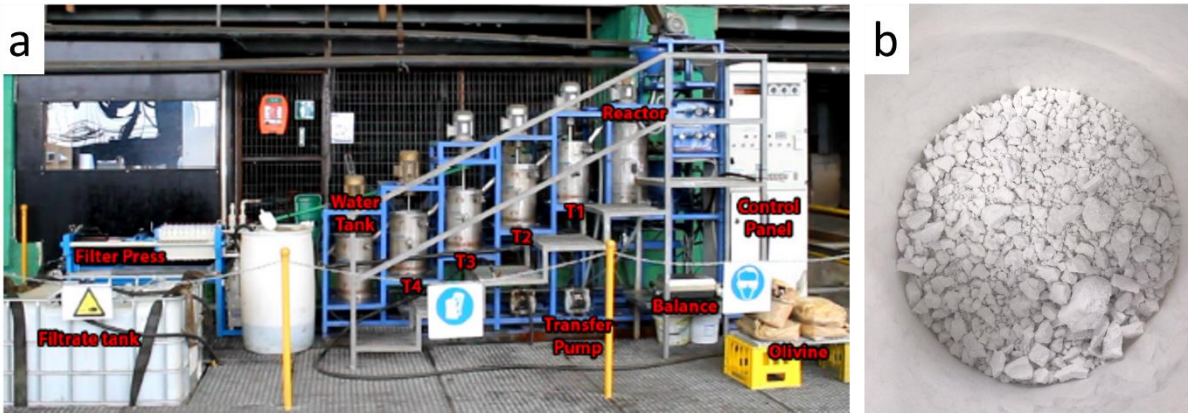

Fig. 5.3. (a) The production plant of olivine silica in Hellas Gold (Greece) and (b) the produced olivine silica [36].

Olivine-derived sodium silicate with a modulus of 1.5 and 8% silica content was prepared by reacting the nano-silica with sodium hydroxide (NaOH) solution at 80 ℃ for 4 hours. The reaction equations are as follows:

$$SiO_2 + 2NaOH \rightarrow Na_2SiO_3 + H_2O \quad (5.2)$$

$$SiO_2 + 4NaOH \rightarrow Na_4SiO_4 + 2H_2O \quad (5.3)$$

The recipe for preparation of sodium silicate is presented in **Table 5.2**. The practical modulus was determined by using XRF.

Table 5.2. Recipe of the preparation of OSS.

Group	Olivine silica (g)	Sodium hydroxide (g)	Distilled water (g)	Temperature (℃)	Theoretical modulus	Measured modulus	SiO_2 content (%)
OSS	9	8	95.5	80	1.50	1.45	7.9

5.2.2.2 Silica aerogel preparation

The primary procedures for olivine silica aerogel production include precursor preparation, gel formation, solvent exchange, surface modification and ambient pressure drying. The prepared sodium silicate was passed through a strong ion exchange resin to substitute sodium ions with hydrogen ions. The silicic acid obtained afterwards had a pH in the range of 2.0~3.0. Then, a diluted ammonia solution with a concentration of 0.5 mol/L was added dropwise as a base catalyst to the silicic sol, adjusting the pH of the sol to 4.0~6.0 to accelerate gelling. A graduated injection syringe with a diameter of 20 mm was used to cast the silica sol, thus a hydrogel bead could be obtained after gelation. After gelation the silica hydrogel was aged at 50 ℃ in an oven for 36 hours and 48 hours, respectively.

Afterwards hydrogel was extruded from the injector and cut into round beads with a height of 6 mm. The obtained hydrogel beads were immersed in a 50% ethanol/water solution for 1 day to start the solvent exchange. Then the hydrogel was immersed in 50 ml ethanol for 1 day at 50 ℃ and then the same procedure was repeated with 50 ml n-heptane for the hydrogel. Modification of the silica gel was proceeded by adding 12 ml TMCS and 40 ml heptane as a

solvent. To investigate the effect of TMCS dosage on the hydrophobicity of silica aerogel, 4, 8, 12 and 16 ml of TMCS in 40 ml heptane were used to modify the pH 5.5 silica aerogel with an aging time of 36 hours. Afterwards 50 ml of heptane was used to immerse the modified silica gel for 1 day at 50 ℃ so that residual TMCS was removed. Lastly, the modified silica gel was dried at ambient pressure at 20 ℃ for 24 hours and then dried in a furnace at 230 ℃ for 1 hour to fully evaporate the remaining pore solvent. The final silica aerogel products can be seen in **Fig. 5.4.** The prepared silica aerogel was transparent with a yellowish color due to Rayleigh scattering in a white background.

Fig. 5.4. The morphology of prepared olivine silica aerogel.

5.2.2.2 Preparation of titania-silica aerogel composite

The silica aerogel was first calcined at 500 ℃ for 4 hours to remove the $–CH_3$ groups on the surface of silica. Subsequently, 1 gram of silica aerogel was weighed and then milled with a mortar. Then silica aerogel was dispersed in a 500 ml ethanol absolute solution and the pH was adjusted to 3~4 by adding small amounts of sulfuric acid in order to have a slower hydrolysis reaction and opposite charge between the silica and formed titania. The molar ratio of titania and silica aerogel was kept at 1:1, which was determined according to our previous study [6]. Afterwards, 4.16 g TP (Titanium isopropoxide) was added into the solution quickly to avoid any contact with moist air. Then water was slowly added during 12 hours by using syringe pump (Instrument model Harvard Apparatus Pump 11 Elite) until the water content of the dispersion medium reached 2.5 vol%. After the synthesis of the composite, the resulting sample was filtered and washed 2 times with 100 ml ethanol and 4 times with 100 ml distilled water. Lastly, the sample was dried overnight at 105 ℃ and then calcined at 300 ℃ for 3 hours. The illustration of the titania doped silica aerogel process is shown in **Fig. 5.5.**

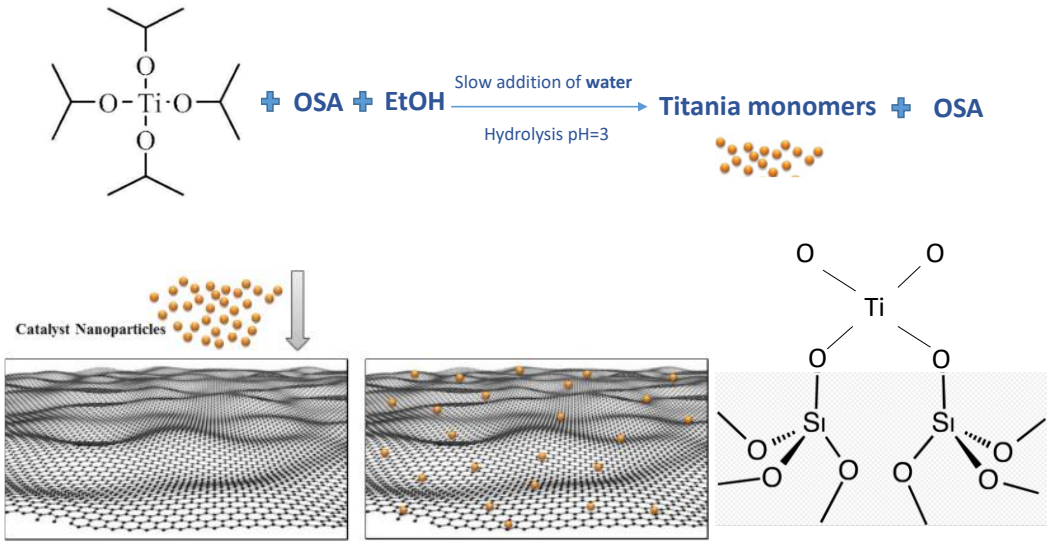

Fig. 5.5. Illustration of the reaction process of titania doped olivine silica aerogel (OSA).

5.2.2.3 Characterization methods

The as-prepared silica aerogel-TiO_2 composite was coated on a glass plate with the size of 100 mm × 200 mm × 1 mm. In specific, 1g of silica aerogel-TiO_2 composite powder was dispersed in 30 ml distilled water. Afterwards the suspension was coated on the glass plate and dried at room temperature overnight. Finally, the coated glass plate was used for the photocatalytic test. The resulting photocatalytic properties of silica aerogel-titania composites were evaluated by testing their photocatalytic conversion of NO under UV-light using the ISO 22197-1 standard for comparative purpose. The setup for these measurements is shown in **Fig. 5.6.**

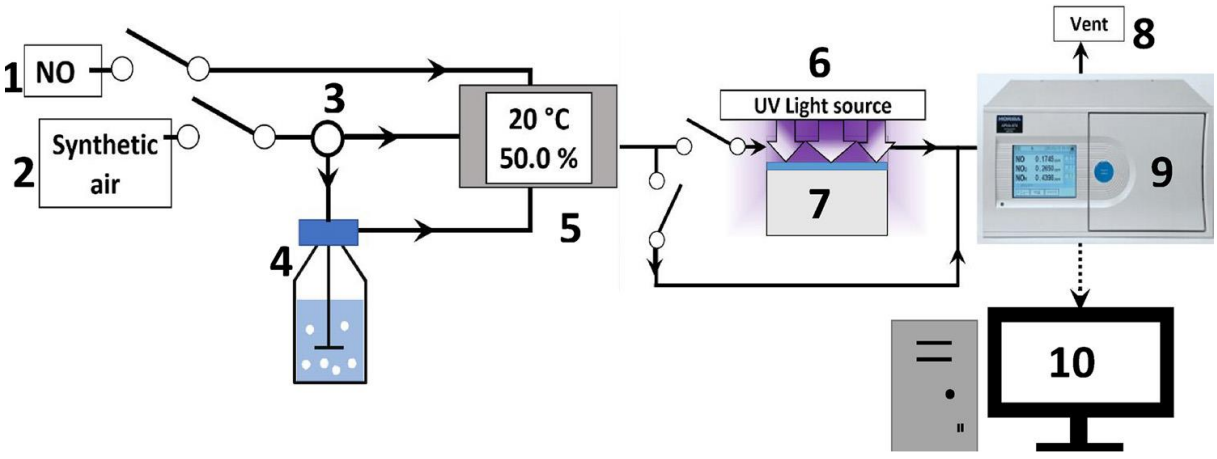

Fig. 5.6. Schematic view of the PCO measurement setup: 1) NO gas source, 2) synthetic air source, 3) valve, 4) bottle containing water, 5) humidity and temperature sensor, 6) light source, 7) reactor, 8) air vent, 9) NO_x detector and 10) computer to control inflow of gasses and data collection.

Chemical bonds in the silica aerogel were detected by Fourier-transform infrared spectroscopy (FTIR), which was performed with a Varian 3100 instrument with the wavenumbers ranging from 4000 to 400 cm^{-1} at a resolution of 2 cm^{-1}. Nitrogen physisorption

was performed with a Tristar II equipment at 77 K using liquid nitrogen to determine the specific surface area using the BET theory and pore size distribution using the BJH theory.

The particle size of the anatase crystals can be calculated with Scherer equation, which is shown below:

$$L = \frac{K\lambda}{\beta \cos\theta} \tag{5.4}$$

where L is the crystal size (m), K is the particle shape factor (0.89 was used), λ wavelength of the used X-ray, β width of a peak at half the maximum intensity in radians and θ corresponding peak angle. An approximation on the average size of the measured crystal structure can be calculated using this equation because the width of the XRD peaks depends on this value if the material consists of nano-sized crystal.

The bulk density of hydrophobic aerogel was measured using Archimedes law. The aerogel particle was immersed in distilled water that was placed in a beaker on a balance to measure the increased mass. The bulk density of silica aerogel can be determined according to:

$$\rho_b = \frac{m_a \times \rho_w}{\triangle m} \tag{5.5}$$

where ρ_b is the bulk density of silica aerogel, m_a is the mass of the silica aerogel, ρ_w is the density of water, $\triangle m$ is the increased mass presented on the balance.

The porosity of silica aerogel was determined according to:

$$\Phi_a = \left(1 - \frac{\rho_b}{\rho_s}\right) \times 100\% \tag{5.6}$$

where Φ_a is the porosity of the silica aerogel, ρ_s is the skeletal density of silica aerogel that was determined by Helium pycnometer (AccuPyc II 1340 Micromeritics), which is equal to 2.11 g/cm^3.

The specific surface area and pore size distribution were measured according to Brunauer–Emmett–Teller (BET) and Barrett-Joyner-Halenda (BJH) theory using nitrogen physisorption, which was carried out with a Tristar 3000 Series micrometer employing nitrogen at 77 K. The samples were pretreated by nitrogen gas flow with a heating rate of 10 ℃/min and heated at 120 ℃ for 4 hours to remove moisture and impurities. Chemical bonds in the silica aerogel were detected by Fourier-transform infrared spectroscopy (FTIR), which was performed with a Varian 3100 instrument with the wavenumbers ranging from 4000 to 400 cm^{-1} at a resolution of 2 cm^{-1}. The microstructure of silica aerogel was observed with transmission electron microscopy (TEM), conducted with a Tecnai 20 operated at 200 kV. The sample was prepared by breaking it into smaller pieces with the use of liquid nitrogen and then applying it on a Cu 200 mesh grid with a carbon support layer. The hydrophobicity of silica aerogel was measured with a Dataphysics Contact Angle System in the chemical department of TU/e. The silica aerogel powder was evenly distributed on a slide with a double-sided tape after being milled to pass an 80 μm sieve. The volume of the Milli-Q water droplet used for contact angle testing was 3 μL. The thermal stability was characterized with a thermogravimeter and differential

scanning calorimeter (TG/DSC). The NETZSCH STA449-F1 instrument was utilized with a heating rate of 5 °C/min^{-1} under N_2/O_2 atmosphere. An additional heating step at 500 °C for 1 hour was programmed to fully remove organic groups on the aerogel. The thermal conductivity of silica aerogel was measured with a Trident C-Thermal using MTPS (Modified Transient Plane Source) method with a liquid cell. Temperature was room temperature of 21.5 °C during testing.

5.3. Results and discussion

5.3.1 Characterization of olivine-derived silica and sodium silicate

The surface area, pore volume, pore size and particle size of prepared olivine silica are shown in **Table 5.3**. The amorphous form of olivine silica is visible via XRD as shown in **Fig. 5.7** (a). The olivine silica has a surface area of 274 m^2/g, indicating numerous reactive sites that can react with sodium hydroxide. Also, the pore volume and pore size are both very high, reaching 0.72 cm^3/g and 10 nm, respectively. The particle size of olivine silica is ~17 μm due to the high surface area leading to agglomerate (**Fig. 5.7** (b)). However, the size of silica particles is small enough to dissolve in NaOH solution at a relatively fast rate.

Table 5.3. Properties of olivine silica.

Properties	Surface area (m^2/g)	Pore volume (cm^3/g)	Pore size (nm)	Particle size (μm)
Olivine silica	274	0.72	10	17

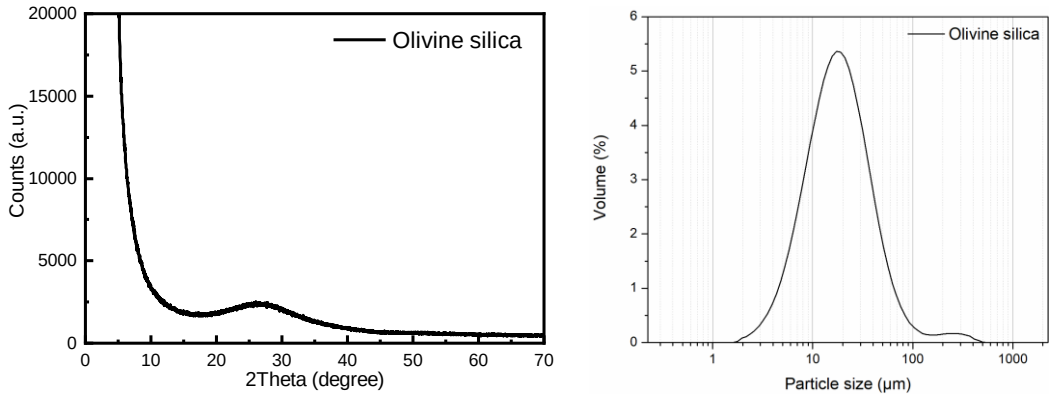

Fig. 5.7. (a) X-ray diffraction pattern and (b) particle size distribution of olivine silica.

The as-prepared sodium silicate solution from olivine silica was characterized afterwards. The dissolution of olivine silica in NaOH was supposed to be completely but still exist trace amount of undissolved silica. Therefore, Mastersizer 2000 was used to test the particle size of undissolved silica particle and result is shown in **Fig. 5.8 (a)**. As observed the undissolved silica shows particle sizes situated at around 10 μm. A 200 nm filter was used to determine the percentage of the undissolved silica in NaOH. As observed in **Fig**. **5.8 (a)**, the mass percentage of dissolved silica in sodium hydroxide was around 99.73%, indicating a nearly completely dissolve of olivine-silica. The undissolved micro silica particles, which could come from the impurities in olivine, have limited influence on the quality of sodium silicate prepared since the

very small fraction in the amount of sodium silicate (0.27%). The pH of the prepared OSS was measured as 13.29, which is similar to the commercial water glass (13.69).

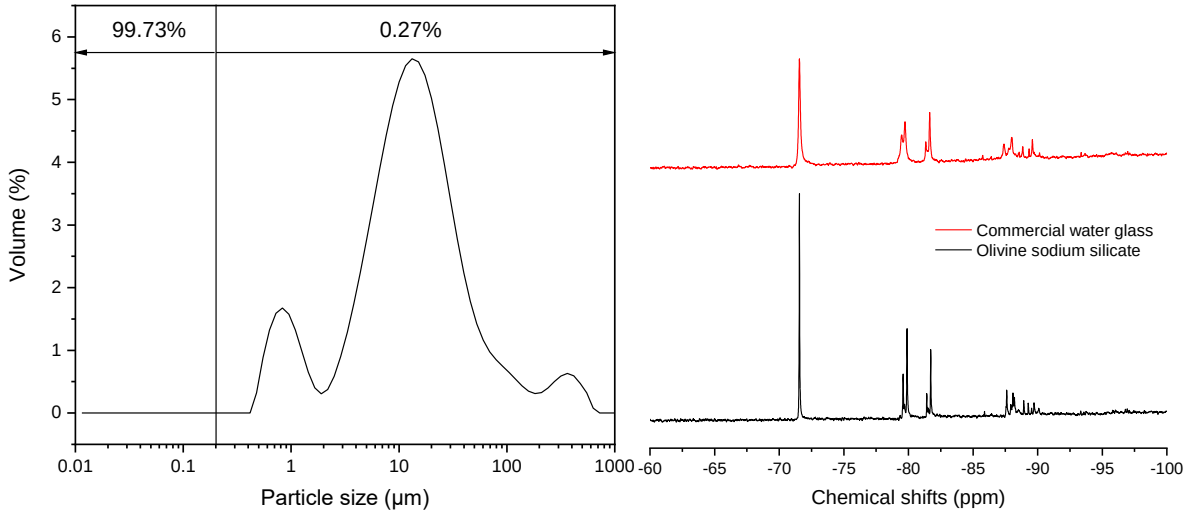

(a) (b)

Fig. 5.8. (a) Particle size distribution and (b) NMR spectra of OSS and commercial water glass.

In order to test the type of silica species in sodium silicate, ^{29}Si NMR test was carried out to measure the silica state and the result is shown in **Fig. 5.8 (b)** and **Table 5.4.** The sharp peak at -72 ppm represents the existence of Q^0 monomers, while Q^1 dimers and Q^2 trimers at c.a. -80 and -82 ppm can also be observed. No Q^4 sites can be seen, which located at lower than -100 ppm. The characteristic peaks of Q^2/Q^3 sites in the range of -85 to -90 ppm is also obvious. This result means the olivine-derived sodium silicate have two kinds of existence, one is the silicate monomers and others are the polymerized silicate. Compared to commercial water glass, there is only slight difference with OSS indicating a nearly same type of silica species.

Table 5.4. The silicate structure in sodium silicate.

Group	Q^0 (%)	Q^1 (%)	Q^2 (%)	Q^2/Q^3 (%)	Q^3 (%)
OSS	17	18	13	42	10
WG	20	21	16	37	6

5.3.2 Gelation and spring back effect of silica aerogel

The gelation time of ion exchanged sodium silicate at different pH values is presented in **Fig. 5.9.** The kinetics of gelling can be indicated by the gelation time, because a faster gelation indicates a faster condensation reaction among silica colloidal particles. The gelation time reduced with the rising pH of silicic acid. The fastest gelation happened at pH of 5.9, which is in accordance to the findings by Iler [215]. It is generally assumed that above the iso-electric point (pH=2), the condensation rate is proportional to OH- as in the following reaction sequence:

$$\equiv \text{Si-OH} + \text{OH}^- \xrightarrow{fast} \equiv \text{Si-O}^- + \text{H}_2\text{O} \tag{5.7}$$

$$\equiv \text{Si-O}^- + \text{HO-Si} \xrightarrow{slow} \equiv \text{Si-O-Si} \equiv + \text{OH}^- \tag{5.8}$$

Therefore, with the increasing pH of silicic acid, silicate ions first polymerize monomer to form particles. Afterwards, the particles link into chains then network extend throughout in water, thickening it to a gel. The gelation time may affect the microstructure of the final silica aerogel due to the different secondary particle size. Therefore, it influences the physical properties of silica aerogel thereafter.

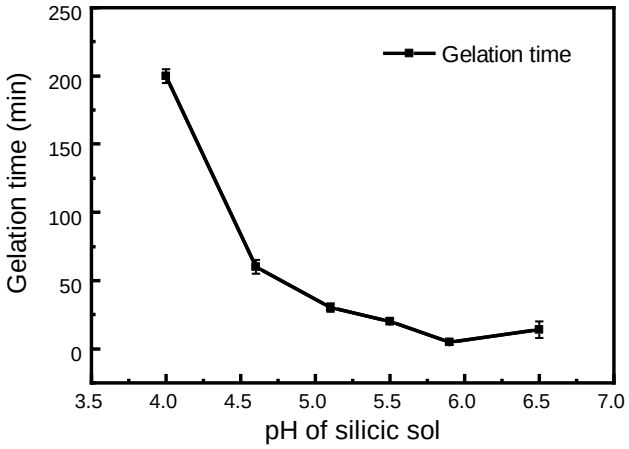

Fig. 5.9. Gelation time of ion exchanged sodium silicate at pH ranging from 4.0 to 6.5.

When drying at ambient pressure, the TMCS modified aerogel first shrunk and later re-expanded back to its original volume. The 'spring back' effect further lowers the density of the silica aerogel due to the -CH_3 groups on the surface. When the solvent is mostly evaporated and drying shrinkage occurs, the silyl groups detach with little activation energy and increase the volume of the aerogel. **Fig. 5.10** shows the detailed volume change of one aerogel (pH 5.5, aging time of 36 hours and 12/40 TMCS dosage) during ambient pressure drying.

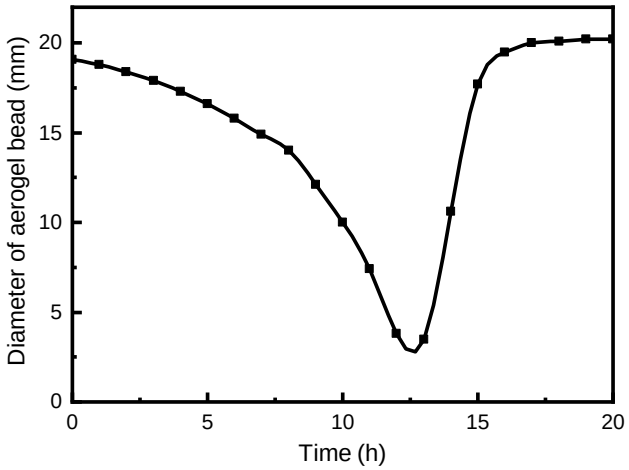

Fig. 5.10. Spring back efficiency of silica aerogel when drying at ambient pressure at 20 ^{O}C.

5.3.3 Mesoporous structure of olivine silica aerogel

Afterwards, the as-prepared silica aerogel was characterized. The mesoporous structure of silica aerogel was measured with nitrogen physisorption. The nitrogen absorption and desorption isotherms of different OSAs at different pH and aging times are shown in **Fig. 11**. All physisorption isotherms of OSA show a hysteresis loop corresponds to a Type IV isotherm [216], indicating a characteristic feature of mesoporous structures. The specific surface area

(SSA) of all silica aerogels were determined to be in the range from 559 m^2/g to 665 m^2/g. The highest specific surface area and pore volume was 665 m^2/g and 3.15 cm^3/g, which was synthesized with a silicic sol pH of 5.5 and an aging time of 36 hours.

The pH of the silicic sol has a significant influence on the nanoporous structure of silica aerogel. When the pH of the silicic sol is 5.1, the silica monomer concentration increases too fast and the silica nucleates rather than forming cross linked silica networks, leading to an increase in density, decrease in SSA and pore volume, and a broad pore size distribution (PoSD). With increasing pH of the silicic sol, silica particles tend to condensate more and the condensation reaction rate is increased. At a pH of 5.5, the hydrolysis rate and condensation rate are close to each other, causing a uniform mesoporous structure. Therefore, the strength of the gel is higher than that at lower pH and less shrinkage occurs, leading to a high SSA, large pore volume and narrow PoSD. With a higher pH of the silicic sol of 5.9, the condensation reaction rate increases further, leading to larger silica clusters and a more brittle hydrogel, thus decreasing the SSA and broadening the PoSD. Therefore, the silica aerogel produced with a pH of 5.5 has the highest specific surface area and lowest particle density and can be considered as the optimal value.

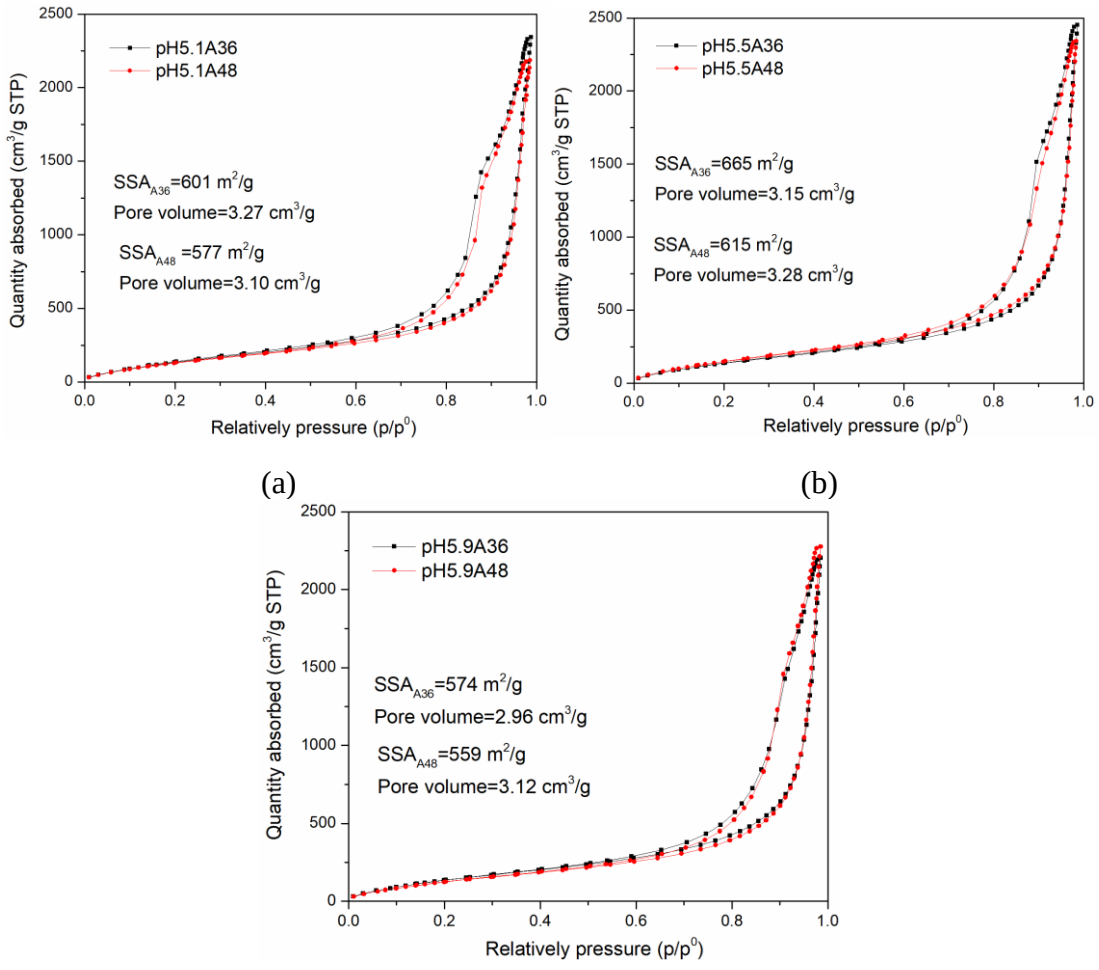

Fig. 5.11. Nitrogen adsorption-desorption isotherm and specific surface area of silica aerogel derived from olivine by using BET method: (a) pH 5.1 (b) pH 5.5 (c) pH 5.9 (A36: 36 hours aging, A48: 48 hours aging).

The reason the specific surface area of the silica aerogel is significantly lower with the increased aging time (from 36 h to 48 h) is the Ostwald ripening that silica nanoparticles undergo. During this aging process, silica monomers are mostly transported to the neck region between two aggregated silica particles, forming a stiffer silica network. The difference between the solubility of small and large particles is the key factor influencing the silica transport. The solubility of silica, *s*, is given by the Kelvin Equation:

$$s = s_0 \exp\left(\frac{2\gamma_{sl}V_m}{RTr}\right) \tag{5.9}$$

Where s_0 is the solubility of a flat surface of the solid phase, γ_{sl} is the solid-liquid interfacial tension, V_m is the molar volume of the solid, R is the ideal gas constant, T is the temperature, and r is the radius of curvature. As shown in **Fig. 5.12** (a), necks between silica particles have a negative curvature ($r_n < 0$), and therefore, a low solubility according to Eq. (5.9). On the other hand, the smallest silica particles have high solubility dissolve due to their small positive radius of curvature ($r_p > 0$). Hence the result of the dissolution-precipitation process is that the smallest silica particles dissolve and reprecipitate on the neck between larger silica particles. Therefore, Ostwald ripening contributes to a coarsening of the silica network, as shown in **Fig. 5.12** (b), leading further to a decrease in specific surface area and an increase in the pore sizes of the silica aerogel.

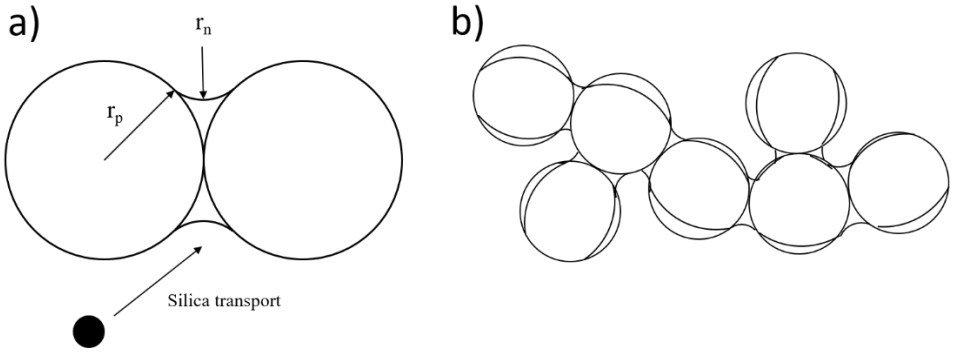

Fig. 5.12 (a) Schematic drawing of small silica particle transport to the neck; (b) Schematic drawing of growth of necks between silica particles caused by dissolution and reprecipitation.

Fig. 5.13 shows the pore size distributions of OSAs with different aging conditions and different pH of the silicic sol. It can be observed that the average pore size of all aerogels is in the range from 14.2 nm to 20.8 nm. According to IUPAC classification, the developed aerogels possess a mesoporous structure. A significant shift to larger pore sizes with increasing aging time can be observed by comparing **Fig. 5.13 (a) and (b).** This further proves that increased aging time results in enlarged pore sizes, which is attributed to the coarsening of the silica structure and increased size of silica particles. Moreover, the OSA synthesized at a pH of 5.5 have a more uniform pore size distribution than those at pH 5.1 and 5.9, showing that it is the optimal pH of the silicic sol for a uniform mesoporous microstructure.

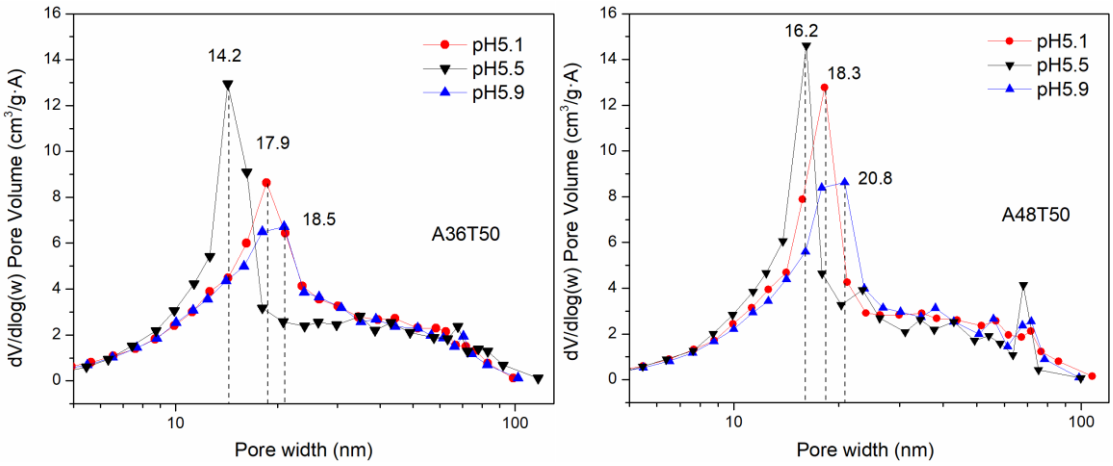

Fig. 5.13. Pore size distribution of OSA determined by using BJH method; (left) A36: aging 36 hours; (right) A48: aging 48 hours at 50 ^{O}C.

TEM pictures of silica aerogels produced with different aging times at a pH of 5.5 (**Fig. 5.14**) show the silica network of aerogel and the skeleton of the silica backbone with a cross linked microstructure. The silica aerogel aged for 48 hours shows a mesoporous microstructure with primary particles of around 5 nm in size, as shown in **Fig. 5.14** (b). While the size of the primary silica particles of the aerogel aged for 36 hours was around 4 nm. It can also be observed the pore size of both silica aerogel is c.a. 13~16 nm. Which is in accordance with the result shown in BJH pore size distribution (**Fig. 5.13**).

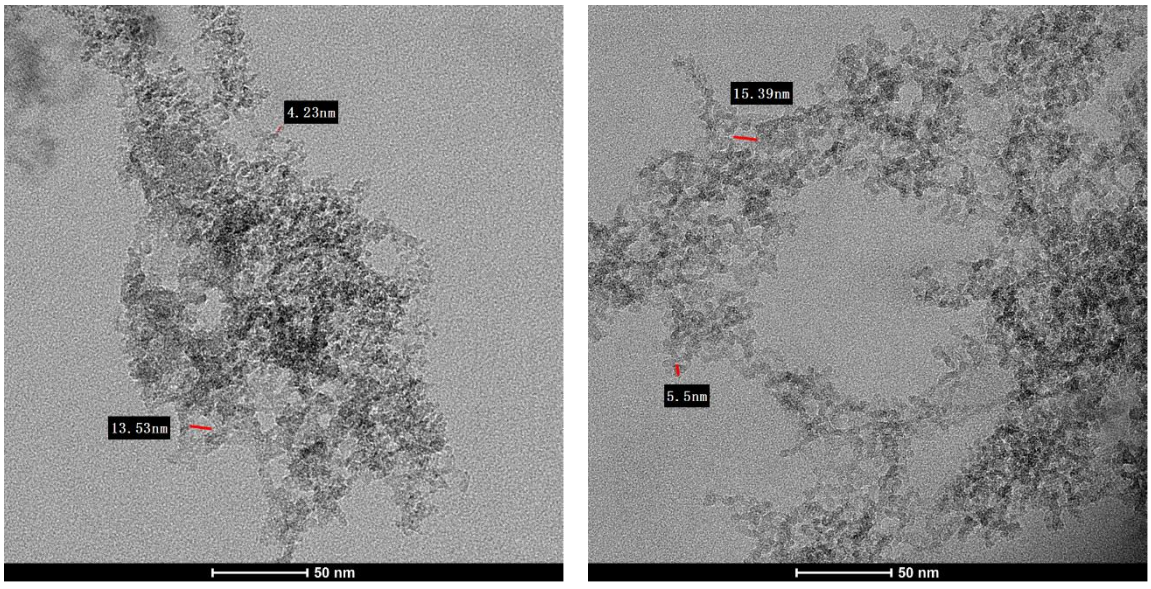

Fig. 5.14. Transmission electron microscopy of OSA produced with different aging times. (left) 36 hours aging; (right) 48 hours aging.

5.3.4 Density and porosity of olivine silica aerogel

The particle density and porosity of OSA versus the gelation time are presented in **Fig. 5.15**. The lowest particle density of silica aerogel was 0.08 g/cm^3, achieved at a gelation time of 20 minutes and an aging time of 36 hours. A very short gelation time below 10 minutes led to an uncontrolled condensation of silica aerogel, while a long gelation time above 50 minutes indicated a slow condensation reaction [33]. When the gelation time was longer than 200

minutes, the strength of the silica backbone was too weak to resist the capillary pressure during ambient pressure drying, due to the low degree of poly-condensation. The pores shrank significantly, and the particle density was increased to 0.24 g/cm^3. Therefore, a proper condensation rate of silica gel produces an optimized silica network and aerogel microstructure.

It could also be observed that the 48 hours aging slightly increased particle density of the silica aerogel. A longer aging means a higher degree of poly-condensation between colloidal particles and hence a denser silica gel structure. It increases the strength of the silica network and its resistance to the pressure caused by the evaporation of the pore liquid; however, excessive aging also reduces the permeability of the silica gel and makes solvent exchange slow and inefficient. Therefore, a time of 36 hours aging is suggested as optimal in this study.

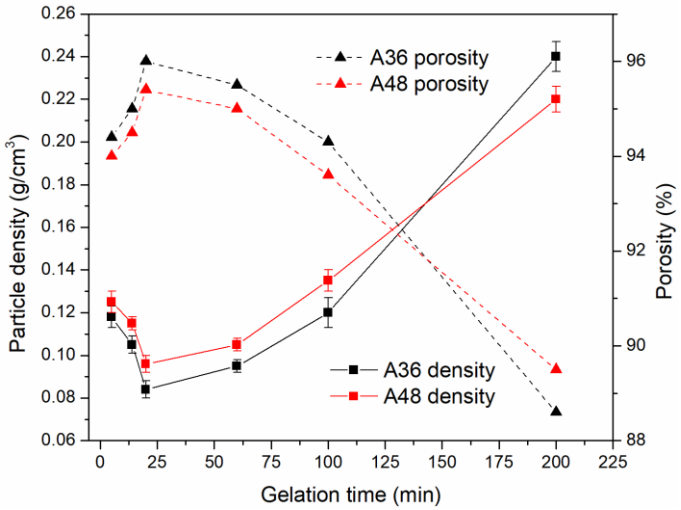

Fig. 5.15. Particle density and porosity of OSA versus gelation time. (A36: 36 hours aging, A48: 48 hours aging).

5.3.5 Influence of TMCS dosage on the properties of OSA

The particle density and porosity of OSAs with increasing TMCS dosage prepared at a pH of 5.5 and 36-hours aging are presented in **Table 5.5**. The suitable TMCS dosage to prepare the lowest density aerogel (0.08 g/cm^3) is 12/40 ml. As the TMCS dosage increases from 4/40 to 12/40, the amount of surface methyl group increases and the re-expanded volume of the silica aerogel increases due to the spring beck effect, resulting in a lower density of aerogel. However, as the TMCS dosage increases from 12/40 to 16/40, the capillary pressure caused by the replacement of hydroxyl group with methyl group is too high causing the silica network structure to break down, leading to visible cracks, and an increase in particle density and reduction in porosity. Therefore, the TMCS/heptane ratio of 12/40 ml is chosen as the best ratio among the 4 samples.

Table 5.5. Density and porosity of silica aerogel with increasing TMCS dosage.

TMCS/Heptane (ml)	4/40	8/40	12/40	16/40
Particle density (g/cm^3)	0.139 ± 0.031	0.105 ± 0.026	0.08 ± 0.01	0.128 ± 0.025
Porosity (%)	93.4%	95.0%	96.2%	93.9%

The contact angle of OSAs with different TMCS/heptane volumetric ratios is shown in **Fig. 5.16.** The contact angle of all the silica areogels ranges from 140° to 152°, indicating super-hydrophobicity (＞150°) of some of the synthesized aerogels. The increased TMCS dosage in the modification agent increases the contact angle of the aerogels. There exists an optimal content of TMCS in the modification agent (TMCS/heptane 12/40), beyond which the contact angle remains nearly stable, because most of the hydroxyl groups on the surface are replaced by methyl groups through the silylation reaction. Excessive TMCS dosages increase the CO_2 footprint without a significant hydrophobicity increase.

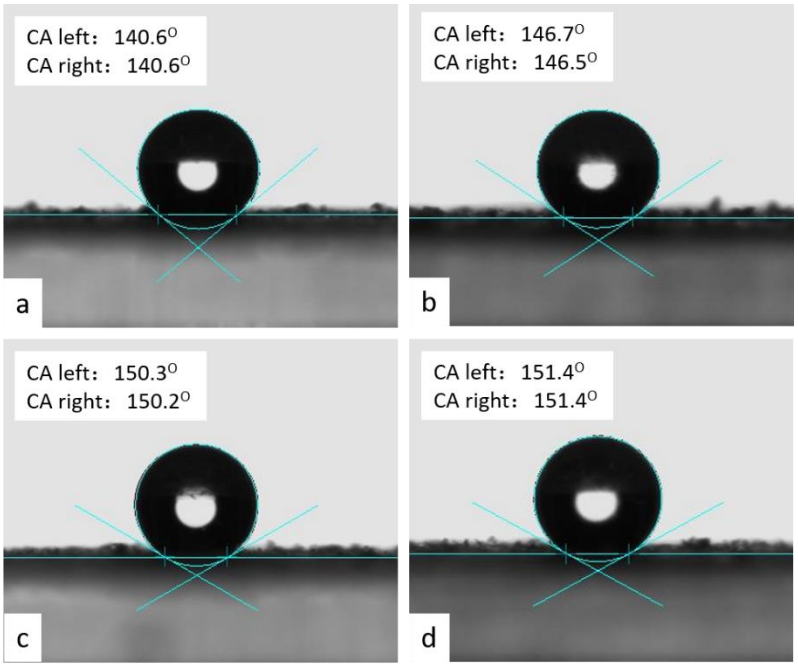

Fig. 5.16. Contact angle test of OSA with different TMCS/heptane volumetric ratios (a) 4/40 (b) 8/40 (c) 12/40 (d) 16/40.

The FTIR spectrum of OSA with and without surface modification is presented in **Fig. 5.17**. The strong characteristic peaks of Si-O-Si at 1089 cm^{-1}, 799 cm^{-1} and 463 cm^{-1} are attributed to the stretching, bending and rocking vibration of the Si-O bonds, respectively. Due to the modification with TMCS, the surface of the aerogel is hydrophobic. The characteristic peaks of the Si-C bonds are visible at 846 cm^{-1} and 1256 cm^{-1} and the bending vibration of $–CH_3$ group appears at 754 cm^{-1}. Furthermore, the characteristic peak of the Si-OH bond at 962 cm^{-1} disappears after surface modification, which means the hydroxyl group was substituted by the $-CH_3$ group.

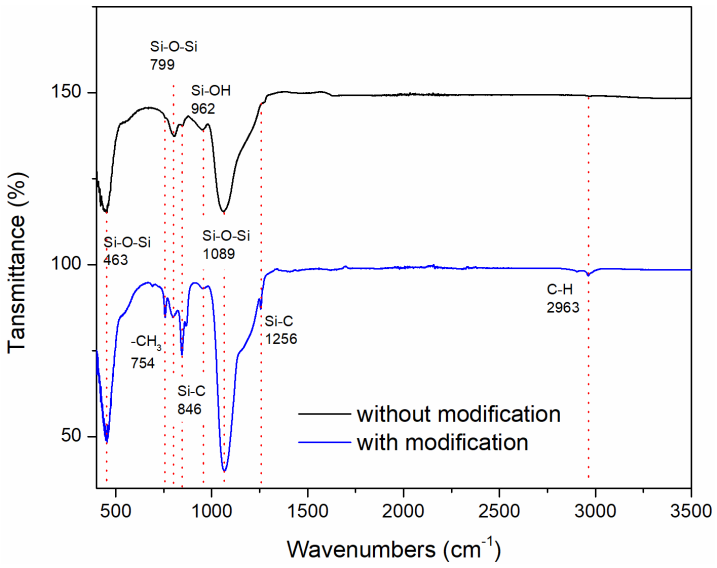

Fig. 5.17. FTIR spectrum of OSA with and without surface modification.

5.3.6 Thermal stability and conductivity

Fig. 5.18 shows the thermal stability of OSA measured with thermal gravimetry. No significant change in DTG curves is found between 40 ℃ to 300 ℃ due to dehydration and evaporation of residue solvent (heptane and TMCS), owing to the previous heating to 230 ℃ for 1 hour in the preparation process. The abrupt mass loss between 330 ℃ to 380 ℃ is due to the oxidization of silyl groups on the surface of the aerogel. The OSA is thermally stable till 337 ℃, while the commercial silica aerogel supplied by Cabot used for reference shows a decomposition temperature of 377 ℃.

The break at 500 ℃ in **Fig. 5.18** is due to isothermal heating at 500 ℃ for 1 hour. The motivation is to oxidize all the silyl groups in the aerogel. However, almost all organic groups are already removed from the aerogel below 400 ℃. Therefore, there is no mass loss at 500 ℃, indicating a fast decomposition of organic groups at the decomposition temperature.

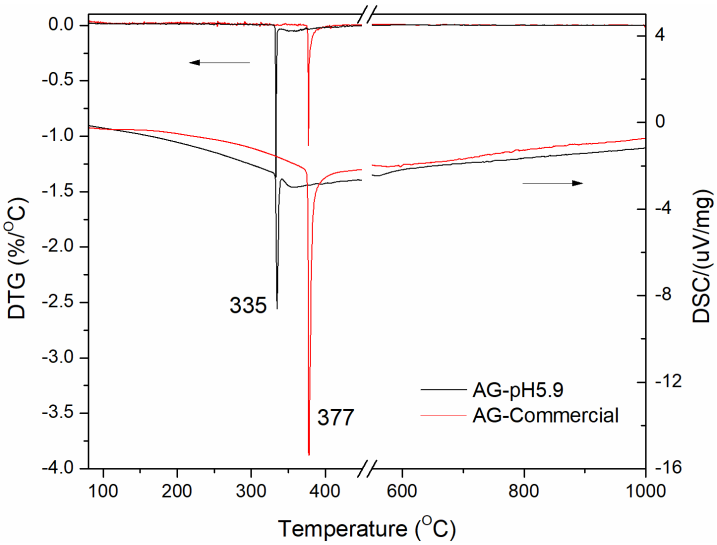

Fig. 5.18. Thermal stability of OSA and commercial silica aerogel.

The thermal conductivity of aerogel synthesized at different pH values is presented in **Fig. 5.19.** The thermal conductivity shows a U-shape curve with increasing pH value. The thermal conductivity of silica aerogel aged for 36 hours is slightly lower than that aged for 48 hours. The thermal conductivity is closely related to the porosity and pore size of aerogel. The smaller the pore size, the higher degree of immobilization of entrapped air molecules because of the difference between pore size and mean free path of air (68 nm). While high porosity means low solid thermal conductivity due to reduced conductive solid path. This observation agrees with other research results. According to,

$$\lambda = \lambda_s + \lambda_g + \lambda_r \tag{5.10}$$

where λ_s is solid heat transfer, λ_g is gaseous heat transfer, and λ_r is radiative heat transfer. The thermal conductivity of aerogels is the accumulation of the three components. Assuming the radiative thermal conductivity to be the same, the lower the gas and solid thermal conductivity, the lower the effective thermal conductivity of silica aerogel. Because the silica aerogel prepared at pH 5.5 and an aging time of 36 hours contains the smallest pore size and highest porosity **(Fig. 5.15**), the aerogel shows the lowest thermal conductivity of 0.015 W/m·K.

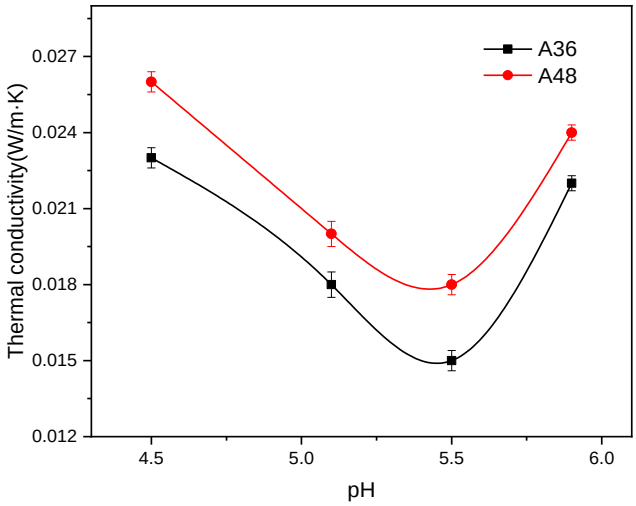

Fig. 5.19. Thermal conductivity of OSA with different pH of silicic acid.

5.3.7 Calcination of olivine silica aerogel

The specific surface area and pore size distribution of the silica aerogel (pH 5.5, A36) is shown in **Fig. 5.20.** The specific surface area and pore volume of the original aerogel is 694 m^2/g and 2.99 cm^3/g, respectively. After calcination at 500 ℃ for 4 hours, the SSA of silica aerogel rises to 920 m^2/g and pore volume to 5.30 cm^3/g.

The reason behind this result is that the calcination process makes the aerogel expand its pore size and coarsens the backbone of silica particles. The silica aerogel after heating to 500 ℃ has a larger pore size, which is around 18 nm, indicating a different pore structure and silica network. Also, the amount of absorbed nitrogen increases at a high relatively pressure, indicating a higher SSA and bigger pore size as well. A few researchers have also investigated the effect of pyrolysis on silica aerogel microstructure. He et al. [217] demonstrate the surface area reduced after thermally treated at 500 ℃, but with an increase in pore size of silica aerogel. Gordienko et al. simulated the structure of Si-F-R before and after pyrolysis, and determined

that the particles within the aerogel would expand after heat treatment [218]. These properties are suitable for silica aerogel function as a catalytic support with the aim of a better spread of titania both around and inside the pores of silica aerogel.

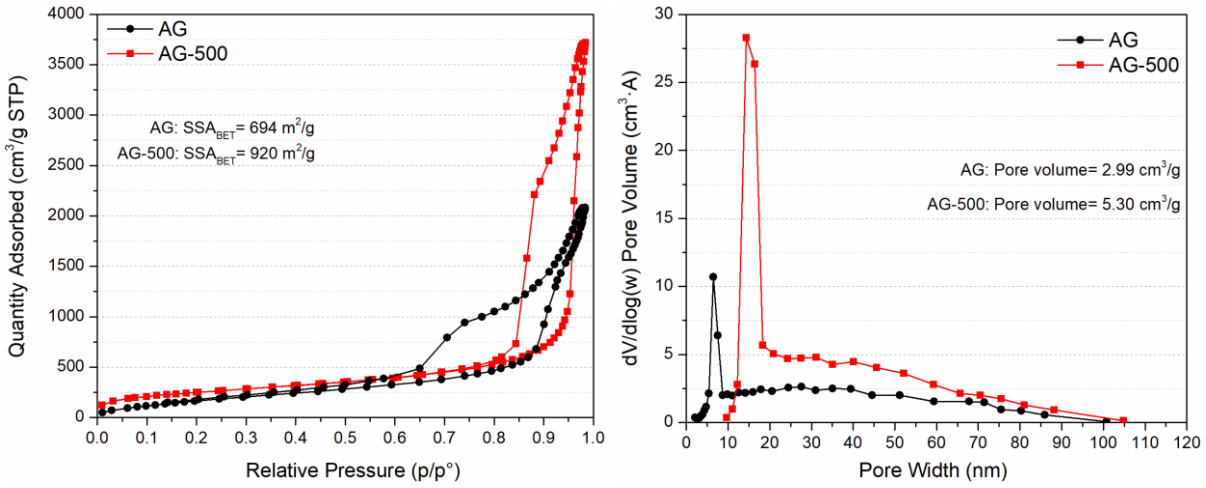

(a) (b)

Fig. 5.20. Physisorption isotherm (a) and pore size distribution (b) of olivine silica aerogel before and after 500 ℃ calcination using BET and BJH methods.

5.3.8 Microstructure of titania-silica aerogel composite

The physisorption isotherm and pore size distribution before and after incorporation of titania are shown in **Fig. 5.21**. The hysteresis loop of the silica aerogel-titania composite is quite small compared to the pure silica aerogel, indicating a smaller pore size of the composite samples, as shown in **Fig. 5.21 (b**). The pore size shrank to 10 nm and pore size distribution is broader than the sole silica aerogel. Moreover, the pore volume decreased significantly, which reduced from 4.99 cm^3/g to 1.77 cm^3/g. The thermally treated silica aerogel also obtained moderate amounts of pores larger than 20 nm. However, these mesopores and macropores of modified silica aerogel were disappeared after titania doping. Therefore, it can be inferred from the nitrogen physisorption results that titania crystals are inside the pores of silica aerogel which makes the pore volume decrease significantly.

As can be observed in **Fig. 5.21 (a)**, the surface area of the silica aerogel-titania composite has very large surface area, reaching 613 m^2/g. This high surface area is due to the substrate of silica aerogel, which can increase the absorptivity of pollutants and also increase the activity of photocatalysts. Pure P25 has a surface area around only 50 m^2/g. Therefore, the much higher surface area of silica aerogel-titania composite can be an important factor that influence the degradation efficiency of NO and NO_x.

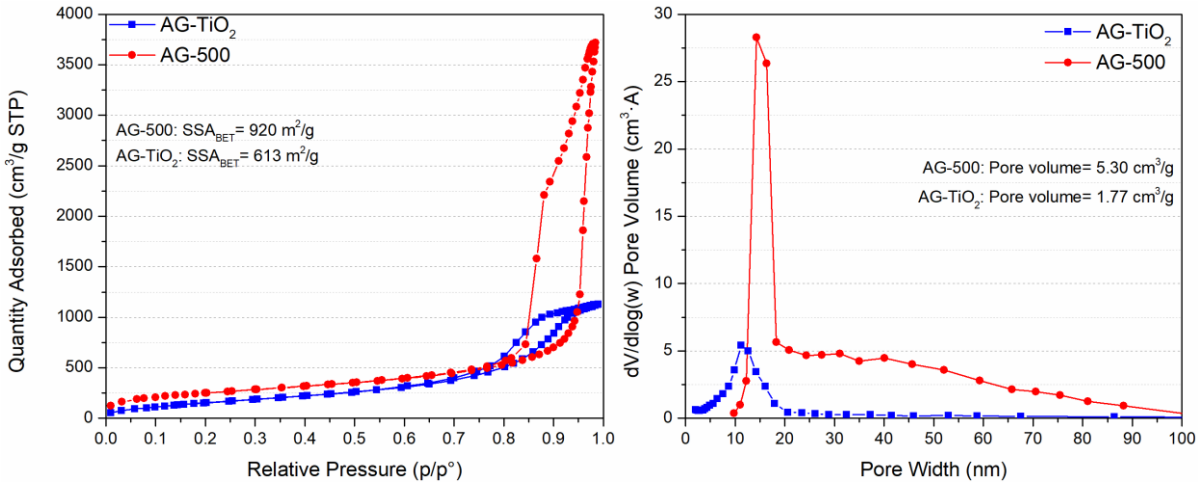

(a) (b)

Fig. 5.21. Physisorption isotherm (a) and pore size distribution (b) of thermally modified silica aerogel before and after incorporation of titania.

The FTIR spectra (**Fig. 5.22**) shows the $–CH_3$ groups are grafted on the surface of the original silica aerogel. After 500 °C heat treatment, the $–CH_3$ groups disappear and –OH groups are visible, which may be due to the moisture in the atmosphere forming the silanol bond. With the incorporation of titania, the Si-O-Ti bond is visible at 960 cm^{-1}, indicating a good chemical combination between silica aerogel and titania. The reason behind this is that the pH around 3-4 of the reacting solution leads to opposite charge between the silica aerogel and formed titania. Moreover, the pH value is lowered to 3~4 for the sake of a slower hydrolysis reaction of TP. According to a model proposed from [14], the ratio between the Ti-O-Si bond and Si-O-Si bond is around 0.059, indicating a moderate bonding between these two materials.

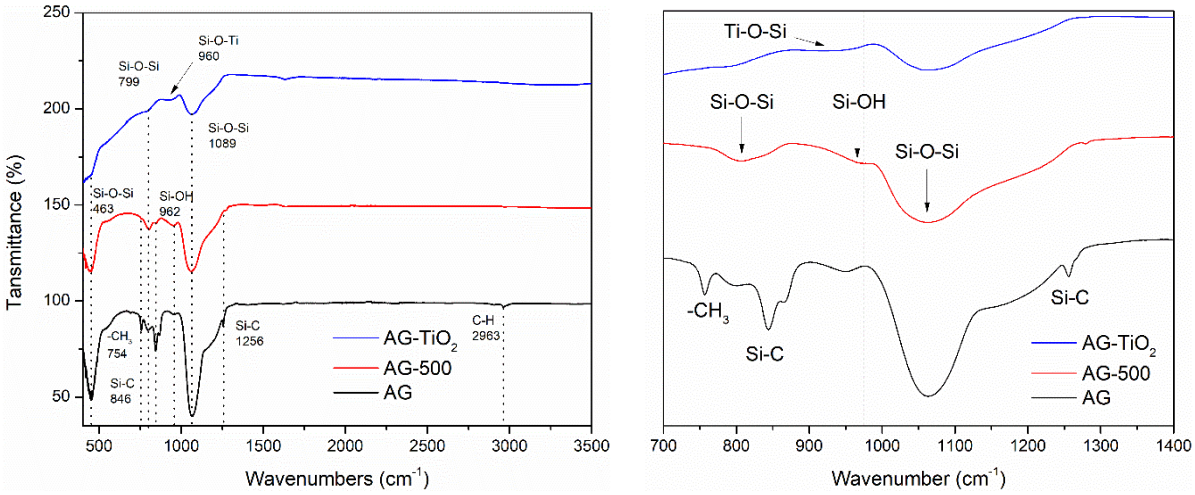

(a) (b)

Fig. 5.22. FTIR spectra of silica aerogel and silica-titania composite (a) 400-4000 cm^{-1} (b) 700-1400 cm^{-1}.

XRD was performed to observe the anatase crystals formed inside and around the silica aerogel as shown in **Fig. 5.23**. The calculated crystal size of the prepared anatase is around 12 nm. This size is below the average pore size of olivine silica aerogel (18 nm), which means the

anatase crystals can be loaded into the mesopores of silica aerogel and chemically bonded to the silica network according to FTIR analysis. The broad peak around 29 degree is the indication of amorphous silica aerogel substrate.

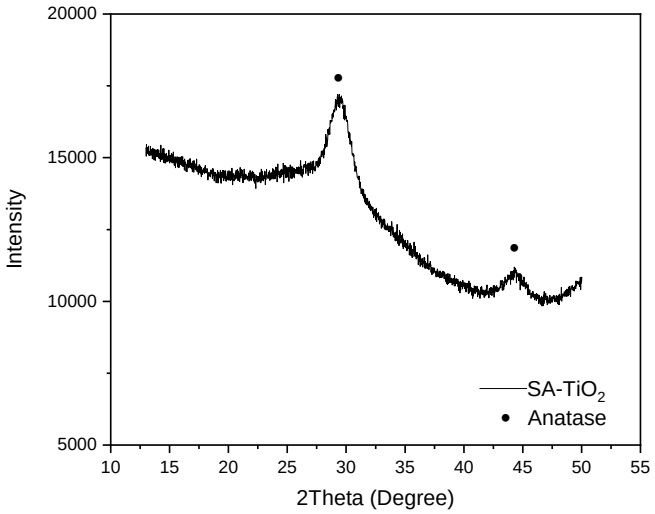

Fig. 5.23. XRD pattern of silica aerogel-TiO_2 composite.

5.3.9 PCO efficiency of the titania-silica composite

The degradation efficiency of the NO and NO_x gases by oxidation of silica aerogel-TiO_2 composite and reference sample P25 is shown in **Fig. 5.24**. The degradation of NO with P25 is 99.2%, which is almost the same as that of the coating using silica aerogel-TiO_2 composite (99.6%). However, the degradation of NO_x (which is the combination of NO and the intermediate NO_2) is higher with the silica aerogel composite. The overall conversion on the composite of NO_x is 93.6%, while only 57.8% for the reference P25. The higher conversion of NO and NO_x is due to the titania forming inside and around the silica aerogel, which fills the pores and as a result, some of the titania being spread evenly. This is confirmed by the nitrogen adsorption and FTIR test in the previous section. Therefore, the silica aerogel-TiO_2 composite is a promising photocatalyst and can be applied on the surface of construction materials to improve the air quality.

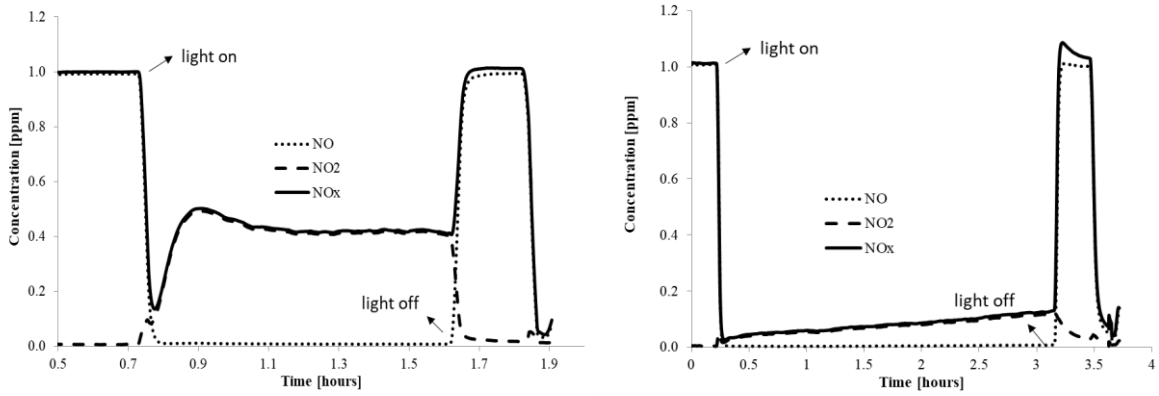

Fig. 5.24. Concentration of NO, NO_2 and NO_x in time, showing degradation due to conversion by titania. (a) Reference P25 (b) Silica aerogel-TiO_2 composite.

Table 5.6. Degradation efficiency of NO and NO_x by P25 and silica aerogel-TiO_2 composite.

Group	Degradation of NO (%)	Degradation of NO_x (%)	Concentration of titania (g/m^2)
Pure titania P25	99.2	57.8	25
Aerogel-TiO_2	99.6	93.6	25

5.3.10 Sustainability evaluation

A significant motivation and potential advantage of recycling olivine to synthesize aerogel is the reduction of the carbon emission associated with the silica aerogel synthesis. Ambient pressure drying creates less CO_2 emission than supercritical drying since less energy is required during the drying process and no liquid CO_2 is used [219]. It is also more favorable than low temperature (40 °C) supercritical drying (SCD) because this SCD consumes higher amounts of solvents (liquid CO_2) during the aging process.

The carbon emission of the silica from olivine is calculated without taking the extra heat from the exothermal reaction into account. If this heat can be used, the carbon footprint could be even lower. Therefore, if only the sodium silicate for aerogel production is replaced from standard to the one from olivine and the rest of the synthesis is assumed to be the same, OSA has a lower CO_2 footprint and is thus more environmentally friendly.

Table 5.7. LCA of sodium silicate hydrothermally produced in an autoclave [194].

	Emissions from manufacturing	
	Energy (MJ/1000 kg)	Emissions (kg CO_2-e/kg)
Electricity	3118	1.065
Coal	296	0.027
Oil (heavy)	9	0.001
Oil (average/light)	456	0.033
Diesel oil	144	0.010
Gas	1270	0.076
Others	78	0.009
Total	5371	1.222
	Emissions from transport	
	Air emissions (kg/1000 kg)	Emissions (kg CO_2-e/kg)
Carbon dioxide (CO_2)	288.7	0.289
Methane (CH_4)	0.128	0.003
	Total	0.292
	Grand total	1.514

In terms of ambient pressure drying, generally commercial water glass is used as the precursor. However, commercial water glass that is prepared using hydrothermal treatment has a CO_2 emission of 1.514 tCO_2/t [220], the detailed energy use is presented in **Table 5.7**. The traditional hydrothermal method uses silica sand and sodium hydroxide as the raw material at temperatures from 150 ℃ to 300 ℃ at elevated pressures (1.8-2.0 MPa) to dissolve the crystallized silica sand. Therefore, electricity (1.065 tCO_2/t) is the major energy source to produce traditional water glass. In addition, the extraction of raw silica sand also requires energy, for instance, sand dredging, washing and drying.

The CO_2 emission of silica from olivine is only 0.461 tCO_2/t according to a life cycle analysis performed by VTT. It can be calculated from **Table 5.2** that only 0.073t olivine silica is needed to produce 1 ton of OSS, which equals 0.034 tCO_2/t which is much lower compared to the CO_2 from electricity in **Table 5.7**. Silica from olivine dissolves in a solution with sodium hydroxide at 80 ℃ and ambient pressure in just 4 hours, which is also a significantly lower electricity requirement in the production process for water glass.

5.4. Conclusions

In this chapter, hydrophobic silica aerogel is successfully produced from olivine at low temperatures via ambient pressure drying. Silica is first produced from olivine and applied as the silica source to react with sodium hydroxide to synthesize sodium silicate. Then ion-exchange, sol-gel method, solvent exchange and ambient pressure drying are applied to produce the olivine silica aerogel. Titania was loaded into the mesopores of silica aerogel by using a precipitation method. The specific surface area and pore size both decrease significantly after titania doping. The crystal size of the prepared anatase in silica aerogel is around 12 nm, which is below the average pore size of the modified silica aerogel. According to the current results, the following conclusions can be drawn:

- Olivine silica has a high surface area and pore volume, indicating a fast and nearly complete reaction with sodium hydroxide at low temperatures, forming olivine sodium silicate. OSS has two forms of silicate species: sodium metasilicate and sodium orthosilicate. The silica aerogel with the lowest density (0.08 g/cm^3) and highest porosity (96.6%) is produced at a pH of 5.5 with 36 hours aging. At a pH of 5.5 the hydrolysis rate of silicic acid and the poly-condensation rate of colloidal silica are balanced.
- The specific surface area of the aerogels decreases with increasing aging time from 36-hours to 48-hours due to Ostwald ripening. The pore size of silica aerogel increases simultaneously due to coarsening of the silica network. The size of silica particles also increases from around 4 to 5 nm according to TEM observation.
- The OSAs show a super-hydrophobicity after replacement of the hydroxyl groups by methyl groups. The optimal TMCS/heptane volumetric ratio in this study is 12/40 ml, and the lowest density of silica aerogel could be obtained.
- The specific surface area and pore volume of silica aerogel increase after heat treatment at 500 ℃ for 4 hours. The reason of this phenomena may be due to the coarsening of the silica aerogel 3D network and also the spring back effect caused by $–CH_3$ groups. The prepared

silica aerogel-titania coating shows a higher conversion efficiency (99.6% for NO and 99.3% for NO_x) than the reference sample P25. Therefore, it is a promising alternative to the current photocatalysts for air purifying in building environment.

- OSA has a lower CO_2 emission than silica aerogel that uses commercial water glass as precursor. Hence the developed OSA may become a promising and sustainable replacement of the current commercial silica aerogel.

Chapter 6 One-pot synthesis of monolithic silica-cellulose aerogel applying a sustainable sodium silicate precursor

This chapter investigates silica-cellulose aerogel to enhance the performance of aerogel. Cellulose aerogel is an advanced thermal insulating biomaterial. However, the application of cellulose aerogel in thermal insulation still faces critical problems, for instance, the very low strength and large pore size so it cannot employ the Knudsen effect. In this study, a silica aerogel developed in Chapter 5 is employed to synthesize silica-cellulose composite aerogel applying a facile one-pot synthesis method. The silica aerogel nanoparticles are formed inside the cellulose nanofibrils by using a sol-gel method and freeze-drying. The developed silica-cellulose composite aerogel has a lower thermal conductivity and is significantly stronger compared to plain cellulose aerogel. The microstructure of silica-cellulose aerogel was characterized by SEM, TGA, FTIR and N_2 physisorption tests. The developed silica-cellulose aerogel had a bulk density of 0.055~0.06 g/cm^3, compressive strength of 95.4 kPa, surface area of 900 m^2/g and thermal conductivity of 0.023 W/(m·K). The thermal stability of the composite aerogel was also improved and showed the higher cellulose decomposition temperature. Furthermore, the composite aerogel is modified by trimethylchlorosilane making it hydrophobic, reaching a water contact angle of ~140°, enhancing its volumetric and thermo-physical stability when applied in a humid environment. In conclusion, the resulting green silica-cellulose aerogel is a promising candidate for utilization as a high performance insulation material.

This chapter is partially published elsewhere:

Y.X. Chen, S. Sepahvand, F. Gauvin, K. Schollbach, H.J.H. Brouwers, Q. Yu, One-pot synthesis of monolithic silica-cellulose aerogel applying a sustainable sodium silicate precursor, Construction and Building Materials 293 (2021) 123289.

6.1. Introduction

Aerogel was first synthesized in 1931 by extracting the solvent from a silica gel without collapsing the silica gel structure [29]. Aerogel shows unique properties compared to other lightweight materials, such as polycarbonate, carbon fiber reinforced plastic or aluminum [221]. Thanks to the high porosity ($\Phi > 95\%$) and low thermal conductivity, aerogels are excellent materials for thermal insulation, catalytic support and chemical absorber [222–227]. Nowadays, with the increasing demand on green chemistry, aerogel made from nanocellulose have gained much focus due to its wide availability and renewability. Cellulose nanofibers are lightweight, mechanically strong nano/microfibers produced from plant-based materials [228]. Normally, it is applied in the textile industry and in bio/polymer composite fields as well. Cellulose mainly consists of repeating glucose molecules units attached to each other. Compared to other polymer fibers from petrochemical resources, naturally occurred cellulose fibers are acknowledged as a sustainable and green alternatives with high aspect ratio and specific surface area [229].

However, although cellulose aerogel has a very high porosity that beyond 97% and good formability, the thermal insulation property still cannot be comparable to conventional silica aerogel. This is due to the much bigger pore size between cellulose fibers (around tens of micrometers) and hence the Knudsen effect cannot play a major role in the thermal conduction. Moreover, cellulose aerogel has a quite low strength compared to other aerogels, for instance, polymer aerogels like PU (Polyurethane) and PI (Polyimide) aerogels, which limits the application of its use in real world. Therefore, finding a suitable method to decrease the thermal conductivity and increase the strength simultaneously is still in demand.

Silica aerogel, on the other hand, is a conventional aerogel mainly used for thermal insulation, for instance, building energy saving, subsea pipeline heat conservation and interior insulation coatings [4,230–232]. However, silica aerogel is more fragile than other aerogel materials, such as cellulose aerogel. Therefore, most commercial silica aerogels are in the form of small granules or powder, making it difficult to apply them in practical conditions like thermal insulation [233]. Hence, it is important to smartly utilize silica aerogel to improve its engineering properties while without compromising porosity and thermal insulation properties significantly.

Currently available silica aerogel is mainly produced from organic silica sources or commercial water glass. For instance, tetrathoxysilane (TEOS) and methyltrimethoxysilane (MTMS), are relatively expensive and contain high embedded energy [224]. Meanwhile, commercial water glass is conventionally manufactured by reacting sodium carbonate (Na_2CO_3) with quartz sand in the molten state at 1300~1600 ℃ [194]. Therefore, exploring a cost-effective and environmentally friendly method to produce silica aerogel is of great interest [180,193], especially considering the sustainability development and environmental impact [234]. For the silica precursor, the silica produced by dissolving the mineral olivine in waste acid has lower energy requirements than conventional methods which include a spray pyrolysis (1200-1600 ℃) process. In our previous research [59,200,235,236], it was shown that silica produced from olivine at 50-90 ℃ had a purity higher than 99% and a specific surface area between 100 to 400 m^2/g, which is much higher than normal silica [237], while the cost and CO_2 emission are much lower. Thus, the obtained nano-silica can react rapidly with sodium

hydroxide (NaOH) to produce low modulus (SiO_2/Na_2O) sodium silicate at ambient pressure and low temperatures, thanks to its high surface area and reactivity. Thus, applying olivine-derived sodium silicate as a precursor instead of organic silica source (TEOS or TMOS) or commercial water glass can help to significantly reduce the energy consumption to produce aerogel.

In the past few years, several studies were focusing on the silica-cellulose composite aerogel (SCA). For example, Demilecamps et al. (2015) explored the possibility of impregnating silica into the cellulose aerogel scaffolds via molecular diffusion and forced flow, with a final supercritical drying. The resulting composite aerogel showed a higher Young's modulus and lower thermal conductivity compared to the original cellulose aerogel. Zhao et al. (2015) investigated the multiscale assembly of super-insulating silica aerogels within silylation nano-cellulosic scaffolds. It was demonstrated that the novel composite aerogel had low thermal conductivity and improved mechanical strength. However, most of these studies prepared silica-cellulose aerogel by forming cellulose aerogel first and with organic silica source. To be specific, the cellulose scaffold needs to be prepared first and later impregnated with silica components from sols derived from organic precursor.

Therefore, it is interesting to explore methods to prepare silica-cellulose aerogel from the sol-gel process of green sodium silicate and impregnate cellulose fibers in the silicate sol. **Table 6.1** lists several typical synthesis methods mentioned in recent literatures using water glass. As can be seen, most of the studies investigate the cellulose hydrogel immersed in commercial water glass with a high modulus (3.3) and then used acid to form silica nanoparticles, followed by supercritical drying. However, it was found that with the cellulose nanofibers in silica hydrogel, the hydrogel can withstand the safer and more cost-effective freeze drying to obtain the aerogel. Hence, the conventional supercritical drying could be avoided.

Table 6.1. Production methods and properties of silica-cellulose aerogel using commercial water glass as precursor.

Literatures	Synthesis methods	Drying method
Liu et al. 2013b	Cellulose hydrogel film dipped in water glass followed by ethanol and sulfuric acid catalyst.	Supercritical drying
Demilecamps et al. 2014	Cellulose-8%NaOH-1%ZnO suspension was added with sodium silicate solution to form cellulose gel. Acid was used to form silica particles in the composite aerogel.	Supercritical drying
Sai et al. 2014	Bacterial cellulose hydrogels immersed in sodium silicate solution to gel and followed by acid catalyst.	Freeze drying

In this study, the cellulose nano-fibrils are introduced in the inorganic and cost-effective silicate sol-gel process. The hydroxyl groups of the polymerized silicate sols during condensation and gelation can react with the -OH groups on chains of the cellulose fibers, leading the two materials chemically attached with each other and form composite hydrogel. The final silica hydrogel was reinforced with the cellulose fibers. Since the purpose of using the composite aerogel was to explore the possibility to apply for thermal insulation, the volume stability and cost-effective of the developed aerogel are significantly important. Therefore,

hydrophobization of the silica-cellulose composites aerogel is necessary to avoid water penetration into the hydrophilic aerogel, to increase the volume stability and service life of the composite aerogel. Because the wetting-drying processes caused by moisture in the environment can damage the pore structure of the composite aerogel, leading to the collapse of the structure. Hence, TMCS was applied for hydrophobization by chemical vapor deposition. The schematic diagram of the mechanism is shown in **Fig. 6.1**.

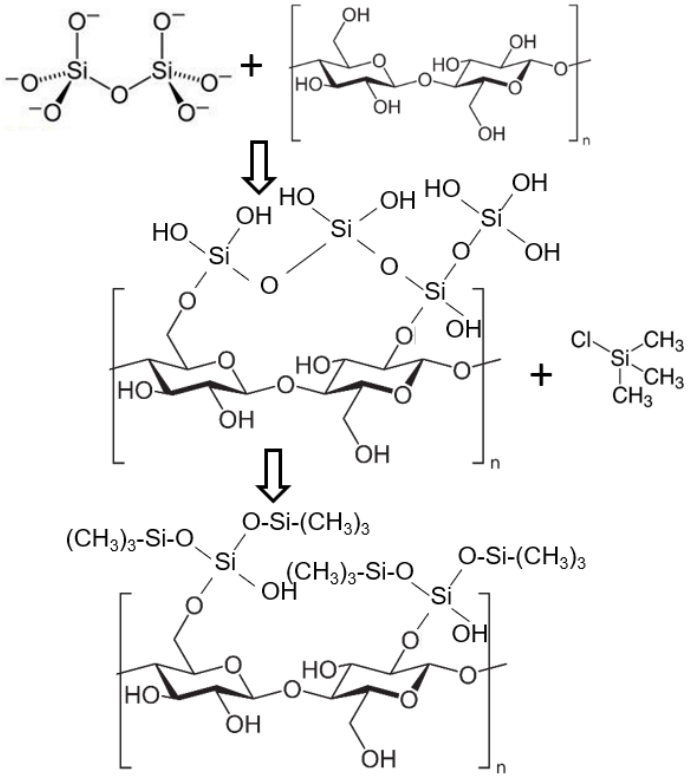

Fig. 6.1. Schematic diagram of mechanism for SCA preparation and TMCS modification.

Overall, a facile synthesis of silica-cellulose aerogel (SCA) was presented by incorporating renewable cellulose nano-fibrils into the low-cost silicate sol-gel process and freeze-drying the composite gel. Olivine silica was used to prepare the green sodium silicate precursor. The procedure is promising to prepare sustainable SCA with ultra-low density, low thermal conductivity and relatively higher mechanical properties than plain cellulose aerogel.

6.2. Materials and experiments

6.2.1 Starting materials

Olivine silica used for aerogel preparation was provided by Eurosupport. The specific surface area, pore volume, pore size, particle size and silanol content of olivine silica are shown in **Table 6.2**. The olivine silica has a surface area of around 274 m^2/g, indicating a fast reaction rate with sodium hydroxide. Moreover, the pore volume and pore size are both high, reaching 0.72 cm^3/g and 10 nm, respectively. The silanol content of olivine silica reaches 8~20 OH/nm^2, which is far beyond the commercial fumed silica and pyrogenic silica, which have a silanol content of 3~4 OH/nm^2 [242].

Table 6.2. Properties of olivine silica.

Properties	Surface area (m^2/g)	Pore volume (cm^3/g)	Average Pore size (nm)	Average Particle size (μm)	Silanol content (OH/nm^2)
Olivine silica	274±14	0.72±0.05	~10	~17	8~20

Olivine-derived sodium silicate with a modulus of 1.5 with 8% silica content was prepared by reacting the olivine silica with sodium hydroxide (NaOH) solution at 80 ℃ for 2 hours. The recipe for preparation of sodium silicate is presented in **Table 6.3**. The practical modulus was determined by using X-ray florescence. The undissolved silica particles have limited influence on the quality of prepared sodium silicate due to the very small fraction in sodium silicate (0.27%). The pH of the prepared sodium silicate solution was 12.98, which is slightly lower than that of the commercial water glass (13.69).

Table 6.3. Recipe of water glass preparation from olivine silica and sodium hydroxide.

Olivine silica (g)	Sodium hydroxide (g)	Distilled water (g)	Temperature (℃)	Theoretical modulus	Measured modulus	SiO_2 concentration (%)
9	8	95.5	80	1.50	1.45	7.9

In order to determine the types of silicate species in olivine sodium silicate, ^{29}Si NMR test was carried out to measure the silicate state and the results are shown in **Fig. 6.2**. The sharp peak at -72 ppm represents the existence of Q^0 monomers, while Q^1 dimers and Q^2 trimers at c.a. -80 and -82 ppm can also be observed. Meanwhile, a moderate number of Q^2/Q^3 groups can be observed at around -86 to -90 ppm. No Q^4 sites can be observed, with the locations lower than -100 ppm, which means all the silica in Q^4 form is dissolved in solution.

For the olivine sodium silicate, a significant peak at -72 ppm indicates most of the silicate structure is monomers silicate. While the minor peaks at the chemical shifts of around -80 ppm show a less extent of Q^1 and Q^2 sites for silicate. Trace number of Q^2/Q^3 sites can be observed at -87 to -90 ppm, indicating few percentages of highly polymerized silicate. However, compared to the NMR analysis of commercial water glass with a modulus of 3.3, there is significant difference, indicating a much higher polymerized silicate species. This is because commercial water glass production includes a silica sand at a much higher temperature of 1300 to 1600 degree of calcination with sodium carbonate (Na_2CO_3), so more silicates are supposed to polymerize in solid solutions and thus more Q^4 silicate species are expected. However, more energy is also supposed to be involved in this process which is not sustainable and green. Therefore, the difference in structure of silicate species in sodium silicate solution may influence the properties and microstructure of the resulting aerogel.

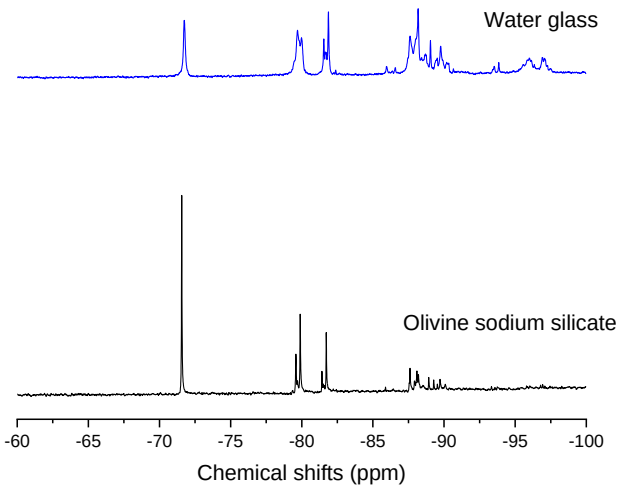

Fig. 6.2. ^{29}Si NMR spectra of olivine derived sodium silicate and commercial water glass.

Water suspensions of two kinds of cellulose nanofibrils (CNF) were provided by Sappi, the Netherlands. CNF1 has a Fine S of 94% and Fine P of 4.6% while CNF2 had a Fine S of 48% and Fine P of 23.5%. The cellulose was derived from wood pulp that has been sourced from sustainably managed forests. The CNFs were prepared by the mechanical super-milling method with the α-cellulose source in the form of a white gel. The original concentration of CNF1 and CNF2 were 2.7 wt.% and 3.1 wt.%, respectively, which was determined by heating the raw CNF suspension at 105 ℃ until constant mass and then calculate the concentration of solid content in the suspension. The pH of the CNFs was between 6.5 and 7.5. A good dispersion of cellulose fibers is critical to utilize its full benefits. The two CNFs were mixed for 30 minutes at 2000 rpm with a high shear mixer (Model L5M, high shear laboratory mixer, Silverson Machines Ltd.) to improve their dispersion until showing efficient thickening effect with a cream-like appearance. The SEM and TEM images of these two CNFs are presented in **Fig. 6.3.** The diameters of the two kinds of nanofibers are similar, however, the length of these two fibers were different, ranging from a few micrometers to tens of microns. The surface charge of CNF1 and CNF2 measured by zeta potential was -52.5 mV and -40.5 mV, respectively.

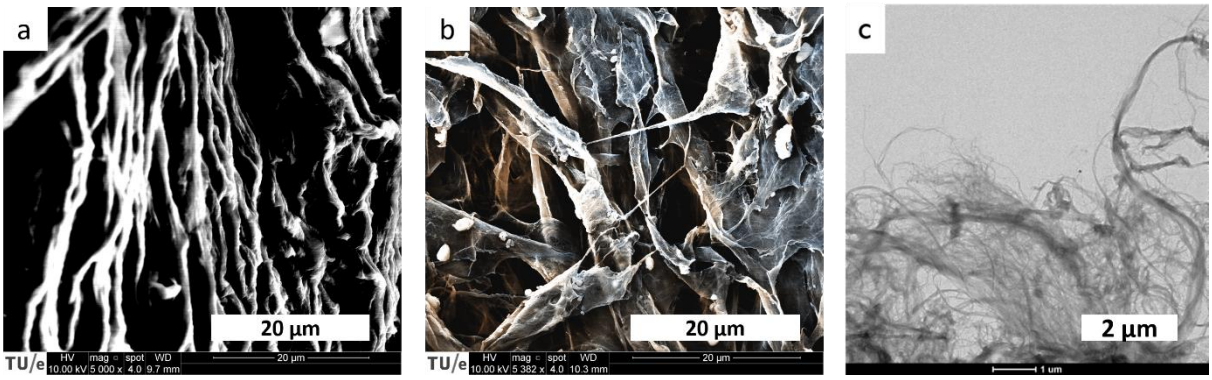

Fig. 6.3. SEM of (a) CNF1 and (b) CNF2 and (c) TEM of cellulose nanofibrils.

Other chemicals used were sodium hydroxide pellets (NaOH), n-heptane (C_7H_{16}), ammonia solution ($NH_3 \cdot H_2O$, 25%), trimethylchlorosilane (C_3H_9SiCl, 99%) and Amberlyst 15 hydrogen form (H^+ cation exchange resin) for preparation of silica-cellulose composite aerogel.

6.2.2 Preparation of silica-cellulose composite aerogel

The 8% as-prepared olivine sodium silicate was passed through ion exchange resin to obtain silicic acid, with a final pH of 2.0~2.5. Then, 25 ml of silica sol was mixed with CNFs in a beaker for 60 min at room temperature. Later, the pH of the silica-cellulose composite suspension was increased to 5.0~5.5 by adding 1M ammonium hydroxide to accelerate the gelation process. Afterwards, the suspension was placed into a mold to cast the silica-cellulose hydrogel. For all the hydrogels, the gelation times were around 20 min. Lastly, the mold was sealed air-tight with a plastic film. After 1 day aging at room temperature, the silica-cellulose composite hydrogel was freeze-dried. Specifically, the hydrogel was immersed in liquid N_2 at a temperature of −196 °C. The frozen sample was dried in a freeze dryer (Alpha 2–4 LD plus from Martin Christ, Salmenkipp) under the following conditions: ice condenser=−57 °C; vacuum $\leqslant$ 0.1 mbar; and time =48 h. For the hydrophobic treatment of SCA, the as-prepared composite aerogel was treated by thermal chemical vapor deposition with trimethylchlorosilane (TMCS). Magnesium chloride saturated solution was poured into a vacuum desiccator for regulating relative humidity at range from 35% to 65% for 24 h. SCA was placed in a 200 mL beaker, while a 3 mL of TMCS was inserted in another 10 mL beaker. The smaller beaker containing TMCS was placed inside the 200 mL beaker. This double beaker setup was placed in the desiccator and was designed to prevent direct contact of the aerogel with TMCS. The 200 mL beaker was sealed with a cap and placed in a vaccum oven at 160 degree for 1 h. Unreacted silanes were removed by keeping the aerogel in vacuum drying oven until the pressure reached 0.03 mbar or less. The prepared hydrophobic SCA was ready for characterization. The schematic diagram of the preparation of silica-cellulose composite aerogel is presented in **Fig. 6.4**.

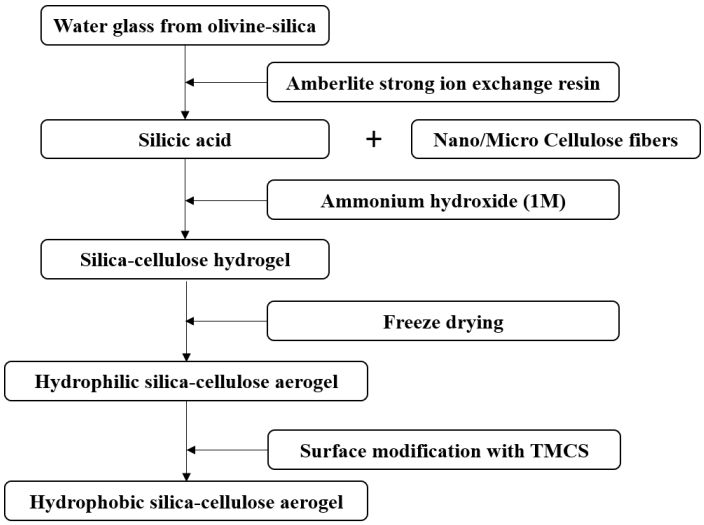

Fig. 6.4. Schematic diagram of the preparation of silica-cellulose composite aerogel.

6.2.3 Preparation of plain cellulose aerogel

Plain cellulose aerogel was prepared according to the previous researches as reference [243,244]. The CNF1 and CNF2 suspensions were first diluted with distilled water to a concentration of 0.55% and 0.60%, respectively. The diluted suspensions were continuously stirred at 480 rpm at 20 ℃ for 30 min using a magnetic stirrer. Then, the diluted suspension was moved into a cylindrical plastic mold with a diameter of 10 mm and a height of 20 mm. Afterwards, the assembly was frozen dried with liquid nitrogen and then moved to a freeze dryer to extract the solvent for 2 days. The recipe of all the six samples is shown in **Table 6.4**.

Table 6.4. Recipe design of the investigated aerogel samples in this study.

Groups	CNF1 (mL)	CNF2 (mL)	8% Silica sol (mL)	Distilled water (mL)	TMCS modification
SS-CNF1	5	0	25	0	N*
SS-CNF2	0	5	25	0	N
SS-CNF1-M	5	0	25	0	Y*
SS-CNF2-M	0	5	25	0	Y
NCA1	5	0	0	25	N
NCA2	0	5	0	25	N

*N=No, *Y=Yes

6.2.4 Characterization of the composite aerogel

The skeletal density of the prepared silica-cellulose aerogels was determined with a Helium pycnometer (AccuPyc II 1340 Micromeritics). The bulk density of the as-prepared SCAs was determined by using the bulk volume and mass of the prepared samples. Based on the two densities, the porosity of the SCAs was determined according to:

$$\Phi = (1-\frac{\rho_b}{\rho_s})\times 100\% \tag{6.1}$$

where Φ is the porosity of the tested aerogel, ρ_s the skeleton density of the tested aerogel, ρ_b the bulk density of the tested aerogel.

Water suspension of CNF was prepared for TEM analysis. The suspension was diluted to 1% of original concentrated CNF solution. A 200 mesh Cu grid covered with a continuous carbon film was used to support the CNF sample. FEI Tecnai 20 Sphera instrument with a LaB6 filament was operated at an accelerating voltage of 200 kV to observe the microstructure of CNF.

The mechanical property of the SCAs with a cylindrical shape (10mm diameter × 20mm height) was tested in an MTS Criterion equipped with a load cell of 200 N at a speed of 1 mm/min to $\varepsilon = 80\%$ of its original height. The thermal conductivity of the SCAs was determined with TPS-instruments (Hot disk). The water contact angle (WCA) measurements using sessile drop technique was used to determine the hydrophobicity of SCAs (Dataphysics Contact Angle System, TBU 90E). The volume of the Milli-Q water droplet used for the contact angle test was

3.000 μL. The final results correspond with the average measured WCA of five droplets on the surface of SCAs. The margin of error was defined as the 95% confidence interval of the five measurements.

The microstructure of the SCAs was observed with scanning electron microscopy (SEM), by using a JOEL JSM-5600 instrument at an accelerating voltage of 15 kV. The thermal stability of the SCAs was determined with thermogravimetric analysis by using a NETZSCH STA449-F1 instrument with a heating rate of 5 ℃/min under air atmosphere. Chemical bonds in the SCAs were detected by using a Varian 3100 Fourier-transform infrared spectroscopy (FTIR) with wavenumbers ranging from 4000 to 400 cm^{-1} at a resolution of 2 cm^{-1}. The specific surface area and pore size distribution were measured by nitrogen physisorption, which was carried out with a Tristar 3000 Series micrometer employing nitrogen at 77 K. The samples were pretreated by nitrogen gas flow with a heating rate of 10 ℃/min and heated up at 80 ℃ for 4 hours to remove moisture. Solid state MAS NMR spectra were carried out using a Bruker Advance 400WB spectrometer. The ^{29}Si NMR spectra were collected at 79.5 MHz on a 7 mm probe, with a pulse width of 6.5 μs, a spinning speed of 15.9 kHz and a relaxation delay of 10 s.

6.3. Results and discussion

6.3.1 Microstructural analysis

6.3.1.1. SEM analysis

The SEM of SCA with different cellulose nanofibrils and modification are shown in **Fig. 6.5**. The SCA shows a random distribution of silica and cellulose fibers, due to the heterogenous nature of cellulose fibers and because silica aerogel was also attached to these randomly distributed fibers. As observed in **Fig, 6.5**, the silica aerogel has a relatively strong affinity with cellulose fibers. For SS-CNF1, the nanofibers were crossly linked within the silica aerogel structures; the silica surface was very smooth and showed a more homogeneous structure. This silica microstructure was rather different from those of conventional silica-cellulose aerogels using commercial water glass as shown in **Table 6.1**, which implies silica monodisperse spherical particles inside the cellulose matrix (Liu et al. 2013; Demilecamps et al. 2014). Therefore, the developed SCA in this study could have a higher surface area and enhanced homogeneity. As can be seen from the NMR analysis of silica precursors in section 6.2.1, the commercial water glass contains more highly polymerized silicate (Q^3/Q^4) than olivine sodium silicate, which may be the reason of the difference in the silica morphology. Most of the micrometer-sized pores (20~50 μm) in original cellulose aerogel [244] are filled with silica aerogel, making it a more compacted composite than plain cellulose aerogel. However, there still exists a few pores with the size of 10~20 μm between cellulose fibers. For SS-CNF2, the cellulose fibers are slightly wider and the less homogeneous than SS-CNF1 due to the higher fraction of coarser cellulose nanofibrils in the raw material.

After surface modification of SCA by TMCS reagent, the shape of the cellulose fibers remained the same while the surface of silica aerogel particles became rougher and clustery, which is in accordance with the BET results shown later, showing lower surface area of SS-CNF1-M. This change in morphology was expected since the Si-O-H group was substituted by the Si-O-Si$(CH_3)_3$ group as presented in **Fig. 6.1**.

The plain cellulose aerogel contains the macropores between cellulose fibers with the size of around 20~50 μm, which was rather large compared to that of silica aerogel (10~20 nm) and SCA. Therefore, this loose structure makes plain cellulose aerogel less thermal insulating due to the air molecules can still move freely in the micron-sized pores and promote gaseous heat transfer via convection. Therefore, the silica-cellulose composite aerogel can overcome this drawback by incorporating silica aerogel in the pores to decrease gaseous heat transfer and even improve the thermal stability of cellulose fibers.

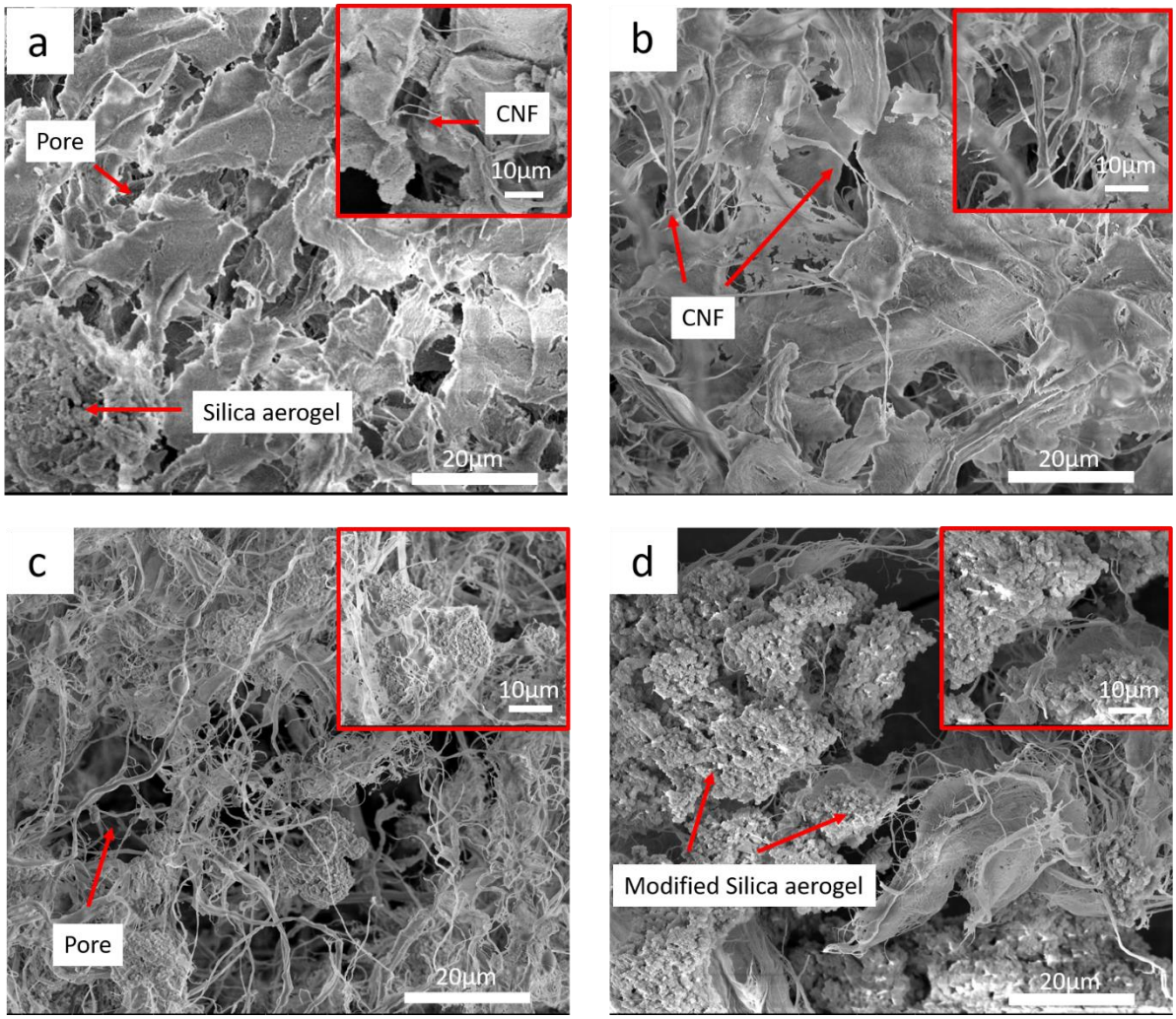

Fig. 6.5. SEM of SCA with different CNFs and surface treatment: (a) SS-CNF1 (b) SS-CNF2 (c) SS-CNF1-M (d) SS-CNF2-M (Table 6.4).

6.3.1.2. Specific surface area and pore structure

The physisorption isotherm and pore size distribution of SCAs from nitrogen physisorption test are presented in **Fig. 6.6.** The specific surface area, total pore volume and average pore size of the developed SCAs are shown in **Table 6.5**. Pure cellulose aerogel has a SSA_{BET} of around 100~200 m^2/g, while silica aerogel has a SSA_{BET} of 600~700 m^2/g. It indicates that the specific surface area of all the composite aerogels increased significantly compared to cellulose aerogel, suggesting the existence of nanostructured silica aerogel filling in the surface and pores of the cellulose matrix.

Table 6.5 shows the SSA of SS-CNF1 and SS-CNF2 are much larger than that of pure cellulose aerogel and are similar to pure silica aerogel, reaching 958 m^2/g and 614 m^2/g, respectively. This result probably relates to the silica 3D network that has a higher surface area and thus leads to the increased surface area in the composite aerogels. The SSA of SS-CNF1 is also much higher than other researchers' work, which obtain a SSA of silica-cellulose aerogel reaching only 340 m^2/g and 150 m^2/g, respectively [228,245]. This phenomenon can be explained by the difference in the silicate structure as shown in the NMR test for the silicate precursor. It may indicate that low modulus silicate could form smaller silica particles inside the cellulose nanofibrils and increase the surface area. The physisorption isotherms of SS-CNF1 and SS-CNF2 present a typical Type IV isotherm, with a relatively small hysteresis, which is due to the narrow pore size distribution, with uniformly distributed pores below 4 nm. (See **Fig. 6.6 (b)).** At p/p_0=0.1 of the nitrogen isotherm exist a slight leap, indicating a moderate amount of micro-porosity, which may contribute to the large surface area as well. Therefore, this indicates silica aerogel covers the surface of cellulose fibers, thus changing the randomly distributed nanopores of cellulose to uniformly distributed nanopores of silica aerogel.

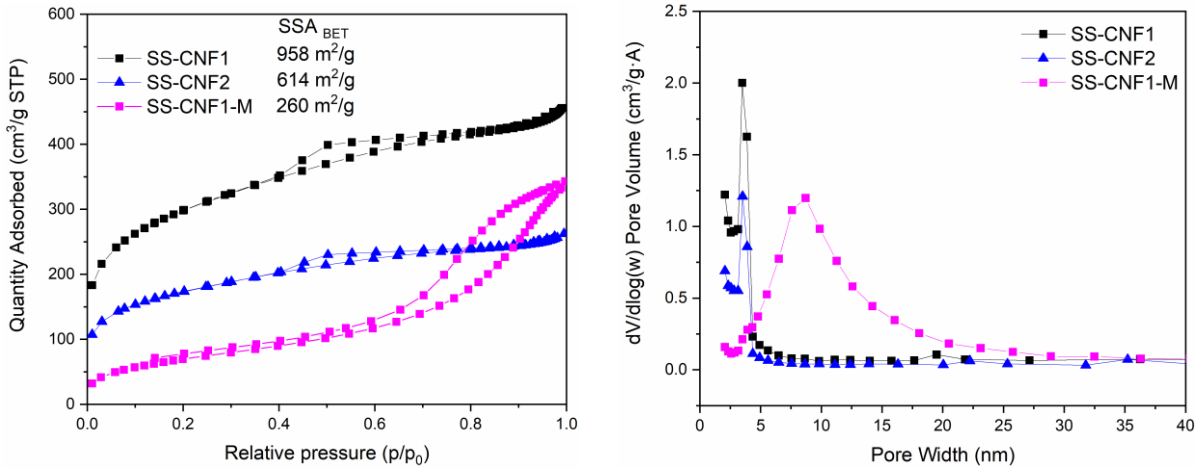

(a) (b)

Fig. 6.6. Nitrogen physisorption isotherm (a) and pore size distribution (b) of the as-prepared SCAs.

Table 6.5. Specific surface area, total pore volume and average pore size of the developed SCAs and comparison with silica aerogel and cellulose aerogel.

Groups	BET surface area (m^2/g)	Total pore volume (cm^3/g)	Average pore width (nm)
SS-CNF1	958±12	0.53±0.01	3.51±0.11
SS-CNF2	614±10	0.29±0.01	3.52±0.19
SS-CNF1-M	260±9	0.55±0.02	7.94±0.36
Cellulose aerogel	200~300	0.24~0.30	10~30
Silica aerogel	600~700	2.5~3.0	10~20

The isotherm and pore structure of SCA changed significantly after TMCS modification, as shown in **Fig. 6.6**. The isotherm changed to a non-typical Type IV isotherm, indicating

hydrophobic modification of aerogel result in a change in the pore size distribution. The relatively large hysteresis was caused by the broad pore size distribution with most pores ranging from 5 nm to 20 nm and concentrated in 8 nm. The larger pore sizes could be attributed to -CH_3 groups attached on the surface of silica, resulting in swelling of pores due to the repulsive force between the -CH_3 bonding.

6.3.1.3. FTIR spectra

The FTIR spectra of reference NCA and SCA before and after TMCS modification are shown in **Fig. 6.7** (arbitrary scale used with consistency for each curve). The reference NCA spectra present typical bands of cellulose fibers, for instance, the hump at 3340 cm^{-1} and 1632 cm^{-1} suggesting O-H stretching and bending, and the sharp peak at 1053 cm^{-1} indicating C-O-C skeletal vibrations. Meanwhile, the characteristic peaks of C-H bending, C=C and C=O stretching are visible at 1376, 1310, and 1253 cm^{-1}, respectively.

The SCA before hydrophobic treatment has typical Si-O-Si peaks, corresponding to 1059 cm^{-1} (asymmetrical stretching vibration), 795 cm^{-1} (asymmetrical stretching vibration) and 455 cm^{-1} (rocking vibration). Also, the Si-O-H bond can be observed at 967 cm^{-1}, showing the large amounts of hydroxyl groups on the silica surface that are available to react with the TMCS reagents for hydrophobic treatment. Minor amounts of H-O-H groups can be observed at 1632 cm^{-1} and 3340 cm^{-1} corresponding to bending vibration and stretching vibration of physically bound water. It shows the water was mostly removed through freeze drying. However, due to the hydrophilic nature of unmodified SCA, moisture in the air can be easily absorbed on the surface of aerogel, thus hydrophobic modification was necessary to resist water penetration that can damage the structure of SCA.

Due to the modification with TMCS, the SCA becomes hydrophobic. TMCS has a Si-Cl bond that can react with the silanol groups of the unmodified SCA. For SS-CNF1-M and SS-CNF2-M, the characteristic peaks of the Si-C bonds are visible at 896 cm^{-1} and 1273 cm^{-1}. Also, the bending vibration of the –CH_3 group appears at 760 cm^{-1}. Furthermore, the characteristic peak of the Si-OH bond at 967 cm^{-1} disappears after surface modification, which means the silanol group was substituted by the Si-O-Si$(CH_3)_3$ group (896 cm^{-1}, 760 cm^{-1}).

The intensities of Si-C and -CH_3 bands of the two SCA are slightly different, even though the volume of TMCS used for surface modification remains the same. Hence, as discussed before, the BET result show that SS-NFC has a significantly higher surface area than SS-MFC. Therefore, the TMCS usage for NFC should be higher than that of MFC to reach the same level of trimethyl silyation, leading to the reduced intensity of Si-C and -CH_3 bands for SS-NFC.

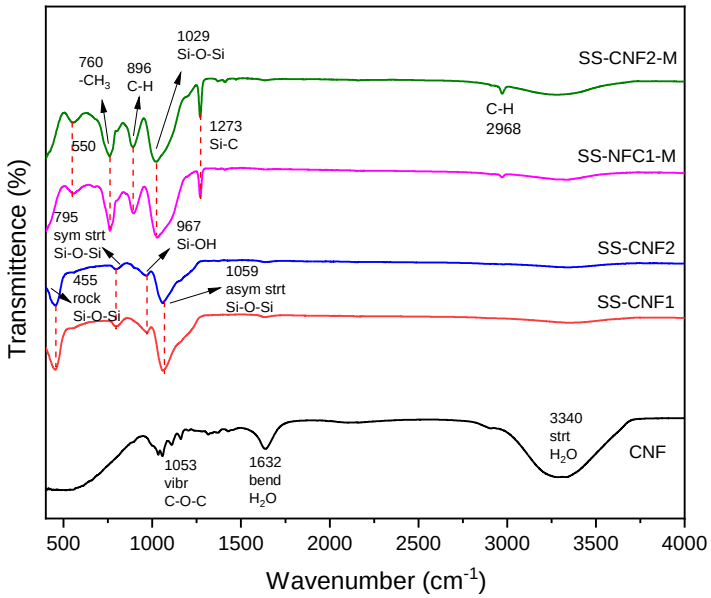

Fig. 6.7. FTIR of silica-cellulose aerogel before and after TMCS hydrophobic modification.

6.3.1.4. TG/DTG analyses

The thermal gravimetry (TG) and differential thermal gravimetry (DTG) curves of SCA with different cellulose fibers and surface modification are illustrated in **Fig. 6.8**. The thermal decomposition of the reference NCA aerogel both consists of two phases. Firstly, the physical bound water to the surface of cellulose fibers evaporates before 105 ℃. It can be observed the physical bond water was 4 wt.% for NCA. The second phase of decomposition lasts from 250 ℃ to 375 ℃, which was attributed to the burning of cellulose fiber. The carbon chain normally decomposes at around 300~350 ℃. At this stage, most of the mass of the cellulose aerogel was lost. After heating from 375 ℃ to 1000 ℃, the residual mass of the cellulose aerogel is carbon black, which is only 5 wt.% for NCA. Therefore, pure cellulose aerogel can be vulnerable to higher temperatures and then loses the structural stability, consequently leading to a total collapse.

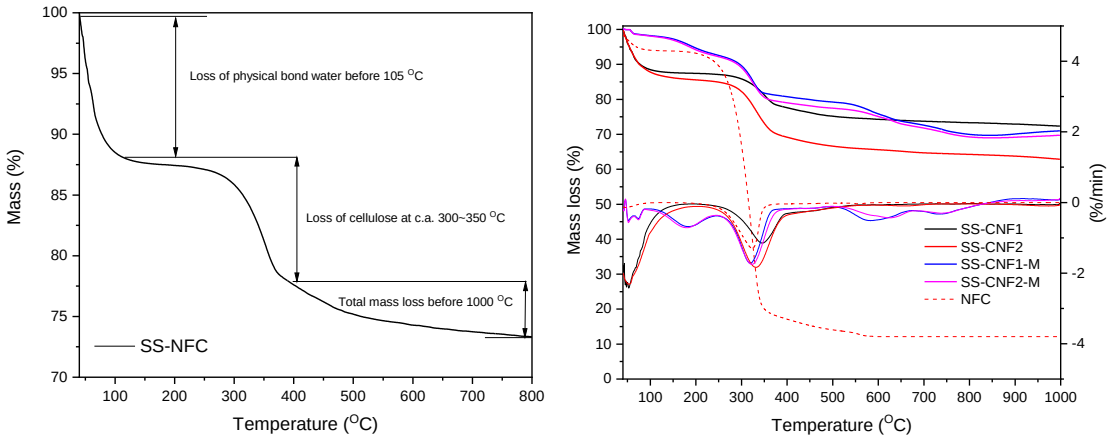

(a) (b)

Fig. 6.8. Thermogravimeter analysis of (a) SS-CNF1 and (b) reference CNF and SCA of different cellulose fibers and surface modification.

However, the SS-CNF1 and SS-CNF2 aerogels showed different decomposition phases and residual mass at 1000 ℃, as shown in **Fig. 6.8 (a).** The amount of physical bound water for SS-CNF1 and CNF2 are higher than CNF1 and CNF2 samples, reaching 11.6% and 12.5%, respectively, indicating a more hydrophilic property. The mass loss of SS-CNF1 and SS-CNF2 between 250~400 ℃ was 9.36% and 15.57%, respectively. Also, it can be noticed that the peak position in the DTG curve for this temperature range was different for SS-CNF1 and SS-CNF2. For SS-CNF1, the peak situated at 345.5℃, while for SS-CNF2 the peak shifted to 333.0 ℃. The residual mass after 1000 ℃ of both samples showed a relatively high value due to the existence of silica, reaching 72.35% and 62.89%, respectively, indicating that the thermal stability of silica aerogel was much higher than that of cellulose aerogel. As observed from **Table 6.6**, the decomposition temperature of the DTG peak was increased due to the incorporation of silica, rising from 309 ℃ to 345.5 ℃ for CNF1 and to 333 ℃ for CNF2, respectively. Therefore, silica dosage can slightly improve the thermal stability of the composite aerogel.

After modification by TMCS, the physically bond water was significantly reduced for both SS-CNF1-M and SS-CNF2-M, showing the successful hydrophobic treatment. The decomposition temperature of cellulose fibers also increased to 331 ℃ and 329 ℃ for SS-CNF1-M and SS-CNF2-M, as compared to reference cellulose fibers. However, surface modification cannot further increase the thermal stability of the composite aerogel compared to hydrophilic SCA. The peak DT was still situated at around 329~331 ℃.

Table 6.6. Decomposition temperatures of cellulose fibers of each group.

Groups	Initial cellulose decomposition T (℃)	Peak of cellulose decomposition T (℃)	End of cellulose decomposition T (℃)
SS-CNF1	249.5	345.5	410.0
SS-CNF2	248.6	333.0	408.5
SS-CNF1-M	260.6	331.3	390.6
SS-CNF2-M	261.3	329.3	391.6
NCA1	240.6	309.0	375.0

6.3.2 Density and porosity of silica-cellulose aerogel

The skeletal density ρ_k, bulk density ρ_b and porosity Φ of cellulose aerogel and silica-cellulose composites aerogel are shown in **Table 6.7**. The bulk density of the SCAs varied from 0.052 to 0.061 g/cm^3, which is in between the pure silica aerogel (~0.1 g/cm^3) and cellulose aerogel (~0.012 g/cm^3). This is because the silica aerogel was attached on the surface of cellulose fibers and thus increases the pure cellulose density, while the scaffold of cellulose aerogel provides an ultralight matrix for silica aerogel. Thus, the density of SCA falls in the middle of the density of cellulose aerogel and silica aerogel, which was in line with the SEM and FTIR analysis. Pure cellulose aerogel obtains a much lower density than SCA, because silica aerogel (~0.1 g/cm^3) fills in the interparticle pores of cellulose nanofibrils (~0.02 g/cm^3). Also, the pore size of silica aerogel and cellulose aerogel was very different: silica aerogel has nanometer-sized meso-pores while for cellulose aerogel the pore size was tens of micrometers.

Therefore, it is reasonable for SCA to have a higher density than that of cellulose aerogel, while it has a lower bulk density than silica aerogel.

It is also observed that the four types of SCAs have slightly different densities and porosities (**Table 6.7**). SS-CNF2 has the lowest density (0.052 g/cm^3) among all the SCAs, showing the highest porosity of 97.1%. However, the density of SS-CNF1 was similar to SS-CNF2 ones. Furthermore, the density increases after TMCS modification, indicating the replacement of –OH group by –Si(CH_3)$_3$ group can increase the density of SCA since it has a larger molecular mass. Although the density of SCA increases, the porosity only slightly decreases, indicating a minor influence of surface modification on the porosity of SCA.

It also can be observed that NCA1 has a slightly higher bulk density than NCA2. NCA1 contains more finer nanoscale fibers, so more fibers are in close contact with each other. The NCA2 has much longer fibers and thus the micrometer pores are much larger than for NCA1, resulting in a looser structure. Overall, the SCA composite aerogel has a lower bulk density than plain silica aerogel, while higher than that of reference cellulose aerogel.

Table 6.7. Skeletal density, bulk density and porosity of the investigated aerogels.

Groups	Skeletal density (g/cm^3)	Bulk density (g/cm^3)	Porosity (%)
SS-CNF1	1.82±0.02	0.054±0.01	97.0±0.01
SS-CNF2	1.78±0.01	0.052±0.01	97.1±0.02
SS-CNF1-M	1.87±0.03	0.061±0.02	96.7±0.01
SS-CNF2-M	1.85±0.01	0.059±0.02	96.8±0.02
NCA1	1.53±0.01	0.013±0.01	99.1±0.03
NCA2	1.51±0.02	0.011±0.02	99.3±0.03
Silica aerogel	2.1	0.08~0.13	95~99

6.3.3 Mechanical properties

The uniaxial compression results of the reference cellulose and SCAs are presented in **Fig. 6.9**. The mechanical parameters are summarized in Table 6.8. The stress-strain curves of the tested groups show three stages: a linear trend at very low strains (＜5%), an increased slope at higher strains, and a final densification because of the collapse of the fibers pore walls. The tests were all performed until the sample was about to break at around 80% strain. For the reference CNF aerogel, the curve was typical for aerogel prepared from cellulose fibers at a very low concentration of 0.60% and 0.55% in aqueous solution [243]. The main deformation was due to the bending of the fibers and collapsing of the pores, while the compressive strength was provided by the physical cross-linking fibers and hydrogen bonds [238]. When the strain reaches higher values, the micrometer-sized pores were compressed and broken, leading to the densification of the pores resulting in load bearing of the samples. As can be seen from Table 8, the Young's modulus and compressive strength of the reference NCA was very low, reaching only 29.8 kPa. This is attributed to the ultralow density and high porosity and weak cellulose

strength of the cellulose aerogels. The plain silica aerogel shows a very low stress value at low strains, according to silica aerogels prepared by other researchers, which is due to the brittleness of silica aerogel and lack of flexibility that lead to the limitation to reach higher strain [181]. Although differences exist among the accurate stresses of different silica aerogels, the nature of brittleness of the silicon-oxygen bond is widely acknowledged.

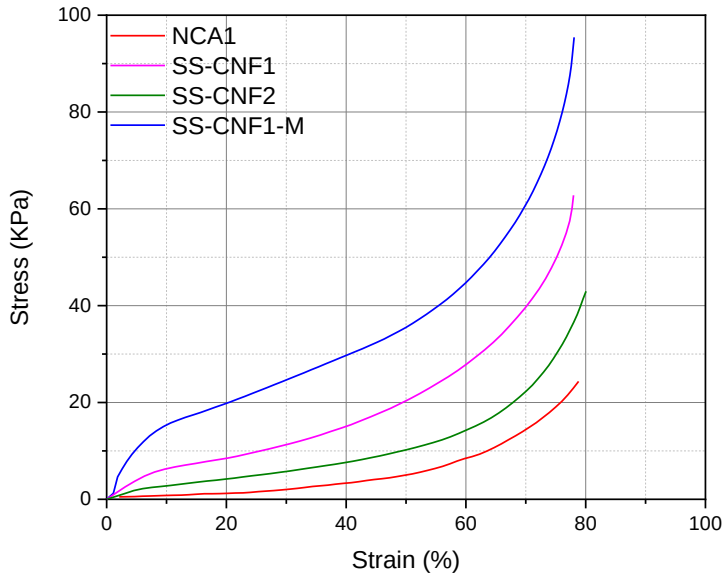

Fig. 6.9. Stress-strain uniaxial compressive curves of SS-CNF1, SS-CNF2, SS-CNF1-M and reference NCA1.

However, cellulose-silica composites aerogels presented a relatively clear improvement in Young's modulus and stress-strain curves, compared to both reference silica aerogel and cellulose aerogel. The fracture stress of SS-CNF1 and SS-CNF2 reached 62.8 and 42.8 KPa, respectively. The improvement in compressive strength was firstly due to the increase in density and decrease in total porosity. As more silica aerogel was impregnated in the pores of cellulose fibers, the density was increased thus also the strength. Another important reason was the covalent bond between cellulose changed to silicon-oxygen bond as seen in FTIR analysis. In fact, the Si-O bond is a very strong bond (452 kJ/mol), however not ductile due to the silicon-oxygen tetrahedron. Therefore, it is interesting to compensate for this shortcoming by combining cellulose fibers which can improve the ductility of the composite materials. At higher strain when the interpore of cellulose fibers is condensed, the impregnated silica can also support the pores from collapsing. Therefore, the SCAs have improved mechanical properties.

After surface modification, the density of SCA further increases and the strength of SS-CNF1-M increases significantly, reaching 95.4 kPa. The synergy of -CH_3 groups with cellulose silica aerogel matrix provides stiffer and more ductile aerogel [246]. The repulsive forces between -CH_3 groups further increase the compressive strength of SCAs. Therefore, surface modification of SCAs can improve the mechanical properties of SCAs significantly.

Table 6.8. Young's modulus *E*, fracture stress σ^* and strain S^* for reference cellulose/silica aerogel and SCAs.

Groups	E (KPa)	σ* (KPa)	S* (%)
NCA	35.3±0.4	29.8±0.1	84.3±0.3
SS-CNF1	80.5±0.2	62.8±0.2	78.0±0.3
SS-CNF2	62.8±0.2	42.8±0.1	84.1±0.1
SS-CNF1-M	122.2±0.3	95.4±0.1	78.1±0.2

6.3.4 Thermal conductivity

The thermal conductivity of SCAs and reference cellulose and silica aerogels are shown in **Table 6.9**. The reference silica aerogels possess thermal conductivities of 0.016-0.018 W/(m·K) at room temperature and pressure, which are known to be super-insulating materials. The reference NCA1 and NCA2 have much higher thermal conductivity of 0.036 W/(m·K) and 0.038 W/(m·K), respectively. Although cellulose aerogel has very low bulk density (~0.01 g/cm^3), they contain numerous micron-sized open pores inside the aerogel, which cannot immobilize the air inside. The silica aerogel, however, has nanometer-sized open pores of around 5~20 nm. These tiny mesopores can immobilize the air movement inside the nanopores. The mean free path of air is 68 nm at ambient pressure and room temperature. Due to the Knudsen effect, the movement of air molecules was restricted and thus the thermal conductivity was significantly decreased and even lower than air [230].

For SS-CNF1 and SS-CNF2, the silica aerogel with lower thermal conductivity filled the micron-sized pores of the cellulose aerogel and covered the surface of the cellulose fibers as well. Thus, the thermal conductivity was reduced to 0.023~0.026 W/(m·K). These results also support the conclusion that the silica component was successfully incorporated into the matrix of cellulose fibers. However, the thermal conductivities of SCA were higher than that of plain silica aerogel. This is due to the remaining macrospores (cannot restrict air movement) inside the composite aerogel which are not fully occupied by silica aerogel and due to the increased density of SCA increases the phonon conduction through the skeleton network of silica and cellulose fibers.

Table 6.9. Thermal conductivities of reference cellulose/silica aerogel and SCAs.

Groups	SS-CNF1	SS-CNF2	SS-CNF1-M	SS-CNF2-M	NCA1	NCA2	SA
Thermal conductivity (W/m·K)	0.026 ±0.001	0.023 ±0.002	0.030 ±0.001	0.029 ±0.001	0.036 ±0.001	0.038 ±0.001	~0.018

There is also a slight difference among these four SCAs samples in terms of thermal insulation properties. SS-CNF1 has the thermal conductivity reaching 0.026 W/(m·K). While for SS-CNF2, this value decreases to 0.023 W/(m·K), most probably because of the difference in bulk density, as shown in Table 8. It is noticed that surface modification increases the thermal

conductivity for both SS-CNF1 and SS-CNF2. The reason can be that more –CH_3 groups are attached to the silica aerogel which can increase the density of silica components in these samples. Also, the pore size of silica was bigger and randomly distributed after modification as discussed in BET analysis. Above all, the thermal conductivity of SCAs can reach a very low value which is desirable in thermal insulation fields. Since the composite aerogel can obtain low thermal conductivity and high thermal stability at the same time, it has the advantage over traditional insulation materials, for instance, styrene foam (0.4 W/(m·K)) and asbestos (0.08 W/(m·K)).

6.3.5 Hydrophobicity

The water contact angle of SCA with surface modification by the TMCS/heptane reagent solution is shown in **Fig. 6.10.** For the original SS-CNF1 and SS-CNF2, the Mill-Q water was immediately absorbed into the matrix due to the hydrophilic nature of the Si-OH bond and also due to the numerous micron-sized pores of hydrophilic cellulose fibers (-CH_2-OH bonds in cellulose), which makes the measurement of the water contact angle impossible. Contrariwise, the water contact angle was very high for both SS-CNF1-M and SS-CNF2-M, reaching an average water contact angle of 137.0° and 140.4°, respectively, indicating their high hydrophobicity. Hydrophobicity was classified by a water contact angle above 90°. In addition, **Fig. 6.10 (c) and (d)** show that the water droplets stand on the surface of cylindrical and cubic composite aerogel without penetration.

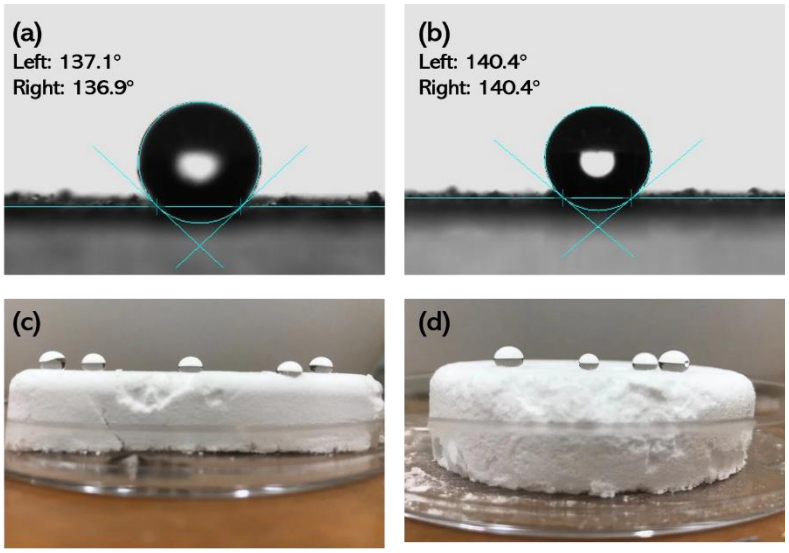

Fig. 6.10. Water contact angle of SCA: (a) SS-CNF1-M (b) SS-CNF1-M and A few drops of water on the surface of SS-CNF1-M and SS-NFC2-M.

The surface modification method is in accordance with other researchers using silane containing materials [247–249]. The high level of hydrophobicity can improve the durability of SCAs applied in the indoor environment because the moisture in the air can constantly penetrate the matrix of hydrophilic SCA leading to the wet-drying shrinkage of silica aerogel or even corruption of the cellulose fibers. The deterioration of the pore structure of SCA can result in significant increase of thermal conductivity, leading to the loss of thermal insulating performance. Therefore, surface silylation treatment can further prolong the service life of SCA.

Also, thanks to its high thermal insulation and thermal stability, it could be an ideal candidate for interlayer thermal insulation material.

6.4. Conclusions

This chapter presents a method to prepare green sodium silicate from olivine silica, a low-cost alternative silica source to impregnate silica aerogel within cellulose matrix. The silica-cellulose aerogel (SCA) shows improved compressive strength (95.4 KPa), high surface area (958 m^2/g) and low thermal conductivity (c.a. 23 mW/(m·K)) compared to plain cellulose aerogel. Moreover, it has an ultralow density (0.055g/cm^3) and high porosity (98%). Based on these results, the following conclusions can be drawn:

- Specific surface area of the SCA reaches c.a. 958 m^2/g for SS-CNF1 and 614 m^2/g for SS-CNF2, compared to pure cellulose aerogel with SSA of 200~300 m^2/g, indicating the sol-gel process of olivine silica derived low modulus silicate can result in higher surface area.
- The compressive strength of SS-CNF1 and hydrophobized SS-CNF1-M increased from 29.8 kPa to 62.8 kPa and 95.4 kPa, respectively, showing the silica-cellulose aerogel has a better mechanical property than plain cellulose aerogel.
- Thermal conductivity of composite silica-cellulose aerogel was significantly lower than pure cellulose aerogel due to the incorporation of fine silica aerogel particles.
- Surface modification by TMCS trimethyl silylation can make SCA composites hydrophobic, with a water contact angle reaching 137.2~140.4°, which will potentially improve durability and thermal insulating performance of SCAs in the relatively high humidity environment.

Chapter 7 MTMS-PDMS aerogel with reinforcement of nano-fibrillated cellulose

This chapter aims at improving the mechanical performance and insulation of a methyltrimethoxysilane (MTMS) and polydimethylsiloxane (PDMS) co-precursor aerogel with the addition of modified nano-fibrils cellulose. A special and facile synthesis route of MTMS-PDMS aerogel was developed and showed promising result. The performance of the modified MTMS aerogel was assessed with acoustic absorption, water contact angle, stress-strain curve and thermal conductivity. Furthermore, the microstructure was analysed by scanning electron microscopy and nitrogen physisorption. It is demonstrated that the mechanical performance and sound absorption of MTMS-PDMS aerogel with modified NFC is dramatically strengthened compared to plain MTMS aerogel. The microstructure shows that the nanoporous structure of MTMS aerogel are interconnected, which contribute to this enhanced acoustic absorption performance and increased mechanical performance.

The chapter is partially from the following article:

Y.X. Chen, R.M.L.M. Dalessi, H.J.H. Brouwers, The development of co-precursor silica-cellulose aerogel via ambient pressure drying (in preparation).

7.1. Introduction

Aerogel is an advanced ultra-lightweight material that can be applied in many fields, especially in thermal insulation and acoustic absorption. However, the application of silica aerogel in thermal insulating materials still faces critical problems, one of which is the brittle nature of silica aerogel itself. Therefore, the mechanical reinforcement of aerogel is desirable, without compromising its insulation properties.

In previous chapter, it is discovered that nano-cellulose fibres can be introduced into the 3D network of silica aerogel during the sol-gel process applying a one-pot synthesis method. Moreover, the composite gel can be dried via freeze drying. However, the freeze drying and supercritical drying methods are more complex and expensive than ambient pressure drying (APD) method. One way to tackle the expensiveness of aerogel is to modify the surface properties of aerogel or change the silica source to make a silica-cellulose gel that can be dried at ambient pressure and temperatures.

Methyltrimethoxysilane (MTMS) as a kind of silicon source, presents exceptional advantage, thanks to the existence of hydrophobic groups in the chemical formula, which are usually employed to synthesize some specific aerogels and can be dried at ambient conditions. Cheng et al. [50] prepared monolithic MTMS based aerogels using water as the only solvent. By controlling the dosage of CTAB, solvent exchange and surface modification were successfully avoided. Rao et al. [250] prepared superhydrophobic silica aerogels using MTMS as a precursor, thus further surface modification was needless. Xu et al. [251,252] successfully obtained low-density MTMS based aerogels in organic solvent via APD, however solvent exchange process still needs to be adjusted. Above all, MTMS is believed to be a promising candidate in preparing aerogel at ambient conditions.

However, the plain MTMS aerogels are still mechanically weak, can be easily explode or break by impact, making it difficult to apply in real applications. Therefore, further mechanical reinforcement in MTMS aerogel is desirable. Another issue is to further increase the hydrophobicity of MTMS aerogel. Although the MTMS aerogel is already a kind of hydrophobic materials, the lesser water it can resist, the better performance it can achieve in hygrothermal performance. Hence, suitable additives should be selected to enhance the hydrophobicity of plain MTMS aerogel.

Polydimethylsiloxane (PDMS) belongs to a group of polymeric organosilicon compounds that are commonly referred to as silicones. PDMS is the most widely used silicon-based organic polymer due to its versatility and properties leading to many applications. The hydrolysis reaction of PDMS works as a base catalysed hydrolysis and follows an Sn2-reaction mechanism [253]. The reaction takes place in a solution with the presence of a strong base such as $NH_3 \cdot H_2O$ or KOH. PDMS itself has an oily character and hardly dissolves in a solution, due to its viscosity and being a long chain of silicon-polymers. It normally ends up absorbing the solvents instead of getting hydrolysed. A way was found to hydrolyse elongated chains of PDMS. It is stated that the hydrolysis of PDMS only affects the monomer at the end of its polymer chain, which in turn results in a long hydrolysis process. Therefore, the pre-hydrolyzed PDMS solution using

KOH is applied as a precursor in MTMS aerogel preparation. Moreover, the alkali solution containing PDMS monomers can be used to catalyse the condensation reaction of MTMS.

Another suitable material is the nano-fibrillated cellulose. Nano-fibrillated cellulose (NFC) is a cellulosic material composed of nano-sized fibrils and has the possibility to form bonds with silanol-groups due to the presence of the high amount of hydroxy-groups it obtains [254]. However, the hydrophilic nature of NFC is unsuitable to be used in MTMS aerogel preparation. Therefore, a further pre-treatment of NFC should be applied to increase the hydrophobicity of NFC to make it successfully incorporated in the MTMS-PDMS aerogel. With a modification of cellulose by maleic anhydride (MA), it can be made into a hydrophobic and flexibility additive for the aerogel [255]. When the partially modified MA-NFC is added to the sol-gel mixture, hydrolysed MTMS or PDMS molecules can react with the leftover hydroxy-groups attached to the modified NFC through a condensation-reaction. Through this reaction an ester-bond will be formed between the NFC and the silanol-group and the material gets incorporated into the overall structure of the sol-gel.

In this chapter, we develop a co-precursor silica aerogel with modified nano-fibrillated cellulose (NFC) in a one-step drying method at ambient temperature and pressure to find optimal processing conditions, suitable agents and materials. Together with the two co-precursors, methyltrimethoxysilane (MTMS) and polydimethylsiloxane (PDMS), the modified cellulose is expected to provide a positive increase in mechanical properties, such as a more compressible and hydrophobic aerogel compared to the plain MTMS aerogel.

7.2. Materials and experiments

7.2.1 Starting materials

Methyltrimethoxysilane (MTMS 98%) and polydimethylsiloxane (PDMS) solution were purchased from Sigma-Aldrich as precursors to prepare MTMS aerogel. A nano-fibrillated cellulose (3.27w/w%)/ water suspension was provided by Sappi-Valida. Dimethylformamide (DMF, Biosolve BV.), maleic-anhydride (MA, Sigma-Aldrich) pyridine, ethanol/acetone (100% pure, VWR chemicals) were used to modify the NFC. Potassium hydroxide (KOH, VWR chemicals), cetyltrimethyl ammonium bromide (CTAB 99%), 5M $NH_3 \cdot H_2O$ (25%, Fischer scientific), 1M HCl (32%, diluted, Fischer scientific) were used to prepare the composite aerogel.

7.2.2 Experimental

7.2.2.1 Maleic anhydride modified nano-fibrillated cellulose

This modification method of NFC is described in [255]. In specific, firstly, 100 g of the NFC water suspension were first solvent exchanged with DMF by three cycles of centrifugation and redispersion. These cycles exist of each 5 minutes at 4000 rpm. After the last centrifugation step, the NFC in DMF suspension was introduced in a 250 ml beaker and 160 ml of DMF was added. This mixture was then thoroughly homogenized for 30 s and after that, the contents were introduced into a three-necked round-bottomed flask equipped, a plug with a condenser with a loose plug on top (so that the gas can escape) and a mechanical stirrer.

After the setup was complete, 19.8 g (0.20 M) of maleic-anhydride and 4.78 g of pyridine were introduced into the three-necked flask and the mixture. After mixing intensively for 3 mins, the solution was heated up to 105 °C, where the reaction can take place for at least 3 hours, under continuous nitrogen flow.

After the previous step was complete, the end-mixture was allowed to cool down whilst still under the nitrogen flow. After the mixture was completely cooled down to room temperature, the modified NFC was washed five times with an ethanol/acetone mixture of 50 ml and 50 ml, respectively, to eliminate any remaining non-bonded chemicals and filter off the dark brown color, and the washing was then repeated multiple in pure ethanol until the material held a yellowish color. Each washing cycle includes a homogenization and centrifugation step.

The final MA-modified NFC concentration in ethanol was to be adjusted to 0.85 ± 0.02% w/w. The success of grafting is confirmed by FTIR spectroscopy with the use of a Parkin-Elmer Frontier, where a broad signal between 1750 and 1690 cm^{-1} was appeared, corresponding to the carbonyl stretching vibrations of the ester formed (C-O-C) and the acid terminal function are visible as shown in the below **Fig. 7.1**.

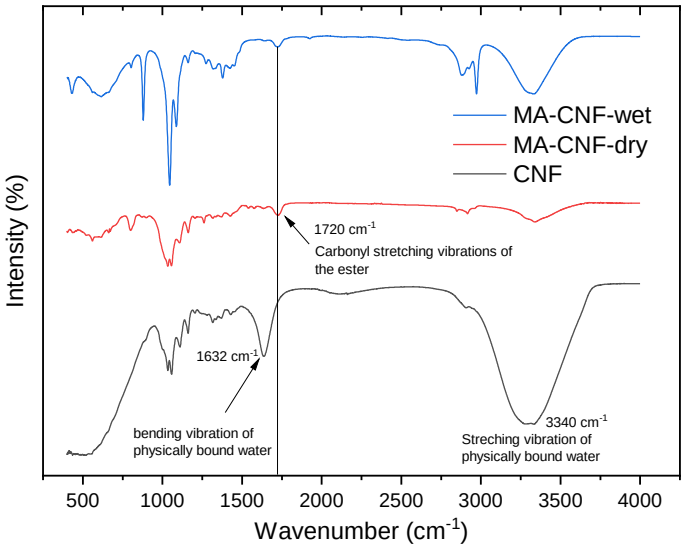

Fig. 7.1. FTIR spectrum of NFC modified with MA.

7.2.2.2 Co-precursor 2-solvent MTMS-PDMS aerogel

7.2.2.2.1 Pre-hydrolysed PDMS

Firstly, 90 ml of ethanol and 10 ml of 1.5M KOH solution were mixed into a 200 ml beaker to give a 90:10 ratio alcohol/water solution. Herein 0.2 ml of PDMS solution was added and the temperature was raised to 70 °C. This mixture was mixed at 500 rpm for 24 hours. The next day the PDMS was completely dissolved (depolymerized and hydrolyzed) in solution and cooled down to room temperature. After that, 50 ml of demi-water was slowly added to reach a EtOH : H_2O ratio of 60:40. The pre-hydrolyzed PDMS was ready for use.

7.2.2.2.2. Pre-hydrolysed MTMS

Ethanol and water were mixed in a beaker as co-solvents, consisting of a 60:40 volume ratio and in a total volume of 100 ml. After that, 0.25 gram of CTAB as surfactant and 50 ml MTMS

solution as the co-precursor were added. The total mixture was continuously mixed with a magnetic stirred at 200 rpm. During mixing, 10 ml of 1M HCl was added to the mixture and then the total solution was kept in a 45 ℃ oil bath for hydrolysis for 45 min. The pre-hydrolyzed MTMS was ready for use.

7.2.2.2.3. Preparation of MTMS-PDMS aerogel with modified NFC

Afterwards, the 150 ml of the base solvent-phase consisting of pre-hydrolysed PDMS solution was slowly added to the mixture. During the mixing process, the solution was vigorously stirred at 400 rpm and the pH was continuously checked whether it had reached the required pH of 8.5/9. If there is need for adjustments, droplets of either 1.5M KOH or 1M HCl are added if the pH is too low/high. After adding both phases together, 2.5 ml of MA-modified NFC was added to the mixture and vigorously stirred for 30 seconds till homogenous. After that, the mixture was added into the desired moulds for specific tests.

After the samples were covered with lids, they were placed in a preheated oven for 4 hours at 60 ℃ to start the gelation process in a sealing system. After 4 hours, the aged gels were retrieved from the oven. As the last step in this procedure, the wet gels were dried at the thresholds of 80 ℃ for 2 hours, 100 ℃ for 2 hours and 1 hour at 120 ℃. After drying, the aerogel was prepared. During this project, the decision was made to only vary the amounts of NFC, PDMS and CTAB used. The schematic illustration of the preparation process was shown in **Fig. 7.2**. The morphology of the prepared aerogel is shown in **Fig. 7.3**.

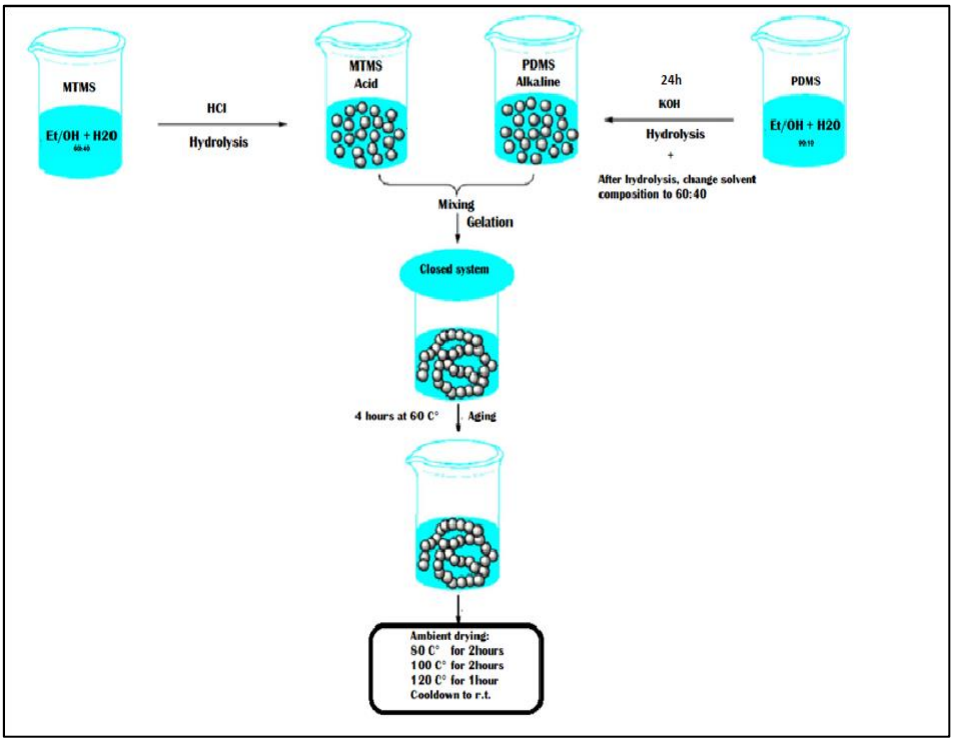

Fig. 7.2. The schematic illustration of the co-precursor MTMS-PDMS process and condensation-reaction between MA-modified NFC and hydrolyzed MTMS/PDMS.

7.2.2.3. Plain MTMS aerogel preparation

Firstly, ethanol and demi-water were mixed in a beaker as co-solvents, consisting of a 60:40 ratio and a total of 250 ml. Herein after 0.20 grams of CTAB as surfactant and 10 ml of MTMS

as precursor were added per 50 ml of mixed solution, i.e. 1.0 gram of CTAB and 50 ml of MTMS respectively. The total mixture was continuously mixed with a magnetic stirrer at 200 rpm.

During the mixing process, 5 ml of 1M HCL was added to the mixture and then the overall solution was kept in a 45 ℃ silicon oil bath for hydrolysis. After around 45 mins of sufficient hydrolyzation, 5 ml 5M $NH_3 \cdot H_2O$ was added to start the condensation reaction and reached the required pH of around 8.5/9 for the optimal gelation process. After around 2 minutes of high-speed stirring, the mixture was added into the desired silicone moulds (squares, circles, or cylinder) covered with a silicone lid, or self-made lid (aluminum foil) and placed in a preheated oven for 4 hours at 60 ℃ to start the gelation process. After 4 hours of aging, these aged samples were dried at the thresholds of 80 ℃ for 2h, 100 ℃ for 2h and 120 ℃ for 1h. The drying process was carried out in an oven (Memmert UF160 plus).

Fig.7.3. Morphology of the prepared MTMS-PDMS aerogel.

7.2.3 Characterization

7.2.3.1 SEM

To determine and visualize the pore size, pore size distribution and the 3d-network created in the developed aerogels, pictures were made with the use of the Phenom Pro-X. The samples were gold-plated, which was done with the gold-sputter machine Quorum Q 150T plus, in order to prevent charging of the sample with the electron beam of the SEM. The particle sizes of each batch were calculated via Image J.

7.2.3.2 Thermal conductivity test

To determine the thermal conductivity of the developed MTMS aerogel, the ISOMET model 2104 was used. This apparatus is a heat transfer analyser, meaning it has a multifunction of measurements for; Thermal conductivity (λ in ($W/m \cdot K$)), thermal diffusivity (a in ($m^2 \cdot s$)), heat capacity (c_p in ($J/m^3 \cdot K$)) and temperature (K). The measurement is based on the analysis of the temperature response of the analysed material to heat flow impulses. Heat flow is excited by electrical heating of the resistor heater inserted into the probe which is in direct heat contact with the tested material. Evaluation of thermal conductivity and heat capacity is based on periodically sampled temperature records as function against time, provided that heat

propagations occur in unlimited medium. A final value is taken based from the average of the number of samples that were tested in the particular batch.

7.2.3.3 Acoustic absorption test

To determine the sound absorption coefficient, the impedance tube method was used. In brief, the measurement principle is through generating a plane wave by a loudspeaker on the one side of the tube that is then spreading through the tube before reflecting by the aerogel. The aerogel changes the reflected wave and by collecting the generated standing wave, the sound absorption coefficient of the samples can be determined. The wave is than measured at six different locations in the tube. This was done to increase the accuracy as described in the measurement protocol for the impedance tube. The sample is inserted at the end of the impedance tube and backed by a rigid surface and the sound absorption. The sound absorption coefficient is a function of frequency, and measurements over the frequency range of interest are required, which in this projects case is up to 2500 Hz. The aerogel samples that will be measured need to have a diameter of 40 mm in width and need to have a thickness of 10 to 15 mm. This measurement has to be done over the total frequency spectrum of 0 to 2500 Hz and was done with a simulation.

7.3.3.4 Nitrogen physisorption test

To determine the surface area of the aerogel samples, the Micromeritics Tristar II plus was used. This specific test was used to compare and analyses the surface area and the pore size distribution of different prepared aerogels. With this specific test, the effect of aging on the MTMS aerogel can also be tested. The surface area was calculated via the use of the BET equation and the pore size distribution was calculated according to BJH theory.

7.3.3.5 Compression/stress-strain test

To determine the compressive strength and stress-strain character of the aerogels, a compression-test can be applied with the use of an Instron 5967. With the use of this mechanical apparatus, a material's behavior under applied pressures/force can be measured and determined.

7.3.3.6 Water contact angle test

To determine the hydrophobic character of the prepared aerogel, the water contact angle test was used. Together with the measuring-system, the materials repellent character to that specific solvent can be determined by measuring the angle in which the droplet is placed. The higher the water contact angle of the aerogel, the higher the hydrophobicity of the overall material is. Measure each sample on 4 places, to get an average WCA of the sample.

7.3.3.7 Sample density and porosity

The density (ρ) of the material was calculated via the total sample mass being divided its by total volume. After the volume of aerogel was calculated, the sample was weighed on an analytical balance from Mettler Toledo ML. If these void spaces are filled with air, which is the case with silica aerogel, the following form can be used. Here the only required data is the density of the bulk of the sample, and the density of the silica-particle which is approximately 2.65 g/cm^3.

7.3. Results and discussions

7.3.1 Microstructure analysis

7.3.1.1 SEM observation

The SEM pictures of MTMS-PDMS aerogels are shown in **Fig. 7.4**. The purpose of the analysis of the SEM made from the aerogel samples is to check if the particle structures from all different samples have a mono-shape size and are evenly distributed and have a proper formed 3D-network of silica. The other expectation is that the modified cellulose that was added is nicely incorporated into the overall 3D-network. It's also hypothesized that over the longer period of aging, a process called Oswald ripening will occur.

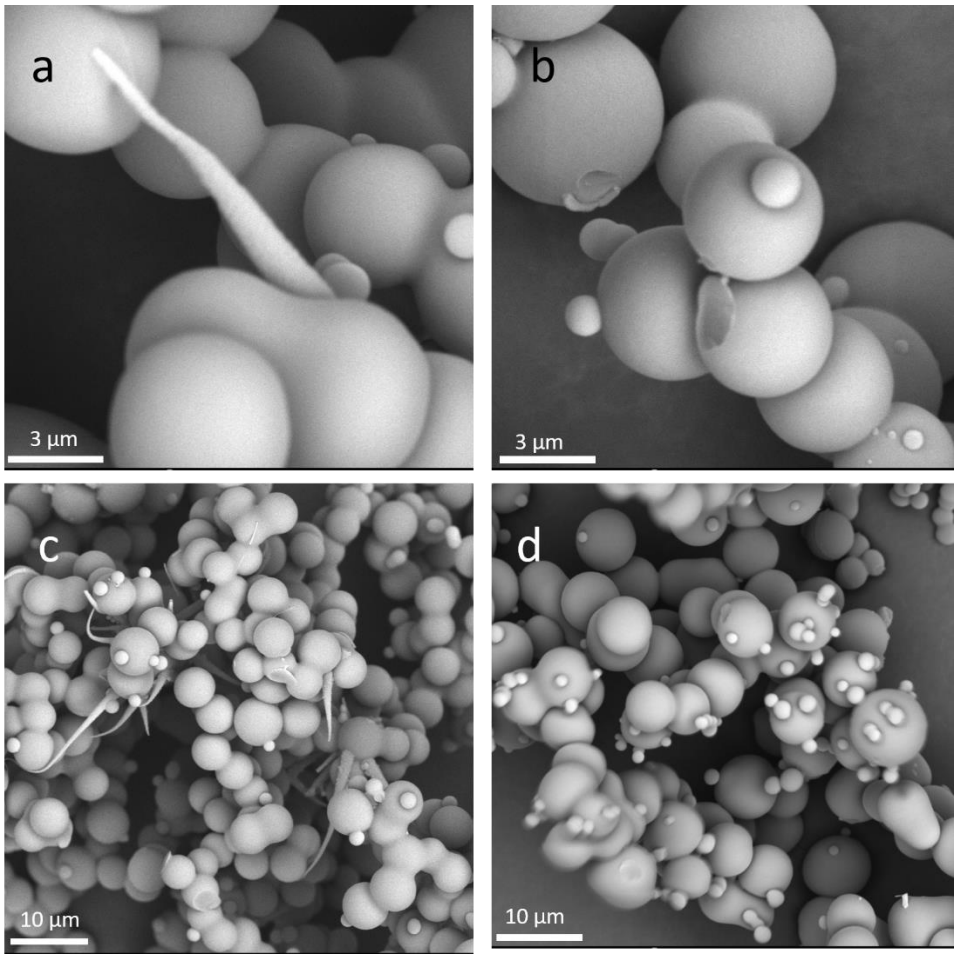

Fig. 7.4. SEM of MTMS-PDMS silica aerogel with modified nano-fibrillated cellulose (a) resolution of ×18000 with NFC (b) ×15000 without NFC (c) ×4000 with NFC (d) ×5000 without NFC.

The overall results from the pictures in **Fig. 7.4**. show a well-formed 3D-network and have a particle-size of around 2-5 µm in diameter. This large particle size of silica aerogel can be linked to the strong base conditions during condensation of silica gel. From the pictures of the samples in which the modified NFC was added, it can be observed that the modified NFC was properly incorporated in the material, being attached to particles instead of being packed.

Another observation from SEM picture is that the addition of PDMS in the MTMS aerogel could result in formation of smaller silica particles on the surface of bigger silica particles. This phenomenon is related to the different formation mechanism of different silicate precursor under base catalyst condensation process. This multi-shape structure could lead to different properties and performances in mechanical and surface area of co-precursor silica aerogel.

Aging could also influence the particle size of silica aerogel. As can be observed from the 3 pictures, **Fig. 7.5. (a)** is 1d aging co-precursor aerogel, where the particles are completely separate from one another but still have a very refined structure. They are interconnected and have a well-formed 3D-network. The middle picture, **Fig. 7.5. (b)** shows that the particles in the 3D-structure slowly start to fuse together. This is due to the fact that the material has more time to react/crosslink. This phenomenon is also discussed in the theory and is called Oswald ripening. The small amounts of residual KOH-salts are occasionally visible as small white crystals.

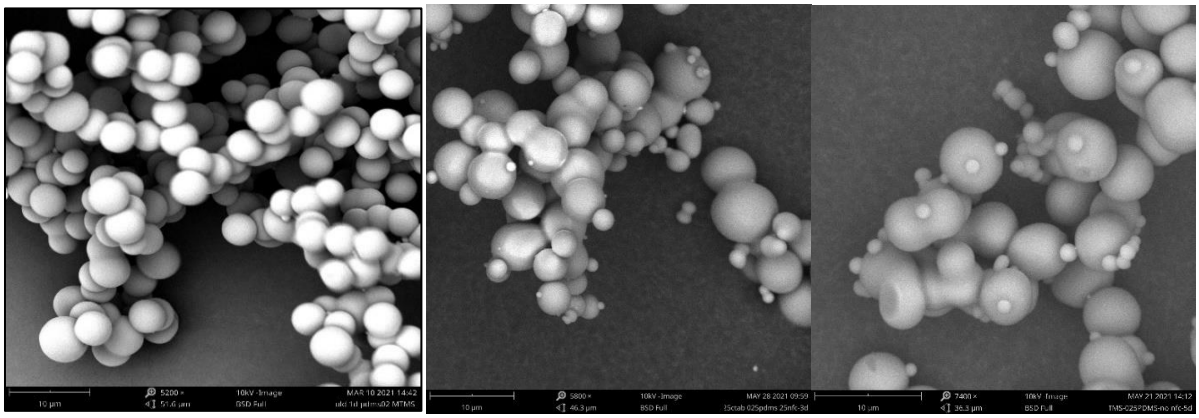

(a) (b) (c)

Fig. 7.5. SEM of the prepared silica aerogel (a) 1 day (b) 3 days (c) 5 days.

In **Fig. 7.5. (c)**, in the 5 days sample, as was hypothesized, the process of crosslinking/particle-fusion is clearly visible. The picture show that the particles are almost completely fused with one another it strengthens the material, but at the cost of the small particle sizes and increases the pore sizes. This results in the weakening of some of the overall mechanical properties of the material, such as thermal conductivity, flexibility and overall contact angle, but also strengthens some of them due to the crosslinking, which results in higher stress/strain resistance.

After the use of the program Image J, the particle size distribution (PSD) in each of the samples has been measured. Via this program, a graph has been composed of the average particle size distribution in each of the aged batches. As can be observed from the **Fig. 7.6**. is that average size of the particles is 3.88 µm in the 1 day aged samples, 4.55 µm at 3 days aged samples and 4.84 µm in the 5 days aged samples. From observing these graphs and values, it can be concluded that the average particle diameter increases after the samples being exposed to a longer aging process. It is indicated that the longer aged samples show lesser amounts of the smaller sized particles, while bigger particles are formed. These particles are also more uniform and have a better relative fraction distribution. This is in accordance with the particle fusion explained from the Oswald ripening theory.

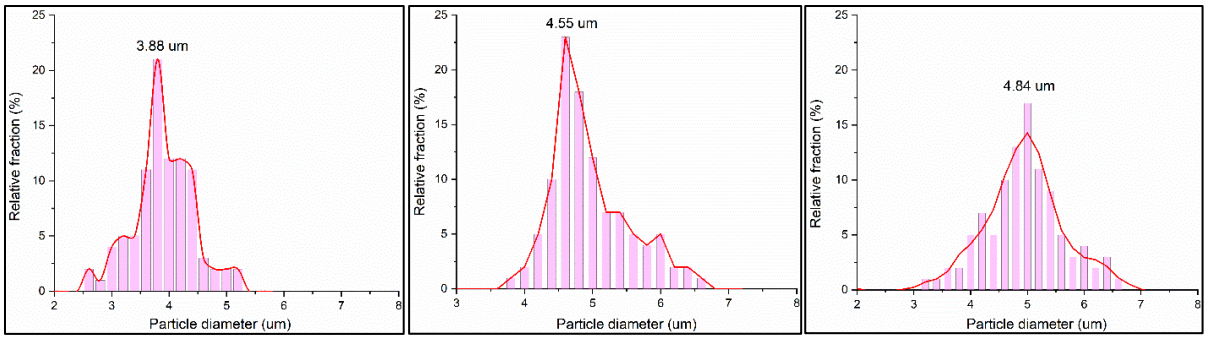

(a) (b) (c)

Fig. 7.6. Particle size distribution of the prepared silica aerogel (a) 1d (b) 3d (c) 5d.

7.3.1.2 Nitrogen physisorption results

The nitrogen physisorption isotherm and pore size distribution of the MTMS-PDMS aerogel is presented in **Fig. 7.7. (a)** and (**b**). Through data-analysis, it is shown that the plain MTMS aerogel has a lower surface area of 254.6 m^2/g. While the newly developed MTMS-PDMS aerogel obtains a surface area of 302.2 m^2/g, indicating the incorporation of PDMS could have a positive effect on the surface area. The phenomenon could be due to the smaller secondary silica particles attached on the surface of the MTMS formed silica, resulting in an increase in surface area of the aerogel. This can be observed from the SEM images. Further, the use of PDMS co-precursor and CTAB as a surfactant exemplifies that the modification of the standard MTMS aerogel with the PDMS/CTAB has a positive effect on the overall surface area of aerogel.

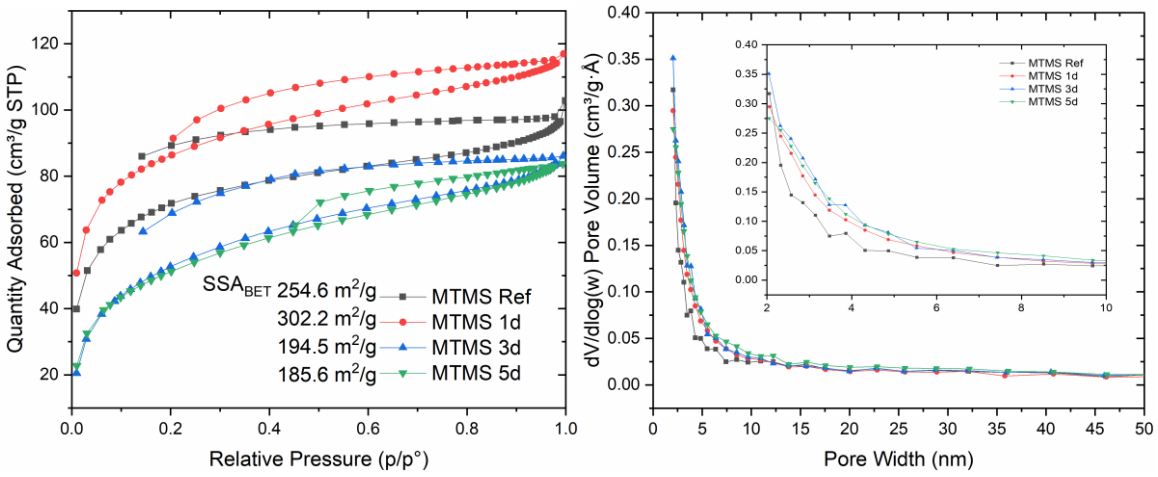

Fig. 7.7. (a) Sorption isotherm and **(b)** pore size distribution of MTMS-PDMS aerogel.

When the aging time increase to 3 days, the surface area decreases to 194 m^2/g. This can be due to the fact that the chemical reactions in the aerogels had a longer reaction time, in which small primary particles in the secondary particles react with one another and formed larger secondary silica particles, as well as a stronger 3D-network, which can be related to the Oswald ripening theory. The 5 days aged samples drop slightly in surface area to 185 m^2/g. This is due to the particle fusion reaction that has happened longer over the course of 5 days. This reaction will have high reaction rate in the beginning but will slow down overtime due to the cross-

linking as a result. This result in a slower drop of surface area in between 3-5 days, than it was in 1-3 days, which was visible in the SEM pictures and particle size distribution.

It is also observed from the isotherm of the aerogels that a large amount of micropores (0-2 nm) are detected at the very beginning of the isotherm (where there exists an exponential increase at $p/p_0=0$), which cannot be measured by the nitrogen adsorption test. As can be observed in **Fig. 7.7 (b)**, the pore size is mainly accumulated in the range of 2-10 nm, which means numerous numbers of pores are inside the micron-sized secondary silica particles. The reference MTMS aerogel presented the lowest number of pores during this range, while with the increasing aging time, the nanometer pores become larger. This is due to the Oswald ripening and particle fusion as well.

7.3.2 Insulation performance

7.3.2.1 Acoustic absorption

The acoustic absorption result of the MTMS-PDMS aerogel samples with the use of the impedance tube method are displayed in **Fig. 7.8**. Form the data, it is displayed that the addition of PDMS together with NFC has an increased sound absorption coefficient for aerogel. This is indicated from the higher maximum absorption coefficient of MTMS-PDMS aerogel of 0.77 at 1062 Hz, compared to the MTMS aerogel, whose maximum absorption coefficient is 0.68 at a frequency of 909 Hz. Furthermore, with the addition of modified NFC in the aerogel structure, the maximum sound absorption coefficient increased to 0.86 at a frequency of 1308 Hz. The addition of PDMS forms a number of smaller silica particles, function as linking particles in the bigger particles. This two-level particle size can lead to a higher acoustic absorption due to the different pore size. Also, the micropores in the secondary silica particles starts to increase when PDMS added in the aerogel, increasing the nanopores inside and thus the sound wave could enter multi-scale spaces in the aerogel, lose much more energy and fiction happens and transform into heat. The modified NFC incorporated in the microstructure could further increase the sound absorption. This can be attributed to the vibration of fibers during the sound absorption test, which also contribute to the sound energy losses.

The acoustic absorption result displayed in **Fig. 7.8.(b)** shows that the aging process leads to a steady slight increase in sound absorption, up until the 3 days of aging with a maximum of 0.77 of sound absorption coefficient. The results of the 5 days aging show that the material starts to increase in sound absorption slightly, which correlates to the microstructure of aerogel, indicated by the SEM and particle size distribution of aerogel. The inter-particle pores of the 5 days aging aerogel are relatively larger than the aerogels with the 1d and 3d aged samples due to the fusion of the particles (Oswald ripening) where gas molecules and sound have a better possibility to travel through the material due to the increased pore size.

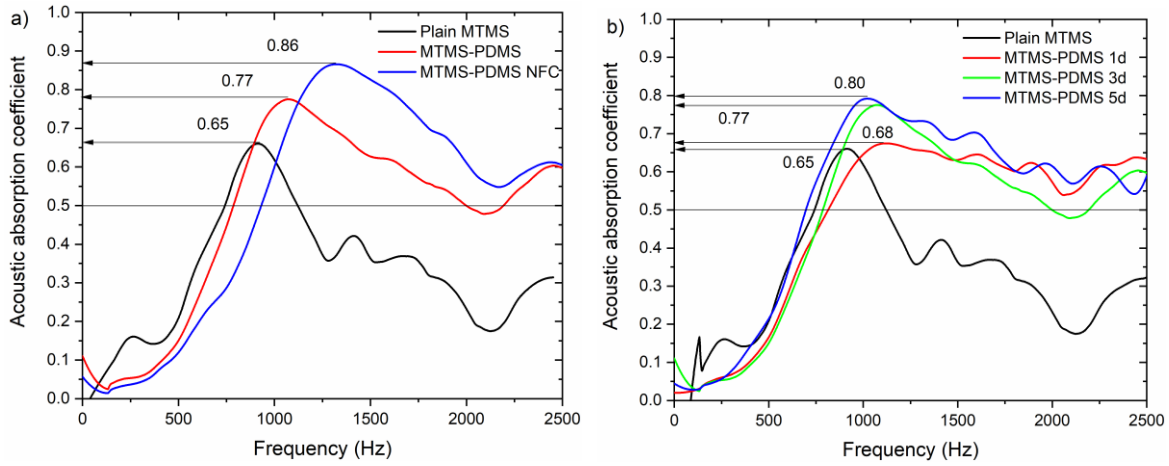

Fig. 7.8. Sound absorption performance of MTMS-PDMS aerogel (a) NFC factor (b) Aging factor.

Table 7.1. Sound absorption average of MTMS based aerogel.

Sample	MTMS aerogel	MTMS-PDMS aerogel 1d	MTMS-PDMS aerogel 3d	MTMS-PDMS aerogel 5d	MTMS-PDMS-NFC aerogel 1d
SAA	0.334	0.488	0.494	0.538	0.516

7.3.2.2 Thermal conductivity

Thermal conductivities of prepared MTMS-PDMS aerogels are shown in **Table 7.2**. The plain MTMS aerogel shows the thermal conductivity of 0.0404 (W/m·K), which is similar to the MTMS aerogel prepared in another research, which is stated as 0.037±0.005 (W/m·K) [256]. It is shown that there is a 5.1% increase of the thermal conductivity from the MTMS-PDMS-NFC aerogel to 0.0425 W/(m·K). This is the result of the addition of PDMS and the change in the sol-gel method. The number of additives also influence the thermal conductivity. The addition of increased amounts of the maleic anhydride modified NFC, shows a small but steady increase of the thermal conductivity of aerogels. This increase of the thermal conductivity was expected, since the thermal conductivity of NFC is higher than the thermal conductivity of silica aerogel, results in an increase in the overall thermal conductivity.

From the results between the 1 day, 3 days and 5 days aging samples, there is also a visible but expected pattern. During the longer aging times, the 3d-network could crosslink, which is attributed to the Oswald ripening. Aerogel particles start to fuse with each other, which leads to a decrease in surface area and an increase in pore size. Due to the increase in pore-size, the value of the Knudsen diffusion rises, increasing the free path of gas molecules and increasing the chances that these molecules transfer the individual heat through collision instead of their mean free path.

Overall, the thermal conductivity of MTMS-PDMS aerogel slightly increase and very similar to the plain MTMS aerogel. Therefore, the PDMS and modified NFC should only have a limited effect on thermal insulation of MTMS based aerogel.

Table 7.2. Thermal conductivity of prepared MTMS-PDMS aerogels.

Sample Name	Av. λ (W/m·K)	Increase TC in %
Plain MTMS	0.0404	0
MTMS-PDMS 1d	0.0419	3.7
MTMS-PDMS-NFC 1d	0.0425	5.1
MTMS-PDMS 3d	0.0416	3.0
MTMS-PDMS-NFC 3d	0.0429	6.2
MTMS-PDMS 5d	0.0445	10.1
MTMS-PDMS-NFC 5d	0.0413	2.2

7.3.3 Mechanical performance and hydrophobicity

7.3.3.1 Compression/stress strain results

Data analysis of the stress-strain test of MTMS-PDMS aerogel with the use of the Instron are depicted in **Fig. 7.9**. The results displayed in **Fig. 7.9. (a)** shows that the increasing addition of PDMS concentration in MTMS aerogel has a strong positive effect on the maximum amount of stress the material can hold. The compressive strength of 0.25% PDMS concentration in MTMS is the lowest among the three aerogels, reaching 17 kPa at a strain of 38%. However, it is larger than the plain MTMS aerogel, whose strength is only 12 kPa at strain of 31%. Therefore, even with a slight PDMS in the MTMS aerogel can still result in a higher strength. When the concentration of MTMS increases to 2% in MTMS solution, the strength continues the increasing trend, reaching 26 kPa at a strain of 24%. However, the flexibility of the aerogel seems decrease due to the moderate addition of PDMS, i.e. the maximum strain the aerogel can hold is reduced. The 4% PDMS in MTMS can also increase the strength further to 36 kPa. However, the strain it can hold decreases to 28%, which is the same trend as 2% PDMS, showing a reduction in flexibility. Therefore, the co-precursor MTMS-PDMS aerogel result in a higher compressive strength while could decrease the flexibility.

Aging to a maximum of 3 days also increases the materials maximum strength to around 37 kPa and shows a more compressive character to the material. This increase in stress/strain is also linked to the aging time, where the material during aging continues to crosslink and react with its 3D network. By doing this, it results in a higher stress resistance of the developed aerogel. The same mechanism applies to the 5 days aging aerogel, presenting a compressive strength of 30 kPa at a strain of 27%. As observed from **Fig. 7.9. (b)**, the increase in strength of the 5-day aging aerogel is lower than the 3-day aging sample, which could be a reason of the excessive cross-linking of the 3D network of the silica particles. Therefore, in this study, the optimal condition of aging is 3-day, that can reach the best mechanical property of MTMS aerogel.

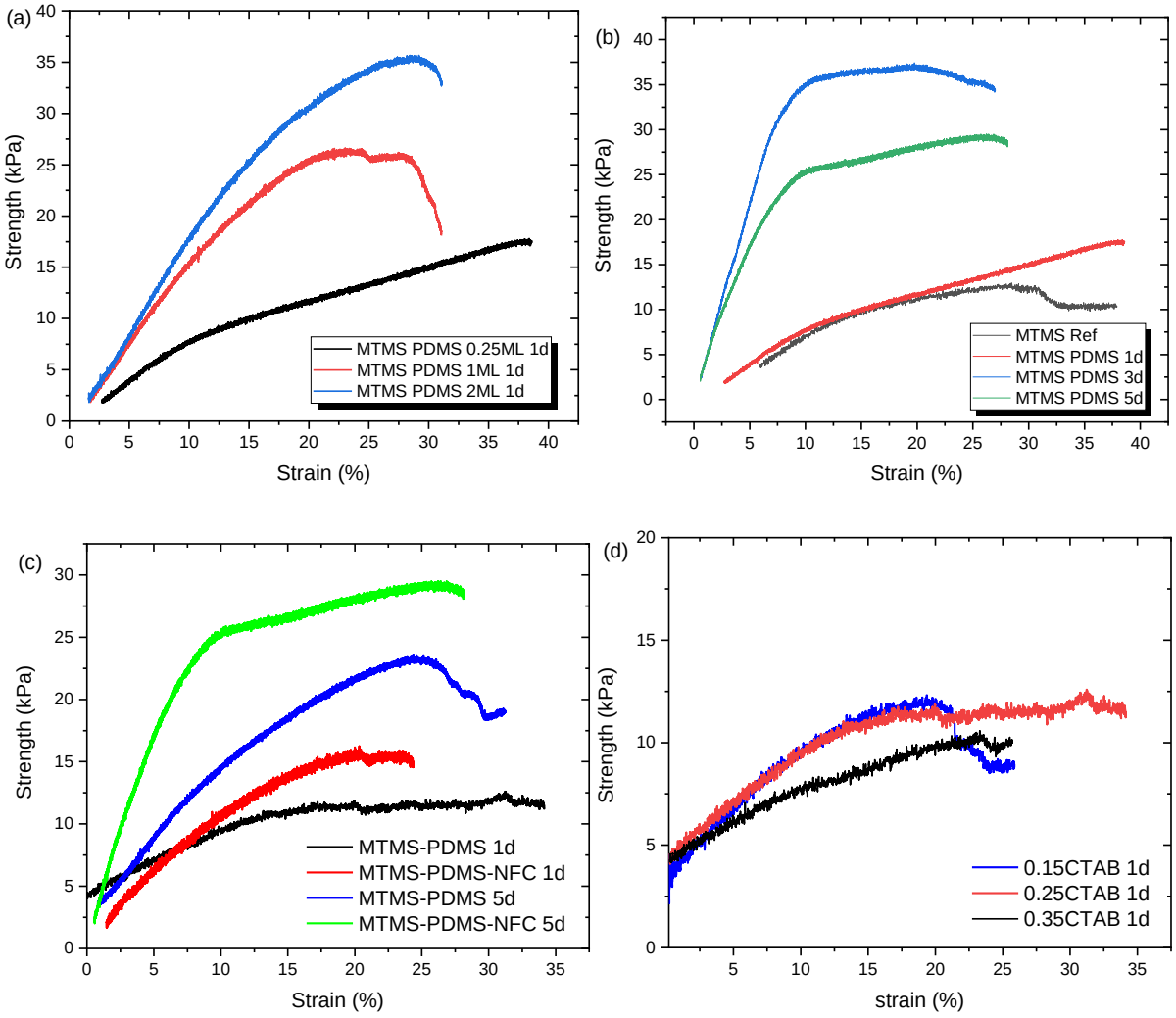

Fig. 7.9. The stress-strain curve of MTMS-PDMS aerogel: **(a)** factor of PDMS concentration **(b)** factor of aging time **(c)** factor of NFC **(d)** factor of Cetrimonium bromide (CTAB).

The effect of addition of NFC in MTMS aerogel strength is displayed in **Fig. 7.9. (c)**. The results from the stress-strain curve show that the 2.5 ml NFC can both increase the compressive strength of MTMS-PDMS aerogel at the age of 1 day and 5 days. However, the NFC incorporated into the MTMS aerogel does not increase the flexibility to the aerogel, as can be observed from the less strain the aerogel can handle. The reason may be is that the NFC is a nanosized fibre, which is too short to have a bridging effect on the mitigation of the crack formation. Nevertheless, the NFC addition does have a slight increase in strength, which may due to the higher degree of cross-linking in the 3D-network in silica particles, that fill in the voids or inter-particles, which can be observed in SEM analysis.

Different amounts of surfactant also show a decrease or increase in strain and maximum amount of stress the material can handle, and its effects are displayed in **Fig. 7.9 (d)**. The samples with 0.15 g and 0.35 g of CTAB show lower stress and the maximum strain, whereas the 0.25 g CTAB gives the best compressive strength. This reason of the problem is the addition of surfactant, that too much or too less of surfactant can negatively influence the mechanical strength of aerogel. Explained in the theory, it was speculated that the amount of surfactant used can positively or negatively impact the material by disrupting or promoting cross-linking.

Therefore, in this study, the 0.25 g CTAB is the optimal amount of surfactant used in the MTMS-PDMS aerogel synthesis.

7.3.3.2 Water contact angle (WCA)

The average water contact angle of the prepared samples was calculated and displayed in **Table 7.3**. It is shown that the plain MTMS aerogel had an average WCA of 136.1°. The results from the co-precursor MTMS-PDMS aerogel clearly shows that the addition of PDMS has a positive effect on the increase of the hydrophobic character of aerogel. Here the increase from the MTMS aerogel to MTMS-PDMS aerogel is around 3% to reach a WCA of 140.6°,

Further, comparing the data from the aerogel samples with modified NFC, it can be observed that the addition of modified NFC shows an increase of the WCA as well. It is shown that there is an increase of WCA from MTMS-PDMS to a contact angle of 142.9° of the sample with 2.5 ml NFC. This is a slight increase of 2.5° or 2% in the WCA. This shows that the addition of this water-repellent MA modified NFC and the addition of PDMS have positive effect on the hydrophobicity of developed aerogel samples.

Table 7.3 Water contact angle of MTMS-PDMS aerogel.

Sample name	Average WCA (degrees)	% increase
Plain MTMS aerogel	136.1	-
MTMS-PDMS 1d	140.6	3%
MTMS-PDMS-NFC 1d	142.9	5%
MTMS-PDMS 3d	142.9	5%
MTMS-PDMS-NFC 3d	144.7	6%
MTMS-PDMS 5d	138.3	2%
MTMS-PDMS-NFC 5d	141.7	4%

The results also show that aging has a significant influence on the WCA of the material. The results show that there is a steady increase in the WCA the longer the material is aged, up to 3 days aging, where the increase of the WCA is around 8.6° or 6%. After this point, the hydrophobic character of the material is decreasing and this can be linked due to the particle-fusion effect that is visible in the same pictures of the 5 days aging SEM-pictures, which is Oswald ripening and it decreases surface area and increases pore-size.

These molecular interactions of the surface depends on the amount of dimethylsilyl or trimethylsilyl (SiR_2 $(CH_3)_2$ and $SiR(CH_3)_3$ groups present on the surface. If the surface still has some unreacted hydroxy-groups, the water droplet has a lower WCA due to the formation of water-bridges. Over the course of the aging process, these OH-groups slowly react due to intermolecular crosslinking leading to less OH- left for the water to bond with. This overall increases the WCA of the surface. Up until a point in the aging process, the Oswald ripening will happen. Here the formed particles will start to fuse, creating bigger pores and this in turn lowers the WCA. Due to these two processes being active during the aging time, it is observed

in the results that the 3 days aged samples have the highest WCA. This is because of the more uniform particle size as shown in section 3.1.1 and sufficient enough of the di and trimethylsilyl groups that the water droplet won't react with the intermolecular OH-groups.

7.3.4 Density and porosity measurement results

The density and porosity of the prepared aerogels are shown in **Table 7.4**. With the addition of both NFC and PDMS, it is observed that there is an increase in overall density. This is due to the high molecular weight of NFC and the influence of the CH_3 groups on the PDMS. The overall increase and decrease in density can be linked back to the times of aging. Here the crosslinking and Oswald ripening have a large effect on the overall end product and shrinkage. It is observed that the material with the longer aging time is less prone to shrinkage, which in turn decreases the overall density.

Table 7.4. Results of the density and porosity measurements.

Sample name	Average density (g/cm^3)	Porosity (%)
MTMS reference material	0.084	96.8
MTMS-PDMS 1d	0.101	96.2
MTMS-PDMS-NFC 1d	0.109	95.9
MTMS-PDMS 3d	0.097	96.3
MTMS-PDMS-NFC 3d	0.092	96.5
MTMS-PDMS 5d	0.101	96.1
MTMS-PDMS-NFC 5d	0.094	96.5

7.4. Conclusions

The goal of this chapter is to develop a co-precursor MTMS-PDMS aerogel with modified nano-fibrillated cellulose (NFC) in a one-step drying method at ambient temperature and pressure to find optimal processing conditions. Together with the MTMS, PDMS, the modified NFC the newly developed aerogels should have a positive increase in performances, such as acoustic absorptive, mechanically stronger and hydrophobic property compared to the plain MTMS aerogel. The following conclusions can be drawn:

- SEM images show that the modified NFC is completely incorporated in the aerogel structure. The 3D-network and cross-linking level of co-precursor aerogel can be perfectly observed. Interestingly, there exists a two-stage silica particle of size around 0.5-1 um and 3-5 um. The particle size distribution of the developed aerogels shows the average particle size of 3.88 µm at 1 day, 4.55 µm at 3 days and 4.84 µm at 5 days.
- The surface area of plain MTMS aerogel is 254.6 m^2/g, while the addition of PDMS increases the surface area to 302.2 m^2/g. When the aging time prolonged to 3 days, the surface area decreases to 194 m^2/g, and the 5 days aging aerogel reaches a surface area of 185 m^2/g.

- The density of the modified aerogels has been increased from 0.0844 g/cm^3 to 0.1066 g/cm^3 with the addition of PDMS and NFC.
- The maximum sound absorption coefficient increased from 0.68 to 0.88 with the addition of modified NFC. While the aging process increase the sound absorption from 0.65 as a reference to 0.68 at 1 day, 0.77 at 3 days and 0.80 at 5 days. The result show that both the NFC and aging have a positive effect on sound absorption.
- The co-precursor MTMS-PDMS aerogel obtains a higher WCA of 143°, which increases to 145° after 3 days of aging. The effect of aging, introduction of CH_3 from PDMS and addition of the NFC has a substantial impact on the hydrophobicity of the aerogels and surface property.
- The addition of PDMS and modified NFC in co-precursor aerogel increase the stress of aerogel can handle. However, the PDMS and NFC could not increase the flexibility of the aerogel.
- The shortcoming of the novel synthesis method and modification is that there is a slight increase in the overall thermal conductivity, which is due to the addition of both the PDMS and the maleic anhydride modified NFC.

The co-precursor method invented in this project is a promising way to incorporate silanes into silica aerogels. The alkali which is normally used as a base catalyst can be used as a carrier in the synthesis of co-precursor silica aerogel. Hence it opens up another possibility to add pre-hydrolysed silanes in the silica precursors.

Chapter 8 Effect of silica aerogel on thermal insulation and acoustic absorption of geopolymer foam render: Towards the role of different particle sizes

This chapter investigates the application of silica aerogel in building materials. High-performance insulating materials are in dire need due to the increasing demand in sustainability and energy saving of buildings, as well as a comfortable living environment. Silica aerogel is a kind of high porosity material, featuring super thermal insulating and sound absorption. Geopolymer foam render (GFR) is a recent invented lightweight mortar, obtaining high porosity, insulation properties and fire resistance. However, the heat transfer and sound propagation in GFR is rarely investigated. In this study, four kinds of silica aerogels with different particle sizes are applied in GFR as an insulative additive to improve the hygrothermal and acoustic absorption. The effect of the dosage and particle size of silica aerogel on the insulation performance is systematically studied. The optimized geopolymer foam aerogel render (GFAR) has a thermal conductivity of 0.143 W/(m· K) and a noise reduction coefficient (NRC) of 0.50. The microstructure of GFAR was investigated in-depth with the use of micro-CT, scanning electron microscope, optical microscope and UPV test. The mechanism of the improved performance of GFAR with silica aerogel is explained. The result of this study is essential to enlighten the development of a geopolymer foam render with a low dosage of silica aerogel for the building sector.

This chapter is partially from the following article:

Y.X. Chen, K.M. Klima, K. Schollbach, Qingliang Yu, H.J.H. Brouwers, Effect of silica aerogel on thermal and acoustic insulation of geopolymer foam concrete: Towards the role of different particle sizes (in preparation).

8.1. Introduction

The energy-saving of building sector and the comfort of the indoor living environment have been received rising attention due to the increasing awareness of sustainability and the quality of life [4,257]. The building industry are responsible for almost 40% of the total energy in some developed countries and the CO_2 emission [258]. Therefore, the motivation for developing high-performance insulating materials is strong. For now, many countries have already initiated policies to decrease heat loss through building shells [259]. Moreover, the functionalization of the insulation materials is also very important, for instance, the acoustic absorption property to improve the quietness of the indoor environment and reduce the noise pollution generated from daily life.

Silica aerogel is a super-insulating inorganic material, consisting of a 3D network of crosslinking silica nanoparticles and 95%~99% of air [29]. Hence, due to the high porosity and the low solid thermal conductivity, the effective thermal conductivity of silica aerogel is pretty low, normally achieves 0.012 to 0.018 W/(m · K) [260]. However, since the silica aerogel is very brittle and easy to break, the commercial silica aerogels are always produced in a powder or particle form. It is often incorporated in other matrices, like fibreglass mats or other lightweight materials to facilitate its full benefits [261]. Several investigations related to the incorporation of silica aerogel in building materials have already been carried out as presented in **Table 8.1.**

However, most of the research investigated the silica aerogel incorporated in cement-based materials. Ng et al. [262] have prepared high-performance aerogel concrete, with bulk density and thermal conductivity of 1.3 kg/m^3 and 0.4-0.5 W/(m · K), respectively. The concrete has a low water to binder ratio of 0.20 to 0.25 and a silica aerogel replacement ratio of 50% to 70% with sand. Tao et al. [263] has synthesized normal cement mortar with an aerogel replacement ratio of 60%, featuring a compressive strength of 8.3 MPa and thermal conductivity of 0.26 W/(m · K). Fatima Júlio et al. [264] has prepared lightweight aerogel aggregate concrete with a 100% replacement ratio of silica aerogel with sand, resulting in concrete with very low thermal conductivity of 0.085 W/(m · K) and compressive strength of only 0.41 MPa. Seo et al. [54] has investigated the silica aerogel used in fly ash/slag geopolymer concrete, with an aerogel concentration of 25% to 75%. However, the thermal conductivity is relatively high, reaching 0.8 W/(m · K). Zhu et al. [265] has investigated the cement-based mortars and coatings with the addition of silica aerogel. The thermal conductivity is low (0.17 W/(m · K)) and achieves a compressive strength of 1.4 MPa. Above all, the silica aerogels are mainly used as a replacement for normal-weight aggregate and aim at low thermal conductivity and insulation properties. However, no research investigates the effect of different particle sizes of silica aerogel on the insulation property and the sound absorption of the prepared lightweight materials. Moreover, the concentration of silica aerogel is relatively high, indicating the cost of the materials is high as well, which is difficult to apply in the real world. Therefore, finding a sustainable and cost-effective building material for silica aerogel to facilitate its thermal and acoustic insulation performance is very important.

Table 8.1. Comparison of lightweight insulating concrete with the addition of silica aerogel.

Authors	Raw materials	w/b	AG RR/ PS	BD (g/cm^3)	CS (MPa)	TC (W/(m·K))	Literature
Ng et al.	CEM, quartz fines, SF, AG, SP	0.2~ 0.25	50% 0.01~4 mm	1.3	20	0.55	[262]
Ng et al.	CEM, quartz fines, SF, sand, AG, SP	0.2	60/70% 0.01~4 mm	~	19/5	0.4/0.1-0.2	[266]
Tao et al.	CEM, SF, sand, SP and AG.	0.4	60% 2~4mm	1.0	8.3	0.26	[263]
Fatima Júlio et al.	CEM, AG, surfactant	0.66 ~2.0	100%	0.41	~	0.085	[264]
Seo et al.	FA, slag, activator, AG	0.5	25/50/75%	1.28	20	0.8	[54]
Zhu et al.	CEM, SF, SP, Sand, AG	0.4	33~67% 1.2–4 mm	0.74~1.55	1.4~13.0	0.17	[265]

Note: AG-aerogel, CEM-cement, SF-silica fume, SP-superplasticizer, RR-replacement ratio, PSD-particle size, BD-bulk density, CS-compressive strength, TC-thermal conductivity

Thermal insulating mortars/plasters are the potential materials in this regard, whose thermal conductivities are normally lower than 0.2 W/(m · K) [267]. Foam render is a kind of this insulating material, however, with high energy consumption due to the use of cement, which is responsible for 3% of CO_2 emissions around the world [268]. From the point of reducing the CO_2 footprint and the cost, geopolymer foam render is a promising choice. Fly ash-based geopolymer is a promising alternative building material obtained via activation of aluminosilicate source, in this work fly ash by highly alkaline-silicate solution (MOH and M_2SiO_3 M = Na, K) [269,270]. It is feasible to obtain good high-temperature resistance because of the bonds generated in polysialates [271], which performance is further enhanced by employing a potassium-based rather than a sodium-based activator [272]. Moreover, the use of the by-products from industry in geopolymer features low energy consumption and is environmentally friendly, providing sustainability from material manufacture to construction operation [273].

In order to create the porous structure of geopolymer foam concrete, a bunch of chemical foaming agents or a mechanical pre-foaming technique can be used, both providing high numbers of pores inside the geopolymer matrix [274–276]. Certain techniques, however, may be more appropriate depending on the intended pore structure. When using chemical aeration, hydrogen peroxide (H_2O_2) is the cheapest and easiest to manage foaming agent [277–279]. Surfactant specificities and mixing ability, on the other hand, can be used to lower their total critical micelles concentration (CMC), resulting in a large number of micelles produced and

better foam stability. Furthermore, by producing a greater number of pores across a wider range, a greater number of pores come into touch with one another.

However, one concern about the use of highly porous concrete is its water uptake, which means the hygrothermal behavior is a disadvantage of the materials [280]. The wetting and drying of the building materials could result in different thermal transfer behavior through the wall or roof [281]. Another concern is the acoustic absorption for plain foam concrete is relatively low, due to the pores are not interconnected and the pore size is relatively large, with no multiscale pore size in the matrix. Therefore, a further increase in thermal insulation and acoustic absorption, meanwhile reduce the moisture transport through the foam concrete is desired.

Therefore, silica aerogel is a suitable material to improve the overall insulation performance of geopolymer foam renders. Silica aerogel prepared at ambient pressure and temperature is intrinsically hydrophobic [56]. This is due to the surface modification of silica hydrogel during preparation with the silanes [282]. Hence, silica aerogel barely reacts with the alkali in the geopolymer and thus mitigate the reaction with the hydroxyl group. Meanwhile, silica aerogel can be situated in the geopolymer matrix and act as an insulation barrier for heat and sound. However, commercial silica aerogel has different forms and sizes. Normally, several kinds of silica aerogel particles are existed on market and the particle size of silica aerogel ranges from 2 μm to 4000 μm. Four different kinds of silica aerogel are selected to investigate the effect of particle size on the insulation properties of geopolymer foam renders.

In this study, a geopolymer foam renders with the addition of a low dosage silica aerogel is prepared, focusing on the different particle sizes of aerogel on the insulation performance of geopolymer foam render (GFR). The microstructure of geopolymer foam aerogel render (GFAR) is investigated through SEM, optical microscopy, micro-CT, and UPV test. The insulation performances of GFAR are measured by thermal conductivity test and acoustic impedance tube mothed. The result of this research shed light on the smart application of silica aerogel in ultralightweight building materials.

8.2. Materials and experiments

8.2.1 Starting materials

Four different kinds of silica aerogel were purchased from Cabot, which are IC3100, IC3110, IC3120 and LA1000. The difference between the silica aerogels are the different particle sizes and the translucency of the aerogel. The particle size range of IC3100, IC3110, IC3120 and LA1000 are 2-40 μm, 100-700 μm, 100-1200 μm and 700-4000 μm, respectively. The particle size distribution of silica aerogel is shown in **Fig. 8.1 (a)**, measured with laser light scattering, except for LA1000 due to the limitation of the device (Mastersizer 2000). The particle size of LA1000 is calculated from sieving. The physical properties of aerogel are shown in **Table 8.2**. The TEM image is shown in **Fig. 8.1. (b),** showing a nanoporous structure and a 3D network of silica nanoparticles. **Fig. 8.1 (c)** shows the water contact angle of IC3100, reaching 146.6°. Therefore, the silica aerogel is highly hydrophobic. **Fig. 8.1 (d)** shows the morphology of the four types of silica aerogel used. The main difference is the particle size of silica aerogel and its transparency.

Table 8.2. Physical properties of the four types of silica aerogel.

Groups	Particle size (μm)	SSA (m^2/g)	Pore size (nm)	BD (g/cm^3)*	TC* (W/(m·K))
IC3100	2~40	699	14.0	0.12-0.15	0.012
IC3110	100~700	688	12.5	0.12-0.15	0.012
IC3120	100~1200	694	13.1	0.12-0.15	0.012
LA1000	700~4000	683	12.4	0.12-0.15	0.018

*Data provided by Cabot. SSA-Specific surface area; BD: Bulk density; TC-Thermal conductivity

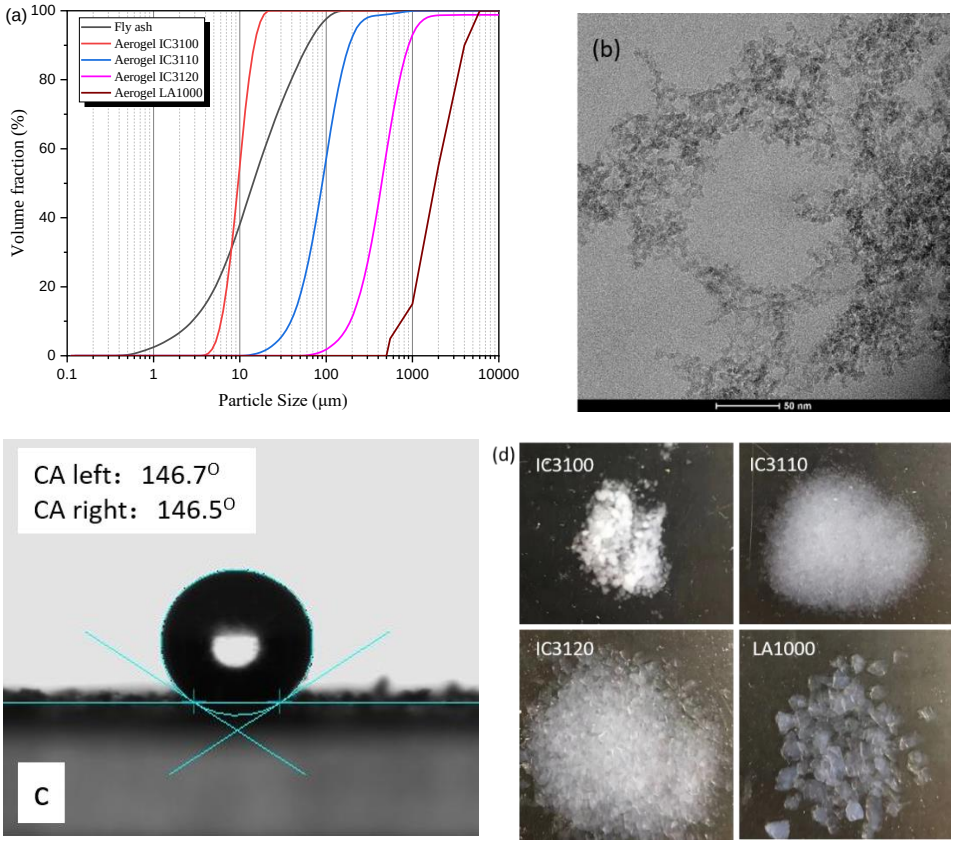

Fig. 8.1. (a) Particle size distribution of fly ash and silica aerogel (b) TEM of silica aerogel (c) water contact angle of IC3100 (d) Morphology of the aerogels.

For the preparation of geopolymer matrix, the silica modulus of SiO_2/K_2O 1.4 and 5.5% K_2O was achieved by combining potassium hydroxide pellets (VWR life science, reagent grade) and potassium-silicate solutions (WHC GmbH, K_2O 8%, SiO_2 20.8%, 72.8% H_2O by mass). As-prepared activator solution was stored for a period of 24 hours to reach equilibrium before it was utilized for geopolymer preparation. Hydrogen peroxide (30% Sigma-Aldrich, Germany) was utilized as a chemical foaming agent in combination with the surfactant mix solution, non-ionic Triton X-100 (VWR chemicals) and anionic sodium dodecyl sulfates (SDS) (98% purity, Sigma-Aldrich, Germany). Coal combustion fly ash class F (Vliegasunie) was utilized as the solid precursor for geopolymer production in this investigation. **Tables 8.3** and **8.4** show the oxide and mineral compositions, which were used to calculate the potential reactivity of fly ash (**Table 8.5**) [283].

Table 8.3. Chemical composition of fly ash and silica aerogel.

Composition (%)	CaO	SiO_2	Al_2O_3	Fe_2O_3	K_2O	Na_2O	SO_3	MgO	TiO_2	MnO	SSA (m^2/g)	SD (g/cm^3)
Fly ash	6.1	54.5	21.5	9.1	2.8	0.4	1.3	1.3	0.9	2.0	0.4	2.2
Silica aerogel	-	99.6	-	-	-	-	-	-	-	-	680	0.10

Note: SSA: Specific surface area; SD: Specific density

Table 8.4. Phase quantification via Rietveld refinement of fly ash.

Amorphous	Quartz	Mullite	Hematite	Periclase	Magnetite	Anatase
ICSD Amount	83849	66451	22505	9863	85807	24276
84.99 (0.30)	5.03 (0.09)	7.19 (0.16)	1.69 (0.12)	0.56 (0.09)	0.24 (0.09)	0.22 (0.05)

Note: Uncertainty in the brackets, as taken from Topas.

Table 8.5. Potential reactivity of fly ash.

	Moles of Si per 100 g of FA	Moles of Al per 100g of FA	Si/Al molar ratio
Total content (XRF)	0.9071	0.7969	1.14
Crystalline content (XRD)	0.1170	0.1018	1.15
Amorphous content	0.7901	0.6951	1.14

8.2.3 Preparation of the geopolymer foam aerogel render

The pastes were made in a Hobart mixer with a 5-litre capacity. First, the dry components (fly ash and silica aerogel) were combined until homogenized (60s), depending on the paste design, as shown in **Table 8.6**. The activator was then added and mixed for 30 seconds at low speed, followed by 60 seconds at high speed. Hydrogen peroxide solution and then the surfactant solution was added and mixed at high speed for 30 seconds. Afterwards, the slurry was used to measure fresh density and cast into the moulds 40×40×160 mm^3 and 100×100×160 mm^3. All samples were sealed and cured for 24 hours at 20 °C and then for 24 hours at 60 °C. Subsequently, specimens were stored for a further 26 days at room temperature (20°C).

Table 8.6. Recipe of geopolymer foam aerogel render (GFAR) (kg/m^3).

Groups	FA	Activator	HP	SDS	TX100	IC3100	IC3110	IC3120	LA1000
Ref	1172	421.9	7.9	3.5	2.6	-	-	-	-
AG1-10	1055	379.7	7.1	3.1	2.3	8.87	-	-	-
AG2-10	1055	379.7	7.1	3.1	2.3	-	8.87	-	-
AG3-10	1055	379.7	7.1	3.1	2.3	-	-	8.87	-
AG4-10	1055	379.7	7.1	3.1	2.3	-	-	-	8.87

Note: HP-Hydrogen peroxide; SDS: Sodium dodecyl sulphate TX100: Triton X-100

8.2.3 Characterization

8.2.3.1 Density and porosity of GFAR

The fresh concrete density was measured according to EN 12350-1 [284]. The dry bulk density of the prepared GFCA was measured by the simple mass to volume ratio, according to BS EN 12350-1 [285]. The prepared samples were first dried at 105 ℃ in an oven until a constant mass. The skeleton density of the prepared samples was measured by the density analyser Helium pycnometer model (AccuPyc II 1340 Micromeritics), according to EN 1097-7 (1999) [286]. The average density of three tested samples was calculated as the final density of the GFCA. The porosity of the GFCA was calculated according to:

$$\Phi = (1 - \frac{\rho_b}{\rho_s}) \times 100\% \tag{8.1}$$

where ρ_b is the dry bulk density of the GFAR, ρ_s is the skeleton density of the GFAR, Φ is the porosity of the GFAR.

8.2.3.2 Thermal conductivity and acoustic absorption

The thermal conductivity of the GFAR was measured with a heat transfer analyser ISOMET model 2104. The thermal conductivity λ (W/(m $\cdot$ K)), the specific heat capacity c_ρ (J/(kg $\cdot$ K)) and thermal diffusivity α (mm^2/s) of the GFAR can be tested. The temperature during the test is constant at around 20 ℃. The average thermal conductivity of three test specimens was calculated as the final thermal conductivity of the GFAR. The testing image of the thermal conductivity of GFAR is shown in **Fig. 8.2**.

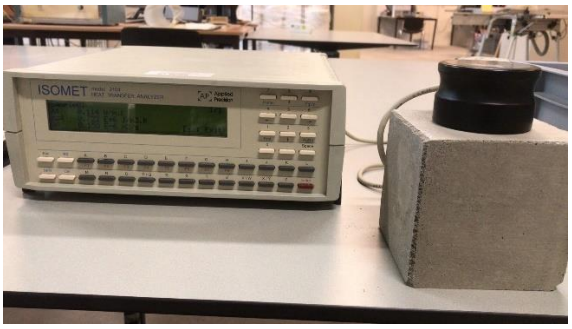

Fig. 8.2. Measurement of thermal properties of geopolymer foam aerogel render (GFAR).

The acoustic absorption test for GFAR was conducted with an impedance tube method as shown in **Fig. 8.3**. The hardened cylinder GFAR sample with a dimension of a height of 80 mm and a diameter of 40 mm was tested. In specific, the measurement principle is through generating a plane wave by a loudspeaker on the one side of the tube that was then spreading through the tube before reflecting by the GFAR. The GFAR changes the reflected wave and by collecting the generated standing wave, the sound absorption coefficient of the samples can be determined. The wave was measured at six different locations in the tube. This was done to increase the accuracy as described in the measurement protocol for the impedance tube. GFAR samples were inserted at the end of the impedance tube and backed by a rigid surface.

Fig. 8.3. Measurement of acoustic absorption of GFAR.

The noise reduction coefficient (NRC) and sound absorption average (SAA) were calculated to evaluate the performance of GFAR, according to ASTM C384-1. The SAA was calculated as the average of the sound absorption coefficients of material for the twelve one-third octave bands from 200 through 2500 Hz, measured according to this test method. The NRC was calculated as the average of the sound absorption coefficients for 250, 500, 1000, and 2000 Hz to the nearest multiple of 0.05.

8.2.3.3 Compressive and flexural strength

The GFAR samples with the size of 40 mm × 40 mm × 160 mm were used to determine the flexural strength at 7 and 28 days, following EN196-1 [287]. The GFAR samples with the size of 40 mm × 40 mm × 40 mm were used to determine the compressive strength at 7 and 28 days, following EN12390-3 [288]. The average strength of three test specimens was calculated as the final strength of the GFAR.

8.2.3.4 Micro-CT

For pore size and silica aerogel particle dispersion analysis, μCT 100, Scanco Medical AG, Switzerland scanner was used. The scanning voltage was applied to 70 kV, and the X-ray current was set at 200 mA. A 0.5 mm aluminium filter has lowered the beam's hardness. 205 images with a 2048 ×2048 resolution were generated in a single measurement, each sample was measured three times at different specimen heights, whose voxel size was 10 μm. In preparing binarization processes and separating air voids and aerogel silica particles from the denser geopolymeric matrix, 3D- reconstruction program was utilized. As a result, in the examination of pore size distribution and open porosity, the two media were regarded as a single-air-derived medium.

8.2.3.5 UPV test

Ultrasonic pulse velocity (UPV) test was used to measure the compactness and voids of GFAR samples, following ASTM C597-02 [289]. Pulses of longitudinal stress waves are generated by an electro-acoustical transducer that is held in contact with one surface of the concrete under test. After traversing through the concrete, the pulses are received and converted into electrical energy by a second transducer located a distance L from the transmitting transducer. The transit time T is measured electronically. The pulse velocity V is calculated by dividing L by T. Direct method was used during the whole test, which requires access to two surfaces of the concrete cubes. A viscous grease is used to ensure efficient transfer of energy between the concrete and the transducers. Each specimen was tested thrice, and the average value was determined as the final velocity of the foam concrete.

8.2.3.6. Water uptake

A measurement was performed in a climate chamber while maintaining a constant temperature of 23 °C and humidity of 80% to study the impact of air humidity on thermal insulation characteristics and the potential of water sorption. The water uptake (WU) was determined using an analytical balance with a precision of 1 mg as the difference between the mass of the dry sample and conditioned in a climate chamber specimen, and the thermal conductivity was determined using the technique described above. Cubic samples with dimensions of 100x100x100 mm^2 were used in this investigation:

$$WU = \frac{(m_1 - m_0)}{m_0} \times 100\% \tag{8.2}$$

where WU is the water uptake, m_0 is the initial mass of the sample, m_1 is the final mass of the sample after being stored at 80% humidity environmental chamber.

8.2.3.7 Microstructure observation

2.3.7.1 SEM

The microscope FEI quanta 600 environmental scanning electron microscope was used to perform SEM tests on 28 days of hydrated porous composite pastes to evaluate the morphology of the pastes. The samples have been sputtered with platinum using a Quorum Q150V Plus sputter coater before analysis (current 65 mA, coating time 30 s). A secondary electron detector at 5 kV at various magnifications was observed in micrographs.

2.3.7.2 Optical microscopy

The ZEISS Axio Imager equipped with ZEISS Axiocam 305 CAMERA Colour, Z2 optical microscope (Carl Zeiss, Göttingen, Germany) was used to examine the microstructure morphology and silica aerogel particle location in the geopolymeric matrix. An objective lens Zeiss EC Epiplan Neofluar 5x BD was used for each measurement.

8.3. Results and discussion

8.3.1 Physical and mechanical properties of GFAR

The fresh density, bulk density, skeleton density, porosity and compressive strength of the GFAR are presented in **Table 8.7**. It can be observed that the fresh density and dry bulk density are related to the particle size of the aerogel. The REF has a fresh density of 1195.8 kg/m^3, while the dry bulk density reaches 873.0 kg/m^3. The more silica aerogel in the GFAR fresh paste, the lighter the paste could be. This is due to the silica aerogel particles occupy the space in the fresh paste and increase the total volume of the paste. As a result, the specific density of fresh paste will be decreased. The lowest fresh density was achieved for the AG3-10 sample. Therefore, it can be found that the addition of silica aerogel could result in the formation of more voids that are provided by the aerogels.

On the other hand, the particle size of silica aerogel has a significant influence on the bulk density of GFAR. It can be observed that AG1-10 has the highest density while AG3-10 has a slightly lower density than other groups. The reason could be attributed to the fractions of the

silica aerogel. The AG1-10 sample contains 10% 2-40 µm silica aerogel, so the addition of silica aerogel could result in compacted packing of the silica aerogel and fly ash, resulting in a denser matrix, as shown in **Fig. 8.4**. It can be observed the optimal packing curve is close to the actual curve of the GFAR, which means the packing of the two materials is dense. However, with the increasing particle size of the aerogels, the difference between optimal packing and real packing curve become larger. Hence, with the incorporation of much larger silica aerogel granules, the inter-particle porosity will become higher, and thus obtaining a looser packing than finer silica aerogel, indirectly generate more pores in the geopolymer matrix.

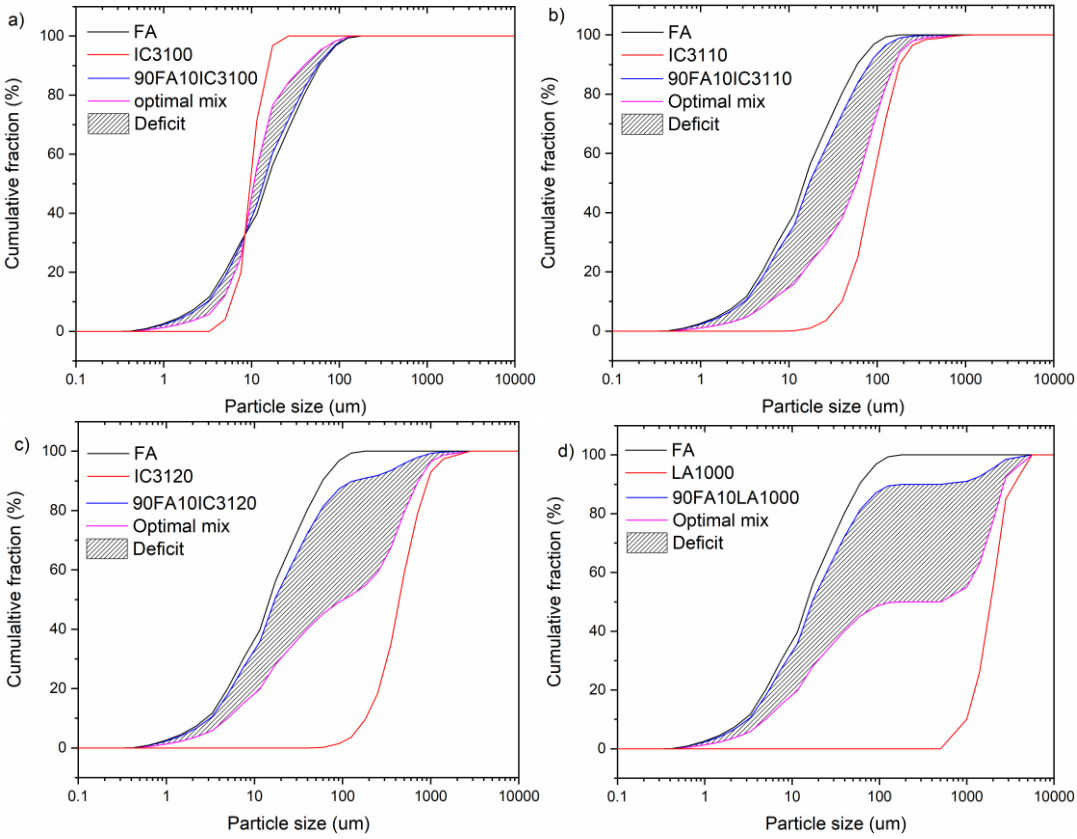

Fig. 8.4. The difference between optimal mix curve and the actual curve of the mix from AG1 to AG4.

The skeleton density is related to the inherent properties of the raw materials. The skeleton density measured by pycnometer is almost the same for all GFAR, which is due to the fact that all the raw materials used are solely fly ash and silica aerogel. Therefore, the skeleton density is in the range of 2308 kg/m^3 to 2350 kg/m^3, with very small deviations.

The porosity is thus calculated according to the dry bulk density and skeleton density. As presented in **Table 8.7**. The lowest porosity is 62.25%, obtained from the plain geopolymer foam concrete. However, the porosity only slightly improved for the AG1-10, the finest aerogel powder, reaching 62.68%. This result indicates the AG1 has no obvious effect on the improvement of total porosity of GFAR. This could be attributed to the fact that the IC3100 aerogel is too small that cannot support the structure. By adding a part of the aerogel particles instead of some of the pores, good formability can be obtained as demonstrated in [53]. This is because the larger aerogel particles are rigid solids that can support the pores. Another

interesting finding is that the bulk density for AG4-10 is the lowest, suggesting the large grain of the silica aerogel particles can increase the porosity of GFAR, achieving a porosity of 69.56%. Therefore, the silica aerogel with a large grain size plays a better role to create the porous structure of geopolymer foam concrete. To be specific, the 1200-4000 μm silica aerogel has the best pore generation for GFAR.

The compressive strength of GFAR at 28 days is shown in **Table 8.7**. The reference sample has a compressive strength of 2.52 MPa, while with the addition of silica aerogel, the aerogel samples show lower strength as expected, which is attributed to the low strength of silica aerogel (10-100 kPa) [290]. The strength of the AG1-10 sample is similar to reference, so the finest silica aerogel has limited influence on the mechanical performance. However, the AG2-10, AG3-10 and AG4-10 have a higher degradation on compressive strength, reaching 1.84, 1.58 and 1.49 MPa, respectively. This result can be indicated by the total porosity of the GFAR as discussed above. Another aspect is the weak bonding between the paste and the filler (silica aerogel particles).

Table 8.7. Fresh density, bulk density, skeleton density, porosity and strength of the GFAR.

Groups	Fresh density (kg/m^3)	Bulk density (kg/m^3)	Skeleton density (kg/m^3)	Total Porosity (%)	Compressive strength 28d (MPa)
Ref	1195.8	873.0±3.6	2312±1	62.25±0.20	2.52±0.10
AG1-10	1137.2	861.5±6.4	2308±6	62.68±0.39	2.41±0.09
AG2-10	1065.8	773.0±5.5	2344±6	67.02±0.68	1.84±0.05
AG3-10	1037.3	747.8±3.3	2374±6	68.50±0.06	1.58±0.05
AG4-10	1060.5	715.2±5.9	2350±5	69.56±0.30	1.49±0.08

8.3.2 Thermal conductivity of GFAR

8.3.2.1 Thermal conductivity at 100% dry condition

The thermal properties of the GFAR with a different particle size of silica aerogel is presented in **Table 8.8.** The reference sample shows the highest thermal conductivity of 0.173 $W/(m \cdot K)$ and a specific heat capacity of 1.14 $J/(kg \cdot K)$. The AG1-10 sample shows a slight reduction in thermal conductivity, while is not obvious on the improvement of thermal insulation of GFAR. With the increasing particle size of silica aerogel, the GFAR shows a lower thermal conductivity and heat capacity. The lowest thermal conductivity achieves 0.143 and 0.144 $W/(m \cdot K)$ for the AG3-10 and AG4-10 samples. The silica aerogel plays a role as a filler with ultralow thermal conductivity in the paste, thus reducing the thermal conductivity of all GFAR samples.

The reason of silica aerogel with different particle size on the thermal properties of GFAR are different can be attributed to two aspects. Firstly, large silica aerogel particles can create more inter-particle pores in the geopolymer matrix as discussed in section 3.2. The thermal insulation of GFAR is closely related to the total porosity of the foam geopolymer. As can be referred in Table 7, the total porosity is slightly higher for AG4-10 and AG3-10 than the ones

of AG1 and reference. This factor can greatly influence the thermal properties of GFAR as less solid conductivity is included in the calculation of the total effective thermal conductivity.

On the other hand, the influence of particle size on thermal performance of GFAR mainly comes from the interfacial thermal resistance (ITR) of silica aerogel. Generally, the finer silica aerogel has more interfacial area than the coarser silica aerogel, due to the smaller radius of the particles. Therefore, it is hypothesized that finer silica aerogel has a higher interfacial thermal resistance than larger aerogel particles, assuming the interfacial area mainly consists of low density geopolymer or air having a lower thermal conductivity. However, in this study, it is found that the AG1-10 and AG2-10 has no obvious improvement on the thermal insulation of GFAR. It indicates that the ITR is not a decisive factor determining the thermal conductivity in this case. The reason could attribute to the fact that the thermal conductivity of interfacial transition zone is even higher than silica aerogel, which is not the case compared to the study in other literatures [54], where the ZnS/diamond composites show a lower thermal conductivity when finer diamond is incorporated. Therefore, it is demonstrated that particle size of silica aerogel mainly influences the total porosity of GFAR while the interfacial thermal resistance is not significant.

Although finer silica aerogel has a larger contacted surface interfacial area with geopolymer, the ITR is not a decisive factor for GFAR. Therefore, the larger particle size of aerogel can even function better as a thermal insulator in the geopolymer foam concrete, due to the creation of more interparticle pores and maximum porosity, and also the optimization and stability of the pores in the matrix.

Table 8.8. Thermal properties of the GFAR.

Groups	Ref	AG1-10	AG2-10	AG3-10	AG4-10
λ (W/(m · K))	0.173±0.015	0.163±0.025	0.149±0.017	0.143±0.013	0.144±0.027
C_ρ (e^6 J/(kg · K))	1.14	1.10	0.963	0.922	0.954
α (e^{-6} (mm^2/s))	0.156	0.153	0.154	0.156	0.151

Note: λ -Thermal conductivity; C_ρ - Specific thermal capacity; α- Thermal diffusive coefficient

The thermal conductivity versus the density and compressive strength versus thermal conductivity of building materials with the addition of silica aerogel particles are shown in **Fig. 8.4** (a) and (b). Compared with the GFAR prepared in this study, other materials with silica aerogel has a higher thermal conductivity. The UHPC aerogel concrete obtains similar thermal property, but the silica aerogel loading is much higher, replacing 70% of the natural aggregate. Cement-based aerogel foam concrete has a lower density, showing a linear trend as the silica aerogel dosage increased from 20% to 70%. The thermal conductivity decreases from 0.164 to 0.07 W/(m · K). Cement aerogel render shows a higher thermal conductivity at the same density range. Also, the AIC (aerogel incorporated concrete) obtains higher density because coarse aggregate is used, showing a linear trend as well. Alkali-activated fly ash/slag concrete with silica aerogel has an even higher thermal conductivity than AIC, mainly because the used sand is highly conductive compared to the replaced aerogel. Cement aerogel mortar coating has a higher density and thermal conductivity. However, the slope of the linear fit is similar to this

study. Therefore, it can be inferred the aerogel incorporated building materials all show a linear trend for the density versus thermal conductivity curve. However, the GFAR has a lowest thermal conductivity compared to other aerogel incorporated samples.

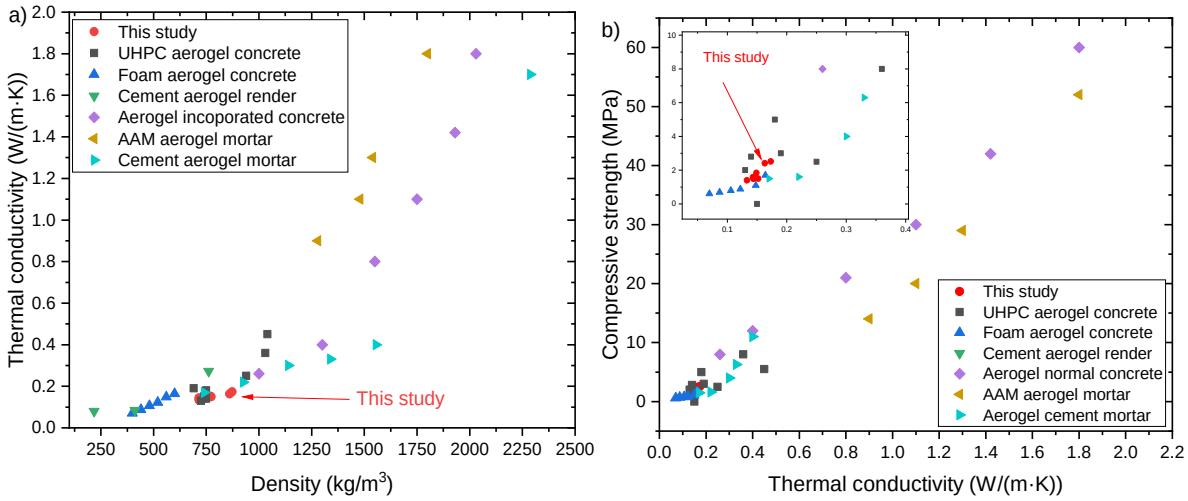

Fig. 8.5. (a) Thermal conductivity vs density (b) Compressive strength vs thermal conductivity of GFAR with other aerogel incorporated building materials.

The comparison of compressive strength with other aerogel incorporated materials is shown in **Fig. 8.5** (b). It is noteworthy that the compressive strength of GFAR is only slightly lower than UHPC aerogel concrete. This is mainly because the UHPC recipe has a very low water to binder ratio of 0.20 to 0.25 and a better packing of the mixtures. For the other materials with silica aerogel, the compressive strength is relatively lower. One reason for the higher compressive strength for GFAR is the geopolymer inherently has a higher strength than cement-based materials. Moreover, as can be observed in other materials, the loading of silica aerogel is very high, normally achieving 50%, which also contribute to the low strength. For the GFAR, the aerogel loading is only 10%, while can reach the lower thermal conductivity. Therefore, the optimized geopolymer foam matrix plays an important role. The smaller amount of aggregates in the matrix, the fewer defects in the interface of materials could have, leading to higher compressive strength.

8.3.2.2 Water uptake and the effect on thermal conductivity

The water uptake at 80% humidity environment chamber and its effect on thermal conductivity of GFAR is shown in **Table 8.9**. The water uptake of the reference sample is the highest reaching 6.52%. This higher water uptake indicates a significant rise in thermal conductivity, which shows a rise to 0.214 W/(m · K), increasing by 23.6% compared to the sample in 100% dry condition. Therefore, the hygrothermal performance is dependent on the moisture content inside the matrix. As can be observed, the silica aerogel incorporated samples show lower water uptake from AG1-10 to AG4-10. This is attributed to the hydrophobic nature of silica aerogel, as shown in the water contact angle image in section 2. As a result, the aerogel samples all have a smaller rise in thermal conductivity.

Different particle size seems has limited influence on the water uptake of GFAR. The WU of AG1-10, AG2-10, AG3-10 and AG4-10 are similar, around 5.13% to 5.35%. Therefore, the

particle size of silica aerogel cannot influence the hygrothermal performance of foam concrete. Moreover, the rise in thermal conductivity of GFAR is also similar. Compared to the 0% humidity condition, the increase in TC is all-around 8.39% to 12.2%.

Among the 10% aerogel incorporated GFAR, the AG2-10 has a better performance than other groups in terms of water uptake. This increase in hygrothermal insulation could be due to the much higher range of particle size from 100 μm to 1200 μm. It can be observed the mixing particles could have a positive effect on the hygrothermal performance than the narrow pore size distribution particles like AG1 and AG4. The reason to this phenomenon could be considered in two aspects. Firstly, the finer silica aerogel has a higher hydrophobic surface area that can resist water from transportation as discussed in previous section. The interfacial water resistance could be directly related to the water resistance of GFAR. Hence, the much finer silica aerogel could result in more hydrophobic surface site in the matrix. Thus, the AG4 with the largest particle shows a worse performance in water uptake and increment in thermal conductivity. Secondly, the tortuosity of water transport changed by adding smaller silica aerogel particles, because the more hydrophobic positions in the matrix that spread evenly. With a wide range of silica aerogel particles, the packing of the silica aerogel become better and thus more channels for water transport are blocked by aerogels.

However, the AG1-10 sample show a less effective effect on thermal properties. The reason is the narrow particle size distribution of IC3100 from 10-40 um that cannot effectively increase the tortuosity of moisture transport. It is demonstrated the addition of randomly distributed graphene particles can enhance the tortuosity and decrease the chloride transport in both concrete and mortar [55,56]. Therefore, a wider range of silica aerogel particles could improve the tortuosity better than IC3100 and LA1000.

Table 8.9. Water uptake at 80% humidity condition and thermal conductivity of GFAR.

Groups	Ref	AG1-10	AG2-10	AG3-10	AG4-10
λ (W/(m·K))	0.214	0.183	0.164	0.155	0.161
Increment (%)	23.6	12.2	10.7	8.39	11.8
Water uptake (%)	6.52	5.35	5.13	5.29	5.34

8.3.3 Acoustic absorption

The acoustic absorption coefficient of GFAR with different particle size of silica aerogel are shown in **Fig. 8.6.** The noise reduction coefficient (NRC) and sound absorption average (SAA) of GFAR are presented in **Table 8.10**. The reference GFAR present a relatively low acoustic absorption efficiency. The maximum absorption occurs at 719 Hz with a coefficient of 0.37. The NRC and SSA are 0.10 and 0.13, respectively. Nevertheless, this value is higher than plain hardened cement paste, which only has a maximum coefficient of 0.20 and a pretty low NRC of nearly 0 [117,143]. Therefore, geopolymer foam concrete obtains better acoustic insulation properties than much denser cement mortar. It is attributed to the much higher open porosity and the inter-connected pores generated from H_2O_2 and surfactant solution during mixing.

With a 10% aerogel dosage in GFAR, the samples AG1-10, AG2-10, AG3-10 and AG4-10 all present higher acoustic insulation performance than the plain GFAR. The AG1-10 sample shows a slight increase in the acoustic absorption efficiency, with only an 8.1% increase in maximum efficiency, achieving 0.40 at a frequency of 759 Hz. The NRC increases to 0.20. The max acoustic absorption of AG2-10 also increased but was limited to 0.56 at a frequency of 468 Hz, with NRC reaches 0.35. It indicates the finer silica aerogel only slightly increase the acoustic absorption. On the other hand, the AG3-10 and AG4-10 samples both increase the acoustic absorption to a much higher degree. The AG3-10 silica aerogel with 100-1200 μm particle size increases the max acoustic absorption to 0.63 at 444 Hz, while the largest rise happens for AG4-10, with an increase of 113.5% compared to plain geopolymer foam concrete, achieving 0.79 at a frequency of 505 Hz. Furthermore, the NRC of both AG3-10 and AG4-10 increase to 0.5. Therefore, the 700-4000 μm silica aerogel could play a better role to improve the acoustic absorption of geopolymer foam concrete. Therefore, it is suggested that the silica aerogel with a larger particle size could function better as an enhancer for improvement in insulation properties, which is better than the much finer fraction of silica aerogel.

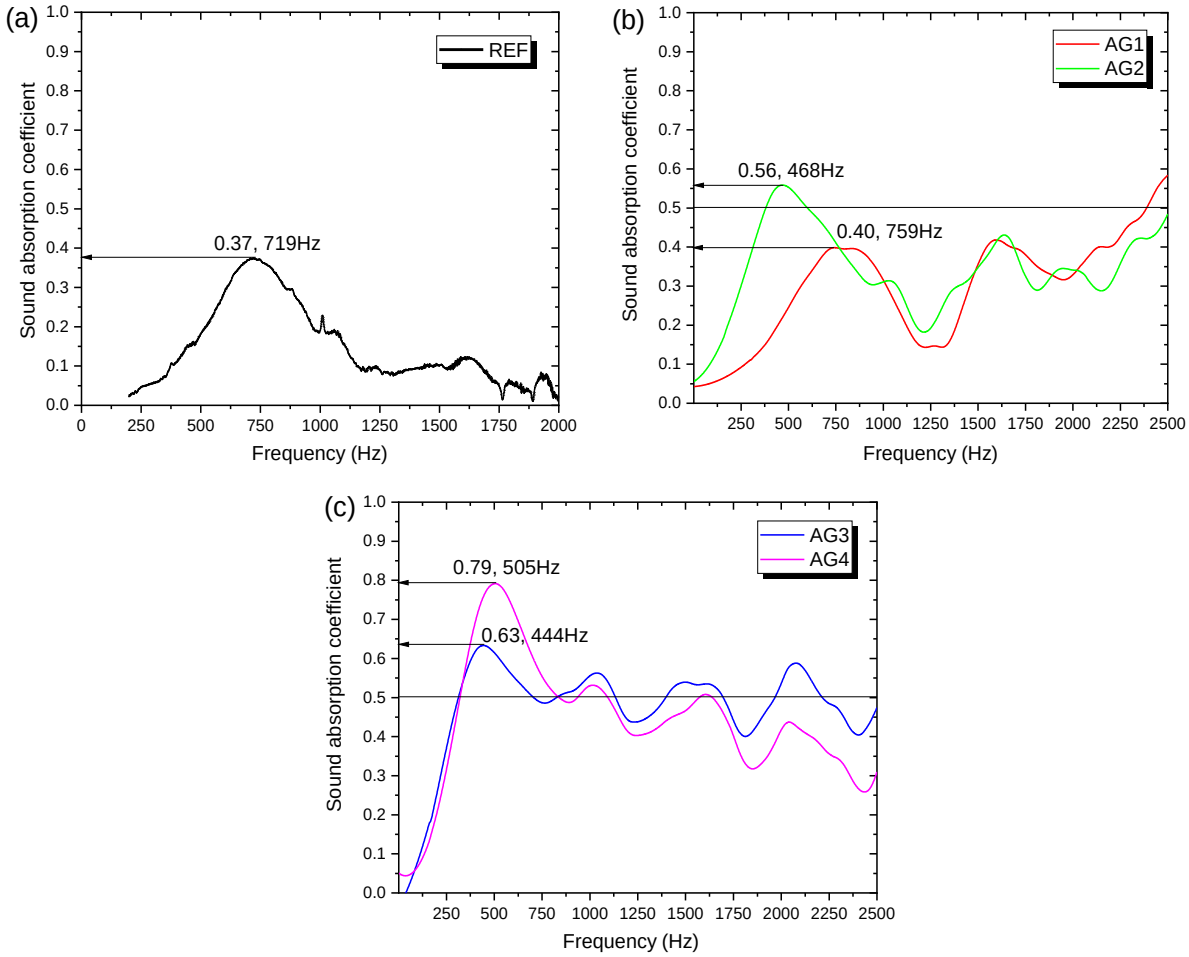

Fig. 8.6. Acoustic absorption of GFAR with different dosage and particle size of silica aerogel.

Table 8.10. Noise reduction coefficient and sound absorption average of GFAR.

Samples	Ref	AG1-10	AG2-10	AG3-10	AG4-10
NRC	0.10	0.20	0.35	0.50	0.50
SSA	0.13	0.30	0.34	0.47	0.44

The detailed studies on the acoustic absorption of foam concrete are relatively rare. Compared to other kinds of foam concrete, the sound absorption of GFAR is higher, and the range of coefficient above 0.5 is wider, from around 500 Hz to 2500 Hz. The rise in acoustic absorption should be attributed to the higher open porosity and the inherent insulation property of silica aerogel. As shown in **Table 8.11**, the acoustic absorption of other foam concretes presents different values at different frequencies. The foam concrete can be prepared with different methods, for instance, the pre-foamed concrete and the aerated autoclaved concrete. Zhang et al. [291] has investigated the acoustic absorption of fly ash/slag geopolymer pre-foam concrete, which has a maximum coefficient of 0.8, but with a very narrow absorption peak at 40-150 Hz. Therefore, the calculated NRC is relatively low, indicating a poor absorption frequency from 250 Hz to 2500 Hz. Neithalath et al. [292] prepared foamed concrete samples obtaining absorption coefficients in the range of 0.20 to 0.30 with a bulk density of 400-700 kg/m^3. However, the foam concrete prepared had a closed pore network, mitigating the sound propagation leading to reduced sound absorption. Therefore, it is also important to optimize the processing parameters to make foam concrete with a much higher open porosity if the acoustic insulation property is desired.

Table 8.11. Acoustic absorption of different kinds of foam concrete.

Foam concretes	Maximum sound absorption coefficient	Peak frequency (Hz)	NRC	Density (kg/m^3)	Literature
Foam concrete with aerogel	0.79	450-700	0.53	700-800	This study
Geopolymer foam concrete	0.8	40-150	~0.2	600-1200	[291]
Foam cement concrete	0.12-0.24	-	-	250-500	[75]
Foam concrete	0.2-0.3	-	-	400-700	[292]

8.3.4 Microstructural analysis

8.3.4.1 SEM analysis

The scanning electron microscopy of the cross-sections from GFAR samples in different scales are shown in **Fig. 8.7**. Typical for fly ash-based geopolymers is the multiplicity of unreacted spherical particles (cenospheres, ferrospheres) that are embedded in a geopolymer

matrix with an amorphous structure. Their reaction is limited despite the high pH of the activator solution because geopolymerization is additionally a thermally induced process. At higher temperatures, it is possible to homogenize the structure due to the continuous geopolymerization. The effect of these reactions in the form of a visible gel can be observed on spherical ash particles. **Fig. 8.7.** (A) presents the K (N) -A-S-H gel formed in the GFAR, which is observed from the amorphous products and the fine structure on the surface. There exist numbers of mesopores range from 0.5 μm to 2 μm generated in the geopolymeric structure, which may further lead to the increased insulation properties of thermal and acoustic. Furthermore, the resulting homogeneous mass is characterized by interstitial porosity. In **Fig. 8.7. (c**), a silica aerogel like structure can be observed, however, should be further connected to an optical image to determine its existence. The inter-particles cracks are obvious, which may contribute to the very low mechanical properties of GFAR, while these cracks could also result in the increase in thermal insulation owing to the interfacial thermal resistance (ITR). **Fig. 8.7. (d)** presented the zoomed-out image of GFAR. The big pores around 500 μm are attributed to the formation of gas from hydrogen peroxide in the geopolymer paste. It is noteworthy that the interconnected pores inside the big pores can be clearly observed, which contributes to the increased acoustic performance of GFAR. It should be mentioned that due to the very low dosage of silica aerogel particles and the nature of SEM imaging, silica aerogel is hardly be found in the picture. However, the optical image is used to further analyse the structure of GFAR as followed.

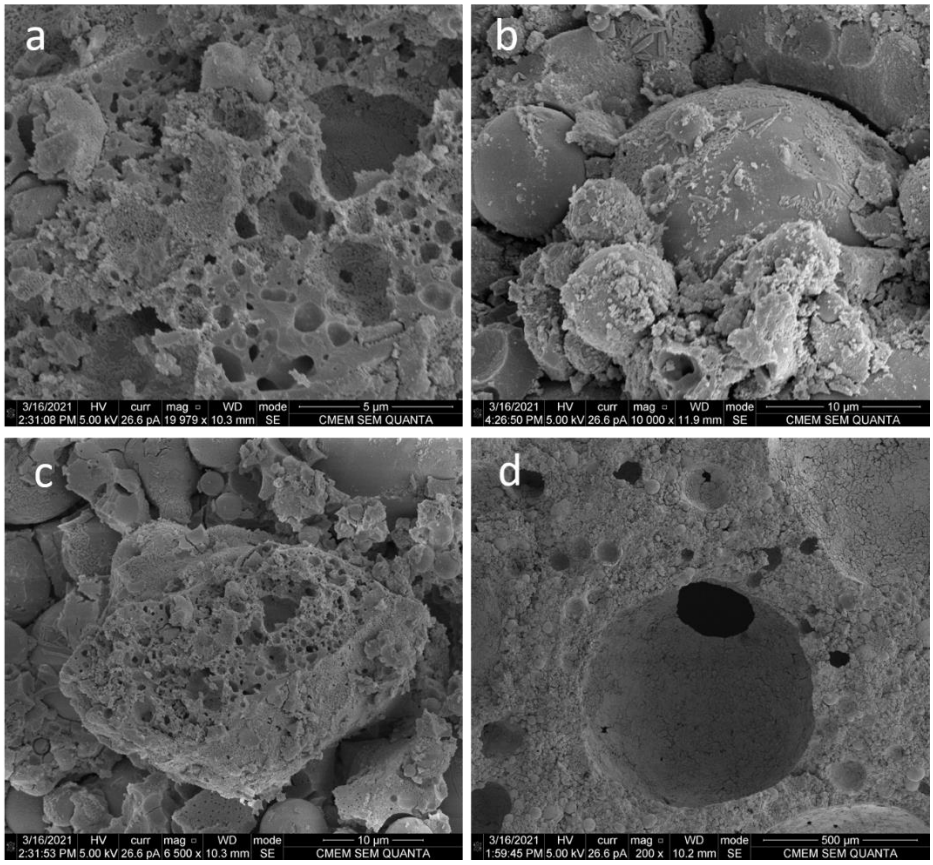

Fig. 8.7. SEM of the cross-section of GFAR (a)×20000 (b) ×10000 (c) ×6500 (d) ×200.

8.3.4.2 Optical image analysis

Fig. 8.8 shows an optical image of a GFAR cross-section, which is valuable for observing macropores and macrostructure. Many open channels may be found in the structure of geopolymer paste (**Fig. 8.8 (a)**). Although the smallest silica aerogel particles were not detected in the pores, it is presumed that they are incorporated in the matrix of the geopolymer solid network, reducing the paste's thermal conductivity. Furthermore, as depicted in **Fig. 8.8. (b)**, the open pores are linked, and the matrix contains a large silica aerogel. **Fig. 8.8. (c)** illustrates a large-sized silica aerogel stuck within a void, which may act as a thermal barrier and absorbent for acoustic waves, as well as providing a link and backbone between the air voids.

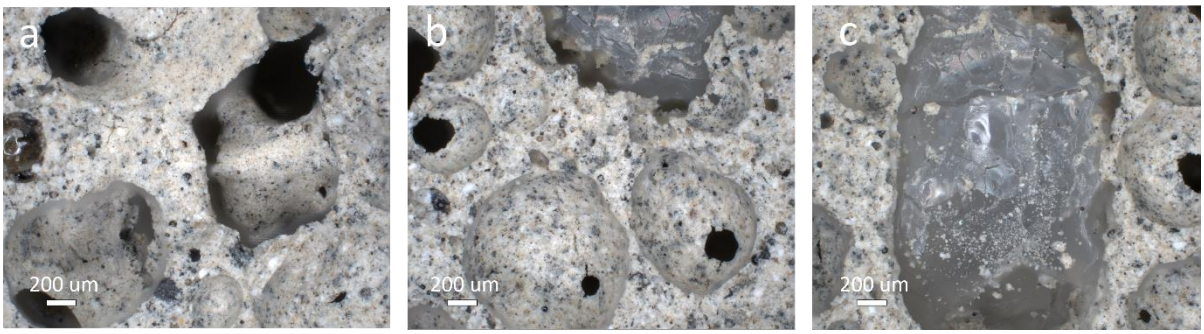

Fig. 8.8. Optical images of the cross-section of GFAR.

8.3.4.3 Micro-CT analysis

The software IPLFE v1.16 (Scanco Medical AG, Switzerland) was used to analyze the pore distribution of each composite on a 3D slice view. The pixel intensity is related to the density of the object, due to that it was possible to separate the surrounding air, air voids and aerogel particles from the denser matrix (**Fig. 8.9**). Due to this obvious distinguishing in intensity distributions, the pictures can segment the image into void and solid. However, the density difference between air and silica aerogel was impossible to detect.

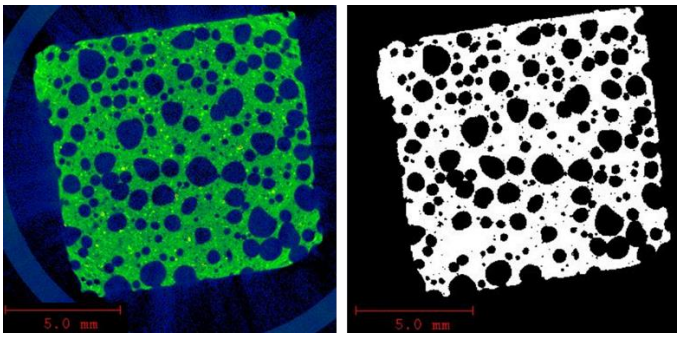

Fig. 8.9. Binary representation of the image (Ref sample).

A distance transformation was applied [293] which enables the collection of the data in the 3D visualisation form in 3D model of the sample. The empty region surrounding the geopolymer has been turned into a solid by filling. Following the identification of all pores on the surface and inside the prescribed contour, the pores were colored differently depending on the size of the examined pore/particle [294]. It was able to generate a 3D-pore shape visualization in all geopolymer renderings using the data gathered in this way on both the

distribution and size of the pores (**Fig. 8.10**). The resulting pore size data was then additionally saved as a histogram in the form of a text file to provide also quantitative analysis of pore size distribution. Noteworthy, as mentioned in the methodology, micro-CT covers the pores above 10 µm which provides some limitations related to small size pores. The pore size was divided into the groups related to the silica aerogel particles used in order to see the variations between samples, as well as the values, were normalized to 100 vol.% (**Fig. 8.10**)

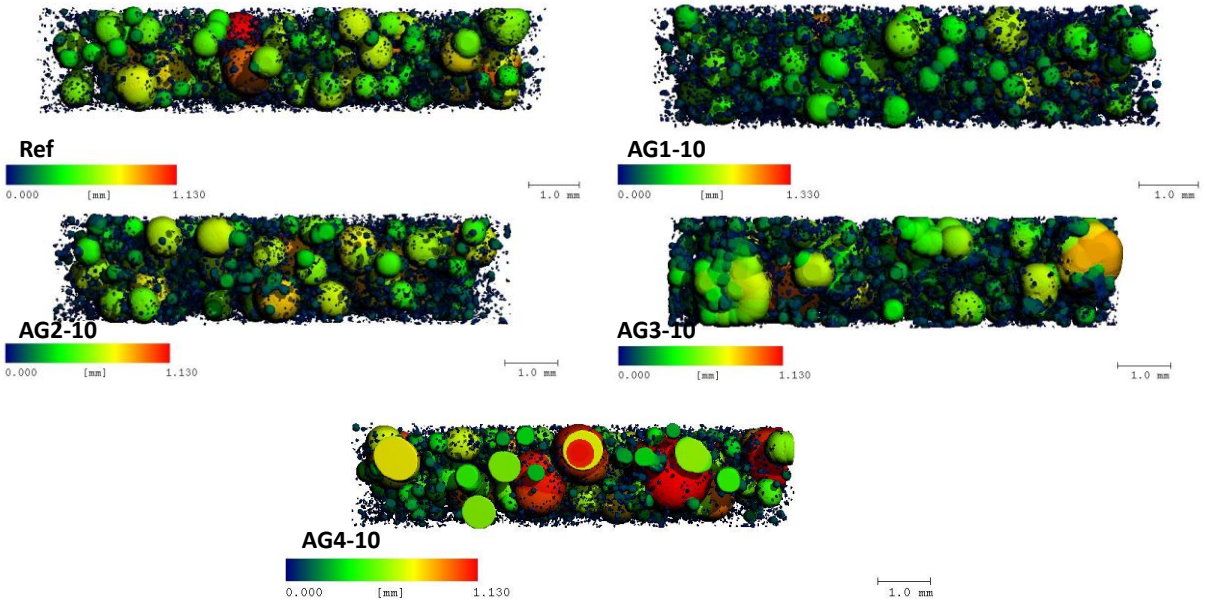

Fig. 8.10. Isolated air voids and silica particles system.

The goal of the porosity distribution analysis is to see whether silica aerogel particles affect the material's pore size distribution. The size of the silica aerogel particles was used to establish the prescribed intervals in order to observe their impact on the possible pore size, which is also related to the presence of these particles in the matrix (**Fig. 8.10**). As can be observed, tiny particles have a no larger influence on the matrix, but particles ranging in size from 100 to 1200 µm enrich the structure with voids of various sizes, which contribute favorably both in terms of thermal and acoustic insulation, as evidenced by the AG3 -10 in **Table 8.10**. Empty gaps with a restricted range of sizes are undesirable because they influence the material's acoustic and strength characteristics. The size and distribution of pores in the materials are depicted in **Fig. 8.10**, where the order of magnitude has been standardized in the form of a color scale, allowing to compare the matrices obtained. As can be seen, adding a particle with a size of up to 40 µm enriched the mixture with numerous fine air/silica aerogel gaps, and as the particle size increased, so did the number of bigger components equally disperse throughout the structure. Due to the presence of a big size fraction of silica aerogel, AG4-10 contains many open spaces with a dimension of 1.13 mm or more. Moreover, **Fig. 8.10** reveals that the AG4-10 sample is distinguished by the sole domination of space over 700 µm compared to those in the range of 100-700 µm, which results in a reduced compressive strength when compared to other enriched by 10% of silica aerogel materials and is also the cause for the greatest total volume of pore.

Second, the resulting void space is analyzed for connectivity to identify individual void objects, as well as the connectivity between the void objects. First, the images were segmented to distinguish void space from solids. Second, the resulting void space is analyzed for connectivity to identify individual void objects, as well as the connectivity between the void objects. During the pore separation process, the resulting void spaces were examined for connection to identify individual objects, their volume, as well as the connectivity between them [293]. After that, disconnected pores were separated from linked pores in a 3D representation (**Fig. 8.11**), with closed pores and potential silica particles highlighted in purple and connected pores and matrix set as an 85% transparent background to show close pores dispersion.

Table 8.12 Pore size distribution of GFAR related to total porosity of each sample retrieved from µCT.

	[0-10)	[10,50)	[50,100)	[100,700]	<700
Ref	24.51	1.12	0.53	22.96	13.13
AG1-10	22.09	1.64	1.12	25.65	12.18
AG2-10	21.24	1.40	1.04	24.45	18.91
AG3-10	20.02	1.46	1.27	24.26	21.49
AG4-10	17.45	1.14	0.92	17.81	32.24

The interconnected pore separation displays the closed pores as well as any silica aerogel particles that may be distributed in the matrix. What is evident is that the disconnected portions of the smaller particles AG1 are more conspicuous. In the instance of AG1, a type of accumulation is seen, which might be silica aerogel aggregates produced in a very alkaline environment. Small particles are embedded in the gel, while larger particles are close to the pores, resulting in a low-density air-silica aerogel connection that is considered as a single-phase during this measurement.

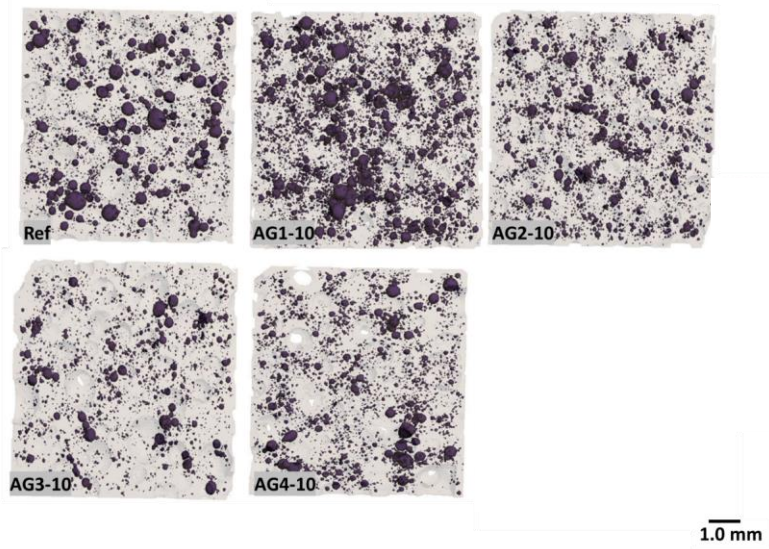

Fig. 8.11. Closed pores dispersion in GFAR calculated from µCT.

8.3.4.4 UPV analysis

The UPV test of GFAR was carried out to evaluate the internal voids and defects inside the samples. The results are shown in **Table 8.13**. The reference GFAR without silica aerogel present the highest speed to cross the sample, suggesting a more compacted structure than other samples. AG1-10 shows fewer voids or pores inside the structure than other samples with 10% silica aerogel, which is in accordance with the porosity result. However, the AG4-10 sample with the largest grain of silica aerogel shows the second-high speed among the 10% silica aerogel samples, contradicting the porosity results. Therefore, the large grains of silica aerogel is mainly existed in the pores of the GFAR rather than in the solid network of geopolymer, hence a high velocity. While the finer silica aerogels are mainly placed inside the geopolymer matrix, resulting in a slow velocity of sound. Therefore, it may indicate as evidence of the microstructure of the GFAR.

Table 8.13. UPV test of GFAR.

Groups	Ref	AG1-10	AG2-10	AG3-10	AG4-10
Speed (m/s)	1447±11	999±6	745±9	860±3	970±5

8.3.5 Insulation mechanism

The insulation mechanism of the GFAR with silica aerogel can be described and schematically shown in **Fig. 8.12**. The small particle sizes of silica aerogel, mainly the AG1 and AG2 particles, are placed more dispersed in the geopolymer matrix. However, the silica aerogels are too small in size that most of the particles are situated in the 3D network of the matrix. The larger particle size of silica aerogel, mainly for AG3 and AG4, are linked to the pores of the GFAR. It should be noted that the open porosity of the prepared geopolymer is relatively higher than other kinds of geopolymer foam concrete, thanks to the optimal selection of the surfactants (Triton 100 and SDS). The TX-100 / SDS surfactant mix has a synergistic effect in lowering surface tension [295][296], as well as increased foam generation and stability was observed [297][298]. Therefore, the number of interconnected pores is much higher than other foam concrete.

8.3.5.1 Thermal transfer

The thermal insulation mechanism of the GFAR can be explained as follows. Firstly, the thermal energy through the GFAR occurs through three mechanisms: solid conductivity, gaseous conductivity and radiative (infrared) transmission. The sum of the three components gives the total thermal conductivity of GFAR. The gaseous conductivity is relatively low due to the nature of air, achieving 0.026 W/(m·K) at room temperature. While the radiative transmission can be related to the temperatures. At room temperature, the radiative component of thermal transport is low. The solid conductivity thus becomes the most dominant component of the total thermal conductivity of GFAR. Therefore, the aerogel situated in the solid matrix can be used as a thermal barrier. The low dosage of silica aerogel can enhance the thermal insulation of the solid matrix. If the same concentration of aerogel is applied in GFAR, the same reduction effect on thermal conductivity should be reached. However, for different particle sizes

of silica aerogel, the main difference is the contact surface area of the aerogel with geopolymer matrix. Thus, the interfacial thermal resistance, which is applied in many high conductive materials, should be different. However, due to the silica aerogel already possess a lower thermal conductivity, the ITR cannot further decrease the thermal conductivity of solid. Hence, considering the higher porosity for silica aerogel with a large particle size, the lesser solid in GFAR means the lower solid conductivity could be achieved. Therefore, the advantage of the higher surface area of finer silica aerogel is not facilitated. While the larger silica aerogel could function better as a thermal insulating additive in GFAR.

8.3.5.2 Acoustic absorption

The acoustic absorption mechanism of the GFAR can be explained as follows. The geopolymer matrix can be treated as an interconnected porous structure already, as the open porosity is relatively high. However, as discussed before, the finest silica aerogels are dispersed in the solid network of geopolymers. Therefore, the sound wave cannot get in direct contact with the aerogel, hence the absorption of sound by aerogel is limited. Meanwhile, the large particles of silica aerogel could function as a large void, in addition, with much higher sound absorption. Therefore, sound transmitted through the interconnected pores can also enter the nanopores of the large silica aerogel particles, contributing to the prevention of the sound wave transmission. The small silica aerogel particles, however, has no obvious effect on the connection of the pores, therefore, showing a less positive effect on the acoustic insulation.

Another reason is the porosity increase of the GFAR. During mixing, it is found the large silica aerogel could result in higher porosity than the much smaller sized silica aerogel. This is due to the inter-particle space formed from the large particles. The packing of the materials is looser than finer silica aerogel and so the porosity and density has become lower consequently. Therefore, it is suggested to use the low dosage of silica aerogel with a large particle size.

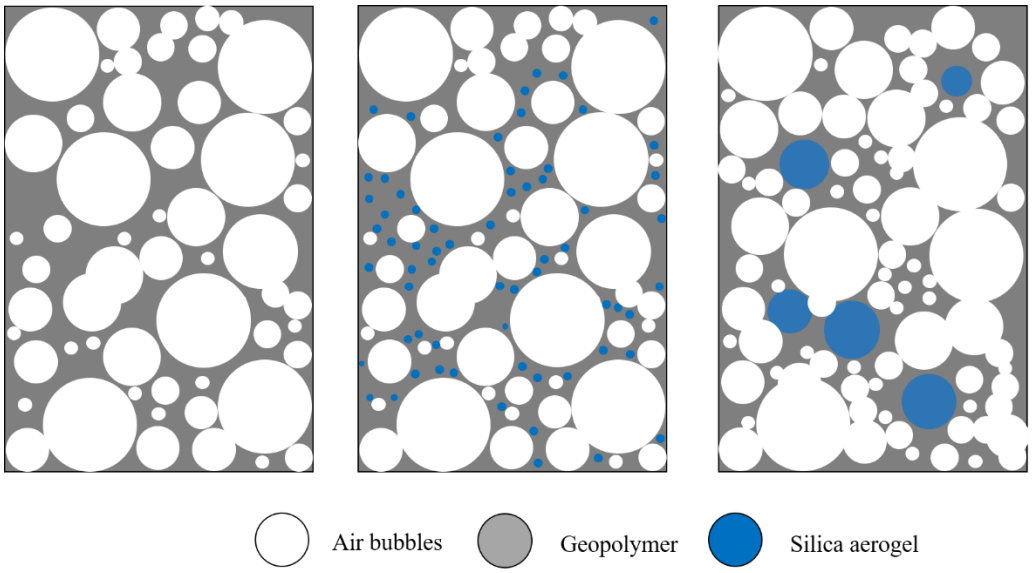

Fig. 8.12. Schematic illustration of GFAR microstructure

8.4. Conclusions

In this chapter, the performance of geopolymer foam concrete with the incorporation of silica aerogel with different particle sizes is investigated. The effect of different silica aerogels on thermal conductivity and acoustic absorption of GFAR is the focus of this study. According to the results and discussion of this research, the following conclusions can be drawn:

- The total porosity of the geopolymer foam concrete with silica aerogel is increased due to the high number of internal pores of silica aerogel. The open porosity is higher for GFAR with silica aerogel of large particle size, mainly because of the bridging effect between air bubbles.
- The acoustic absorption of geopolymer foam render with the addition of silica aerogel is much higher than the plain foam geopolymer render, which is contributed from the more open porosity in GFAR, and the inherent sound absorption property of silica aerogel itself. Silica aerogel with a larger particle size plays a better role to improve sound absorption due to the bridging effect between the pores generated from hydrogen peroxide.
- The thermal insulation property of GFAR is improved with the addition of silica aerogel. 1200 μm - 4000 μm silica aerogel has a higher increase ratio than finer aerogel particles (2-40 μm). The hygrothermal behavior is better than the plain GFR, suggested by the lower water uptake and thermal conductivity after exposure to an 80% humidity environment.
- The microstructure analysis indicates the GFAR with larger silica aerogel particles has a higher open porosity than plain GFR. The fine silica aerogel can be placed in the solid network of geopolymer matrix, while the large fraction of silica aerogel can be bridging between the pores, thus providing an additional opening**.**

It is suggested that the large particle sized aerogel could play a better role in geopolymer foam concrete than finer silica aerogel. The thermal and acoustic properties can be improved as well as the thermal performance in a high humidity environment.

Chapter 9 One-step synthesis of mesoporous silica from olivine and the pore size tuning

This chapter investigates the reaction of sulfuric acid with olivine for the synthesis of ordered mesoporous silica at low temperatures. The silicic acids released from olivine are directly guided to form high quality ordered mesoporous silica in a one-step synthesis with the use a micellar liquid crystal prepared from the non-ionic surfactant TX-100. The produced mesoporous structures feature surface areas of up to 1000 m^2/g and narrow pore size distributions around 2-4 nm. Furthermore, the pore size can be tailored into larger sizes, either by changing the surfactant to P123 or using additional swelling agent like n-heptane. The results show olivine can be a sustainable silicate source for the synthesis of well-tailored mesoporous silica, which is potential for application in nano-insulation materials or photocatalytic supports.

This chapter is partially published elsewhere:

A. Lazaro, Y.X. Chen, C. Verhoeven, Y. Hendrix, One-step synthesis of ordered mesoporous silica from olivine and its pore size tailoring, Journal of Cleaner Production 238 (2019) 117951.

9.1. Introduction

Mesoporous silica is an advanced multifunctional inorganic material with a mesoporous network that is being developed since the early 1990s' [299]. This type of silica has a high surface area, relatively uniform pore size distribution within the mesoporous range (2~50 nm) [57,300]. Thanks to its unique properties, it is now widely applied in many advanced fields, for instance, molecular sieve, catalytic support, biosensor, drug delivery and nano-insulation materials [58,301–303]. Currently, the most common types of mesoporous silica are MCM-41 and SBA-15. Mesoporous silica is normally produced from organic precursors like TEOS or TMOS with the Stöber process and with surfactants forming the template for silica to grow onto, for instance, CTAB, Triton X-100 and P123 [304]. The pore structures and particle size can be varied depending on the type of surfactants and the processing conditions.

The preparations of mesoporous silica have been widely investigated during the last decades. One of the directions is the reduction of the energy consumption and material cost to produce mesoporous silicas on a large-scale [302,305]. In that way, the silica can be produced in a cost-effective way so that it can be applied in the fields where large quantities of mesoporous silica are needed, for example, as nano-insulation materials (NIM) or photocatalytic support for NO_x degradation [209]. Generally, there are two ways to make it more cost-effective: 1) Reduce the amount of solvent used, like by using solvent-free preparation [306] and 2) using cost-effective silica sources like rice husk ash and fly ash [307,308]. However, most of these silica sources need a two-step preparation process, i.e. first water glass preparation and then mesoporous silica synthesis from the water glass [198,309]. Therefore, finding a facile and high-quality one-step preparation is of significantly importance, which contributes to produce high-quality and cost-effective mesoporous silica.

The recently developed novel method to synthesize nano-silica is to extract it from olivine [59,302]. Previous investigations show that the nano-silica synthesized from olivine is cost-effective and produced at low temperatures [60]. Olivine is widely abundant in the earth crust and rich in silica (~44%). Thus, it is widely available to produce mesoporous silica. The mechanism of this method is the silica monomers released and precipitated when olivine reacts with acidic solutions at 50~90 ℃, which is explained in Chapter 1. This reaction is exothermic and releases heat, lowering the energy consumption even further. The formed olivine nano-silica contains pores with a random size distribution. Therefore, some researchers have already used this green and cost-effective nano-silica as a support to load titania to be the composite photocatalyst for the abatement of NO_x pollutants [208,303]. The conversion efficiency of converting NO_x into nitrate is relatively high with the resulting composite. The titania is supported on the silica in a randomly distributed style and titania can be situated at the surface and inter-particle pores. However, this disordered nanostructure may prevent the evenly spread of titania onto the silica support, and thus limit the further increase of the photocatalytic efficiency. Hence, it is interesting to prepare a more uniform nanostructured mesoporous silica that can load the titania into the mesopores of silica.

The liquid crystal template method is a typical way to synthesize ordered mesoporous silica. Since the silicic acids released from olivine in solution are the basic units for any silica-based structure, they can easily attach chemically onto the non-ionic template to form self-assembly

ordered structures. According to previous research [57], non-ionic surfactants, Triton X-100 and P123, can be applied to synthesize MCM-41 and SBA-15 like mesoporous silica structures, with an average pore size of 2~4 nm and 5~30 nm, respectively. Since P123 has a large molecular mass and long chain, the formed organic template can be much larger than TX100. Thus, it can be speculated that the prepared silica has a larger mesopores than silica produced using TX100.

Further, the adaptation of the pore size for a certain application plays a very important role. The size of these pores in mesoporous silica can be altered by different methods. One of these methods is the use of a swelling agent. A swelling agent is typically a strong non-polar molecule. It is commonly added after the addition of the surfactant to the polar aqueous mixture, and after the micelles start to form. The non-polar swelling agent is introduced into the core of the micelles, forcing them to grow. The size and morphology of the micelles are dependent on the kind of swelling agent used. In this study, n-heptane is used as a swelling agent. This swelling agent can interact with PPO blocks of the surfactant via dipole / dipole attraction. The polarity of the PPO units can also bring about dipole moments in the hydrophobic hydrocarbons of n-heptane. The interaction of the swelling agent with the corona PEO parts of the surfactant or with the acidic water is unlikely or insignificant due to the lack of miscibility. If any interactions remain to exist, they would likely be weak Van der Waals attractive forces.

Based on the research of a former study, it is demonstrated that the optimal particle size of anatase is around 10~15 nm for a better photocatalytic activity. Therefore, it is desirable to enlarge the pore size of the silica support to around 10~15 nm, thus the anatase crystals can be loaded into the pores and be evenly spread throughout the large specific surface areas of the silica substrate. Thus, P123, a non-ionic and large molecular mass surfactant, is expected to be the candidate that can enlarge the pore size of silica while maintaining the ordered structure. Under the hypothesis mentioned above, the silica may become a better silica support for crystalized titania.

In this study, development of mesoporous silicas with a narrow and large pore size from olivine by using Triton X-100 and P123 was investigated. The effect of surfactant concentration and pore swelling agent on the pore structure of silica was studied. Finally, the produced mesoporous silica was used as photocatalytic support for titania, and the performance of silica-titania catalyst was evaluated by PCO test. The microstructure of mesoporous silica and resulted titania-silica catalyst were observed through TEM and nitrogen physisorption. Overall, the green synthesis of mesoporous silica from olivine is a promising method to produce large quantities of low-cost high-quality mesoporous silica.

9.2. Materials and experiments

9.2.1 Raw materials

Olivine was supplied by Eurogrit. The chemical composition of the olivine is listed in **Table 9.1**. The grain size of the olivine is between 0.10 mm and 0.50 mm. The BET surface area of olivine particles is from 0.22 to 0.28 m^2/g.

Table 9.1. Chemical composition of olivine.

Composition	MgO	Fe_2O_3	SiO_2	Cr_2O_3	Al_2O_3	NiO	MnO	CaO	LOI*
wt%	49.3	7.32	41.4	0.31	0.46	0.32	0.09	0.15	0.59

Aside from the olivine, sulfuric acid (H_2SO_4, 50%, VWR), n-heptane (C_7H_{16}, Analytic grade, Biosolve) and non-ionic surfactant Triton X-100 and Pluronic P123 were used to produce the mesoporous silica. Distilled water was used during the whole experiment. Commercial mesoporous silica was provided by Glantreo Ltd. as a reference, named as OMS-GT in this study. This silica has a large pore size around 12 nm and the pore structure is relatively uniform with a hexagonal shape.

9.2.2 Synthetic procedure of mesoporous silica from olivine

9.2.2.1 Triton X-100 as non-ionic surfactant

The schematic process of OMS production is shown in **Fig. 9.1**. The main procedure to synthesize the ordered mesoporous silica with olivine as precursor was described as follows: Firstly, Triton X-100 was dissolved in a 3M H_2SO_4 solution at 50 °C and stirred continuously for 24 hours. For the preparation of OMS with enlarged pore size, heptane or ethanol was mixed as a swelling agent at this step. The temperature of 50 °C was chosen since it is just below the cloud point (63~69 °C) of Triton X-100, but still high enough to be a suitable temperature for the reaction of olivine with acid. Then, olivine particles were quickly added to this mixture. The mixture was kept being stirred and heated at 50 °C for 48 hours. Afterwards, the formed mesoporous silica was separated from the unreacted residues by centrifugation, followed by decantation of the low-density silica. The produced silica was then aged at 60 °C in an oven overnight. Afterwards, the aged silica was diluted with distilled water for filtration. The produced mesoporous silica was then washed with a diluted H_2SO_4 solution (0.1 M) to prevent recrystallization of the sulfate salts and then washed several times with distilled water. The washed mesoporous silica was dried at 60 °C overnight. Lastly, the remaining surfactants in the mesoporous silica were removed by calcination in an oven at 550 °C for 6 hours.

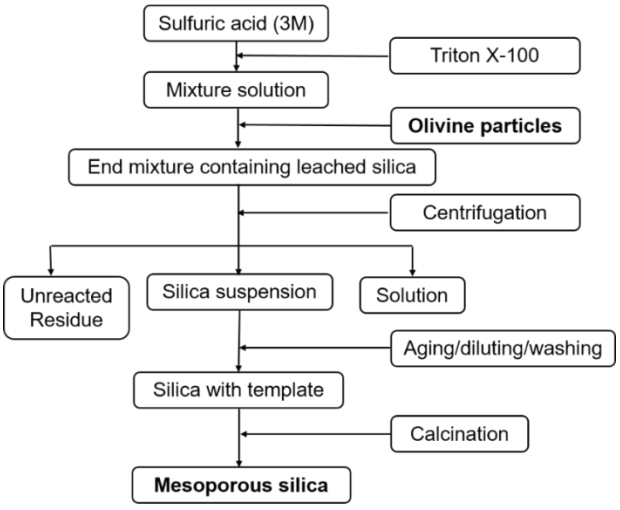

Fig. 9.1. Flowchart for the preparation of ordered mesoporous silica from olivine.

9.2.2.2 P123 as non-ionic surfactant

Firstly, P123 was dissolved in a 3M H_2SO_4 solution at temperatures of 40 ºC. This temperature is chosen according to the cloud point (50 ºC) and critical micelle temperature (CMT) of P123. This mixed solution was stirred at 600 rpm for 2 hours at 40 ℃. Swelling additive n-heptane was added afterwards and stirred for another 3 hours. Finally, the olivine was added to the solution and stirred for 48 hours. After the formation of the mesoporous silica, the separation step commences. This step was again depended on the surfactant and the additives that were added. Typically, the use of block-co polymer surfactants like P123 needs to be diluted before the separation process due to high viscosity. The amount of 0.1 M H_2SO_4 solution to dilute the end mixture was depends on the viscosity of the solution. Afterwards the silica solution was filtrated to remove bigger particles using a sieve, separating the unreacted olivine from the solution. This solution was then further separated by centrifuging. The preferred outcome of centrifuging is that the low-density silica will float on the top layer of the mixture, so it can easily be decantated (**Fig. 9.2**). The solid silica was again diluted and filtered with the use of a Büchner funnel. After a filter cake was formed, the silica was washed two times using the funnel with 2L of 0.1 M H_2SO_4 solution and then with 2L of distilled water. Then, the silica was dried overnight at 40 °C. Afterwards the silica was calcinated at 550°C for 4 hours. The silica agglomerates were then milled into powder to obtain the high purity mesoporous silica.

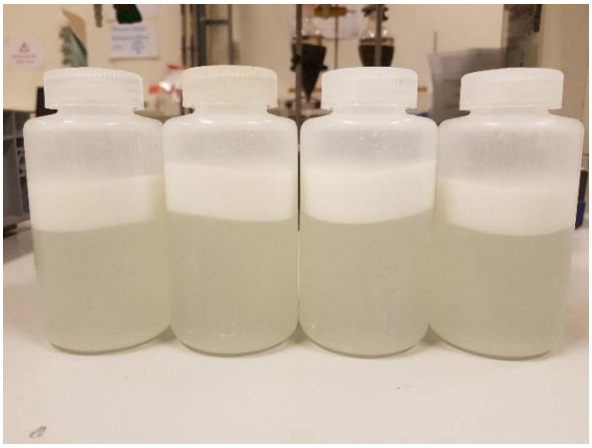

Fig. 9.2. Silica suspension after centrifugation (Upper layer: silica suspension; Middle layer: waste solution; Bottom: unreacted olivine).

9.2.3 Recipe for OMS preparation

Table 9.2 presents the different mix designs for preparation of mesoporous silica from olivine. Firstly, it is designed to investigate the influence of TX100 and P123 on the properties of OMS. This is important because the type of surfactant used in solution influences the shape of the liquid crystal and the viscosity of the mixtures. Secondly, the influence of the swelling agent n-heptane on the properties of mesoporous silica was investigated, especially the pore size distribution of the produced OMS.

Table 9.2. The recipe of mesoporous silica production from olivine.

Group	Olivine (g)	TX-100 (g)	P123 (g)	3M H_2SO_4 (ml)	n-heptane (g)	T (℃)
REF	90	0	0	500	0	50
OMS-T	90	120	0	500	0	50
OMS-TH1	90	120	0	500	120	50
OMS-TH2	90	120	0	500	180	50
OMS-P1	90	0	30	500	0	40
OMS-P2	90	0	45	500	0	40
OMS-PH1	90	0	30	500	120	40
OMS-PH2	90	0	45	500	120	40

9.2.4 Development of silica-titania composite photocatalyst coatings

The silica supported titania photocatalyst was prepared according to Chapter 5. It showed titania can be coated on the silica particles by using a precipitation method. The procedure can be specifically described as follows:

First, mesoporous silicas were milled into fine powder by using a mortar and then dried at 105 ℃ to remove physical bond water. After drying, 1 g of mesoporous silica was placed in a beaker and dispersed in ethanol slowly. The pH of silica the dispersion was measured and later lowered to 3~4 with a few drops of 50% H_2SO_4. Then 3.55 g TP was quickly dissolved in 60 ml ethanol and added into the silica dispersion in the thermostat reactor. A syringe pump was used to add a water/ethanol solution into the reactor at a rate of 2 ml/h. The ratio of water to ethanol was 7g/21g until the water volume percent reached 2.5%. After the addition of water, the suspension was filtrated, and the filter cake was obtained. The filter cake was dried at 120 ℃ for 6 hours to remove extra water. The silica-titania composite was then calcined at 300 ℃ for 3 hours to transform amorphous TiO_2 to crystalized anatase. Finally, the silica-titania composite catalyst was milled to fine powder and 1 g of the catalyst was taken and mixed with 10ml distilled water. A coating was formed by spreading the dispersion onto a glass plate of 20×10 cm^2 after which most of the water was evaporated at room temperature overnight.

9.2.5 Characterization

Nitrogen physisorption was performed with a Tristar II equipment at 77 K using liquid nitrogen to determine the specific surface area of OMS using the BET theory and the pore size distribution using the BJH theory. Small angle X-ray diffraction was carried out to determine the ordered mesoporous structure of OMS. For a microstructure analysis, transmission electron microscopy (TEM) was performed using a Tecnai 20 microscope, operated at 200 kV. For assessment of thermal stability, thermogravimetric curves of OMS were measured by a thermogravimeter and differential scanning calorimeter (TG/DSC), which was conducted in a NETZSCH STA449-F1 equipment in the range of room temperature to 1000 ℃ with a heating rate of 10 ℃/min^{-1} under nitrogen atmosphere. For the confirmation of the removal of the

template, a Fourier transform infrared spectroscopy (FTIR) test was performed with a Varian 3100 equipment with the wavenumbers ranging from 4000 to 400 cm^{-1} at a resolution of 1 cm^{-1}. To compare the photocatalytic properties of all synthesized TS, their photocatalytic conversion ability was determined by oxidizing the pollutant NO under UV-light irradiation. The resulting photocatalytic properties of titania-silica composites were evaluated by testing their photocatalytic conversion of NO under UV-light using the ISO 22197-1 standard for comparative purpose. The detailed procedure can be found in Chapter 5.

9.3. Results and discussion

9.3.1 Properties of mesoporous silica from olivine

9.3.1.1 Specific surface area and pore structure

The specific surface area and pore size distribution of mesoporous silica produced from olivine is shown in **Fig. 9.3.** The pore structure of the prepared silicas all possesses type IV isotherm except REF, indicating that the silica produced with the liquid template have a mesoporous structure. The REF silica prepared without surfactant shows a very broad pore size distribution ranging from 2 nm to 90 nm. The pore structure of REF includes micropores (less than 2 nm), mesopores (2-50 nm) and macropores (beyond 50 nm). This is due to the formation mechanism of olivine silica in acid. The silica monomers being released from olivine first reach a supersaturation state in solution and then nucleate into primary particles. The amount of silica primary particles increases and contribute to the particles forming secondary particles and further link into branched chains and networks. The micropores are mainly attributed to the inter-particle pores between the primary silica particles. While the mesopores are mainly from the interparticle pores between the secondary particles. Therefore, the pore size of REF is randomly distributed and covers a wide range. From **Fig. 9.3**. it is observed that the most probable average pore size should be around 40~50 nm.

On the other hand, the OMS-T silica shows a very tiny hysteresis loop due to the narrow pores of around 2~3 nm. The reason of this phenomena is the small template that TX100 formed in the highly concentrated ionic solutions during the olivine silica synthesis. Thus, silica monomers are deposited on the liquid template formed by TX100 and continue grow into silica particles. The hydrophilic head of TX100 can link to the silanol groups of silicic acid forming the assembly. Once the template is removed from calcination, the ordered mesoporous silica can be produced. The specific surface area of OMS-T is relatively high, reaching 901 m^2/g, which is caused by the thinner pore walls and tiny pores formed in the nanostructure of silica.

The OMS-P1 has much larger pore sizes compared to the OMS-T, with average pore sizes around 10.4 nm. The bigger pore size is attributed to the larger liquid template formed by P123, which is a triblock copolymer with PEO-PPO-PEO liner chains. The silicic acid released from olivine can be attached to the PEO block head and grow into thicker silica walls compared to TX100. It is because more silicic acid is needed to form the larger hollow spheres and thus the pore walls become thicker. Therefore, the specific surface area also decreased to 700 m^2/g compared to OMS-T. Moreover, the pore volume increases to 1.36 cm^3/g which is doubled compared to the OMS-T. However, the uniformity of pores is not as good as the OMS-T silica, showing a pore size ranging from 5 nm to 20 nm.

The reference OMS-GT, however, has an average pore size of 8~9 nm with a relatively uniform pore size distribution. The isotherm is a typical IV isotherm with a large hysteresis loop. The sharp increase of nitrogen absorbed at relatively pressure of 0.7 indicate the uniform pore structures. Compared to OMS-P, the OMS-GT has a smaller pore size but uniform structure. They both contain the H1 hysteresis loop indicating a cylindrical geometry and a facile pore connectivity. The surface area of OMS-GT is slightly lower than OMS-P, however it has a larger pore volume (1.65 cm^3/g), suggesting a more porous structure than P123.

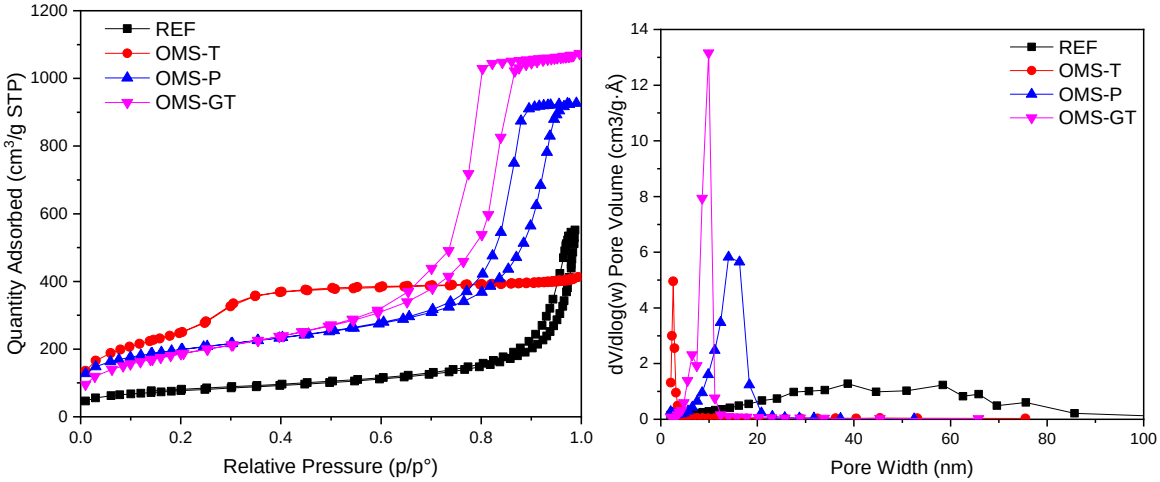

Fig. 9.3. Nitrogen physisorption isotherm and pore size distribution of mesoporous silicas.

Table 9.3. Specific surface area, average pore size and pore volume of the silicas.

Groups	SSA $_{BET}$ (m^2/g)	d_{p-A} (nm)	d_{p-D} (nm)	Pore volume (cm^3/g)
REF	274	16.0	15.9	0.71
OMS-T	901	2.8	2.8	0.63
OMS-P1	700	11.2	10.4	1.36
OMS-GT	682	9.0	8.2	1.65

d_{p-A}: Pore size from adsorption branch; d_{p-D}: Pore size from desorption branch.

9.3.1.2 TEM

The TEM images of the four silicas are shown in **Fig. 9.4**. As can be seen, the ONS shows a randomly distributed silica particles with cross-linking chain network. It is clear the interparticle mesopores are relatively large and range from 20-50 nm. The average pore size determined by BJH method are similar, indicating the inter-particle pores is attributed to the void among the secondary particles in the agglomerate. The silica primary particle size is small, ranging from 2 nm to 5 nm. However, the silica particles are at a highly agglomerated conditions, which is typical for silicas synthesized at pH below the isoelectric point. The pore size in the TEM image shows the same range as calculated by the BJH method.

The OMS-T sample has much larger secondary particles than REF, however it has a more uniform pore structure. This image shows ordered cylindrical pores which is similar to the pores of MCM-41. The average pore size of this sample is observed using software to be 4.1 nm with a standard deviation of 0.3 nm. This result is slightly higher than that determined by the BJH

method. Some researchers demonstrate BJH method could underestimate the pore size below 10 nm, due to the difficulty in separation of mono-multilayer adsorption from micropore filling.

OMS-P1 has a random and larger pore structure than OMS-T. As can be seen from **Fig. 9.4.(c)**, it shows the presence of a non-uniform wormlike structure with narrow mouths. Results of the gas-physisorption isotherm and pore size distribution of OMS-P1 indicate the presence of pores with narrow necks with a relatively uniform channel-like pores, which is in agreement with the TEM observation. The black spots that is visible on the center on both pictures of the silica agglomerate is a sign that there are several layers of silica on top of each other.

The TEM image of the OMS-GT silica shows a clear cylindrical pore geometry of the silica particles. It also confirms that the pores are uniformly distributed. Therefore, GT silica prepared from organic precursor has a more uniform morphology than prepared from olivine.

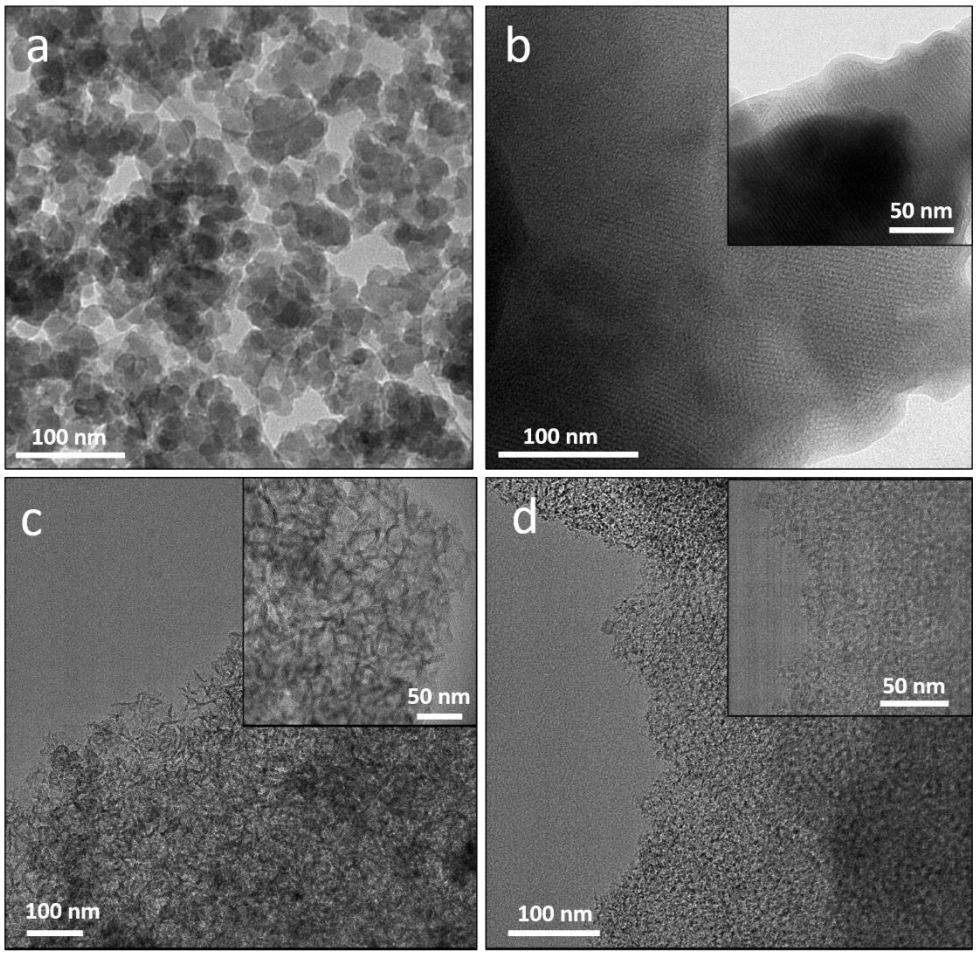

Fig. 9.4. TEM of mesoporous silicas (a) REF (b) OMS-T (c) OMS-P (d) OMS-GT.

9.3.2 Pore size tailoring by n-heptane

9.3.2.1 Influence of n-heptane on OMS-TH

The results of nitrogen physisorption of the swelled OMS samples with addition of n-heptane are shown in **Fig. 9.5.** All physisorption isotherms of mesoporous silicas show a large hysteresis loop which corresponds to a type IV isotherm. The slope of the adsorption curve slightly increased due to capillary condensation takes place at p/p_0 0.50. The change of the

curve shows the homogeneity in pore size distribution of the swelled OMS with heptane because the p/p_0 position of the inflection point is related to the pore diameter [310]. The pore size distribution is narrow and centered at around 7.2 nm (**Fig. 9.5.** (b)).

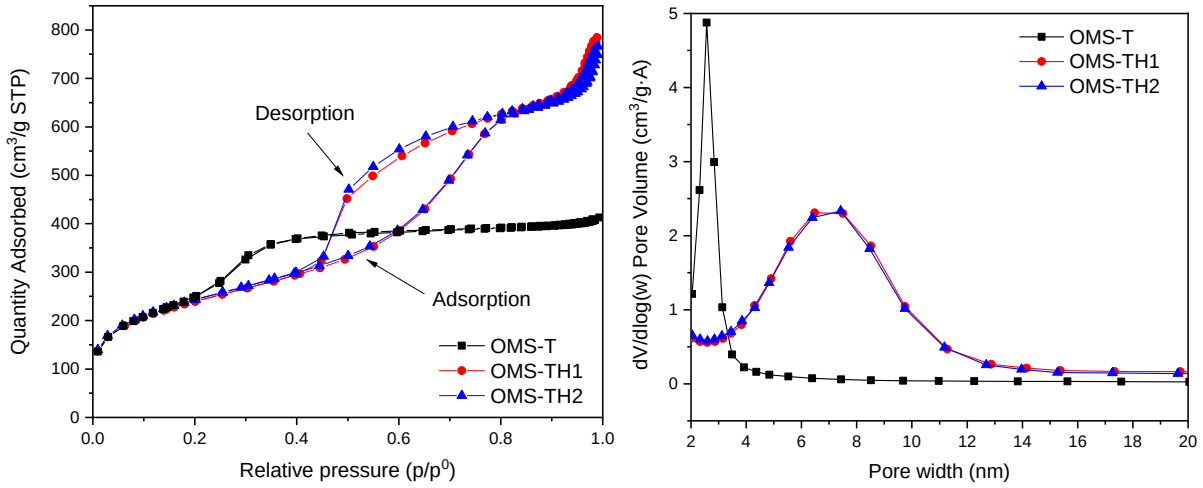

(a) (b)

Fig. 9.5. Nitrogen physisorption results of OMS with heptane and ethanol addition. (a) Physisorption isotherm (b) Pore size distribution.

Table 9.4. SSA_{BET} and pore width of synthesized OMS with heptane addition.

Group	Heptane (g)	SSA_{BET} (m^2/g)	Average Pore width (nm)	Pore volume (cm^3/g)
OMS-T	0	901	2.8	0.63
OMS-TH1	120	860	5.2	1.158
OMS-TH2	180	872	5.0	1.125

Table 9.4 presents the difference of the specific surface area and average pore width with the increase of the heptane/Trition X-100 molar ratio. The average pore width of OMS increased from 2.5 to 5.2 nm from OMS-T to OMS-TH1, and then it remained constant for OMS-TH2. This phenomena indicates that the addition of more heptane has no further effect on the pore width of OMS with addition of heptane, which is in agreement with previous research [310]. The pore volume also increased from 0.55 to 1.15 cm^3/g simultaneously from OMS-T to OMS-TH1. However, the specific surface area of OMS-T decreased from 901 to 860 m^2/g, which could be attributed to the increased silica wall thickness and the coarsening of the silica structure. This finding is in agreement with other researchers [311], demonstrating the pore wall thickness was found to increase as the pore size increased.

The swelling effect was mainly due to the apolar heptane molecules being energetically favorable inside the core of the micellar structure of the surfactant molecules. Therefore, the expanding mechanism for heptane as expander involves one molecule of surfactant for one molecule of expander. The optimized heptane to Triton X-100 ratio is one according to the results, although complementary investigations are still needed to make any further conclusions.

9.3.2.2 Influence of heptane on OMS-PH

The results of nitrogen physisorption of the swelled OMS-P samples with addition of n-heptane are shown in **Fig. 9.6.** It is shown from the isotherms of the OMS-PH that the addition of heptane has a significant influence on the adsorption/desorption curve. Both curves become steeper at a high relative pressure and reach a higher overall adsorption than the samples without heptane. It also makes the adsorption/desorption plots behave more parallel to each other.

Comparing the isotherm curves from OMS-P1 and OMS-P2 in **Fig. 9.6 (a)**, it is shown that the increasing amount of P123 has a positive influence on total amount of nitrogen adsorption of the silica. In the comparison of the isotherms OMS-PH1 and OMS-PH2, it shows that the increment of P123 concentration also slightly steepens the adsorption curve.

Comparing the pore size distribution of OMS-P in **Fig. 9.6 (b)**, it shows that the average pore size of mesoporous silica increases when heptane is added. In the case of the OMS-P1, the results show that the addition of heptane resulted in a dramatic increase of the relative pore size (peaks from 8 to 12 nm). A similar growth is visible for the batches containing OMS-PH2, where the pore size peaks moved from 9 to 16 nm. Moreover, an overall increase of the total pore volume is also a result of the addition of heptane.

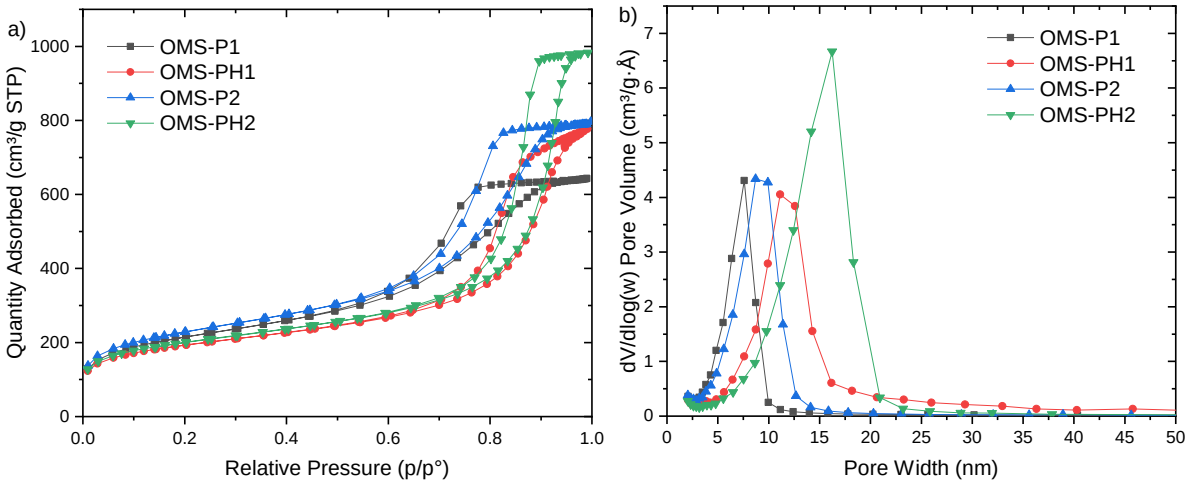

Fig. 9.6. Nitrogen physisorption results of OMS-P with heptane addition. **(a)** Physisorption isotherm **(b)** Pore size distribution.

It is also found that an increase in concentration of P123 surfactant results in growth of roughly 57% the overall pore size. In the case of OMS-P1 and OMS-P2, where no heptane was added, the pore width peaks moved from 8 to 9 nm. For the OMS-PH1 and OMS-PH2, with the addition of heptane, there was an increase of 38%, the peaks moved from 12 to 16 nm. There was also an overall increase of the total pore volume as a result of the addition of extra P123 surfactant.

Table 9.5. SSA_{BET} and pore width of synthesized OMS-P with heptane addition.

Group	Heptane (g)	P123 (g)	SSA_{BET} (m^2/g)	Average Pore width (nm)	Pore volume (cm^3/g)
OMS-P1	0	30	764	6.2	0.99
OMS-P1	0	45	815	7.3	1.22
OMS-PH1	100	30	680	9.7	1.14
OMS-PH2	100	45	708	11.6	1.48

9.3.3 Thermal stability of the prepared OMS

Fig. 9.7 shows the thermal stability of OMS-T and OMS-P1 characterized by thermogravimeter and differential scanning calorimeter (TG/DSC). All test specimens present a significant mass reduction until about 100 °C due to the evaporation of physically bound water in the mesoporous silica. In the range from 100 to 1000 °C the mass loss of OMS-T is significantly higher than that of OMS-P1. The reason of the mass loss in this range is mainly due to the condensation of Si-OH bonds transformed to Si-O-Si bonds. This reaction reduces the mass and also decrease the SSA and pore volume of OMS [312]. From Fig. 8 it is concluded that the OMS-P1 has a better thermal stability than OMS-T. The reason behind this may be attributed to the thicker silica wall, which is also found by other researchers [312].

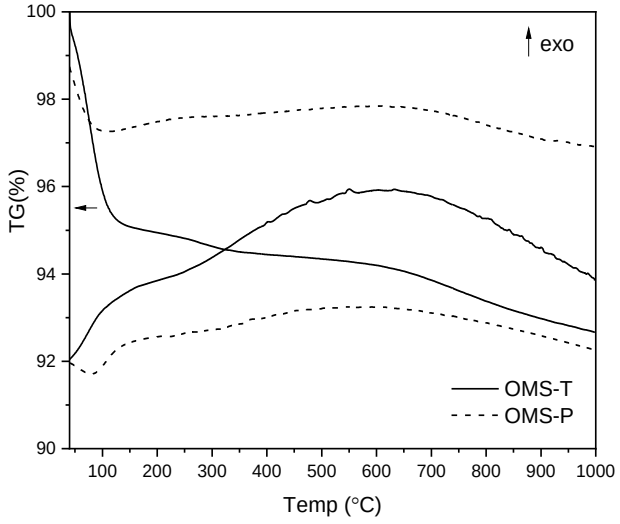

Fig. 9.7 TG and DSC curves of OMS-T and OMS-P from 40 to 1000 °C at a heating rate of 10 °C/min.

The FT-IR spectra of OMS-T and OMS-P after calcination at 550 °C for template removal is presented in **Fig. 9.8**. As confirmed by the FT-IR spectra, the calcination completely removed the TX100 templates. No alkyl bonds were observed in the spectra and only Si-O-Si bonds and Si-OH bond appeared in the spectra. The drawbacks of calcination are the non-recovery of surfactants and the sacrifice of surface hydroxyl groups. However, OMS-T shows a moderate characteristic peak of Si-OH bond at 962 cm^{-1}, indicating OMS-T obtains more silanol groups than that of OMS-P.

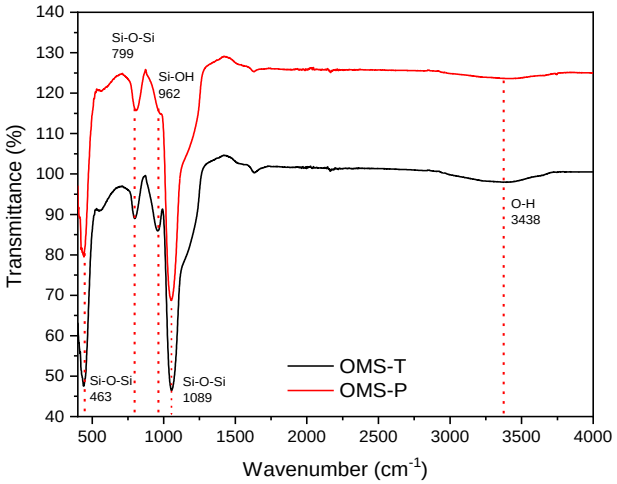

Fig. 9.8. FT-IR spectra of OMS-T and OMS-P1.

9.3.4 Photocatalytic efficiency of abatement of nitrogen oxide pollution

The NO_x abatement efficiency of the four developed TS photocatalyst is presented in Fig. 9.9. and Table 9.6. As observed, all the catalysts can oxidize NO into NO_2 and NO_x to some degree. When the UV light is on, the NO concentration decreased significantly, and the NO_2 is generated and the concentration increased. NO_x is the total concentration of NO and NO_2. It can be noticed the best NO conversion of TS photocatalysts is OMS-GT-TiO_2, reaching 86.5%. The followed photocatalysts are REF-TiO_2 and OMS-P-TiO_2, achieving NO conversion of 79.3% and 64.9%, respectively. The worst photocatalyst is OMS-T-TiO_2 with only 41.1% NO conversion degree.

REF-TiO_2 composite has the second best photocatalyst performance because the support does not contain an ordered mesoporous microstructure or a high surface area. However, it has a relatively high silanol content and large mesopores which indicates a good bonding with titania crystals. Furthermore, the inter-particle mesopores help creating the space for anatase crystals to settle.

Although the TX100-silica has a high potential as silica support for the TS due to its high SSA, the result of the photocatalytic activity test shows a poor NO conversion efficiency of only 41% to NO_2 and 7.4% to NO_x. The low conversion of NO can be attributed to the very small pore sizes of the applied TX100-silica. The average pore size was measured to be around 3.7 nm while the crystal size of the anatase was measured to be 10.2 nm according to XRD. Therefore, it is impossible to make a good spread of the anatase crystals on the substrate.

The P123-TS composite catalyst show a relatively better PCO compared to TX100-TS. Although the uniformity of the P123 silica microstructure is lower than TX100, the better performance is probably attributed to the larger pore size of the silica substrate. The best photocatalyst is GT-TS composite with a NO conversion degree of 86.5%. Hence, it is indicated the better uniformity of pore size distribution and relatively large pore size can result in very promising TS photocatalyst.

Overall, the mesoporous silica products that had pore size distributions that are too small to incorporate titania for photocatalysis showed only a low NO_x conversion efficiency. The high surface area of silica is not a decisive factor influencing the PCO efficiency. Titania coated

using the precipitation method on the ordered mesoporous nanostructured silicas with uniform pore size above 10 nm appeared to be the best silica support for titania photocatalysis.

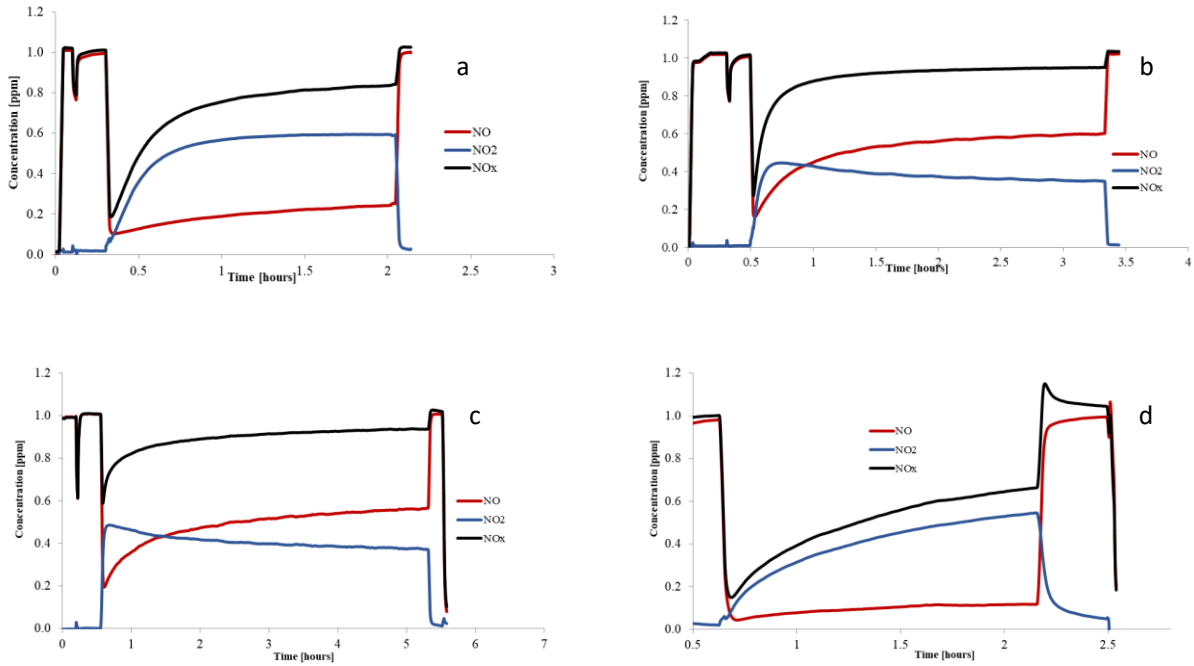

Fig. 9.9. PCO efficiency of four TS photocatalysts for abatement of NO, NO_2 and NO_x.: (a) REF-TiO_2 (b) OMS-T-TiO_2 (c) OMS-P-TiO_2 (d) OMS-GT-TiO_2

Table 9.6. Properties of the prepared TS photocatalysts.

Sample	NO conversion (%)	SSA_{BET} (m^2/g)	Anatase crystal size (nm)	Ti-O-Si bond ratio
REF-TS	79.3	199	11.0	0.089
OMS-T-TS	41.1	684	10.2	0.092
OMS-P-TS	64.9	382	14.3	0.075
OMS-GT-TS	86.5	414	12.0	0.085

9.3.5 Implications on the sustainability and application

By applying the reaction of sulfuric acid with the silicate mineral olivine instead of other silica sources, a more cost-effective and low energy production of ordered mesoporous silica could be achieved. The prepared OMS samples have similar properties to MCM-41, which has been widely investigated since its invention. MCM-41 can be produced by either an organic precursor or alternative silica sources (For instance, fly ash and rice husk ash). **Table 9.7** shows the properties and synthesis conditions of different kinds of MCM-41 to make a comparison with the OMS in this work.

The majority of commercial MCM-41 are produced from organic precursors, which are expensive and energy intensive. Although the synthetic condition of MCM-41 is relatively wide and normally requires only 3~5 min to form the ordered structures, the synthesis also includes a long hydrothermal treatment, for example, three days at 100 °C [313]. The same condition is also observed in MCM-41 production from fumed silica as shown in **Table 9.7**. Furthermore, for the synthesis of MCM-41 with alternative silica sources [307,309,314], most of the

production methods include a silica extraction process. Normally, the silica source has to first react with sodium hydroxide (NaOH) at elevated temperatures for several days to form sodium silicate and then by using the sodium silicate and a traditional method MCM-41 is produced. The two-step process is time consuming and requires more energy than the one-step synthesis.

Table 9.7 Comparison of different kinds of MCM-41 made from different precursors.

Mesoporous silica	SSA_{BET} (m^2/g)	Pore size (nm)	Conditions/ Temperature	Precursor	Literature
Normal OMS	~1000	2.5~3.0	Precipitation, 50 °C, 2 days	Olivine	This study
Heptane OMS	~870	~6.0	Precipitation, 50 °C, 2 days	Olivine	This study
MCM-41	~900	~3.8	Hydrothermal, 100 °C, 3 days	TEOS	[313]
MCM-41	~1020	~3.4	Autoclave, 150 °C, 2 days	Fumed silica	[315]
MCM-41	950~1150	~2.8	Two-step synthesis	Coal fly ash	[307]
MCM-48	~1024	~2.6	Two-step synthesis	Rice husk ash	[314]
MCM-41	~992	2.0~3.8	Two-step synthesis	Bottom ash	[309]

The novelty of the one-step synthesis from olivine is that silicic acid can be directly guided to form silica layers around the liquid template without the silica extraction from the raw materials, so this process requires less energy and resources. In addition, the temperature of this synthesis process is only 50 °C and exothermic. Moreover, olivine from dunite rocks is a cost-effective silica source and can be found as a byproduct from the magnesite industry, which makes this synthesis process even more attractive from the sustainability point of view.

The addition of heptane increased the pore size of OMS, indicating this material can be tailored to meet the demand for more applications. For example, the increase in pore size distribution shows that OMS is a possible support for a catalyst that can reduce NO_x by incorporating titania [316,317]. Furthermore, other applications like CO_2 capture and drug delivery can be applied by using OMS, where large amounts of mesoporous silica are demanded.

9.4. Conclusions

Mesoporous silica is directly produced with one-step synthesis by the dissolution of olivine in sulfuric acid during 48 h of reaction at low temperature (50 °C). The non-ionic surfactant, Triton X-100 and Pluronic P123 are proved to successfully forming the desired micelles in the high ion concentration and negative pH environment. This study demonstrates that converting olivine into mesoporous silica turns a common mineral into a high additional value product using a green process. The method provides another way of applying olivine in high-end application. According to the current results, the following conclusions can be drawn:

- OMS prepared using Triton X-100 has a high surface area of more than 900 m^2/g with pore sizes of around 2.8 nm. Swelling agent n-heptane enlarges the average pore size of this mesoporous silica from 2.8 nm to 5.2 nm.

- OMS prepared using P123 has a surface area of more than 700 m^2/g with pore sizes of around 7-8 nm. Swelling agent n-heptane enlarges the average pore size of this mesoporous silica from 8 nm to 11.2 nm.
- The TEM image of OMS-T shows a long-ranged ordered tubular structure of the mesoporous network inside the particles. While the OMS-P shows the presence of a non-uniform wormlike structure with narrow mouths. The TEM results confirm a cylindrical pore geometry of the commercial Glantreo silica and a uniform distributed pore geometry.
- It is shown that mesoporous silica with a uniform pore size distribution with pore size larger than ~10 nm is the best silica support for titania by using a precipitation method. Therefore, a large pore size mesoporous silica with uniform pore size distribution from olivine is encouraging and promising in the future work.

Chapter 10 Highly dispersed colloidal olivine nano-silica and its effect on the rheology and hydration of ultrahigh performance concrete

This chapter investigates the novel application of highly-dispersed olivine nano-silica in ultrahigh performance concrete (UHPC). Nano-silica is an important admixture for ultrahigh performance concrete (UHPC). However, the limitations of nano-silica applied in UHPC are the complex production process and its dispersion problem. In this chapter, a novel colloidal nano-silica is produced from olivine via acid extraction at low temperatures (50~90 ℃) and further grinded with a colloidal mill to break up the agglomerates. The properties of olivine colloidal nano-silica (C-OnS) are characterized with laser light scattering (LLS), nuclear magnetic resonance (NMR), zeta-potential and X-ray florescence (XRF). The highly dispersed C-OnS is applied as an admixture to enhance the cement hydration of UHPC, thanks to its strong pozzolanic reactivity at early age compared to commercial colloidal nano-silica (C-nS). The effect of C-OnS and C-nS on UHPC is systematically compared by calorimetry, thermal gravimetry (TG), nuclear magnetic resonance (NMR), nitrogen physisorption and mercury intrusion porosimeter (MIP). The results show that the performance of UHPC is enhanced by substituting cement with the novel C-OnS and is even better than that with C-nS at early ages (1, 3, 7 days). The advantages of sustainability, strong pozzolanic reactivity and tailorable particle size thus opens up new possibilities in modifying the olivine silica to meet the demand of building materials industry.

This chapter is partially from the following article:

Y.X. Chen, S. Li, R. Yu, B. Mezari, E.J.M. Hensen, K. Schollbach, Q.L. Yu, H.J.H. Brouwers, Highly dispersed colloidal nano-silica from olivine and its effect on the rheology and hydration of ultrahigh performance concrete (submitted).

10.1. Introduction

Nano-silica is an important cement additive in high performance concrete thanks to its higher pozzolanic reactivity and filler effects compared to other supplementary cementitious materials (SCMs) [61]. The effects of nano silica on the performance of cement and concrete have already been widely investigated in the last few decades [62,63]. It is acknowledged that nano silica can improve the mechanical properties and optimize the microstructure of concrete when added in a proper amount [64,65]. Furthermore, nano-silica can perform more effectively at an early age in cement than micro-silica because of the higher specific surface area (50 to at least 500 m^2/g) and nano-seeding effect [66,67]. However, currently the cement industry applies mainly silica fume or micro-silica, and mostly applied in special cementitious materials, such as, oil well cement [68].

Ultrahigh performance concrete (UHPC) is a type of cementitious materials with a low w/b ratio (water to binder ratio, typically 0.18-0.24) and reinforced with steel fibers, showing high strength (normally exceeding 150 MPa), durability and self-compaction [318]. UHPC normally contains Portland cement, silica fume, ultrafine sand, fine aggregates, steel fibers and high amounts of superplasticizer [319]. However, the low w/b ratio and high dosage of superplasticizer contribute to the slow cement hydration of UHPC at an early age [320–324]. Therefore, the addition of nano-silica instead of silica fume or micro silica to accelerate the cement hydration at early ages is of significant interest [61–63,65,67,325–328]. Since UHPC is mainly used in special applications, such as aesthetic facades, infrastructure protection and earthquake resistance construction [329], nano-silica can be a promising choice as an enhancement for UHPC. In practice, however, the application of nano-silica in UHPC is mainly restricted by its high embodied energy and the tendency to agglomerate, making it difficult to disperse in fresh UHPC during mixing [330,331].

In addition, although the synthesis of nano-silica is well developed and the material is widely applied in many products, for instance, tire, paint, inorganic coating, etc. [332–335], the production of nano-silica is still time-consuming and energy intensive [201,336]. For instance, pyrogenic silica (gaseous route) is produced from the silicon tetrachloride and is vaporized in a hydrogen and oxygen flame at temperatures exceeding 1000 °C (generally 1100−1800 °C) [337]. Silica precipitated with the Stöber method (wet route) is achieved by the hydrolysis and condensation of alkoxysilanes or water glass, allowing the controlled synthesis of spherical, monodisperse, nano- to micrometer-size silica [338]. However, the high-quality silica is normally produced from organic precursors using complex methods like thermal plasma or sol-gel technology, yielding nano-silica of too high purity and small quantity. Therefore, a great demand for industry is to simplify the nano-silica production and use sustainable silicate resources to apply nano silica in cement and concrete efficiently.

For the sake of lower energy consumption, a recently developed novel nano-silica can be produced by using waste acid and olivine, an abundant minerals in earth crust [35,200][339] Specifically according to the reaction:

$$(Mg,Fe)_2SiO_4 + 4H^+ \rightarrow Si(OH)_4 + 2(Fe,Mg)^{2+}, 223KJ/mol \quad (10.1)$$

The silica can be obtained by vacuum filtration and washing with distilled water until no impurities are left. The material is then dried to remove water and produce a powder. The newly developed precipitated nano-silica can be produced in high quantities and lower prices so that application in concrete become feasible. Compared to commercial nano-silica products, the nano-silica can be produced in one-step process at low temperatures (50~90 ℃). Another advantage of olivine silica is the relatively high silanol content compared to other forms of amorphous silica [242]. This is contributed by the precipitation of silica under the isoelectric point (pH = 2), where the surface charge of silica is zero, resulting in a large number of isolated and germinal silanols. A number of researchers [59,69] indicate the promising application of olivine nano silica in cement-based materials, but very few investigated the effect of the silanol content and the silicon species of olivine silica on the cement hydration of UHPC. Recent study performed by Tina Oertel et al. [1] indicates that Stöber particles are by far the most reactive, followed by pyrogenic silica and the less reactive silica fume. This is mainly due to the specific surface area, surface silanol group density, total content of silanol groups and solubility in alkaline suspension. Interestingly, the olivine silica obtains an even higher silanol content than Stöber particles of around 8-15 nm^{-2} [340], while for Stöber particles is around 4-5 nm^{-2}. Therefore, in this study, ^{29}Si and ^{27}Al MAS NMR are used to study the effect of O-CnS on the hydration of UHPC.

Another problem of using olivine nano-silica is that it may cause severe dispersion problem in cement and concrete. Olivine silica in its powder form is produced from the heat treatment of silica filter cake and the removal of water. Finally, the dried silica powder is grinded with ball mill to obtain the silica fine powder. However, the silica produced in this way is in an agglomerate form and the secondary particle size is around 10 to 20 μm [200], hence the secondary silica particle is still beyond the nanometer range**.** Moreover, the water demand of silica powder from olivine is very high [62]. It is also known that the nanoparticles can increase the viscosity of the paste, which is especially relevant for the very low water to binder ratios ranging from 0.18 to 0.24 required for UHPC [319,341]. Therefore, finding a way to break up the agglomerate and decrease the water demand of silica is of significant importance, especially in the low w/b ratio system. In this study, it is found that by using colloidal mill, the nano silica can be deagglomerated with grinding media, specifically, 300 μm and 100 μm ZrO_2 microparticles. The colloidal mill can be used to grind the olivine silica filter cake into silica suspensions, thus avoiding the water removal process. Hence, the olivine colloidal silica can be applied effectively and dispersed better in UHPC. Other methods such as ultra-sonic or high shear mixing have proven to be ineffective for size reduction of nanomaterials that are bonded by hydrogen bonds, which is the case for the olivine nano silica [35].

Commercially available colloidal silica is mainly produced from sol-gel method, which shows good performance in enhancing the properties of UHPC. Therefore, it is interesting to make a comparative study of the two kinds of colloidal silica and their early age performance on UHPC. Above all, in this study, a method to prepare colloidal silica from olivine to break up the agglomerates using colloidal mill is developed. The as-prepared C-OnS from olivine is applied in UHPC to enhance the cement hydration and the overall performance, including rheology, early age strength, pore structure and polymerization degree of C-S-H. The mechanism of the improved performance in UHPC is explained by thermal gravimetry test (TG),

^{29}Si and ^{27}Al MAS NMR, nitrogen physisorption and mercury intrusion porosimeter (MIP). The performance of UHPC incorporating commercial sol-gel colloidal silica (C-nS) is also evaluated and compared with C-OnS.

10.2. Experiments and methodology

10.2.1 Preparation of colloidal olivine nano-silica (C-OnS)

Olivine from Norway was used for the synthesis of colloidal nano-silica, which was supplied by Eurogrit (GL50). **Table 10.1** lists the oxide composition of GL50 measured by X-ray fluorescence (XRF), together with the loss on ignition (LOI) and the olivine content. Sulfuric acid was used for the acid leaching of olivine. The concentration of sulfuric acid for the silica extraction was 3M.

Table 10.1. Composition of GL-50 dunite rocks from Norway and olivine silica (wt.%). [36]

Composition	MgO	Fe_2O_3	SiO_2	Cr_2O_3	Al_2O_3	NiO	MnO	CaO	LOI*	Olivine
GL-50	49.3	7.32	41.4	0.31	0.46	0.32	0.09	0.15	0.59	88.9
Olivine silica	0.03	0.02	99.8	-	-	0.01	-	-	-	-

*Loss on ignition; -Not detected

Olivine nano-silica was produced by Eurosupport in the Netherlands. The purity of the silica reaches 99.8% as shown in **Table 10.1**. In the experiments performed by Eurosupport, Norwegian olivine GL50 was employed in a batch reactor made up of stainless steel covered with enamel. The precipitated silica was produced by dissolving olivine in 3M sulfuric acid. The resulted slurry was washed with diluted acid and distilled water to remove any impurities (mainly Mg^{2+} and Fe^{2+}). The produced nano-silica was in filter cake form. A detailed description of the process can be found in Lazaro et.al. [342], where a schematic diagram of the pilot plant of nano-silica from olivine at Eurosupport is presented. The water content of this nano-silica was determined by heating the silica filter cake in an oven at 105 ℃ until constant mass. The water content was around 80%. However, the agglomeration is quite severe so that the secondary particle size measured by LLS (Laser light scattering) is 17.3 μm in average as shown in **Fig. 10.1 (a)**. Therefore, the deagglomeration of nano silica is strongly needed.

A colloidal mill was used in this study to break up the agglomerates of olivine nano-silica and further colloidization. The model of the colloidal mill is the *MiniSeries* from Netsch Grinding & Dispersing system, using wet grinding and dispersing with agitator beads. The colloidal olivine nano-silica was prepared by mixing 200 g of silica filter cake with 20 g of demi-water and a silica suspension of 18 % can be obtained. Then the silica suspension was further ground with the colloidal mill using two kinds of grinding media (GM), i.e. 300 μm and 100 μm ZrO_2 microparticles, to prepare colloidal nano-silica with a particle size distribution d (90) lower than 1 μm. Since the suspension of the colloidal silica is unstable at neutral pH, sodium hydroxide (NaOH) was added during the colloidal grinding process to adjust the pH to 9 to increase the hydroxyl group (-OH) on the surface of silica for stabilization. To further

stabilize the silica suspension, 0.1% Tween 60, a non-ionic surfactant was used as a surface modifier to increase the zeta potential of C-OnS.

10.2.2 Properties of C-OnS

10.2.2.1 Particle size distribution of C-OnS

The particle size distribution of the untreated olivine silica dispersion and after colloidal milling using two different grinding media is presented in **Fig. 10.1 (a).** The raw olivine silica cake after high shear mixing was in a slurry state because of the high water content (80%). However, the average particle size was around 17.3 µm. No silica particles were below 1 µm, indicating the silica agglomerated severely in the suspension. The d (10), d (50) and d (90) of the silica suspension was 7.16 µm, 18.66 µm and 48.99 µm, respectively. Therefore, further grinding using colloidal mill was carried out to break the secondary silica particles into smaller nanoparticles. The PSD of colloidal silica using 300 µm and 100 µm grinding media (GM) microparticles shows different results. The PSD of colloidal silica using GM300 shows a d (50) of 558 nm, while there still exist a small shoulder at 2.45 µm, showing insufficient grinding of the silica. The d (90) of this nano-silica was 15.6 µm, showing at least 10% severely agglomerated secondary silica particles. However, the PSD of colloidal silica using GM100 shows a d (50) in the nanometer range, reaching 256 nm. It indicates the colloidal grinding using smaller grinding media (GM100) increases the efficiency of deagglomeration. However, there still exists minor amount of microparticles, which is less than 5%. Therefore, the trial of using mixed grinding medias method to increase the efficiency of deagglomeration still needs investigation.

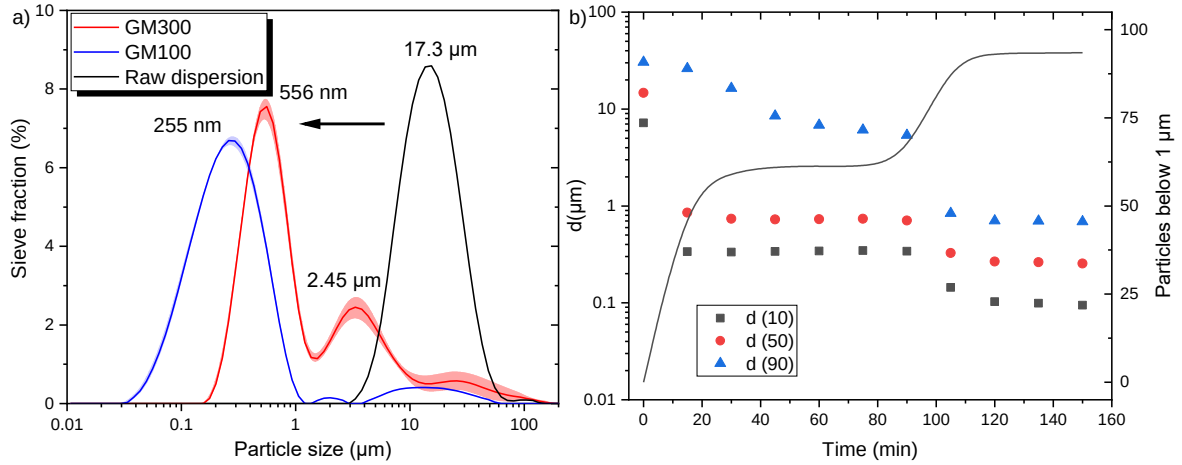

Fig. 10.1 (a) Particle size distribution of raw silica dispersion and treated with GM300 and GM100. **(b)** Evolution of the percentiles d (10, 50, 90) and fraction below 1 µm using GM300 and GM100 with 18% solid content. The wider line shows the deviation of the particle size distribution.

The PSD evolution of C-OnS as a function of time, using both GM300 and GM100 with a mixed strategy in colloidal mill is shown in **Fig. 10.1 (b).** The percentage of silica particles with a size below 1 µm is gradually increasing with the milling time before the first 20 min, the d (50) is less than 1 µm. However, the particle size remained stable for c.a. 60 min after 20 min grinding, with 60.5% of the silica particles are in the nano-sized range. After 91 min, the particle

size of silica decreased dramatically and finally 93.5% of the silica's particle size is below 1 μm after milling for 120 min. The d (90) is now less than 1 μm. Further grinding of the nano-silica has no influence on the particle size of nano-silica and it remained the same.

The particle size distribution of C-OnS using both GM300 and GM100 before and after filtration is compared in **Fig. 10.2.** Most of the nano-silica particle size are located at 164.3 nm after colloidal grinding for 2 hours. The narrow size distribution indicates a uniform particle size distribution with small deviations. The d (10), d (50) and d (90) of C-OnS was 138 nm, 195 nm and 2.12 μm, respectively. The filtration has little influence on PSD and the d (10), d (50) and d (90) of C-OnS becomes 143 nm, 198 nm and 316 nm, respectively. C-OnS can be defined as colloidal nano-silica. **Fig. 10.3 (a)** shows the TEM image of the prepared C-OnS. It is much more dispersed than original P-OnS powder as shown in **Fig. 10.3 (c).**

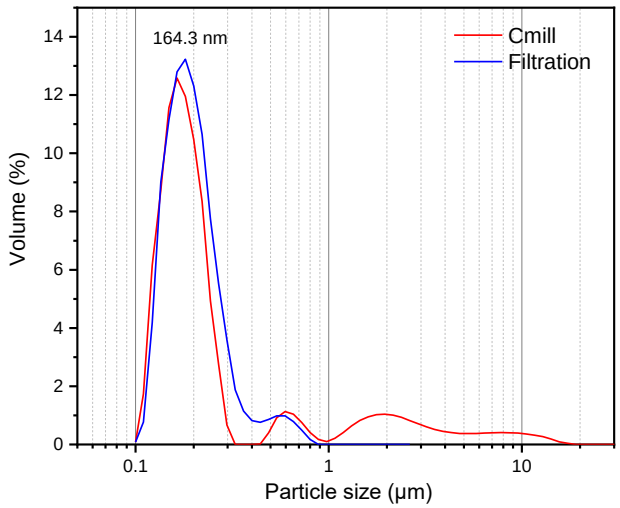

Fig. 10.2. PSD of the nano-silica dispersions after the milling using 300 μm and 100 μm grinding media with a solid content of 18% before and after filtration.

10.2.2.2 Zeta potential of colloidal nano-silica from olivine

The zeta potential of C-OnS with different chemical treatments is presented in **Table 10.2.** The low zeta potential (-17.4 mV) of the original C-OnS indicates its instability and the tendency to agglomerate during storage. Normally, a zeta potential higher than ±30 mV is believed to create a stable colloidal suspension. Therefore, in this study, the C-OnS was kept in stable state by adding sodium hydroxide to adjust the colloidal silica pH to 9 achieving a zeta potential of -26.9 mV.

Table 10.2. Zeta potential of colloidal silica before and after modification with sodium hydroxide and Tween 60.

Suspensions	Olivine nano-silica after colloidal grinding	Olivine nano-silica after pH adjusted to 9	Olivine nano-silica after adding Tween 60
Zeta potential (mV)	-17.4 ± 15.6	-26.9 ± 7.8	-36.0 ± 4.2

However, the absolute value of zeta potential was still less than 30 mV, indicating agglomeration still occurred after one day storage. Therefore, Tween 60 was added as a surface modifier in the colloidal silica to further increase the surface charge between nano-silica

particles. Consequently, the zeta potential of Tween 60 modified C-OnS increased to -37.8 mV and becomes stabilized over time.

The reference colloidal nano-silica (C-nS) was provided by Akzo Nobel, named Cembinder 8. The TEM image of C-nS is shown in **Fig. 10.3 (b)**. It shows the particle size has some variations from 10 nm to 150 nm. The average particle size measured from laser light scattering is around 182.3 nm. The larger particle size is due to the presence of secondary nano-silica particle. However, compared to olivine nano-silica, C-nS shows clear round nanoparticles and less agglomeration. The solid content of C-nS was around 50%. The properties of the two kinds of colloidal silica used in this study are presented in **Table 10.3.**

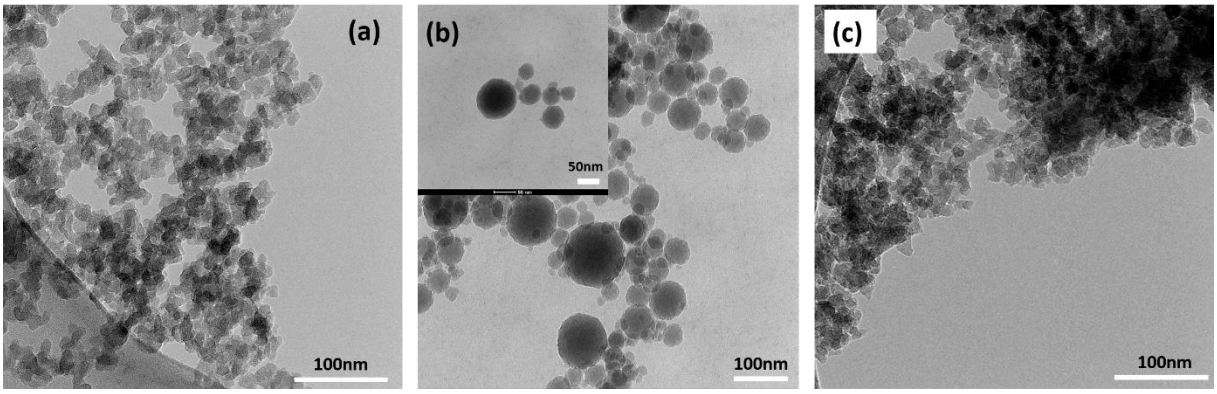

Fig. 10.3. TEM image of (a) C-OnS, (b) C-nS and (c) P-OnS.

Table 10.3. Specification and general characteristic of the silicas.

Groups	Type	Production route	pH	Solid content (%)	BET surface area (m^2/g)	Particle size range by TEM (nm)	Average Particle size by LLD (nm)
C-OnS	Colloidal	Olivine	~9	18	300-400	10-50	163.4
C-nS	Colloidal	Sol-gel	9-10	50	50	19-156	182.3
P-OnS	Powder	Olivine	~6	99.9	300-400	10-720	17000

10.2.3 Mix design of UHPC

Portland cement CEM I 52.5 R (PC), silica fume (SF), limestone powder (LP), sand 0-2 mm (S), tap water (W), and PCE-type superplasticizer (SP) were used to produce UHPC. A water/binder ratio of 0.2 was used to achieve an ultra-high compressive strength. Considering that a high content of unhydrated cement remains in UHPC, LP and SF were used to replace a certain amount of cement to decrease the usage of cement [343,344]. The chemical and physical properties of powders, i.e. PC, SF and LP, are presented in **Table 10.4.**

Table 10.4 Oxides composition and physical properties of raw materials.

Composition (%)	CaO	SiO_2	Al_2O_3	Fe_2O_3	K_2O	Na_2O	SO_3	MgO	TiO_2	MnO	SSA (m^2/g)	SD (g/cm^3)
PC	64.60	20.08	4.98	3.24	0.53	0.27	3.13	1.98	0.30	0.10	1.42	3.15
SF	0.90	93.06	-	2.06	1.15	0.63	1.28	0.70	-	0.07	18.4	2.32
LP	97.21	0.87	0.17	0.13	-	-	0.11	1.17	0.01	0.01	1.08	2.71

*SSA-Specific surface area; SD: Specific density

The UHPC mixture was designed based on a packing model using the Brouwers method [345,346]:

$$P(D) = \frac{D^{q} - D_{\min}^{q}}{D_{\max}^{q} - D_{\min}^{q}} \tag{10.2}$$

where *P(D)* is the cumulative fractions of all particles less than size of *D*. D_{max} and D_{min} are the maximum particle size and minimum particle size, respectively. q is the distribution modulus, here, 0.28 was selected.

An optimization algorithm based on the Least Squares Method (LSM) was used to calculate the optimal mixture of raw materials, according to Eq. (2) [347–349]. The particle size distributions and optimal most compacted curve of the UHPC mixtures are shown in **Fig. 10.4**. The optimal design was selected as the reference recipe, following which 1% and 2% cement were replaced by C-nS or C-OnS by mass. The recipes of the UHPC mixtures are shown in **Table 10.5**.

$$RSS = \frac{\sum_{i=1}^{n}\left(P_{mix}\left(D_i^{i+1}\right) - P_{tar}\left(D_i^{i+1}\right)\right)^2}{n} \tag{10.3}$$

The mixing procedure of the UHPC was conducted as follows: firstly, dry mixing of all powders and sand, then, adding 75% water, which was mixed with C-nS or C-OnS, then superplasticizer and lastly the remaining water. After mixing, the fresh UHPC mixture was poured into molds with the dimensions of 100 × 100 × 100 mm^3 for compressive test. All the samples were covered by plastic film for 24 h. After that, they were demoulded and cured in water at room temperature (20 ℃) until the testing ages.

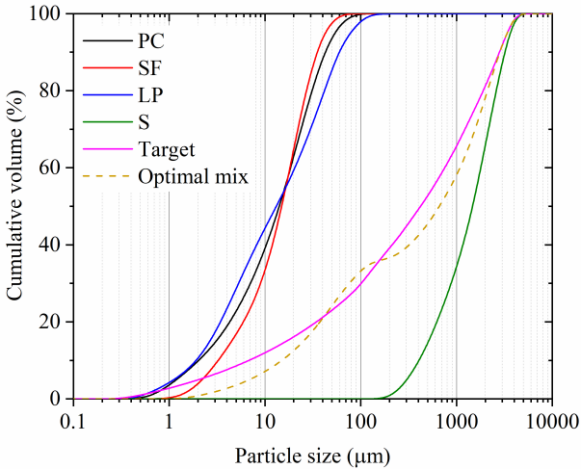

Fig. 10.4. Particle size distribution of raw materials.

Table 10.5. Mix design of UHPC (kg/m^3).

Groups	PC (kg/m^3)	SF (kg/m^3	LP (kg/m^3)	S 0-2 (kg/m^3)	SP (kg/m^3)	Water (kg/m^3)	C-OnS (kg/m^3)	C-nS (kg/m^3)	P-OnS (kg/m^3)
REF	744	42.5	170	1383	8.5	174.3	0	0	0
C-OnS 2%	729.1	42.5	170	1383	8.5	174.3	15	0	0
C-nS 2%	729.1	42.5	170	1383	8.5	174.3	0	15	0
P-OnS 2%	729.1	42.5	170	1383	8.5	174.3	0	0	15

*PC-Portland cement; SF-silica fume; LP-limestone powder; SP-superplasticizer; S-sand

10.2.4 Effect of C-OnS on hydration and pore structure of UHPC

The effect of C-OnS, C-nS and P-OnS on the rheology and hydration of UHPC grout was carried out by adding C-OnS, C-nS and P-OnS in UHPC without fine aggregate. The ingredients used were Portland cement, silica fume, limestone powder, distilled water and superplasticizer. The mass ratio of the components used is shown in **Table 10.5**. The hydration products of UHPC paste and the accelerating effect of C-OnS and C-nS on the UHPC grout were determined by thermal gravimetry (TG) and calorimeter test, respectively. The chemical state of silica and alumina was studied using ^{29}Si and ^{27}Al MAS NMR. The pore structure of UHPC was evaluated by the nitrogen physisorption and mercury intrusion porosimeter (MIP). Details of characterizations are described as follows.

10.2.5 Characterization

10.2.5.1 Colloidal silica from olivine and commercial colloidal silica

The particle size distribution of the two kinds of colloidal silica was measured with a Master sizer 2000 linked via a Hydro S unit to disperse the colloidal silica. The solvent used was distilled water. The used percentage of colloidal silica is below 5% due to the very small size of the silica particles. The zeta potential of colloidal silica was measured with a Nano ZS from Malvern. The TEM analysis of olivine colloidal silica was carried out using a Tecnai 20 microscope for a microstructure analysis, operated at 200 kV.

10.2.5.2 UHPC with C-OnS and C-nS

10.2.5.2.1 Rheology test.

A commercial rheometer (Anton-Paar MCR 302) with a CC27-SS (grooved) coaxial cylinder measuring geometry was used in this study. The grooved wall surface was specially designed for the cementitious system to prevent sliding of the cement particles. UHPC paste was prepared by mixing portland cement, silica fume, limestone powder, water, SP and C-OnS /C-nS/P-OnS. After mixing, the UHPC paste sample was placed in the gap space of the coaxial cylinder. Then, the UHPC paste was pre-sheared at 50 s^{-1} for 2 min for the sake of breaking down the structure of the UHPC paste, creating a uniform structure before testing. The testing temperature was set at 23 ^{O}C. The shear rate was set at 600 s^{-1} for 120 seconds, and later 500, 400, 300, 200 and 100 s^{-1} each for 60 seconds for the dynamic yield stress test.

Generally, UHPC paste is believed to follow a Bingham behavior, which is represented by the following equation:

$$\tau = \tau_0 + \mu_p \gamma \tag{10.4}$$

where τ is the shear stress, τ_0 is the yield stress, μ_p is the plastic viscosity and γ is the shear rate, respectively. The plastic viscosity was determined by calculating the slope of the shear rate versus the shear stress. The yield stress was determined by the intercept of the fitted plot of shear stress and shear rate.

10.2.5.2.2 Calorimeter test.

Hydration heat was used to analyze hydration kinetics of UHPC paste with C-OnS and C-nS, which was carried out by isothermal calorimeter (TAM Air, Thermometric) using an 8-channel setup. The UHPC grout and colloidal silicas were blended with de-ionized water externally for about 1 min and vibrated with an electrical vibration mixer, then the mixed paste was injected into a sealed glass ampoule and loaded into the calorimeter. All measurements were conducted for 72 h under a constant temperature of 20 ℃. The heat release and heat flow results were normalized by mass of cement.

10.2.5.2.3 Thermal gravimetric analysis.

The thermal-gravimetric (TG) analysis of paste samples was conducted with a STA 449 F1 instrument. The temperature range was set from 40 ℃ to 1000 ℃, with a heating rate of 10 ℃/min in a N_2 atmosphere. The weight loss ($WL_{Ca(OH)2}$) due to the evaporation of water can be used to calculate the amount of portlandite present, using the molecular masses of portlandite ($M_{Ca(OH)2}$ = 74 g/mol) and water (M_{H2O} = 18 g/mol). The weight loss of $C_{1.5}SH_4$ due to the evaporation of water can be used to calculate the amount of C-S-H present, using the molecular masses of C-S-H with a C/S=1.5 ($M_{C1.5SH4}$ = 216 g/mol). The percentage of C-S-H and portlandite in cement paste was calculated according to:

$$Ca(OH)_2 = \frac{WL_{Ca(OH)_2} \times M_{Ca(OH)_2}}{4 * M_{(H_2O)}} \tag{10.5}$$

$$C_{1.5}SH_4 = \frac{WL_{CSH} \times M_{CSH}}{M_{H_2O}} \tag{10.6}$$

where $WL_{Ca(OH)2}$ is the mass loss of water during temperature of 440~480 ℃ according to DSC using a tangential method. The WL_{CSH} is the mass loss of water during temperature of 105~400 ℃. $M_{Ca(OH)2}$ is the molecular mass of portlandite, M_{CSH} is the molecular mass of C-S-H using a formular of $C_{1.5}SH_4$.

10.2.5.2.4 Pore structure analysis.

Nitrogen physisorption was performed with a Tristar II equipment (Micromeritics) at 77 K using liquid nitrogen to determine the specific surface area and gel pore structure of hardened UHPC paste at the age of 1, 3 and 7 day using the BET theory and the BJH theory. Before testing, the UHPC was pretreated in nitrogen gas flow at 40 ℃ for 4 hours to remove any moisture and evaporative impurities. UHPC samples with 2% C-nS and 2% C-OnS were tested to indicate the difference. The mercury intrusion porosimetry (Micromeritics) was conducted to determine the pore size distribution of UHPC. The UHPC mortars without fine sand at the age of 7 day were crushed into small fractions (2 mm to 4 mm) for MIP analysis. The intrusion pressure is from 0 to 227 MPa. The contact angle was 130.00°.

10.2.5.2.5 NMR analysis.

NMR measurements were performed on a Bruker AvanceNeo 500 MHz spectrometer operating at 99 MHz and 132 MHz for ^{29}Si and ^{27}Al, respectively. The ^{29}Si MAS NMR spectra were obtained using a 4 mm CPMAS probehead and a 4 mm zirconia rotor by employing a spinning speed of 10.0 kHz. A high-power proton decoupling direct excitation (DE) pulse sequence with a 90° pulse width of 4 μs and a relaxation delay of 20 s was used. The solid-state ^{27}Al MAS NMR spectra were obtained using a 2.5 mm CPMAS probehead and a 2.5 mm zirconia rotor spinning at a speed of 25 kHz. A single pulse sequence with a 18° pulse duration of 1 μs and an interscan delay of 0.5 s was used. The ^{29}Si and ^{27}Al chemical shifts were referenced to Tetramethylsilane (TMS) and saturated $Al(NO_3)_3$ solution , respectively.

The deconvolution of the ^{29}Si MAS NMR spectra was carried out using Origin 2019, which is in accordance with the deconvolution algorithm shown in the literatures [59,350]. The multipeak fit was used to calculate the area of each peak of silicon state exists in the spectra with Gaussian function, thus the cumulative integrated percentage of each silicon in the UHPC is obtained. The mean chain length of C-S-H is calculated according to [351]:

$$MCL_{nc} = \frac{2\left[Q^1 + Q^2 + \frac{3}{2}Q^2(Al)\right]}{Q^1} \tag{10.7}$$

$$MCL_c = \frac{4\left[Q^1 + Q^2 + Q^2(Al) + Q^3 + 2Q^3(Al)\right]}{Q^1} \tag{10.8}$$

where MCL_{nc} is the mean chain length of non-crosslinked C-(A)-S-H structure, MCL_c is the mean chain length of crosslinked C-(A)-S-H structure, Q^n represents the silicon state of Q^1, Q^2, Q^3, while $Q^n(Al)$ represents the silicon is replaced by alumina in the structure of C-(A)-S-H.

The degree of cement hydration is calculated according to:

$$\alpha = \left[100 - I(Q^0)\right] \times 100\% \tag{10.9}$$

where α is the hydration degree of C_3S and C_2S in the cement, $I\ (Q^0)$ is the cumulative integrated intensity percentage of Q^0.

10.3. Results and discussions

10.3.1 Rheology of UHPC paste

The shear stress and shear rate of UHPC paste before and after the addition of C-OnS, C-nS and P-OnS are shown in **Fig. 10.5**. The results show that the plastic viscosity of all the UHPC paste in this study are from 0.4 Pa·s to 1.8 Pa·s. It is observed that the reference UHPC paste without nano silica showed the lowest plastic viscosity compared to other groups, reaching only 0.4 Pa·s, which is due to the high dosage of superplasticizer. The rheology results show a trend of increased shear stress after the addition of nano-silica, whether it is in colloidal or powder form. However, it is observed that P-OnS leads to a much higher shear stress than C-OnS and C-nS. Therefore, the agglomerated P-OnS increases the plastic viscosity of the UHPC paste to a much higher degree, which is 1.8 Pa·s calculated from the slope of the fitted line in **Fig. 10.5 (b)**. This is caused by the uneven distributed agglomerated silica in the UHPC paste and also the higher water demand of dry silica. Firstly, the micron sized secondary silica particles in the paste mitigate the cement particles sliding as shown in **Fig. 10.6 (c)**. Secondly, the silica competes with the water that is needed for cement particles to flow, leading to higher viscosity of UHPC paste after mixing and during testing.

The colloidal silica shows less negative effect on the rheology of UHPC. The addition of C-OnS increases the viscosity of the UHPC paste. However, the rising shear stress and plastic viscosity caused by C-OnS is much lower compared to P-OnS. The plastic viscosity of UHPC paste with 2% C-OnS is 1.18 Pa·s. Hence, the surface modification and colloidization of olivine silica has a positive effect on the reduction of viscosity and leads to a better performance in workability of UHPC paste. This is because the C-OnS is more dispersed in water after colloidal milling. The secondary silica particles are much smaller compared to P-OnS. This reduction in particle size of agglomerates leads to the better filling of inter-particle pores of the micron-sized particles like cement and limestone powder, thus reducing the water demand of the paste. The microparticles can slide much better compared to UHPC paste containing P-OnS. The primary particle size of C-OnS is also smaller than P-OnS, thus could fill smaller nanopores and optimize the particle packing of the mixture, leading to a water reducing effect as shown in **Fig. 10. 6 (a)** and **(b)**. Thus, if the same amount of water is used for the UHPC paste, more water can be used to increase the flowability of the UHPC paste, rather than trapped inside the interparticle pores of cement and other SCMs microparticles.

The C-nS has a better performance than C-OnS in modifying the rheology. The plastic viscosity of UHPC paste with 2% O-nS are 0.81 Pa·s, which are slightly lower than the C-OnS group. This is due to the olivine silica has a rougher surface of silica particles (See TEM in **Fig. 10.3**) and higher surface area (200 to 300 m^2/g) than sol-gel C-nS (50 m^2/g). Hence, although C-nS and C-OnS possess the similar size of secondary particles, the microporosity and primary particle size become decisive factors in controlling the workability of paste.

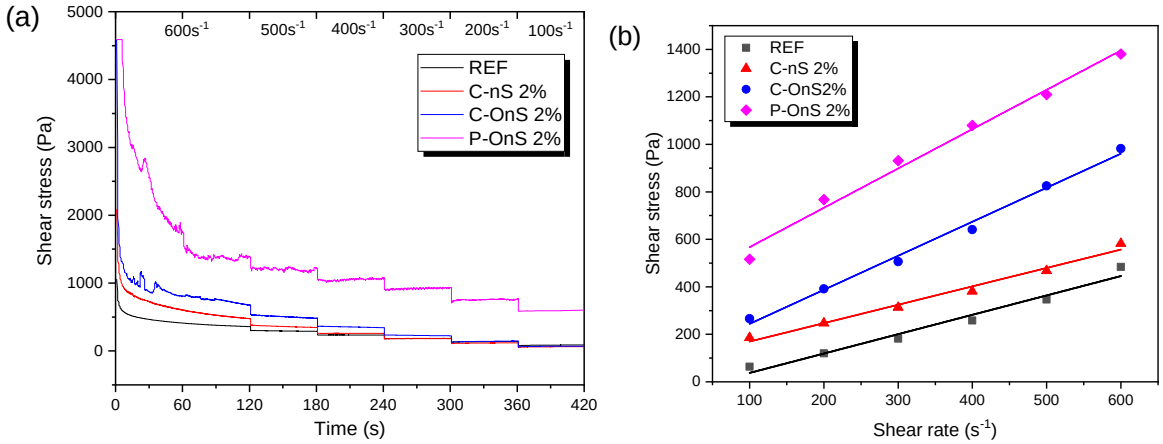

Fig. 10.5. Rheology result of UHPC paste with: (a) Shear stress vs time (b) shear stress vs shear rate.

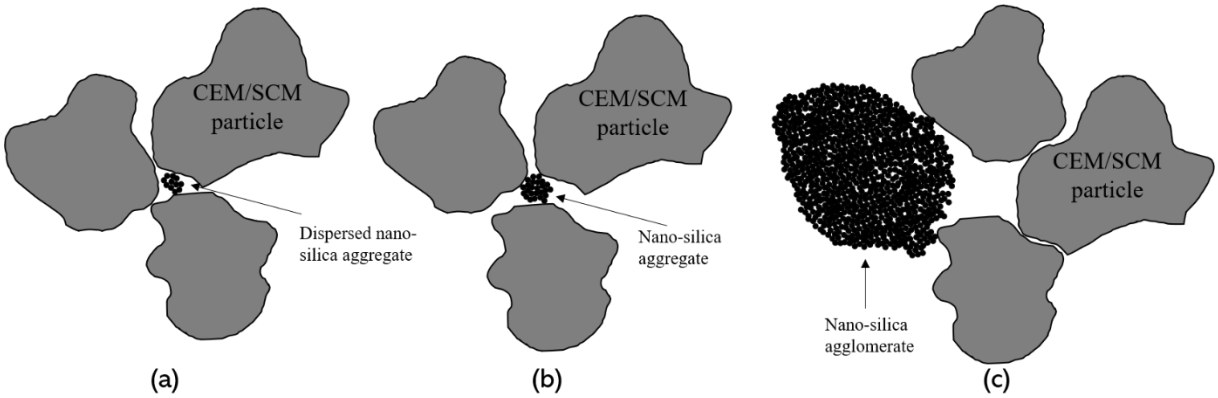

Fig. 10.6. Schematic illustration of dispersed nano-silica and agglomerated nano-silica impact on the packing of UHPC.

Other studies demonstrated that if the PSD lowered in the nanometer range, the workability and stability could be maintained while further decreasing the necessary SP content in cementitious materials [62]. The effect of C-OnS and P-OnS on the optimum packing curve is shown in **Fig. 10.7**. The C-OnS can impact the D_{min} and then reduce the minimum boundary of PSD in the nanometer range. Furthermore, the optimized packing curve is closer to the target curve, especially from 0.1 to 10 um, indicating a better packing of all the ingredients. This explains the reason why C-OnS has a better flowability than P-OnS. In theory, addition of nanoparticles contributes to improvement of fluidity of the UHPC paste. However, it is under the condition that nanoparticles act as inert fillers to occupy the void space among the cement and SCMs particles and thus release extra water to other parts of the paste to increase flowability. However, the fact is nano-silica aggregate or agglomerate possesses numbers of micropores that consumes free water which help to improve flowability. Therefore, the plain UHPC paste still have the best flowability than samples containing colloidal nano-silica.

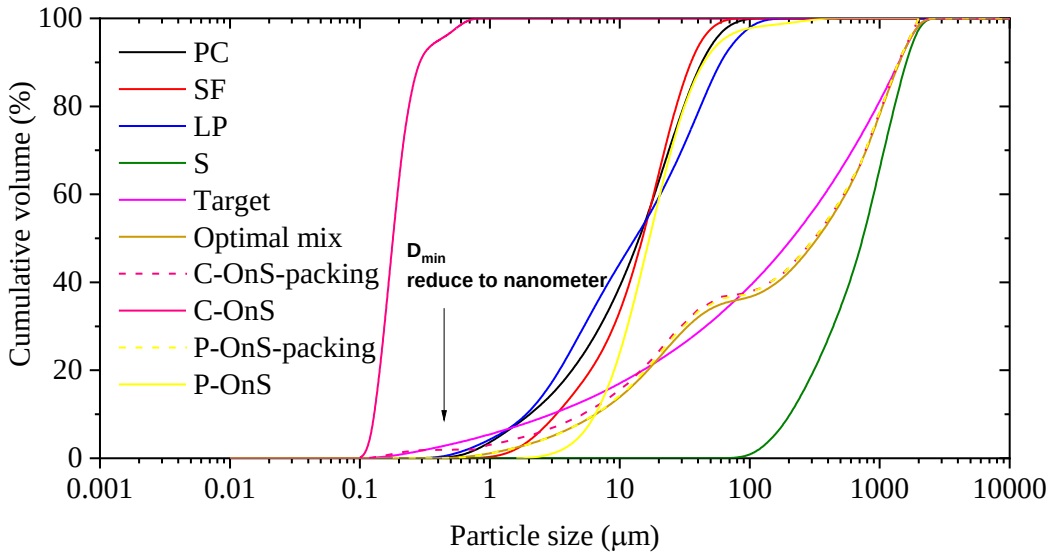

Fig.10.7. Target line and composed mix using the optimization algorithm for UHPC paste with C-OnS and P-OnS.

10.3.2 Reaction kinetics of cement paste and UHPC paste with O-CnS and C-nS

The reaction kinetics of UHPC paste with addition of O-CnS and C-nS using calorimetry is shown in **Fig. 10.8**. The plain UHPC paste shows a longer time to reach the hydration peak than normal cement paste, which is due to the retardation effect of high dosage of superplasticizer and the low w/b ratio. After addition of C-nS and O-CnS, the TRP (Time to Reach Peak) reduced to 16 hours and 14.6 hours for 1% and 2% C-nS, and 14.1 hours and 12.5 hours for 1% and 2% O-CnS. It is obvious that the accelerating effect of O-CnS is stronger than of C-nS. This phenomenon is in accordance with the results from the plain cement paste with these two kinds of nano silica.

The results are attributed to the different silica production process. As shown in the literature [340,342], the olivine silica has a silanol content of 8-15 OH/nm^2, while sol-gel C-nS contains a lower silanol content of around 3-4 OH/nm^2. A higher silanol content on the surface of silica indicates a higher reactivity and compatibility with cement paste, because of the higher solubility of the silicate in water and the reaction with cement hydration products like portlandite is more intense. Another reason should be the higher surface area of C-OnS compared to C-nS. The surface area of C-OnS is 200-300 m^2/g, while for C-nS is around 50 m^2/g. Therefore, the reactive surface area is much larger for C-OnS and can effectively release more silicate species and expose more reactive sites than C-nS.

Another reason could be the filler or nano-seeding effect of nano-silica. However, the nano-seeding effect is not obvious from the calorimetry. It can be observed that the intensities of the hydration peaks from C-nS samples are slightly lower than those of REF and C-OnS. The lower intensity could indicate the filler effect is present during the first 24 hours of hydration for C-nS, showing an accelerated TRP and less hydration heat. However, further investigation is needed to better explain the mechanism.

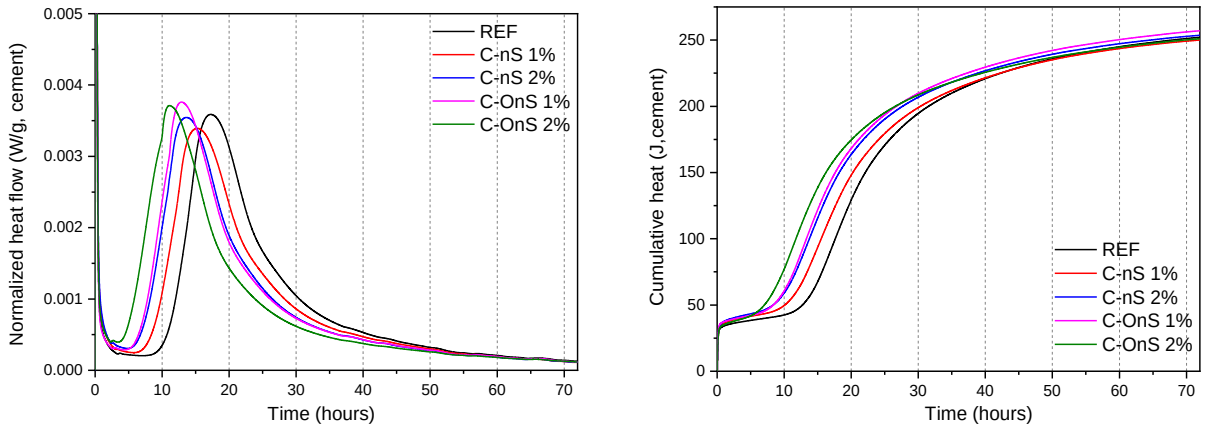

Fig. 10.8. Normalized heat flow and cumulative heat of UHPC grout (w/b = 0.2) with C-OnS and C-nS.

10.3.3 Thermogravimetric analysis

The thermal gravimetric curve of the UHPC paste with addition of C-OnS and C-nS, together with the calculation of the concentration of C-S-H and portlandite in UHPC paste are shown in **Fig. 10.9 (a)** and **(b)**. The amount of C-S-H was calculated assuming a fixed composition for all samples and is only an indication for the true amount of C-S-H present. The main differences of UHPC and plain cement paste are the low w/b ratio and high usage of SP, featuring a slow hydration during the early ages. The C-S-H content in the reference UHPC paste increases with increasing aging time from 1 d to 7 d, reaching 16.1%, 22.0%, and 24.4%, respectively. On the other hand, the C-OnS groups present a higher C-S-H content in the UHPC paste. For group C-OnS 2%, the C-S-H content achieves 17.3% at 1 d and 24.5% at 3d. The commercial C-nS group shows a lower C-S-H content than those of the C-OnS series. The C-nS 2% UHPC paste has C-S-H concentration of 16.83% at 1d and 22.4% at 3d. With the curing time reaching 7 days, the C-S-H content of C-nS 2% shows a higher content than that of C-OnS 2% (25.3%), reaching 25.7%. The results show the pozzolanic reaction happens more intense for C-nS after 7 days curing. Therefore, it can be concluded from this result that the colloidal silica can be considered as C-S-H enhancer in the early curing for UHPC, regardless of the silica type. However, the C-OnS has a better acceleration effect than C-nS during the first 3 days, while at 7 days, C-nS presents a higher C-S-H content due to the relatively slow pozzolanic reaction with portlandite.

Another important indicator is the portlandite content in the UHPC paste. As can be observed in the **Fig. 10.9 (b),** the $Ca(OH)_2$ content in REF sample is 3.27% at 1d. For the C-OnS and C-nS samples, they all show a lower $Ca(OH)_2$ content than REF group at 1d, indicating the CH formed during the early age hydration is consumed by the silica. With the curing time increasing to 3d, more CH is produced due to the further cement hydration, the CH content increases to 4.99% for REF. The C-OnS and C-nS still has a lower CH content, reaching 4.54% and 4.56% for 2% C-OnS and C-nS, respectively. The similar amount of CH for C-OnS and C-nS proves that the pozzolanic reaction of C-nS occurs mainly during the first 3 days. When the curing time prolongs to 7 days, the REF sample presents a CH content of 5.75%, while the C-OnS and C-nS groups show the CH content of 5.27% and 4.96%, respectively. The CH

consumption of C-nS exceeds that of C-OnS, meaning the C-nS starts reacting more with CH in the pore solution.

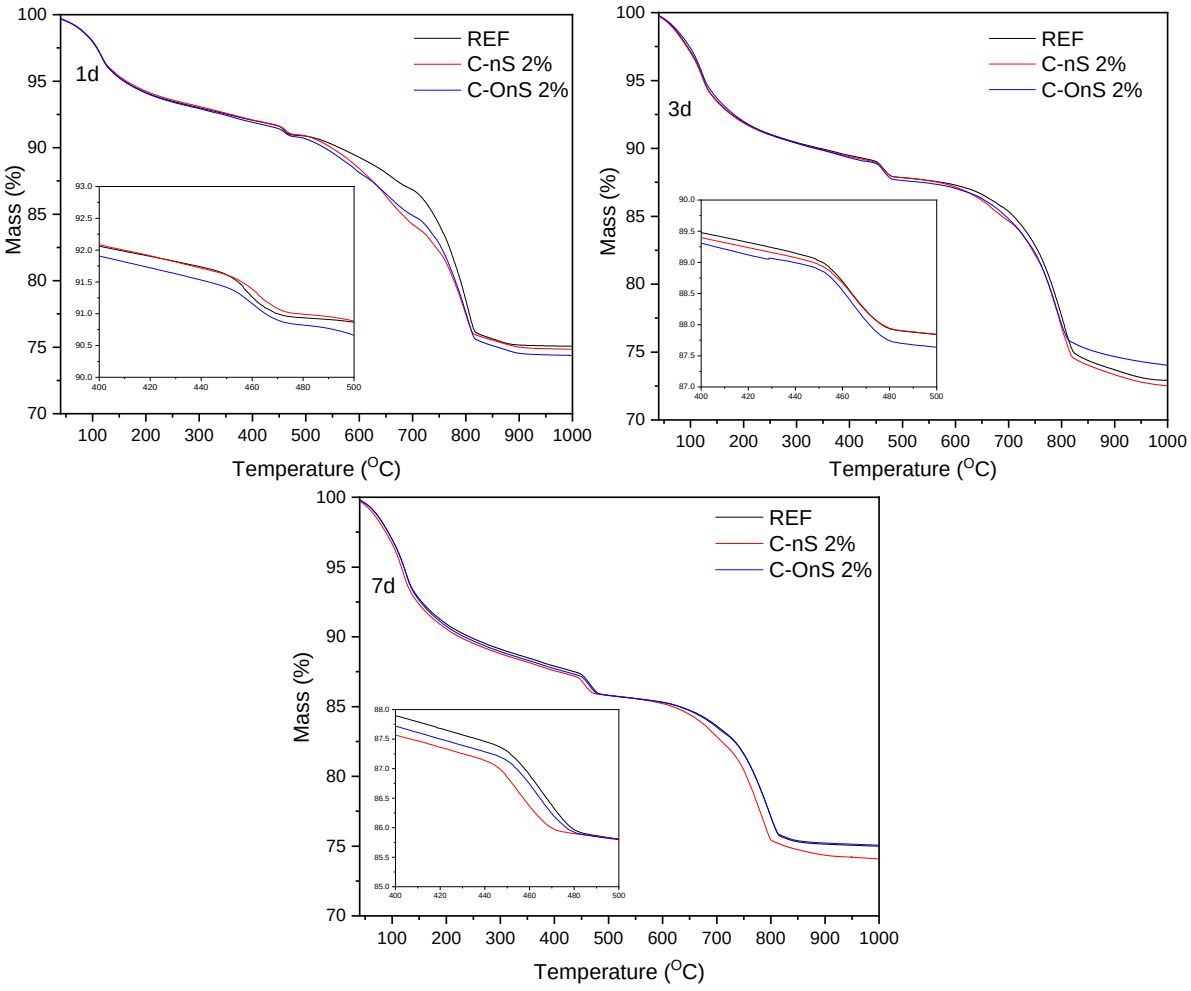

(a)

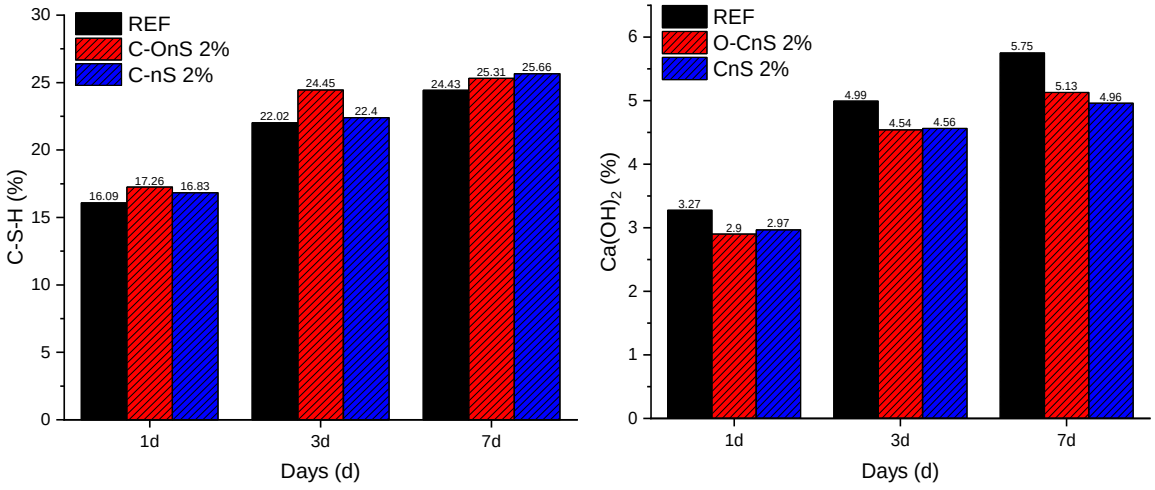

(b)

Fig. 10.9. (a) Thermal gravimetry analysis of UHPC paste with 1% and 2% C-OnS and C-nS at the age of 1d, 3d and 7d. (b) The C-S-H and $Ca(OH)_2$ concentration calculated from thermal gravimetry analysis of UHPC paste.

It can be summarized from the results that the C-OnS and C-nS has a different acceleration effect compared to plain UHPC sample. The interesting finding is that the C-OnS has a higher C-S-H formation and $Ca(OH)_2$ consumption than that of C-nS during the first 3 days. The reason may be the same as explained in the case of plain cement paste. The C-OnS has a more silanol content and surface area that can be exposed to become the reactive site. The reaction with portlandite becomes more intense and the $Ca(OH)_2$ concentration is much lowered at early days. While for C-nS, due to the lower solubility of silicate in the pore solution and slower reaction with the hydration product of cement, the pozzolanic effect happens later for C-nS. Therefore, the C-OnS can better promote the cement hydration at relatively early ages.

10.3.4 NMR analysis

10.3.4.1 ^{29}Si MAS NMR

The ^{29}Si MAS NMR analysis of cement, C-OnS, C-nS are shown in **Fig. 10.10 (a)**. The spectra of CEM 52.5 R shows narrow resonance and all the Si is in Q^0 state, at around -68 ppm to -75 ppm. One sharp peak at -71.4 ppm is attributed to the Belite (C_2S) phase, while the broad shoulder at -72.7 ppm is contributed by the Alite (C_3S) phase [327]. In fact, the C_3S phase has multiple resonance peaks at -69 ppm to -74 ppm contributing to the broad peak. [352]. The spectra of commercial C-nS made from the sol-gel method obtains a broad peak centered at c.a. -111.3 ppm, which is a Q^4 silicate species and is similar to other silicas, for instance, pyrogenic silica or silica fume [327]. However, C-OnS made from olivine shows an additional peak at -101.5 ppm and a small shoulder at -92.1 ppm, indicating the characteristic of Q^3 and Q^2 silicate species, respectively [342]. In **Fig. 10.10 (b),** Q^3 silicate species indicates the silica surface has more isolated silanols, while Q^2 indicates the germinal silanols [353]. More Q^3 or Q^2 silicate species means a better solubility of olivine silica in cement pore solution, which may further lead to different pozzolanic reaction in the UHPC.

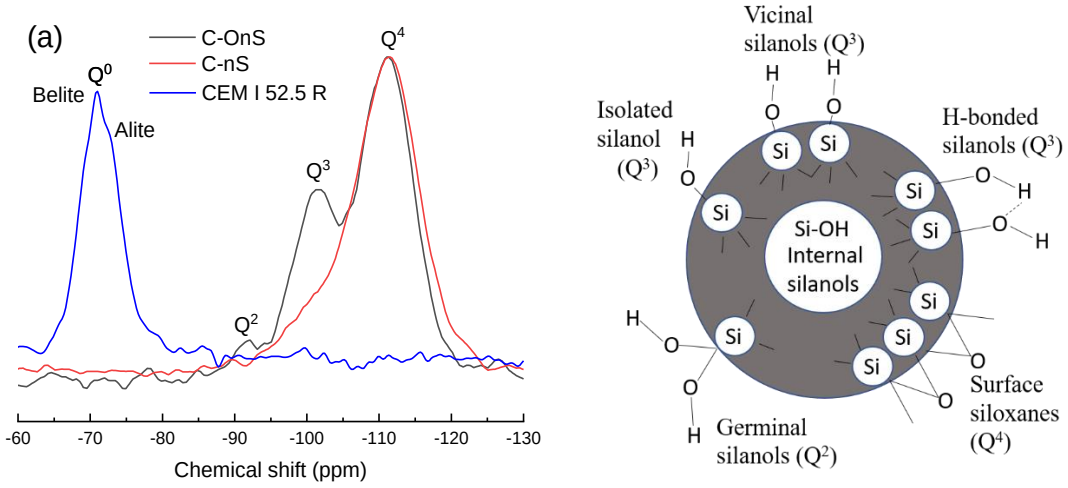

Fig. 10.10. (a) ^{29}Si NMR analysis of raw materials and **(b)** Types of silanol groups of amorphous silica: Q^4-surface siloxanes; Q^3-isolated silanols; Q^2-germinal silanols; Q^1-vicinal silanols.

The plain UHPC paste hydrated at early age from 1d to 7d are mostly Q^0, Q^1 and Q^2 silicate species as shown in **Fig. 10.11 (a)**. Due to the slow hydration of cement in low w/b ratios in UHPC systems, the peak of Q^0 silicate is the highest at -71.4 ppm. While for other silicate

species, the intense bands at -79.4 ppm and -84 ppm are the characteristic peak of Q^1 (chain-end), Q^2_b (bridging) or Q^2_p (pair) site of C-S-H, respectively [351]. There exists another tiny shoulder at -81 ppm, attributed to the Q^2 (1Al) site, where Al species replace Si in the bridging site of C-S-H forming C-(A)-S-H [354]. The resonance at -89 ppm and -94 ppm are attributed to the Q^3 (1Al) site and Q^3 site, which are observed with very low intensity. This is due to the slow cement hydration of UHPC forming short non-crosslinked C-S-H chains, with a relatively low polymerization degree. Therefore, the mean chain length (non-crosslinking) of C-S-H in REF sample only reaches 3.19 as presented in **Table 10.6**.

The ^{29}Si NMR of UHPC paste with the addition of C-OnS and C-nS at the age of 1d in **Fig. 10.11 (a)** showed similar resonance at -71.4 ppm and -79.1 ppm, attributed to the unhydrated cement Q^0 and C-S-H silicate species Q^1. The almost complete lack of a resonance signal at -111.3 ppm indicates that the majority of the C-OnS was consumed in the hydration process of cement within 1 day. While for C-nS, there still exist a tiny peak at the Q^4 site (1.3%), indicating that most of the silica has still not reacted in the pore solution. Therefore, C-OnS can react more rapidly with the hydroxyl group in the pore solution of UHPC and quickly form low Ca/Si ratio C-S-H (α). This is owing to the high specific surface area and the very small particle size of the C-OnS, around 10 nm compared to 50 nm for C-nS. The peak of Q^2 silicate species (-84 ppm) of C-OnS 2% at 1d is higher than that of C-nS group and REF group, indicating olivine silica forming more secondary hydration product C-S-H (α). It is calculated that the non-crosslinking MCL of C-OnS-2% is 4.43, which is longer than that of C-nS-2% (4.28), showing that C-OnS causes a stronger polymerization degree of C-S-H. While the MCL was the lowest for plain UHPC paste, reaching only 3.19. This can also be indicated by the lower hydration degree of cement as presented in **Table 10.6**.

At the age of 3 days, the peaks at -84 ppm and -81 ppm associated with Q^2 and Q^2 (1Al) sites of the C-nS-2% and C-OnS-2% continue to increase and are much higher than that of REF. The resonance signal at -111.3 ppm of Q^4 in the C-nS sample decreases to 0.6%, indicating most of the silica reacted to C-S-H (α). The MCL of the C-S-H formed in C-OnS and C-nS groups are almost the same, reaching 3.86 and 3.61, respectively. The hydration degree of cement is also accelerated at the age of 3 days for C-OnS and C-nS group, which is observed from the lower intensity of Q^0 sites compared to the reference UHPC sample, suggesting more Q^0 of silicate of the colloidal silica group was transformed to Q^1 or Q^2. The cement hydration degree reaches 46.3% and 39.7%, respectively. On the other hand, the intensity of Q^2 and Q^2 (1Al) sites of REF are still much lower than for the UHPC with colloidal silicas. Therefore, the plain UHPC normally forms C-S-H (β/γ) with a low MCL. However, there is no evidence that low MCL means lower mechanical performance of C-S-H.

Fig. 10.11 (d) shows the ^{29}Si NMR spectra of UHPC paste with addition of C-OnS and C-nS at 7 days. The intensity of the Q^1 peak in the CnS-2% sample was much higher compared to that of the 3 day aged samples, indicating a higher hydration degree of cement. It surpasses that of C-OnS. This is owing to the further reaction of the remaining C-nS and hydration of C_3S or C_2S over the course of 3d to 7d. However, the percentage of Q^2 site was lower compared to 3 day according to the deconvolution calculation from **Table 10.6**, meaning more C-S-H (β/γ) is generated from C_3S and the percentage of C-S-H (α) is thus reduced. This phenomenon happens for C-OnS as well. Also, the MCL decreased for C-OnS and C-nS samples. This is owing to

the fact that the main source for C-S-H is from clinker rather than nano-silica with increasing aging time. For the reference UHPC, the Q^2 peak is still very weak, therefore, the lack of colloidal silica means the main calcium silicate product was C-S-H (β/γ) rather than C-S-H (α). The correlation of increased MCL with high pozzolanic reaction in the C-OnS-2% sample is in accordance with other results [327], demonstrating that the C-S-H of UHPC blended with micro silica have a longer MCL than plain UHPC.

Overall, the UHPC paste with a very low w/b ratio and cured at room temperature show a relatively slow hydration at early ages, forming quite short C-(A)-S-H chain. Compared to other literature, the transformation of Q^0 to Q^1 and Q^2 in this study is much slower, because no high temperature curing is used during UHPC preparation. However, it is clear that more C-S-H (α) was formed during the first 7 days for the samples containing silica. Hence, it can be concluded that C-OnS has a more positive effect by increasing the polymerization degree of C-S-H for UHPC paste during the first 3 days. While C-nS could have a better effect on cement hydration during 3d to 7d.

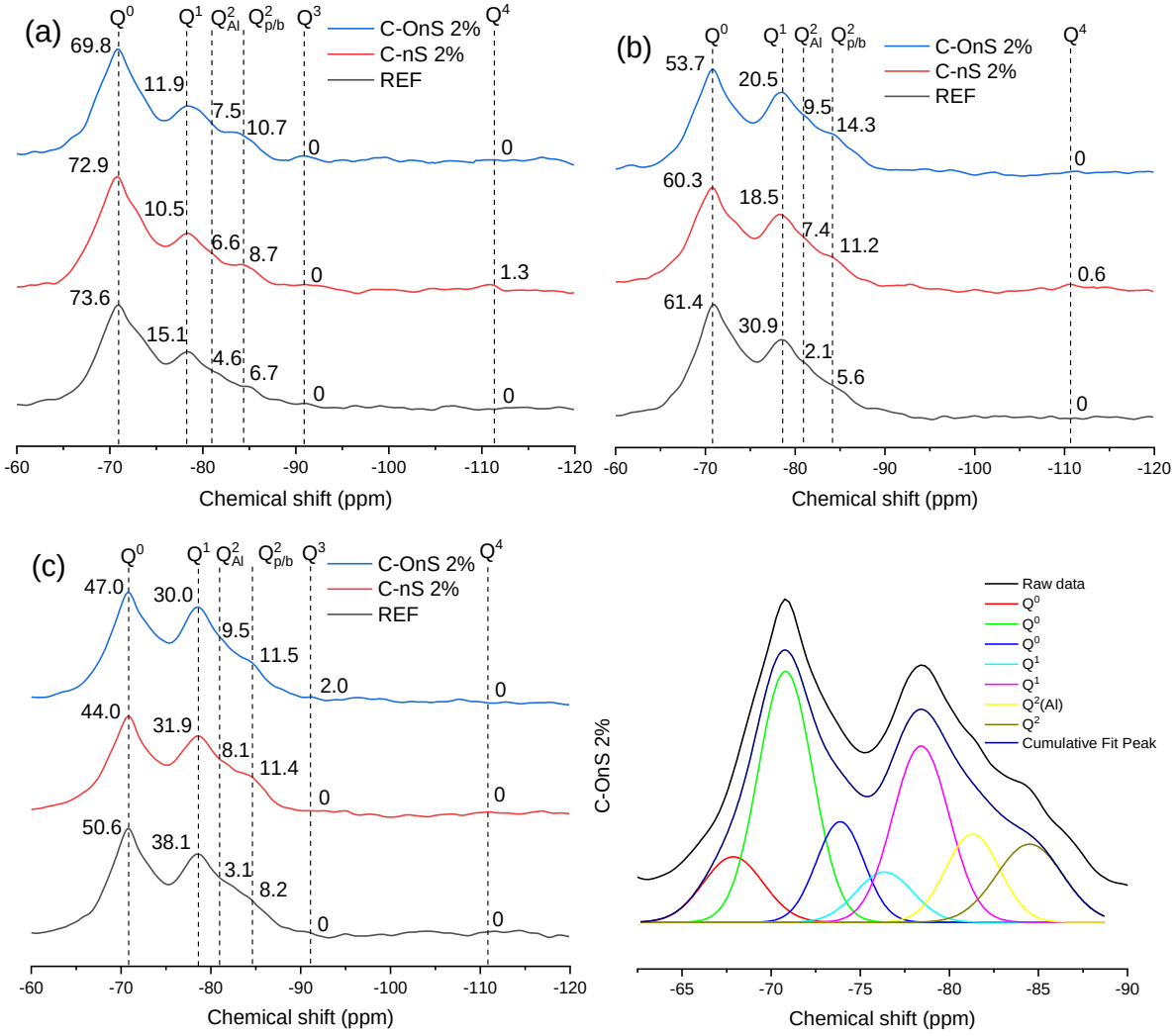

Fig. 10.11. ^{29}Si NMR analysis of UHPC paste at the age of (a) 1d, (b) 3d, (c) 7d and (d) example of multipeak fit for C-OnS 2% 7d.

Table 10.6. Mean chain length of C-(A)-S-H and hydration degree of cement in UHPC.

Groups	MCL_{nc}	MCL_c	Hydration degree of C_3S and C_2S in cement (%)
REF-1d	3.19	6.99	26.4
C-nS 2%-1d	4.28	9.83	27.1
C-OnS 2%-1d	4.43	10.12	30.2
REF-3d	2.43	5.00	38.6
C-nS 2%-3d	3.61	8.02	39.7
C-OnS 2%-3d	3.86	8.64	46.3
REF-7d	2.51	5.19	49.4
C-nS 2%-7d	2.97	6.45	56.0
C-OnS 2%-7d	3.08	7.07	53.0

10.3.4.2 ^{27}Al MAS NMR

Fig. 10.12 (a) presents the ^{27}Al NMR spectra of anhydrous cement 52.5 R. The broad peak situated at around 81 ppm is attributed to four-coordinated aluminum from C_3A phases [355]. The small sharp peak at 12.5 ppm is due to a small amount of cement hydration during storage forming trace amounts of AFt [356]. **Fig. 10.12 (b)** presents the ^{27}Al NMR spectra of UHPC paste at 1 day, showing a sharp peak at 12.5 ppm and a broad peak at 68.0 ppm, corresponding to Al(VI) in AFt and Al(IV) in C-(A)-S-H [351]. The small shoulder at 5 ppm is attributed to the amorphous aluminate hydrates ($Al(OH)_3$) [357]. It can be seen that the REF has the highest AFt peak while the silica containing samples show lower intensities. It can be inferred that the part of the Al species in cement that normally forms AFt is incorporated into C-S-H, thus lowering the ettringite peak. The enlarged picture showing the peak at 68 ppm is higher for C-OnS, indicating the C-OnS is already reacting at 1d. The high pozzolanic activity of C-OnS leads to a relatively low Ca/Si ratio of C-S-H (α), and thus the level of Al substitution for Si in C-S-H is increased.

With the curing time increasing to 3 days, the peaks at 68 ppm become similar for the two silica groups, but higher than the REF as shown in **Fig. 10.12 (c)**. It means the C-(A)-S-H in the two silicas containing samples formed similar amounts of secondary reaction products. Al (IV) tends to substitute the Si and be octahedral-coordinated in C-(A)-S-H at a low Ca/Si ratio. With the curing time reaching 7 days, the typical peak for Al (IV) in C-(A)-S-H at 68 ppm becomes higher for the C-nS containing sample, while that corresponding to Al (VI) in AFm and TAH is also higher in C-nS. This is attributed to the pozzolanic reaction happens at later ages for C-nS. While the C-OnS facilitates the pozzolanic effect at very early ages.

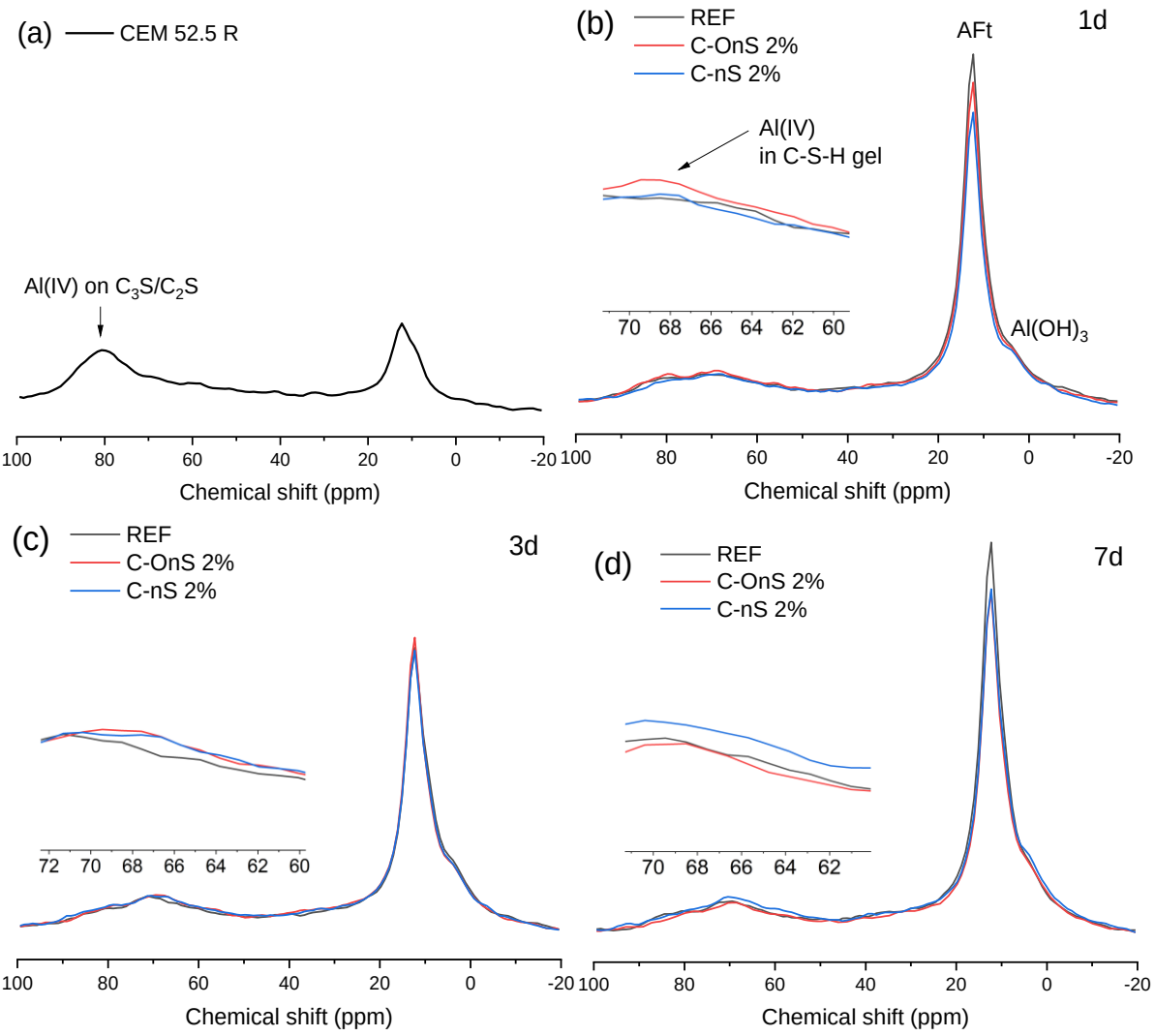

Fig. 10.12. ^{27}Al NMR analysis of (a) CEM 52.5 R and UHPC paste at the age of (b) 1d, (c) 3d and (d) 7d.

In summary, based on the ^{29}Si and ^{27}Al MAS NMR results, the addition of C-OnS and C-nS contributes to the Al substitution for Si in the bridging chains of C-(A)-S-H and also increases the chain length and polymerization degree of C-(A)-S-H as shown in **Table 10.6.** However, significant difference is observed in terms of the speed of pozzolanic effect occurs for C-OnS and C-nS.

10.3.5 Pore structure analysis

The pores in cement paste can be classified into different categories, which are (1) gel pores from 2-5 nm, result from internal porosity of hydration products like C-S-H gel; (2) small capillary pores from 5-50 nm, mainly attributed from the water amount and reaction products; (3) large capillary pores from 50 nm to 10 µm, related to the evaporable bulk water; (4) macropores larger than 10 µm, corresponding to the initial defects and air voids.

The surface area and pore structure analysis of UHPC paste containing silica was performed by N_2 physisorption using BET and BJH theory, respectively. It can be seen from **Table 7** that UHPC mixtures show different surface areas at different ages and silica additions. The addition

of C-OnS and C-nS increases the BET surface area of UHPC compared with the plain UHPC at 1, 3, and 7 days. The plain UHPC paste has the lowest surface area of around 4.73 m^2/g at 1 day. C-OnS 2% UHPC paste presents the highest surface area of around 7.26 m^2/g, while the surface area of C-nS 2% UHPC paste is 6.99 m^2/g. The increase in surface are is mainly due to higher amounts of C-S-H (α) formed with a low Ca/Si ratio (0.7~1.0). In addition, significant decrease in surface area is observed when the curing time is prolonged to 3 and 7 days. This is due to the higher amount of hydration products formed, mainly C-S-H and CH that create a much denser microstructure during the early hydration of cement.

Table 10.7. BET surface area of UHPC paste with addition of C-OnS and C-nS.

Sample	1d (m^2/g)	3d (m^2/g)	7d (m^2/g)
REF	4.73	2.66	2.39
C-OnS 2%	7.26	5.33	5.06
C-nS 2%	6.99	4.79	4.08

The normalized and cumulative pore volume of UHPC paste with the addition of silica using the BJH method are shown in **Fig. 10.13**. The gel pore volume (2-5 nm) of the UHPC increases with the addition of silica. It can be observed that UHPC pastes with these two silicas show higher pore volume than the plain UHPC paste from the absorption branch from 2-5 nm, which is in gel pore range. Combined with the results of BET surface area, it can be suggested that the samples containing nano-silica show higher gel pore volume, which is related to the C-S-H (α) from pozzolanic reaction.

It can also be found that the total pore volume decreased for all samples with increasing time of aging. This result is in agreement with the surface area results and can be attributed to the denser microstructure from the outer hydration products of cement. However, the small capillary pores from 5 to 20 nm become similar at 3 days for all three samples. With the acceleration of cement hydration by silica, more hydration products fill the small capillary pores and thus decrease the pore volume.

When the curing time increases to 7 days, the samples containing C-OnS still shows a higher gel pore volume than the C-nS and REF samples, while it is noteworthy that the total pore volume becomes the lowest for C-nS from 5-50 nm. Therefore, it seems the C-nS is more effective in refining the pore structure of the small capillary pores. Meanwhile, the effect of C-OnS on the optimization of small capillary pores is limited, indicating a limited filler effect for this type of nano-silica.

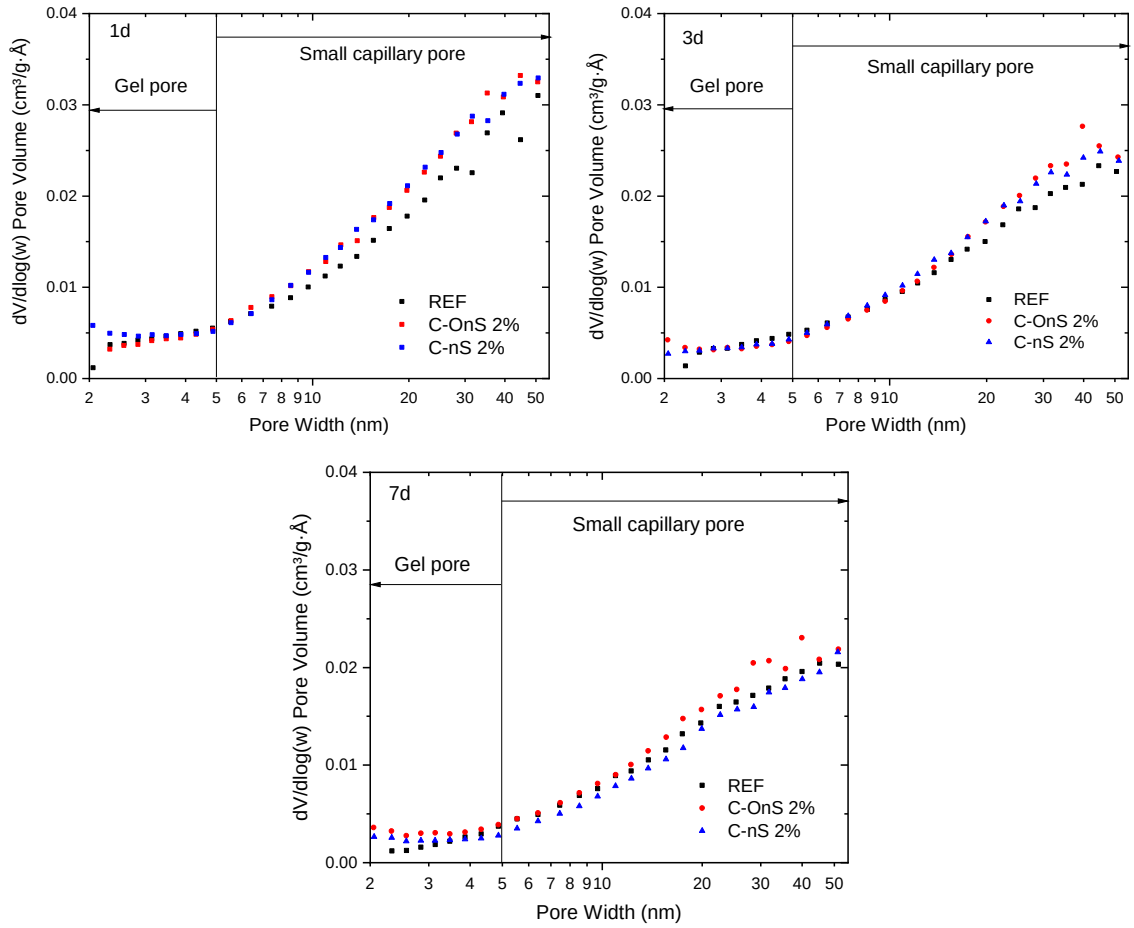

Fig. 10.13. The normalized pore volume of UHPC with addition of 2% C-OnS and C-nS at 1d, 3d and 7d.

The pore size distribution and cumulative pore volume of the UHPC samples at 7 day measured by MIP is shown in **Fig. 10.14**. From **Fig. 10.14 (a)**, it can be observed the difference in critical pore diameter is relatively small for the three groups. However, the intensity of the peak slightly decreased for the two silica groups. Combined with the cumulative pore volume result shown in **Fig. 10.14 (b)**, it indicates the early pozzolanic effect of O-CnS and CnS on the pore structure, and a reduction on the capillary pores could be achieved. The gel pores for O-CnS and CnS groups is higher than that of plain UHPC paste during the first 7 days from BJH and MIP method, indicating more C-S-H gel is formed.

The cumulative pore volume versus the pore size shows a very dense pore structure for UHPC paste as shown in **Fig. 10.14 (b)**. The large capillary pores and macro-pores are very limited and only account for less than 2% of the total pore volume. Most of the pore volume is accumulated from 100 nm and increases fast, and reaches the critical pore diameter at 12-14 nm, which belongs to the small capillary pore region. It is obvious that less small capillary pores are located in this region for CnS groups. Hence another finding is CnS can reduce the small capillary pores better than O-CnS and have more gel pores than that of CnS. It means CnS has a slight better effect on the optimization of the microstructure and facilitates the filler effect.

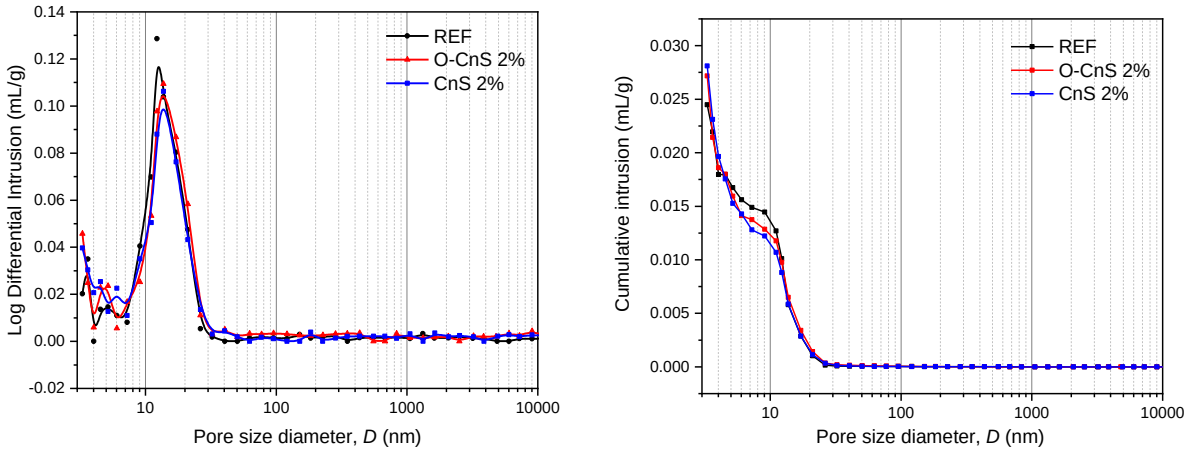

(a) (b)

Fig. 10.14. The differential intrusion (a) and cumulative (b) pore volume of UHPC paste incorporated with O-CnS and CnS at age of 7 day.

10.3.6 Strength of UHPC with addition of colloidal silicas

The compressive strength of the UHPC is shown in **Fig. 10.15**. All the groups show a compressive strength higher than 150 MPa at 28 days, hence reaching the requirement of UHPC [358]. The compressive strength during the first 7 days show a good correlation with the increasing dosage of nano-silica. The reference group shows a strength of 75.5 MPa at 1 day while for the C-OnS and C-nS groups, the compressive strength increases to 89.6 and 79.2 MPa, respectively. However, the P-OnS group shows a very slight increase of strength compared to C-OnS. This is due to P-OnS was added in powder form. The P-OnS has particles which are agglomerated in a 3D network. This agglomerated state prevents the mix from obtaining the maximum packing and due to the presence of larger microporosity, it can produce voids and thus raise the void content as explained in section 3.1. This finding is in agreement with Quercia et al. [69], showing the powder olivine silica has a limited strength increase for cement-based materials. When the curing age is prolonged to 3 days, the strength of C-OnS and C-nS increases to 122.6 and 120.8 MPa, respectively. However, the reference group still obtains a lower strength of 112.2 MPa. As the curing time further increases to 7 days, the strength of plain UHPC increases to 132.6 MPa. The silicas groups still have a higher strength, reaching 143.6 MPa for C-OnS and 138.6 MPa for C-nS. At 28 days, the strength of all the four groups reach above 150 MPa. Nevertheless, the gap among colloidal groups narrowed as the strength for C-OnS and C-nS reach 162.5 MPa and 166.3 MPa, respectively.

While both colloidal silicas can enhance compressive strength by substituting cement, the C-OnS contributes to a higher strength than C-nS at the early age. It is attributed to the stronger pozzolanic reactivity of olivine nano silica, while for C-nS, it facilitates both the filler effect and the pozzolanic effect. The strength at 28 days shows a similar compressive strength for both samples containing colloidal silica. The C-nS even has a slightly higher compressive strength than C-OnS at later ages.

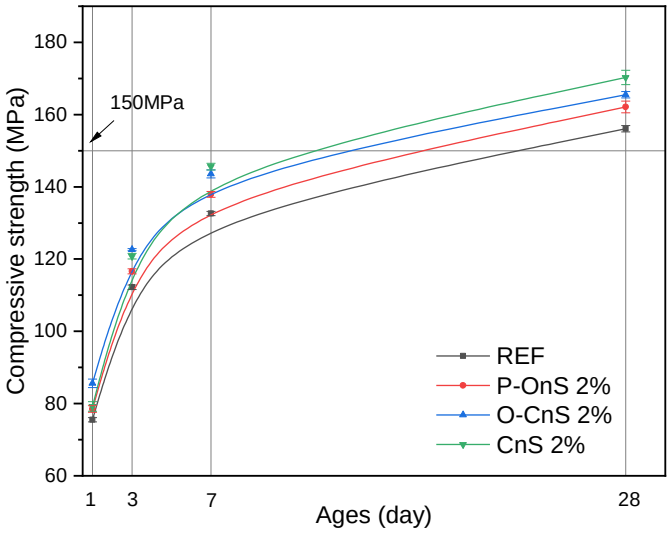

Fig. 10.15. Compressive strength of UHPC.

10.3.7 Discussion

In this study, a novel and sustainable colloidal nano silica from olivine (C-OnS) is produced and its influence on UHPC performance investigated and compared to commercial sol-gel colloidal silica (C-nS) and shows promising results. **Table 10.9** shows a summary of different types of nano silica regarding the properties and their dominant effect on the cement hydration at early ages.

As discussed in the study by Lee et al. [327], the seeding effect and pozzolanic reaction of silica fume are relatively less apparent during the first 4 days. Therefore, silica fume used in ultralow w/b ratio systems has a limited influence on cement hydration at early ages unless 80-degree curing is applied. This is due to the low silanol content and surface area, which is the lowest among the four mentioned silicas in **Table 10.9.** However, the filler effect is obvious for the silica fume at early ages and pozzolanic effect at later ages, but at a slow reaction rate.

Another type of nano silica used in UHPC is the pyrogenic silica [359]. This production process features a lower silanol content of silica to 1-3 OH/nm^2 [359]. As discussed in the investigation by Oertel et al. [61], the pyrogenic silica enhances early age strength and accelerates hydration, dissolution of alite and formation of C–S–H phases. No noticeable dissolution of silica in the pore solution is detected in pastes containing pyrogenic silica. Also, it increases the surface area for nucleation of C–S–H phases. Therefore, it is found the pyrogenic silica can enhance the early age cement hydration and the filler or nano-seeding effect is dominant.

The commercial colloidal silica made from sol-gel technology shows a much higher pozzolanic reactivity at early ages than the pyrogenic silica and silica fume, according to the results in this study. This is attributed to the higher silanol content of silica due to the sol-gel method, which excludes the high temperature process and produce in a wet route. However, the seeding effect seems not obvious for C-nS compared to pyrogenic silica and silica fume. It shows a very limited acceleration on cement hydration, as presented by the calorimeter test. The strength development is also not obvious at the first 7 days.

However, the olivine colloidal silica obtains the highest silanol content and is much higher than C-nS, pyrogenic silica and silica fume. This special production route excludes high temperature sintering and is precipitated below the isoelectric point of silica (pH less than 2) [235]. The olivine silica contains Q^2, Q^3 and Q^4 silicate species, indicating quite different properties compared to the three kinds of silica mentioned above. Its pozzolanic reactivity is the highest among all types of nano silica, while no obvious seeding effect can be found. Most of the olivine silica is consumed during the first 3 days of curing. Therefore, it can enhance the early age performance of UHPC, however, the refinement of the pore structure is weaker than that of C-nS. Thus, the later age performance still needs further investigations

Table 10.9. Comparison of different kinds of nano-silica and their dominant effects on UHPC at early age.

Types of silica	Surface area (m^2/g)	Particle shape	Silanol content (OH/nm^2)	Particle size (nm)	Pozzolanic effect	Filler effect	Literature
C-OnS	200-400	Irregular spheres	8-15	10-20	Strong	Weak	This study
C-nS (sol-gel)	20-50	Round spheres	4-5	50-100	Medium	Medium	This study
Pyrogenic silica	50-100	Round spheres	1-3	73-291	Weak	Strong	[61]
Silica fume	15-30	Round spheres	＜1	200-400	Weak	Strong	[327]

10.4. Conclusions

This chapter investigates the colloidal nano-silica preparation from olivine (C-OnS), which is a sustainable silica compared to commercial colloidal silica and shows a higher acceleration effect on cement hydration in UHPC. The overall influences of the two kinds of colloidal silica on the performance and microstructure of UHPC are investigated. Based on the results of the study, the following conclusions can be drawn:

- Colloidal silica is successfully synthesized by using a colloidal mill to break up the secondary particles of the precipitated silica from olivine. The stable suspension of silica nanoparticles can be achieved by adjusting the pH to 9 and adding 0.1% non-ionic surfactant Tween 60, reaching a high zeta potential of -36.0 mV. The particle size distribution of the C-OnS is centered at 164 nm measured by laser light scattering.
- C-OnS has a better dispersibility in cement paste and UHPC paste compared to olivine silica in powder form. The plastic viscosity is only 1.18 Pa s for C-OnS 2% UHPC paste while for olivine silica powder, the plastic viscosity increases to 1.80 Pa s. Therefore, using C-OnS can have a reduction on the use of SP in the UHPC production if the same workability is expected to be achieved. However, compared to C-nS, the effect on plastic viscosity is similar, they both increase the viscosity of plain UHPC paste to a higher extent due to the high surface area.

- C-OnS can promote the cement hydration better than C-nS at early ages according to the results of calorimeter, thermal gravimetric analysis, and ^{29}Si and ^{27}Al nuclear magnetic resonance. The reason is that C-OnS obtains more silanol content and surface area compared with C-nS. Also, the silicate species of C-OnS include Q^4, Q^3 and Q^2, indicating a better silica solubility in pore solution of UHPC.
- The mean chain length of C-S-H is longer for C-OnS samples than that of C-nS at early ages as indicated by ^{29}Si NMR. The Al (IV) species replace the Si in C-S-H forming C-(A)-S-H due to the formation of secondary hydration products C-S-H (α) by consuming $Ca(OH)_2$. This phenomenon happens at first 3 days for C-OnS while takes place more intense at 7 days for C-nS.
- The gel pore volume of UHPC with 2% C-OnS is higher than that of C-nS and REF at 1 and 3 days, indicating more C-S-H (α) is produced due to quick pozzolanic reaction. The nitrogen sorption and MIP result shows the C-nS can better facilitate filler effect in UHPC paste, thus reducing the small capillary pore volume better than C-OnS.
- The ultrahigh performance concrete obtains a higher early age strength with the incorporation of C-OnS and C-nS. The early age strength from 1 day to 7 days is higher for C-OnS group. While the 28 days strength of UHPC is almost the same for C-OnS and C-nS but still higher than REF. Therefore, the C-OnS mainly increases the first 7 days strength of UHPC.

Chapter 11 Conclusions and recommendations

11.1 Conclusions

Sustainability plays an important role in contemporary building materials as the society and industry are striving to reduce the CO_2 emission, circulate raw materials and lower energy consumption worldwide. Moreover, the insulation properties of buildings are becoming a major concern recently as the energy saving and healthy living environment of buildings are increasingly critical for human life. In this thesis, it is found that bio-based materials, especially miscanthus fibers, can be used as a natural alternative lightweight aggregate in cement and concrete. The miscanthus fibers can also improve the insulation properties of building materials by utilizing its porous structure and rigid fibers. Different parts of miscanthus fibers are investigated to fully utilize its benefit. The long miscanthus fibers are used as lightweight aggregate in ultralightweight concrete successfully and mechanism of influence on cement hydration is explained. The finely ground miscanthus fiber is applied as an accelerator for carbonation of steel slag based artificial lightweight aggregate and proved to be a feasible solution.

For the sake of further improving the insulation properties of building materials, an innovative idea of using olivine silica as the silicate source to produce super-insulating silica aerogel emerge. Compared to silica aerogel produced from organic precursors, this method provides another possibility to prepare silica aerogel at ambient pressure, showing the advantage of sustainability and cost-effective. The insulation performance of silica aerogel was also proved to be competitive. In order to further enhance the monolith and integrity of aerogel, the nano-fibrillated cellulose is applied as the enhancer in silica aerogel to increase the mechanical performance and thermal stability. Moreover, a trimethoxymethylsilane (MTMS) silica aerogel is prepared with a co-precursor method to increase the production efficiency and mechanical performance of the aerogel. Furthermore, the application of silica aerogel in advanced geopolymer foam concrete is also investigated, focusing on influence of different particle size of aerogel. The results show that silica aerogel can enhance the hydrothermal performance and acoustic absorption effectively by using large fraction of silica aerogel.

Lastly, the mesoporous silica from olivine is produced at a one-step process at low temperatures. The pore size can be tailored and the sustainable silica can be utilized as photocatalytic support and potential to be nano-insulation materials. Finally, a colloidal silica from olivine is produced and is applied in ultrahigh performance concrete to enhance the early age performance, including rheology and early age strength of UHPC from 1d to 7d. The main conclusions from this thesis and the recommendations for future research and study are summarized as follows:

11.1.1 Miscanthus fibers as a bio-lightweight aggregate in lightweight concrete

From Chapter 2 to Chapter 4, the miscanthus fibers (MF) are comprehensively utilized in lightweight aggregate concrete (LWC). As a highly porous biomaterial, MF can play a role as the insulating aggregate and improve the thermal and acoustic absorption of bio-concrete. This is because miscanthus fiber is a highly porous materials with very low density. It is found that

2-4 mm fibers obtain intact and large pore structure which are beneficial for acoustic performance. The polysaccharides leached from MF delay the cement hydration. The water absorption of MF can reach 200% to 300% depending on the different type of MF. Therefore, a pre-treatment of MF using pre-wetting or cement impregnation is useful to prepare lightweight concrete. The fresh property of miscanthus lightweight concrete is mainly influenced by aspect ratio of fiber and the percentage in fresh concrete paste. The mechanical performance of LWC can be negatively influenced by addition of MF, while the 2-4 mm MF shows less reduction on strength due to the rigid fibers and less influence on cement hydration. Cement impregnation of MF lead to a significant higher strength than pre-wetting MF concrete. However, the density of concrete also increases significantly. Acoustic absorption properties are significantly enhanced by incorporation of 2-4 mm miscanthus fibers. More miscanthus represents more open pores and voids inside the cement paste and consequently more energy can be consumed and transfer into heat by the miscanthus cement composite. The interaction between miscanthus and cement starts at the initial age. All parts of the MF fibers show retarding effect on cement hydration, but 0-2 mm fibers have the worst effect on the cement hydration. The x-ray diffraction (XRD) evidence indicates the low strength of cement composite is also attributed to a less C-S-H gel formation. The negative effect of polysaccharides is attributed to the ability of organic to be bound onto the hydration product containing Ca^{2+}, hence interrupting the tricalcium silicate (C_3S) hydration and the formation of C-S-H gel.

Miscanthus fibers applied in ultra-lightweight miscanthus concrete (ULMC) with expanded waste glass (EWG) shows good results, especially the different format of MF on acoustic absorption is studied. Acoustic absorption coefficient of ULMC is improved to 0.9 at the frequency of 870 Hz (with a narrow band number) by the incorporation of 2-4 mm Miscanthus fibers. Moreover, the thermal conductivity of ULMC decreases to 0.09 W/(m·K) by the contribution of both EWG and MF. Overall, the developed ultra-lightweight miscanthus concrete (ULMC) can help to reduce environmental impact and to function as indoor insulation and as lightweight material for heat and noise insulation. An increasing percentage of 2-4 mm MF leads to a higher acoustic absorption coefficient of ULMC with a wider frequency band. To obtain a high sound absorption above 0.5 at frequencies of 600~1200 Hz, the incorporated MF percentage in the ULMC mixture should be more than 20% 2-4 mm MF. However, 0-2 mm MF has negligible effect on acoustic absorption of ULMC due to the dense surface structure. The thermal insulation performance of ULMC slightly improves because more air voids and interfacial thermal gaps are introduced by the fibrous miscanthus particles. Ultrasonic pulse velocity (UPV) test shows the large pores exist in the interface of fibers and cement matrix. The lowest thermal conductivity of ULMC reaches 0.09 W/(m·K). The main LWAs adopted to prepare ULMC are the expanded miscanthus fibers and expanded waste glass, indicating a novel approach to efficiently recycle the waste biomass and waste glass, contributing to the sustainable development of cement and concrete industry.

Miscanthus powder (MP) can be successfully incorporated in cement-free bio-based cold-bonded lightweight aggregate (BCBLWAs) using steel slag via CO_2 curing. The prepared BCBLWAs features a low density, low water absorption and high CO_2 uptake capacity. A low density, relatively high strength and superior thermal insulating bio-concrete was prepared

using this artificial aggregate. The miscanthus powders can provide additional routes for CO_2 transportation in artificial aggregate, thus contributing to a more rapid carbonation process of steel slag particles. However, a higher content of miscanthus powder can result in a porous structure of BCBLWAs, as well as low strength. Sample with 10 vol% miscanthus powder shows the best strength performance, which increases by 20% compared to plain carbonated steel slag. The carbonation products of BCBLWAs are mainly calcite and amorphous silica. The calcite acts as a binding agent and increases the mechanical properties of BCBLWAs. Contrary to cement hydration, carbonation was not affected by the presence of polysaccharides leaching from the miscanthus powder, which makes it an effective strategy for producing cold bonded aggregates containing natural fibers. The pelletization also covers the miscanthus powder in carbonation products and reduces their water adsorption, which makes it possible to use them in ordinary Portland cement (OPC) based concrete. Concrete incorporating BCBLWAs meets the standard of lightweight concrete and the strength is relatively high for concrete using BCBLWAs with 10 vol% miscanthus powder, reaching a strength of 34.8 MPa at 28 d. The bonding between BCBLWAs and cement paste is negatively impacted if very high amounts of miscanthus powder are used in the aggregate as the fracture happens at the surface of BCBLWAs rather than at the interface. This also results in lower mechanical strength of the concrete. More work is needed to investigate this and find a method to enhance the interface when high amounts of miscanthus are incorporated into BCBLWAs. The thermal conductivity of LWC-BCBLWAs decreases to 0.255 W/(m·K) when 50% SS50MP50 used in lightweight concrete. Furthermore, the density dropped to 1100 kg/m^3. The thermal insulation property of LWC-BCBLWAs is projected to have a better performance than other non-plant based lightweight concrete.

11.1.2 Silica aerogel from olivine and its enhancement using cellulose fibers

Silica aerogel is successfully produced from olivine at low temperatures via ambient pressure drying. Sustainable silica is first produced from olivine via acid extraction. Next, it is applied as the silica source to synthesize low-cost sodium silicate. Then, ion-exchange, sol-gel method, solvent exchange and ambient pressure drying are applied to produce the olivine silica aerogel. The prepared olivine silica aerogel has a lowest density (0.08 g/cm^3) and highest porosity (96.6%), which is produced at a pH of 5.5 with 36 hours aging. At a pH of 5.5 the hydrolysis rate of silicic acid and the poly-condensation rate of colloidal silica are balanced. The surface area of the aerogels decreases with increasing aging time from 36-hours to 48-hours due to Ostwald ripening. The pore size of silica aerogel increases simultaneously due to coarsening of the silica 3D-network. The size of silica particles also increases from around 4 to 5 nm according to transmission electron microscopy (TEM) observation. The olivine silica aerogels (OSAs) show a super-hydrophobicity after replacement of the hydroxyl groups by methyl groups. The optimal Trimethylchlorosilane (TMCS)/heptane volumetric ratio in this study is 12/40 ml, and lowest density of silica aerogel can be obtained. OSA is thermally stable up to 337 ℃. The lowest thermal conductivity of silica aerogel is 0.0235 W/m·K, which is obtained at pH of 5.5 and an aging time of 36 hours. This phenomenon could be attributed to the smallest pore size and lowest density. OSA has a lower CO_2 emission than silica aerogel that uses commercial water glass as precursor. Hence the developed OSA may become a promising and sustainable replacement of the current commercial silica aerogel.

The prepared silica aerogel is applied as a photocatalytic support. It is found the surface area and pore volume of silica aerogel increase from 694 m^2/g and 2.99 cm^3/g to 920 m^2/g and 5.3 cm^3/g after heat treatment at 500 ℃ for 4 hours. The reason of this phenomena may due to the coarsening of the 3D-network of silica aerogel and also the further spring back effect caused by the repulsion force of concentrated neighboring $–CH_3$ groups. This heat-treated aerogel is applied as support to prepare catalyst. Titania was loaded into the mesopores of silica aerogel by using a precipitation method. The specific surface area and pore size both decrease significantly after titania doping. The crystal size of the prepared anatase in silica aerogel is around 12 nm, which is below the average pore size of the modified silica aerogel. The prepared silica aerogel-titania coating shows a higher conversion efficiency (99.6% for NO and 99.3% for NO_x) than the reference sample P25. Therefore, it is a promising alternative to the current photocatalysts for air purifying in building environment.

In order to further improve the monolith of aerogel, a method to impregnate silica aerogel within cellulose matrix is developed. The silica-cellulose aerogel (SCA) shows improved compressive strength (95.4 KPa), high surface area (958 m^2/g) and low thermal conductivity (c.a. 23 mW/(m·K)) compared to plain aerogel. Moreover, it has an ultralow density (0.055g/cm^3) and high porosity (98%). Specific surface area of the SCA reaches c.a. 958 m^2/g for SS-CNF1 and 614 m^2/g for SS-CNF2, compared to pure cellulose aerogel with SSA of 200~300 m^2/g, indicating the sol-gel process of olivine silica derived low modulus silicate can result in higher surface area. The compressive strength of SS-CNF1 and hydrophobized SS-CNF1-M increased from 29.8 kPa to 62.8 kPa and 95.4 kPa, respectively, showing the silica-cellulose aerogel has a better mechanical property than plain cellulose aerogel. Thermal conductivity of composite silica-cellulose aerogel was significantly lower than pure cellulose aerogel due to the incorporation of fine silica aerogel particles. Surface modification by TMCS trimethyl silylation can make SCA composites hydrophobic, with a water contact angle reaching 137.2~140.4°, which will potentially improve durability and thermal insulating performance of SCAs in the relatively high humidity environment. The monolithic silica-cellulose aerogel can be synthesized from low modulus (1.5) silicate sol-gel process. The embedded CO_2 emission of this new aerogel is significantly reduced, reflected by the obviously lower footprint of olivine sodium silicate compared to commercial water glass, namely 2.481 tCO_2/t and 5.517 tCO_2/t, respectively.

A co-precursor MTMS-PDMS aerogel with modified nano-fibrillated cellulose (NFC) in a one-step drying method at ambient temperature and pressure is developed. Together with the MTMS, PDMS, the modified NFC, the newly developed aerogels have a positive increase in performances, such as acoustic absorptive, mechanically stronger and hydrophobic property compared to the plain MTMS aerogel. SEM images show that the modified NFC is completely incorporated in the aerogel structure. The 3D-network and cross-linking level of co-precursor aerogel can be perfectly observed. Interestingly, there exists a two-stage silica particle of size around 0.5-1 um and 3-5 um. The particle size distribution of the developed aerogels shows the average particle size of 3.88 μm at 1 day, 4.55 μm at 3 days and 4.84 μm at 5 days. The surface area of plain MTMS aerogel is 254.6 m^2/g, while the addition of PDMS increases the surface area to 302.2 m^2/g. When the aging time prolonged to 3 days, the surface area decreases to 194 m^2/g, and the 5 days aging aerogel reaches a surface area of 185 m^2/g. The density of the

modified aerogels has been increased from 0.0844 g/cm^3 to 0.1066 g/cm^3 with the addition of PDMS and NFC. The maximum sound absorption coefficient increased from 0.68 to 0.88 with the addition of modified NFC. While the aging process increase the sound absorption from 0.65 as a reference to 0.68 at 1 day, 0.77 at 3 days and 0.80 at 5 days. The result show that both the NFC and aging have a positive effect on sound absorption. The co-precursor MTMS-PDMS aerogel obtains a higher water contact angle (WCA) of 143°, which increases to 145° after 3 days of aging. The effect of aging, introduction of CH_3 from PDMS and addition of the NFC has a substantial impact on the hydrophobicity of the aerogels and surface property. The addition of PDMS and modified NFC in co-precursor aerogel increase the stress of aerogel can handle. However, the PDMS and NFC could not increase the flexibility of the aerogel. The shortcoming of the novel synthesis method and modification is that there is a slight increase in the overall thermal conductivity, which is due to the addition of both the PDMS and the maleic anhydride modified NFC.

The performance of geopolymer foam render (GFR) with the incorporation of silica aerogel (GFAR) with different particle sizes is investigated in Chapter 8. The effect of different silica aerogels on thermal conductivity and acoustic absorption of GFAR is the focus of this study. The total porosity of the geopolymer foam concrete with silica aerogel is increased due to the high number of internal pores of silica aerogel. The open porosity is higher for GFAR with silica aerogel of large particle size, mainly because of the bridging effect between air bubbles. The acoustic absorption of geopolymer foam render with the addition of silica aerogel is much higher than the plain foam geopolymer render, which is contributed from the more open porosity in GFAR, and the inherent sound absorption property of silica aerogel itself. Silica aerogel with a larger particle size plays a better role to improve sound absorption due to the bridging effect between the pores generated from hydrogen peroxide. The thermal insulation property of GFAR is improved with the addition of silica aerogel. 1200 μm - 4000 μm silica aerogel has a higher increase ratio than finer aerogel particles (2-40 μm). The hygrothermal behavior is better than the plain GFR, suggested by the lower water uptake and thermal conductivity after exposure to an 80% humidity environment. The microstructure analysis indicates the GFAR with larger silica aerogel particles has a higher open porosity than plain GFR. The fine silica aerogel can be placed in the solid network of geopolymer matrix, while the large fraction of silica aerogel can be stuck between the pores, thus providing an additional opening**.**

11.1.3 Mesoporous olivine silica and its potential application in building materials

Mesoporous silica is directly produced with one-step synthesis by the dissolution of olivine in sulfuric acid during 48 h of reaction at low temperature (50 °C) in Chapter 9. The non-ionic surfactant, Triton X-100 and Pluronic P123 are proved to successfully forming the desired micelles in the high ion concentration and negative pH environment. Ordered mesoporous silica (OMS) prepared using Triton X-100 has a high surface area of more than 900 m^2/g with pore sizes of around 2.8 nm. Swelling agent n-heptane enlarges the average pore size of this mesoporous silica from 2.8 nm to 5.2 nm. OMS prepared using P123 has a surface area of more than 700 m^2/g with pore sizes of around 7-8 nm. Swelling agent n-heptane enlarges the average pore size of this mesoporous silica from 8 nm to 11.2 nm. The transmission electron microscopy (TEM) image of OMS-T shows a long-ranged ordered tubular structure of the mesoporous

network inside the particles. While the OMS-P shows the presence of a non-uniform wormlike structure with narrow mouths. The method provides another way of applying olivine in high-end application.

Lastly, a colloidal olivine nano silica (C-OnS) is successfully synthesized by using a colloidal mill to break up the secondary particles of the precipitated silica from olivine in Chapter 10. The stable suspension of silica nanoparticles can be achieved by adjusting the pH to 9 and adding 0.1% non-ionic surfactant Tween 60, reaching a high zeta potential of -36.0 mV. The particle size distribution of the C-OnS is centered at 164 nm measured by laser light scattering. C-OnS has a better dispersibility in cement paste and UHPC paste compared to olivine silica in powder form. The plastic viscosity is only 1.18 Pa s for C-OnS 2% UHPC paste while for olivine silica powder, the plastic viscosity increases to 1.80 Pa s. Therefore, using C-OnS can have a reduction on the use of SP in the UHPC production if the same workability is expected to be achieved. C-OnS can promote the cement hydration better than C-nS at early ages according to the results of calorimeter, thermal gravimetric analysis, and ^{29}Si and ^{27}Al nuclear magnetic resonance. The reason is that C-OnS obtains more silanol content and surface area compared with commercial colloidal nano-silica (C-nS). Also, the silicate species of C-OnS include Q^4, Q^3 and Q^2, indicating a better silica solubility in pore solution of UHPC. The mean chain length of C-S-H is longer for C-OnS samples than that of C-nS at early ages as indicated by ^{29}Si NMR. The Al (IV) species replace the Si in C-S-H forming C-(A)-S-H due to the formation of secondary hydration products C-S-H (α) by consuming $Ca(OH)_2$. This phenomenon happens at first 3 days for C-OnS while takes place more intense at 7 days for C-nS. The gel pore volume of UHPC with 2% C-OnS is higher than that of C-nS and reference at 1 and 3 days, indicating more C-S-H (α) is produced due to quick pozzolanic reaction. The nitrogen sorption and mercury intrusion porosimeter (MIP) result shows the C-nS can better facilitate filler effect in UHPC paste, thus reducing the small capillary pore volume better than C-OnS. The ultrahigh performance concrete obtains a higher early age strength with the incorporation of C-OnS and C-nS. The early age strength from 1 day to 7 days is higher for C-OnS group. While the 28 days strength of UHPC is almost the same for C-OnS and C-nS but still higher than reference. Therefore, the C-OnS mainly increases the first 7 days strength of UHPC.

11.2 Recommendations for future studies

This thesis investigates the high-end application of two abundantly available materials, miscanthus fibers and olivine, in the manufacture of sustainable lightweight insulating materials. Based on the chemical compositions and character of the raw materials, different pretreatment methods are applied for optimal utilization in building materials and for precursor to synthesize super insulating materials, for example, as lightweight aggregates in cement-based system, as a sustainable precursor for silica aerogel and nano-silica. The presented results can be used for an optimal design of sustainable building materials to achieve properties of excellent sustainability, thermal insulating, acoustic absorption and photocatalytic efficiency. Nevertheless, some open questions are remaining for future research:

1. The usage of miscanthus fibers in cement and concrete needs further investigation under different exposure conditions, especially the application in high humidity environment and under high temperatures. This is because the miscanthus fibers has a high water uptake and the tendency to break down at high temperatures. Therefore, the treatment of miscanthus fibers to reduce the water uptake and increase the resistance to heat is important.

2. The lower strength of bio-concrete is a shortcoming and the strategy to further increase the strength of bio-lightweight concrete is important. The possibilities of increasing the strength of bio-concrete includes: 1). Heat treatment of the miscanthus fibers to decrease the organic polysaccharides leached in the cement-based materials. 2). Utilizing compressible machine to compress the miscanthus fibers into a high density material, increasing the fiber strength, thus lead to a higher strength of the bio-concrete.

3. It is proven that silica aerogel can be synthesized from olivine. Hence, it can also be produced from other minerals or waste materials that are rich in silica, for instance, waste glass powder or incineration bottom ash. Treatment of bottom ash can be found in a PhD thesis [360]. However, the attention should be paid to the silica concentration in the raw materials and the complexity to prepare silica aerogel from these materials.

4. Silica aerogel is mainly applied alone in thermal insulation applications. More applications of silica aerogel can be explored as insulative additives, for instance, the combination of silica aerogel and phase change materials or in situ formation in the lightweight aggregate to achieve higher insulating performance.

5. More kinds of non-ionic surfactant need to be investigated to prepare ordered mesoporous silica from olivine with a larger pore size. For now, the pore size of mesoporous silica from olivine is either too small or too randomly distributed that cannot compare with the SBA-15. It is inspiring if ordered large pore size mesoporous silica can be prepared from olivine so mass application in photocatalytic support or nano-insulation materials is within reach.

References

[1] B.P. Jelle, Traditional, state-of-the-art and future thermal building insulation materials and solutions–Properties, requirements and possibilities, Energy Build. 43 (2011) 2549–2563.

[2] B.P. Jelle, A. Gustavsen, R. Baetens, The path to the high performance thermal building insulation materials and solutions of tomorrow, J. Build. Phys. 34 (2010) 99–123. doi:10.1177/1744259110372782.

[3] V. Kodur, S. Banerji, R. Solhmirzaei, Effect of Temperature on Thermal Properties of Ultrahigh-Performance Concrete, J. Mater. Civ. Eng. 32 (2020) 04020210. doi:10.1061/(asce)mt.1943-5533.0003286.

[4] R. Baetens, B.P. Jelle, A. Gustavsen, Aerogel insulation for building applications: A state-of-the-art review, Energy Build. 43 (2011) 761–769. doi:https://doi.org/10.1016/j.enbuild.2010.12.012.

[5] N. Narayanan, K. Ramamurthy, Structure and properties of aerated concrete: a review, Cem. Concr. Compos. 22 (2000) 321–329. doi:https://doi.org/10.1016/S0958-9465(00)00016-0.

[6] K.-C. Thienel, T. Haller, N. Beuntner, Lightweight Concrete—From Basics to Innovations, Mater. . 13 (2020). doi:10.3390/ma13051120.

[7] S. Amziane, F. Collet, Bio-aggregates Based Building Materials, State-of-the-Art Report, 2017. http://link.springer.com/10.1007/978-94-024-1031-0.

[8] T. Linhares, M.T.P. de Amorim, L. Durães, Silica aerogel composites with embedded fibres: a review on their preparation, properties and applications, J. Mater. Chem. A. 7 (2019) 22768–22802.

[9] M.M. Koebel, L. Huber, S. Zhao, W.J. Malfait, Breakthroughs in cost-effective, scalable production of superinsulating, ambient-dried silica aerogel and silica-biopolymer hybrid aerogels: from laboratory to pilot scale, J. Sol-Gel Sci. Technol. 79 (2016) 308–318. doi:10.1007/s10971-016-4012-5.

[10] T. Van Renterghem, J. Forssén, K. Attenborough, P. Jean, J. Defrance, M. Hornikx, J. Kang, Using natural means to reduce surface transport noise during propagation outdoors, Appl. Acoust. 92 (2015) 86–101.

[11] P. Glé, E. Gourdon, L. Arnaud, Acoustical properties of materials made of vegetable particles with several scales of porosity, Appl. Acoust. 72 (2011) 249–259. doi:10.1016/j.apacoust.2010.11.003.

[12] Z. Mazrouei-Sebdani, H. Begum, S. Schoenwald, K. V Horoshenkov, W.J. Malfait, A review on silica aerogel-based materials for acoustic applications, J. Non. Cryst. Solids. 562 (2021) 120770.

[13] T.L.N. Huyen, M.Q. T'Kint, C. Remond, B. Chabbert, R.-M. Dheilly, Saccharification of Miscanthus x giganteus, incorporation of lignocellulosic by-product in cementitious matrix, C. R. Biol. 334 (2011) 837-e1.

[14] H. V. Huth, Ermittlung bauphysikalischer und baustatischer Eigenschaften von Miscanthus-Leichtbeton, Anbau Und Verwertung von Miscanthus Eur. Beiträge Zu Agrar. Bd. 26 (2002) 33–38.

[15] R. Hesch, Bau-und Dämmplatten sowie Schüttdämmung aus Miscanthus x giganteus, Miscanthus–Vom Anbau Bis Zur Verwertung. Beiträge Zu Agrar. Bd. 19 (2000) 63–67.

[16] R. Pude, C.H. Treseler, G. Noga, Morphological, chemical and technical parameters of Miscanthus genotypes., J. Appl. Bot. Food Qual. 78 (2004) 58–63.

[17] M. Bołtryk, E. Pawluczuk, Properties of a lightweight cement composite with an ecological organic filler, Constr. Build. Mater. 51 (2014) 97–105. doi:10.1016/J.CONBUILDMAT.2013.10.065.

[18] R. Pude, C. Treseler, R. Trettin, G. Noga, Suitability of Miscanthus genotypes for lightweight concrete, Bodenkui Tur-wien and Munchen-. 56 (2005) 61.

[19] G. Ramakrishna, T. Sundararajan, Studies on the durability of natural fibres and the effect of corroded fibres on the strength of mortar, Cem. Concr. Compos. 27 (2005) 575–582. doi:10.1016/j.cemconcomp.2004.09.008.

[20] F. Tajra, M.A. Elrahman, D. Stephan, The production and properties of cold-bonded aggregate and its applications in concrete: A review, Constr. Build. Mater. 225 (2019) 29–43. doi:10.1016/j.conbuildmat.2019.07.219.

[21] P. Tang, M.V.A. Florea, H.J.H. Brouwers, Employing cold bonded pelletization to produce lightweight aggregates from incineration fine bottom ash, J. Clean. Prod. 165 (2017) 1371–1384.

doi:10.1016/j.jclepro.2017.07.234.

[22] G. Baykal, A.G. Döven, Utilization of fly ash by pelletization process; theory, application areas and research results, Resour. Conserv. Recycl. 30 (2000) 59–77. doi:10.1016/S0921-3449(00)00042-2.

[23] P. Tang, D. Xuan, H.W. Cheng, C.S. Poon, D.C.W. Tsang, Use of CO_2 curing to enhance the properties of cold bonded lightweight aggregates (CBLAs) produced with concrete slurry waste (CSW) and fine incineration bottom ash (IBA), J. Hazard. Mater. 381 (2020). doi:10.1016/j.jhazmat.2019.120951.

[24] E. Güneyisi, M. Gesoɨlu, I. Altan, H.Ö. Öz, Utilization of cold bonded fly ash lightweight fine aggregates as a partial substitution of natural fine aggregate in self-compacting mortars, Constr. Build. Mater. 74 (2015) 9–16. doi:10.1016/j.conbuildmat.2014.10.021.

[25] P. Tang, D. Xuan, C.S. Poon, D.C.W. Tsang, Valorization of concrete slurry waste (CSW) and fine incineration bottom ash (IBA) into cold bonded lightweight aggregates (CBLAs): Feasibility and influence of binder types, J. Hazard. Mater. 368 (2019) 689–697. doi:10.1016/j.jhazmat.2019.01.112.

[26] Y. Jiang, T.C. Ling, M. Shi, Strength enhancement of artificial aggregate prepared with waste concrete powder and its impact on concrete properties, J. Clean. Prod. 257 (2020) 120515. doi:10.1016/j.jclepro.2020.120515.

[27] J. Thomas, B. Harilal, Properties of cold bonded quarry dust coarse aggregates and its use in concrete, Cem. Concr. Compos. 62 (2015) 67–75. doi:10.1016/j.cemconcomp.2015.05.005.

[28] G. Liu, K. Schollbach, S. van der Laan, P. Tang, M.V.A. Florea, H.J.H. Brouwers, Recycling and utilization of high volume converter steel slag into CO_2 activated mortars – The role of slag particle size, Resour. Conserv. Recycl. 160 (2020). doi:10.1016/j.resconrec.2020.104883.

[29] S.S. Kistler, Coherent Expanded Aerogels and Jellies, Nature. 127 (1931) 741. doi:10.1038/127741a0.

[30] M. Schmidt, F. Schwertfeger, Applications for silica aerogel products, J. Non. Cryst. Solids. 225 (1998) 364–368. doi:https://doi.org/10.1016/S0022-3093(98)00054-4.

[31] J.P. Randall, M.A.B. Meador, S.C. Jana, Tailoring mechanical properties of aerogels for aerospace applications, ACS Appl. Mater. Interfaces. 3 (2011) 613–626.

[32] N. Bheekhun, A.R. Abu Talib, M.R. Hassan, Aerogels in Aerospace: An Overview, Adv. Mater. Sci. Eng. 2013 (2013) 406065. doi:10.1155/2013/406065.

[33] Q. Feng, K. Chen, D. Ma, H. Lin, Z. Liu, S. Qin, Y. Luo, Synthesis of high specific surface area silica aerogel from rice husk ash via ambient pressure drying, Colloids Surfaces A Physicochem. Eng. Asp. 539 (2018) 399–406. doi:10.1016/j.colsurfa.2017.12.025.

[34] W. Hu, M. Li, W. Chen, N. Zhang, B. Li, M. Wang, Z. Zhao, Preparation of hydrophobic silica aerogel with kaolin dried at ambient pressure, Colloids Surfaces A Physicochem. Eng. Asp. 501 (2016) 83–91. doi:https://doi.org/10.1016/j.colsurfa.2016.04.059.

[35] A. Lazaro, H.J.H. Brouwers, G. Quercia, J.W. Geus, The properties of amorphous nano-silica synthesized by the dissolution of olivine, Chem. Eng. J. 211–212 (2012) 112–121. doi:10.1016/j.cej.2012.09.042.

[36] A. Lazaro, Nano-silica production at low temperatures from the dissolution of olivine: Synthesis, tailoring and modeling, PhD thesis, Eindhoven University of Technology (2014).

[37] K.W. Kow, R. Yusoff, A.R.A. Aziz, E.C. Abdullah, From bamboo leaf to aerogel: Preparation of water glass as a precursor, J. Non. Cryst. Solids. 386 (2014) 76–84. doi:10.1016/j.jnoncrysol.2013.11.041.

[38] C.J. Lee, G.S. Kim, S.H. Hyun, Synthesis of silica aerogels from waterglass via new modified ambient drying, J. Mater. Sci. 37 (2002) 2237–2241.

[39] K. Kadoya, N. Matsunaga, A. Nagashima, Viscosity and Thermal Conductivity of Dry Air in the Gaseous Phase, J. Phys. Chem. Ref. Data. 14 (1985) 947–970. doi:10.1063/1.555744.

[40] F. Li, L. Xie, G. Sun, Q. Kong, F. Su, Y. Cao, J. Wei, A. Ahmad, X. Guo, C.-M. Chen, Resorcinol-formaldehyde based carbon aerogel: Preparation, structure and applications in energy storage devices, Microporous Mesoporous Mater. 279 (2019) 293–315.

[41] T. Budtova, Cellulose II aerogels: a review, Springer Netherlands, 2019. doi:10.1007/s10570-018-2189-1.

[42] A. Sharma, M. Thakur, M. Bhattacharya, T. Mandal, S. Goswami, Commercial application of cellulose nano-composites–A review, Biotechnol. Reports. 21 (2019) e00316.

[43] R.R. Choudhury, S.K. Sahoo, J.M. Gohil, Potential of bioinspired cellulose nanomaterials and nanocomposite membranes thereof for water treatment and fuel cell applications, Cellulose. 27 (2020) 6719–6746.

[44] P. Gupta, B. Singh, A.K. Agrawal, P.K. Maji, Low density and high strength nanofibrillated cellulose aerogel for thermal insulation application, Mater. Des. 158 (2018) 224–236.

[45] X. Wei, T. Huang, J. Nie, J. Yang, X. Qi, Z. Zhou, Y. Wang, Bio-inspired functionalization of microcrystalline cellulose aerogel with high adsorption performance toward dyes, Carbohydr. Polym. 198 (2018) 546–555.

[46] Y. Liang, H. Zhu, L. Wang, H. He, S. Wang, Biocompatible smart cellulose nanofibres for sustained drug release via pH and temperature dual-responsive mechanism, Carbohydr. Polym. 249 (2020) 116876.

[47] C.A. García-González, M.C. Camino-Rey, M. Alnaief, C. Zetzl, I. Smirnova, Supercritical drying of aerogels using CO_2: Effect of extraction time on the end material textural properties, J. Supercrit. Fluids. 66 (2012) 297–306. doi:https://doi.org/10.1016/j.supflu.2012.02.026.

[48] M.V. Khedkar, S.B. Somvanshi, A. V Humbe, K.M. Jadhav, Surface modified sodium silicate based superhydrophobic silica aerogels prepared via ambient pressure drying process, J. Non. Cryst. Solids. 511 (2019) 140–146. doi:https://doi.org/10.1016/j.jnoncrysol.2019.02.004.

[49] A.V. Rao, S.D. Bhagat, H. Hirashima, G.M. Pajonk, Synthesis of flexible silica aerogels using methyltrimethoxysilane (MTMS) precursor, J. Colloid Interface Sci. 300 (2006) 279–285.

[50] X. Cheng, C. Li, X. Shi, Z. Li, L. Gong, H. Zhang, Rapid synthesis of ambient pressure dried monolithic silica aerogels using water as the only solvent, Mater. Lett. 204 (2017) 157–160. doi:https://doi.org/10.1016/j.matlet.2017.05.107.

[51] Z. Ma, P. Cooper, D. Daly, L. Ledo, Existing building retrofits: Methodology and state-of-the-art, Energy Build. 55 (2012) 889–902.

[52] Z. Zhang, J.L. Provis, A. Reid, H. Wang, Geopolymer foam concrete: An emerging material for sustainable construction, Constr. Build. Mater. 56 (2014) 113–127.

[53] B. Majidi, Geopolymer technology, from fundamentals to advanced applications: a review, Mater. Technol. 24 (2009) 79–87.

[54] J. Seo, S.J. Bae, D.I. Jang, S. Park, B. Yang, H.-K.K. Lee, Thermal behavior of alkali-activated fly ash/slag with the addition of an aerogel as an aggregate replacement, Cem. Concr. Compos. 106 (2020) 103462. doi:10.1016/j.cemconcomp.2019.103462.

[55] J. He, Q. Gao, X. Song, X. Bu, J. He, Effect of foaming agent on physical and mechanical properties of alkali-activated slag foamed concrete, Constr. Build. Mater. 226 (2019) 280–287.

[56] Y.X.X. Chen, Y. Hendrix, K. Schollbach, H.J.. J.H. Brouwers, A silica aerogel synthesized from olivine and its application as a photocatalytic support, Constr. Build. Mater. 248 (2020) 118709. doi:https://doi.org/10.1016/j.conbuildmat.2020.118709.

[57] G.S. Attard, J.C. Glyde, C.G. Göltner, Liquid-crystalline phases as templates for the synthesis of mesoporous silica, Nature. 378 (1995) 366–368. doi:10.1038/378366a0.

[58] F. Tang, L. Li, D. Chen, Mesoporous silica nanoparticles: Synthesis, biocompatibility and drug delivery, Adv. Mater. 24 (2012) 1504–1534. doi:10.1002/adma.201104763.

[59] A. Lazaro, G. Quercia, H.J.H. Brouwers, J.W. Geus, Synthesis of a green nano-silica material using beneficiated waste dunites and its application in concrete, World J. Nano Sci. Eng. 2013 (2013) 41–51. doi:10.4236/wjnse.2013.33006.

[60] A. Lazaro, L. Benac-Vegas, H.J.H. Brouwers, J.W. Geus, J. Bastida, The kinetics of the olivine dissolution under the extreme conditions of nano-silica production, Appl. Geochemistry. 52 (2015) 1–15. doi:10.1016/j.apgeochem.2014.10.015.

[61] T. Oertel, U. Helbig, F. Hutter, H. Kletti, G. Sextl, Influence of amorphous silica on the hydration in ultra-high performance concrete, Cem. Concr. Res. 58 (2014) 121–130. doi:10.1016/j.cemconres.2014.01.006.

[62] G. Quercia, G. Hüsken, H.J.H. Brouwers, Water demand of amorphous nano silica and its impact on the workability of cement paste, Cem. Concr. Res. 42 (2012) 344–357. doi:10.1016/j.cemconres.2011.10.008.

[63] F. Kontoleontos, P.E. Tsakiridis, A. Marinos, V. Kaloidas, M. Katsioti, Influence of colloidal nanosilica

on ultrafine cement hydration: Physicochemical and microstructural characterization, Constr. Build. Mater. 35 (2012) 347–360. doi:10.1016/j.conbuildmat.2012.04.022.

[64] J.I. Tobón, J.J. Payá, M. V. Borrachero, O.J. Restrepo, Mineralogical evolution of Portland cement blended with silica nanoparticles and its effect on mechanical strength, Constr. Build. Mater. 36 (2012) 736–742. doi:10.1016/j.conbuildmat.2012.06.043.

[65] R. Yu, P. Spiesz, H.J.H. Brouwers, Effect of nano-silica on the hydration and microstructure development of Ultra-High Performance Concrete (UHPC) with a low binder amount, Constr. Build. Mater. (2014). doi:10.1016/j.conbuildmat.2014.04.063.

[66] L.P. Singh, S.R. Karade, S.K. Bhattacharyya, M.M. Yousuf, S. Ahalawat, Beneficial role of nanosilica in cement based materials - A review, Constr. Build. Mater. 47 (2013) 1069–1077. doi:10.1016/j.conbuildmat.2013.05.052.

[67] M. Azimi-Pour, H. Eskandari-Naddaf, Synergistic effect of colloidal nano and micro-silica on the microstructure and mechanical properties of mortar using full factorial design, Constr. Build. Mater. (2020). doi:10.1016/j.conbuildmat.2020.120497.

[68] A. Thakkar, A. Raval, S. Chandra, M. Shah, A. Sircar, A comprehensive review of the application of nano-silica in oil well cementing, Petroleum. 6 (2020) 123–129. doi:10.1016/j.petlm.2019.06.005.

[69] G. Quercia, A. Lazaro, J.W. Geus, H.J.H. Brouwers, Characterization of morphology and texture of several amorphous nano-silica particles used in concrete, Cem. Concr. Compos. 44 (2013) 77–92. doi:10.1016/j.cemconcomp.2013.05.006.

[70] O. Onuaguluchi, N. Banthia, Plant-based natural fibre reinforced cement composites: A review, Cem. Concr. Compos. 68 (2016) 96–108. doi:10.1016/j.cemconcomp.2016.02.014.

[71] T. Le Ngoc Huyen, M. Queneudec T'Kint, C. Remond, B. Chabbert, R.M. Dheilly, Saccharification of Miscanthus x giganteus, incorporation of lignocellulosic by-product in cementitious matrix, C. R. Biol. 334 (2011) 837.e1-837.e11. doi:10.1016/J.CRVI.2011.07.008.

[72] L. Courard, A. Darimont, A. Louis, F. Michel, Mineralization of bio-based materials effects on cement based mix properties, Bull. Polytech. Inst. Jassy, Constr. Archit. Sect. LIV (2011). http://hdl.handle.net/2268/59257.

[73] R. Pude, C.H. Treseler, R. Trettin, G. Noga, Suitability of Miscanthus genotypes for lightweight concrete, Bodenkultur. 56 (2005) 61–69.

[74] S.B. Park, D.S. Seo, J. Lee, Studies on the sound absorption characteristics of porous concrete based on the content of recycled aggregate and target void ratio, Cem. Concr. Res. 35 (2005) 1846–1854. doi:10.1016/j.cemconres.2004.12.009.

[75] A. Laukaitis, B. Fiks, Acoustical properties of aerated autoclaved concrete, Appl. Acoust. 67 (2006) 284–296. doi:10.1016/j.apacoust.2005.07.003.

[76] P. Glé, E. Gourdon, L. Arnaud, Modelling of the acoustical properties of hemp particles, Constr. Build. Mater. 37 (2012) 801–811. doi:10.1016/ j.conbuildmat.2012.06.008.

[77] V.Cerezo, Propriétés mécaniques, thermiques et acoustiques d'un matériau à base de particules végétales : approche expérimentale et modélisation théorique, Thèse Dr. (2005) 247.

[78] I. Merta, E.K. Tschegg, Fracture energy of natural fibre reinforced concrete, Constr. Build. Mater. 40 (2013) 991–997. doi:10.1016/ j.conbuildmat.2012.11.060.

[79] C.J. Knill, J.F. Kennedy, Degradation of cellulose under alkaline conditions, Carbohydr. Polym. 51 (2003) 281–300. doi:10.1016/S0144-8617(02)00183-2.

[80] R.D. Tolêdo Filho, K. Ghavami, G.L. England, K. Scrivener, Development of vegetable fibre–mortar composites of improved durability, Cem. Concr. Compos. 25 (2003) 185–196. doi:https://doi.org/10.1016/S0958-9465(02)00018-5.

[81] G. Mármol, S.F. Santos, H. Savastano, M. V Borrachero, J. Monzó, J. Payá, Mechanical and physical performance of low alkalinity cementitious composites reinforced with recycled cellulosic fibres pulp from cement kraft bags, Ind. Crops Prod. 49 (2013) 422–427. doi:https://doi.org/10.1016/j.indcrop.2013.04.051.

[82] L.Y. Mwaikambo, M.P. Ansell, The determination of porosity and cellulose content of plant fibers by density methods, J. Mater. Sci. Lett. 20 (2001) 2095–2096. doi:10.1023/A:1013703809964.

[83] B.S. EN, Methods of test for mortar for masonry-Part 3: Determination of consistence of fresh mortar (by flow table), (1999).

[84] B.S. Institution, Testing Hardened Concrete: Making and Curing Specimens for Strength Tests, BSI, 2009.

[85] B.S. EN, Testing hardened concrete–Part 7: Density of hardened concrete, London Br. Stand. Inst. (2009).

[86] B. Standard, Methods of testing cement, Determ. Strength. (2005).

[87] H. Savastano, V. Agopyan, A.M. Nolasco, L. Pimentel, Plant fibre reinforced cement components for roofing, Constr. Build. Mater. 13 (1999) 433–438. doi:https://doi.org/10.1016/S0950-0618(99)00046-X.

[88] M.A. Mansur, M.A. Aziz, A study of jute fibre reinforced cement composites, Int. J. Cem. Compos. Light. Concr. 4 (1982) 75–82. doi:https://doi.org/10.1016/0262-5075(82)90011-2.

[89] H.F.W. Taylor, Cement chemistry, Thomas Telford, London, 1997.

[90] Q.L. Yu, P. Spiesz, H.J.H. Brouwers, Development of cement-based lightweight composites - Part 1: Mix design methodology and hardened properties, Cem. Concr. Compos. 44 (2013) 17–29. doi:10.1016/j.cemconcomp.2013.03.030.

[91] A. Kan, R. Demirboğa, A novel material for lightweight concrete production, Cem. Concr. Compos. 31 (2009) 489–495. doi:10.1016/j.cemconcomp.2009.05.002.

[92] X. Liu, K.S. Chia, M.-H. Zhang, Development of lightweight concrete with high resistance to water and chloride-ion penetration, Cem. Concr. Compos. 32 (2010) 757–766. doi:https://doi.org/10.1016/j.cemconcomp.2010.08.005.

[93] V. Ducman, A. Mladenovič, J.S. Šuput, Lightweight aggregate based on waste glass and its alkali–silica reactivity, Cem. Concr. Res. 32 (2002) 223–226.

[94] J. Alduaij, K. Alshaleh, M.N. Haque, K. Ellaithy, Lightweight concrete in hot coastal areas, Cem. Concr. Compos. 21 (1999) 453–458.

[95] M. Schauerte, R. Trettin, Neue Schaumbetone mit gesteigerten mechanischen ind physikalischen Eigenschaften., in: Proc. 18th Ibausil, Int. Conf. Build. Mater., 2012.

[96] L. Arnaud, E. Gourlay, Experimental study of parameters influencing mechanical properties of hemp concretes, Constr. Build. Mater. 28 (2012) 50–56.

[97] H. Acikel, The use of miscanthus (Giganteus) as a plant fiber in concrete production, Sci. Res. Essays. 6 (2011) 2660–2667.

[98] V. Dubois, E. Wirquin, C. Flament, P. Sloma, Fresh and hardened state properties of hemp concrete made up of a large proportion of quarry fines for the production of blocks, Constr. Build. Mater. 102 (2016) 84–93.

[99] A.T. Le, A. Gacoin, A. Li, T.H. Mai, N. El Wakil, Influence of various starch/hemp mixtures on mechanical and acoustical behavior of starch-hemp composite materials, Compos. Part B Eng. 75 (2015) 201–211.

[100] H. Binici, O. Aksogan, C. Demirhan, Mechanical, thermal and acoustical characterizations of an insulation composite made of bio-based materials, Sustain. Cities Soc. 20 (2016) 17–26.

[101] N. Mati-Baouche, H. De Baynast, A. Lebert, S. Sun, C.J.S. Lopez-Mingo, P. Leclaire, P. Michaud, Mechanical, thermal and acoustical characterizations of an insulating bio-based composite made from sunflower stalks particles and chitosan, Ind. Crops Prod. 58 (2014) 244–250.

[102] M. Fan, M.K. Ndikontar, X. Zhou, J.N. Ngamveng, Cement-bonded composites made from tropical woods: Compatibility of wood and cement, Constr. Build. Mater. 36 (2012) 135–140. doi:10.1016/j.conbuildmat.2012.04.089.

[103] R.S.P. Coutts, A review of Australian research into natural fibre cement composites, Cem. Concr. Compos. 27 (2005) 518–526.

[104] N.L. Thomas, J.D. Birchall, The retarding action of sugars on cement hydration, Cem. Concr. Res. 13 (1983) 830–842.

[105] D. Sedan, C. Pagnoux, A. Smith, T. Chotard, Mechanical properties of hemp fibre reinforced cement: Influence of the fibre/matrix interaction, J. Eur. Ceram. Soc. 28 (2008) 183–192.

[106] M. Bravo, J. De Brito, J. Pontes, L. Evangelista, Mechanical performance of concrete made with aggregates from construction and demolition waste recycling plants, J. Clean. Prod. 99 (2015) 59–74.

[107] R. Yu, Z. Shui, Efficient reuse of the recycled construction waste cementitious materials, J. Clean. Prod. 78 (2014) 202–207.

[108] K.-H. Yang, J.-K. Song, K.-I. Song, Assessment of CO_2 reduction of alkali-activated concrete, J. Clean. Prod. 39 (2013) 265–272.

[109] K.-H. Yang, K.-H. Lee, J.-K. Song, M.-H. Gong, Properties and sustainability of alkali-activated slag foamed concrete, J. Clean. Prod. 68 (2014) 226–233.

[110] R. Yu, Z. Shui, Influence of agglomeration of a recycled cement additive on the hydration and microstructure development of cement based materials, Constr. Build. Mater. 49 (2013) 841–851.

[111] F. Pelisser, A. Barcelos, D. Santos, M. Peterson, A.M. Bernardin, Lightweight concrete production with low Portland cement consumption, J. Clean. Prod. 23 (2012) 68–74.

[112] P. Shafigh, H. Bin Mahmud, M.Z. Bin Jumaat, R. Ahmmad, S. Bahri, Structural lightweight aggregate concrete using two types of waste from the palm oil industry as aggregate, J. Clean. Prod. 80 (2014) 187–196.

[113] Q.L. Yu, P. Spiesz, H.J.H. Brouwers, Ultra-lightweight concrete: Conceptual design and performance evaluation, Cem. Concr. Compos. 61 (2015) 18–28. doi:10.1016/j.cemconcomp.2015.04.012.

[114] P. Spiesz, Q.L. Yu, H.J.H. Brouwers, Development of cement-based lightweight composites - Part 2: Durability-related properties, Cem. Concr. Compos. 44 (2013) 30–40. doi:10.1016/j.cemconcomp.2013.03.029.

[115] S. de Castro, J. de Brito, Evaluation of the durability of concrete made with crushed glass aggregates, J. Clean. Prod. 41 (2013) 7–14.

[116] T.-C. Ling, C.-S. Poon, Feasible use of recycled CRT funnel glass as heavyweight fine aggregate in barite concrete, J. Clean. Prod. 33 (2012) 42–49.

[117] Y. Chen, Q.L. Yu, H.J.H. Brouwers, Acoustic performance and microstructural analysis of bio-based lightweight concrete containing miscanthus, Constr. Build. Mater. 157 (2017) 839–851. doi:10.1016/j.conbuildmat.2017.09.161.

[118] S. Elfordy, F. Lucas, F. Tancret, Y. Scudeller, L. Goudet, Mechanical and thermal properties of lime and hemp concrete ("hempcrete") manufactured by a projection process, Constr. Build. Mater. 22 (2008) 2116–2123. doi:https://doi.org/10.1016/j.conbuildmat.2007.07.016.

[119] A. Bouguerra, A. Ledhem, F. de Barquin, R.M. Dheilly, M. Quéneudec, Effect of microstructure on the mechanical and thermal properties of lightweight concrete prepared from clay, cement, and wood aggregates, Cem. Concr. Res. 28 (1998) 1179–1190. doi:https://doi.org/10.1016/S0008-8846(98)00075-1.

[120] M. Bederina, L. Marmoret, K. Mezreb, M.M. Khenfer, A. Bali, M. Quéneudec, Effect of the addition of wood shavings on thermal conductivity of sand concretes: Experimental study and modelling, Constr. Build. Mater. 21 (2007) 662–668. doi:https://doi.org/10.1016/j.conbuildmat.2005.12.008.

[121] M. Bederina, B. Laidoudi, A. Goullieux, M.M. Khenfer, A. Bali, M. Quéneudec, Effect of the treatment of wood shavings on the physico-mechanical characteristics of wood sand concretes, Constr. Build. Mater. 23 (2009) 1311–1315. doi:https://doi.org/10.1016/j.conbuildmat.2008.07.029.

[122] K. Al Rim, A. Ledhem, O. Douzane, R.M. Dheilly, M. Queneudec, Influence of the proportion of wood on the thermal and mechanical performances of clay-cement-wood composites, Cem. Concr. Compos. 21 (1999) 269–276. doi:https://doi.org/10.1016/S0958-9465(99)00008-6.

[123] H.J.H. Brouwers, Particle-size distribution and packing fraction of geometric random packings, Phys. Rev. E. 84 (2006) 59905. doi:10.1103/PhysRevE.84.059905.

[124] H.J.H. Brouwers, H.J. Radix, Self-Compacting Concrete: Theoretical and experimental study, Cem. Concr. Res. 35 (2005) 2116–2136. doi:https://doi.org/10.1016/j.cemconres.2005.06.002.

[125] Q.L. Yu, H.J.H. Brouwers, Microstructure and mechanical properties of β-hemihydrate produced gypsum: An insight from its hydration process, Constr. Build. Mater. 25 (2011) 3149–3157. doi:https://doi.org/10.1016/j.conbuildmat.2010.12.005.

[126] A. International, ASTM C642-13 Standard Test Method for Density, Absorption, and Voids in Hardened

Concrete, (2013).

[127] ASTM, C 597, Standard test method for pulse velocity through concrete, ASTM Int. West Conshohocken, PA. (2009).

[128] B.S. EN, 206-1: 2000, Concr. 1 Specif. Performance, Prod. Conform. (2001).

[129] K.H. Mo, U.J. Alengaram, M.Z. Jumaat, S.P. Yap, S.C. Lee, Green concrete partially comprised of farming waste residues: a review, J. Clean. Prod. 117 (2016) 122–138.

[130] O. Kinnane, A. Reilly, J. Grimes, S. Pavia, R. Walker, Acoustic Absorption of Hemp Walls with Ground Granulated Blast Slag, Int. J. Archit. Environ. Eng. 10 (2016) 1188–1191.

[131] O. Kinnane, A. Reilly, J. Grimes, S. Pavia, R. Walker, Acoustic absorption of hemp-lime construction, Constr. Build. Mater. 122 (2016) 674–682.

[132] M. Degrave-Lemeurs, P. Glé, A.H. de Menibus, Acoustical properties of hemp concretes for buildings thermal insulation: Application to clay and lime binders, Constr. Build. Mater. 160 (2018) 462–474.

[133] E. Gourlay, P. Glé, S. Marceau, C. Foy, S. Moscardelli, Effect of water content on the acoustical and thermal properties of hemp concretes, Constr. Build. Mater. 139 (2017) 513–523.

[134] Q.L. Yu, H.J.H. Brouwers, Development of a self-compacting gypsum-based lightweight composite, Cem. Concr. Compos. 34 (2012) 1033–1043.

[135] R. Yu, D. V Van Onna, P. Spiesz, Q.L. Yu, H.J.H. Brouwers, Development of ultra-lightweight fibre reinforced concrete applying expanded waste glass, J. Clean. Prod. 112 (2016) 690–701.

[136] P.E. Mason, L.I. Darvell, J.M. Jones, A. Williams, Comparative study of the thermal conductivity of solid biomass fuels, Energy & Fuels. 30 (2016) 2158–2163.

[137] A.D. Brailsford, K.G. Major, The thermal conductivity of aggregates of several phases, including porous materials, Br. J. Appl. Phys. 15 (1964) 313.

[138] K. Pietrak, T.S. Wisniewski, T. Wiśniewski, A review of models for effective thermal conductivity of composite materials, J. Power Technol. 95 (2015) 14.

[139] I.B. Topçu, T. Uygunoğlu, Effect of aggregate type on properties of hardened self-consolidating lightweight concrete (SCLC), Constr. Build. Mater. 24 (2010) 1286–1295. doi:10.1016/j.conbuildmat.2009.12.007.

[140] K.H. Kilburn, D. Powers, R.H. Warshaw, Pulmonary effects of exposure to fine fibreglass: irregular opacities and small airways obstruction., Occup. Environ. Med. 49 (1992) 714–720.

[141] D. Felten, N. Fröba, J. Fries, C. Emmerling, Energy balances and greenhouse gas-mitigation potentials of bioenergy cropping systems (Miscanthus, rapeseed, and maize) based on farming conditions in Western Germany, Renew. Energy. 55 (2013) 160–174. doi:10.1016/j.renene.2012.12.004.

[142] S. Chandra, L. Berntsson, Introduction, in: S. Chandra, L.B.T.-L.A.C. Berntsson (Eds.), Light. Aggreg. Concr., William Andrew Publishing, Norwich, NY, 2002: pp. 1–3. doi:https://doi.org/10.1016/B978-081551486-2.50003-1.

[143] Y.X. Chen, F. Wu, Q. Yu, H.J.H.H. Brouwers, Bio-based ultra-lightweight concrete applying miscanthus fibers: Acoustic absorption and thermal insulation, Cem. Concr. Compos. 114 (2020) 103829. doi:https://doi.org/10.1016/j.cemconcomp.2020.103829.

[144] V. Ducman, A. Mladenovic, Lightweight aggregate based on waste glass and its alkali – silica reactivity, Cem. Concr. Res. 32 (2002) 223–226.

[145] Hammer, T.A., van Breugel, K., Helland, S., Holand, I., Maage, M., Mijnsbergen, J.P.G. and Sveinsdóttir, E.L.Economic Design and Construction with Structural Lightweight Aggregate Concrete, F.H. Wittmann (Ed.) 2000.

[146] A.P. Papadopoulos, Inorganic and synthetic organic components of soilless culture and potting mixes, in: M. Raviv, J.H.B.T.-S.C. Lieth (Eds.), Elsevier, Amsterdam, 2008: pp. 505–543. doi:https://doi.org/10.1016/B978-044452975-6.50014-9.

[147] P. Tang, H.J.H. Brouwers, Integral recycling of municipal solid waste incineration (MSWI) bottom ash fines (0–2 mm) and industrial powder wastes by cold-bonding pelletization, Waste Manag. 62 (2017) 125–138. doi:10.1016/j.wasman.2017.02.028.

[148] P. Tang, H.J.H. Brouwers, The durability and environmental properties of self-compacting concrete incorporating cold bonded lightweight aggregates produced from combined industrial solid wastes, Constr. Build. Mater. 167 (2018) 271–285. doi:10.1016/j.conbuildmat.2018.02.035.

[149] P. Tang, D. Xuan, J. Li, H.W. Cheng, C.S. Poon, D.C.W. Tsang, Investigation of cold bonded lightweight aggregates produced with incineration sewage sludge ash (ISSA) and cementitious waste, J. Clean. Prod. 251 (2020). doi:10.1016/j.jclepro.2019.119709.

[150] K. Ramamurthy, K.I. Harikrishnan, Influence of binders on properties of sintered fly ash aggregate, Cem. Concr. Compos. 28 (2006) 33–38. doi:10.1016/j.cemconcomp.2005.06.005.

[151] L. Di Palma, F. Medici, G. Vilardi, Artificial aggregate from non metallic automotive shredder residue, Chem. Eng. Trans. 43 (2015) 1723–1728. doi:10.3303/CET1543288.

[152] S. Geetha, K. Ramamurthy, Reuse potential of low-calcium bottom ash as aggregate through pelletization, Waste Manag. 30 (2010) 1528–1535. doi:10.1016/j.wasman.2010.03.027.

[153] L.A.T. Bui, C.L. Hwang, C.T. Chen, K.L. Lin, M.Y. Hsieh, Manufacture and performance of cold bonded lightweight aggregate using alkaline activators for high performance concrete, Constr. Build. Mater. 35 (2012) 1056–1062. doi:10.1016/j.conbuildmat.2012.04.032.

[154] S. Geetha, K. Ramamurthy, Properties of geopolymerised low-calcium bottom ash aggregate cured at ambient temperature, Cem. Concr. Compos. 43 (2013) 20–30. doi:10.1016/j.cemconcomp.2013.06.007.

[155] F. Tajra, M.A. Elrahman, S.Y. Chung, D. Stephan, Performance assessment of core-shell structured lightweight aggregate produced by cold bonding pelletization process, Constr. Build. Mater. 179 (2018) 220–231. doi:10.1016/j.conbuildmat.2018.05.237.

[156] S. Geetha, K. Ramamurthy, Environmental friendly technology of cold-bonded bottom ash aggregate manufacture through chemical activation, J. Clean. Prod. 18 (2010) 1563–1569. doi:10.1016/j.jclepro.2010.06.006.

[157] M. Gesoğlu, E. Güneyisi, H.Ö. Öz, Properties of lightweight aggregates produced with cold-bonding pelletization of fly ash and ground granulated blast furnace slag, Mater. Struct. Constr. 45 (2012) 1535–1546. doi:10.1617/s11527-012-9855-9.

[158] G.C. Wang, 1 - Introduction, in: G.C.B.T.-T.U. of S. in C.I.C. Wang (Ed.), Woodhead Publishing, 2016: pp. 1–7. doi:https://doi.org/10.1016/B978-0-08-100381-7.00001-X.

[159] EUROFER, European Steel in Figures 2019, (2019). https://www.eurofer.eu/publications/archive/european-steel-in-figures-2019/.

[160] K.R. Reddy, J.K. Chetri, G. Kumar, D.G. Grubb, Effect of basic oxygen furnace slag type on carbon dioxide sequestration from landfill gas emissions, Waste Manag. 85 (2019) 425–436. doi:10.1016/j.wasman.2019.01.013.

[161] Q. Wang, P. Yan, Hydration properties of basic oxygen furnace steel slag, Constr. Build. Mater. 24 (2010) 1134–1140. doi:10.1016/j.conbuildmat.2009.12.028.

[162] E. Belhadj, C. Diliberto, A. Lecomte, Characterization and activation of Basic Oxygen Furnace slag, Cem. Concr. Compos. 34 (2012) 34–40. doi:10.1016/j.cemconcomp.2011.08.012.

[163] V.J. Ferreira, A. Sáez-De-Guinoa Vilaplana, T. García-Armingol, A. Aranda-Usón, C. Lausín-González, A.M. López-Sabirón, G. Ferreira, Evaluation of the steel slag incorporation as coarse aggregate for road construction: Technical requirements and environmental impact assessment, J. Clean. Prod. 130 (2016) 175–186. doi:10.1016/j.jclepro.2015.08.094.

[164] EN1097-3, Tests for mechanical and physical properties of aggregates-Part 3: Determination of loose bulk density and voids, Germany, 1998.

[165] EN1097-6, Tests for mechanical and physical properties of aggregates – Part 6: Determination of particle density and water absorption, Germany, 2005.

[166] EN13055-1, Lightweight aggregates — Part 1: Lightweight aggregates for concrete, mortar and grout, 2002.

[167] F. Colangelo, F. Messina, R. Cioffi, Recycling of MSWI fly ash by means of cementitious double step cold bonding pelletization: Technological assessment for the production of lightweight artificial aggregates, J. Hazard. Mater. 299 (2015) 181–191. doi:10.1016/j.jhazmat.2015.06.018.

[168] C.L. Hwang, V.A. Tran, A study of the properties of foamed lightweight aggregate for self-consolidating concrete, Constr. Build. Mater. 87 (2015) 78–85. doi:10.1016/j.conbuildmat.2015.03.108.

[169] P. Gomathi, A. Sivakumar, Accelerated curing effects on the mechanical performance of cold bonded and sintered fly ash aggregate concrete, Constr. Build. Mater. 77 (2015) 276–287. doi:10.1016/j.conbuildmat.2014.12.108.

[170] N.U. Kockal, T. Ozturan, Durability of lightweight concretes with lightweight fly ash aggregates, Constr. Build. Mater. 25 (2011) 1430–1438. doi:10.1016/j.conbuildmat.2010.09.022.

[171] J.M. Chi, R. Huang, C.C. Yang, J.J. Chang, Effect of aggregate properties on the strength and stiffness of lightweight concrete, Cem. Concr. Compos. 25 (2003) 197–205. doi:10.1016/S0958-9465(02)00020-3.

[172] A.M.A. Nada, M.L. Hassan, Thermal behavior of cellulose and some cellulose derivatives, Polym. Degrad. Stab. 67 (2000) 111–115. doi:10.1016/S0141-3910(99)00100-7.

[173] C.L. Waters, R.R. Janupala, R.G. Mallinson, L.L. Lobban, Staged thermal fractionation for segregation of lignin and cellulose pyrolysis products: An experimental study of residence time and temperature effects, J. Anal. Appl. Pyrolysis. 126 (2017) 380–389. doi:10.1016/j.jaap.2017.05.008.

[174] R. Baciocchi, G. Costa, A. Polettini, R. Pomi, Effects of thin-film accelerated carbonation on steel slag leaching, J. Hazard. Mater. 286 (2015) 369–378. doi:10.1016/j.jhazmat.2014.12.059.

[175] M. Tu, H. Zhao, Z. Lei, L. Wang, D. Chen, H. Yu, T. Qi, Aqueous carbonation of steel slag: A kinetics study, ISIJ Int. 55 (2015) 2509–2514. doi:10.2355/isijinternational.ISIJINT-2015-142.

[176] EN206-1, Concrete Part 1: Specification, performance, production and conformity, 2005.

[177] A. Frankovič, V.B. Bosiljkov, V. Ducman, Lightweight aggregates made from fly ash using the cold-bond process and their use in lightweight concrete, Mater. Tehnol. 51 (2017) 267–274. doi:10.17222/mit.2015.337.

[178] F. Tajra, M. Abd Elrahman, C. Lehmann, D. Stephan, Properties of lightweight concrete made with core-shell structured lightweight aggregate, Constr. Build. Mater. 205 (2019) 39–51. doi:10.1016/j.conbuildmat.2019.01.194.

[179] M.A. Aegerter, N. Leventis, M.M. Koebel, Aerogels handbook, Springer Science & Business Media, 2011.

[180] I. Smirnova, P. Gurikov, Aerogel production: Current status, research directions, and future opportunities, J. Supercrit. Fluids. (2018). doi:10.1016/j.supflu.2017.12.037.

[181] H. Maleki, L. Durães, A. Portugal, An overview on silica aerogels synthesis and different mechanical reinforcing strategies, J. Non. Cryst. Solids. 385 (2014) 55–74.

[182] G. Jia, Z. Li, P. Liu, Q. Jing, Preparation and characterization of aerogel/expanded perlite composite as building thermal insulation material, J. Non. Cryst. Solids. 482 (2018) 192–202. doi:10.1016/j.jnoncrysol.2017.12.047.

[183] Y. Huang, J.L. Niu, Energy and visual performance of the silica aerogel glazing system in commercial buildings of Hong Kong, Constr. Build. Mater. 94 (2015) 57–72. doi:10.1016/j.conbuildmat.2015.06.053.

[184] T. Gao, T. Ihara, S. Grynning, B.P. Jelle, A.G. Lien, Perspective of aerogel glazings in energy efficient buildings, Build. Environ. 95 (2016) 405–413. doi:10.1016/j.buildenv.2015.10.001.

[185] A.C. Pierre, G.M. Pajonk, Chemistry of aerogels and their applications, Chem. Rev. 102 (2002) 4243–4266.

[186] H. Maleki, N. Hüsing, Current status, opportunities and challenges in catalytic and photocatalytic applications of aerogels: Environmental protection aspects, Appl. Catal. B Environ. 221 (2018) 530–555.

[187] M. Anas, S. Ünsal, C. Erkey, Investigation of various aerogels as adsorbents for methane storage, J. Supercrit. Fluids. 141 (2018) 166–172.

[188] Z. Li, L. Shao, Z. Ruan, W. Hu, L. Lu, Y. Chen, Converting untreated waste office paper and chitosan into aerogel adsorbent for the removal of heavy metal ions, Carbohydr. Polym. 193 (2018) 221–227.

[189] H. Maleki, L. Durães, C.A. García-González, P. Del Gaudio, A. Portugal, M. Mahmoudi, Synthesis and biomedical applications of aerogels: Possibilities and challenges, Adv. Colloid Interface Sci. 236 (2016) 1–27.

[190] M.L.N. Perdigoto, R.C. Martins, N. Rocha, M.J. Quina, L. Gando-Ferreira, R. Patrício, L. Durães,

Application of hydrophobic silica based aerogels and xerogels for removal of toxic organic compounds from aqueous solutions, J. Colloid Interface Sci. 380 (2012) 134–140.

[191] R. Ciriminna, A. Fidalgo, V. Pandarus, F. Beland, L.M. Ilharco, M. Pagliaro, The sol–gel route to advanced silica-based materials and recent applications, Chem. Rev. 113 (2013) 6592–6620. doi:10.1021/cr300399c.

[192] J. Fricke, A. Emmerling, Aerogels—recent progress in production techniques and novel applications, J. Sol-Gel Sci. Technol. 13 (1998) 299–303.

[193] G. Carlson, D. Lewis, K. McKinley, J. Richardson, T. Tillotson, Aerogel commercialization: technology, markets and costs, J. Non. Cryst. Solids. 186 (1995) 372–379. doi:10.1016/0022-3093(95)00069-0.

[194] M. Fawer, M. Concannon, W. Rieber, Life cycle inventories for the production of sodium silicates, Int. J. Life Cycle Assess. 4 (1999) 207–212. doi:10.1007/BF02979498.

[195] Y.R. Lee, J.T. Soe, S. Zhang, J.W. Ahn, M.B. Park, W.S. Ahn, Synthesis of nanoporous materials via recycling coal fly ash and other solid wastes: A mini review, Chem. Eng. J. 317 (2017) 821–843. doi:10.1016/j.cej.2017.02.124.

[196] F. Shi, J.X. Liu, K. Song, Z.Y. Wang, Cost-effective synthesis of silica aerogels from fly ash via ambient pressure drying, J. Non. Cryst. Solids. 356 (2010) 2241–2246. doi:10.1016/j.jnoncrysol.2010.08.005.

[197] X. Wu, M. Fan, J.F. Mclaughlin, X. Shen, G. Tan, A novel low-cost method of silica aerogel fabrication using fly ash and trona ore with ambient pressure drying technique, Powder Technol. 323 (2018) 310–322.

[198] Q. Alam, Y. Hendrix, L. Thijs, A. Lazaro, K. Schollbach, H.J.H. Brouwers, Novel low temperature synthesis of sodium silicate and ordered mesoporous silica from incineration bottom ash, J. Clean. Prod. 211 (2019) 874–883. doi:https://doi.org/10.1016/j.jclepro.2018.11.173.

[199] R.C.L. Jonckbloedt, Olivine dissolution in sulphuric acid at elevated temperatures - implications for the olivine process, an alternative waste acid neutralizing process, J. Geochemical Explor. 62 (1998) 337–346. doi:10.1016/S0375-6742(98)00002-8.

[200] A. Lazaro, M.C. Van De Griend, H.J.H. Brouwers, J.W. Geus, The influence of process conditions and Ostwald ripening on the specific surface area of olivine nano-silica, Microporous Mesoporous Mater. 181 (2013) 254–261. doi:10.1016/j.micromeso.2013.08.006.

[201] A. Lazaro, N. Vilanova, L.D. Barreto Torres, G. Resoort, I.K. Voets, H.J.H.H. Brouwers, L.D.B. Torres, G. Resoort, I.K. Voets, H.J.H.H. Brouwers, Synthesis, Polymerization, and Assembly of Nanosilica Particles below the Isoelectric Point, Langmuir. 33 (2017) 14618–14626. doi:10.1021/acs.langmuir.7b01498.

[202] F. Shi, L. Wang, J. Liu, Synthesis and characterization of silica aerogels by a novel fast ambient pressure drying process, Mater. Lett. 60 (2006) 3718–3722. doi:10.1016/j.matlet.2006.03.095.

[203] X. Wu, M. Fan, X. Shen, S. Cui, G. Tan, Silica aerogels formed from soluble silicates and methyl trimethoxysilane (MTMS) using CO_2 gas as a gelation agent, Ceram. Int. 44 (2018) 821–829. doi:10.1016/j.ceramint.2017.10.005.

[204] J.G. Mahy, C.A. Paez, J. Hollevoet, L. Courard, E. Boonen, S.D. Lambert, Durable photocatalytic thin coatings for road applications, Constr. Build. Mater. 215 (2019) 422–434.

[205] E. Boonen, A. Beeldens, I. Dirkx, V. Bams, Durability of Cementitious Photocatalytic Building Materials, Catal. Today. 287 (2017) 196–202. doi:https://doi.org/10.1016/j.cattod.2016.10.012.

[206] M. Gallus, V. Akylas, F. Barmpas, A. Beeldens, E. Boonen, A. Boréave, M. Cazaunau, H. Chen, V. Daële, J.F. Doussin, Y. Dupart, C. Gaimoz, C. George, B. Grosselin, H. Herrmann, S. Ifang, R. Kurtenbach, M. Maille, A. Mellouki, K. Miet, F. Mothes, N. Moussiopoulos, L. Poulain, R. Rabe, P. Zapf, J. Kleffmann, Photocatalytic de-pollution in the Leopold II tunnel in Brussels: NOx abatement results, Build. Environ. 84 (2015) 125–133. doi:https://doi.org/10.1016/j.buildenv.2014.10.032.

[207] E. Boonen, A. Beeldens, Recent Photocatalytic Applications for Air Purification in Belgium, Coatings . 4 (2014). doi:10.3390/coatings4030553.

[208] Y. Hendrix, A. Lazaro, Q.L. Yu, H.J.H. Brouwers, Influence of synthesis conditions on the properties of photocatalytic titania-silica composites, J. Photochem. Photobiol. A Chem. 371 (2019) 25–32. doi:10.1016/j.jphotochem.2018.10.040.

[209] Q.L. Yu, Y. Hendrix, S. Lorencik, H.J.H. Brouwers, Field study of NOx degradation by a mineral-based

air purifying paint, Build. Environ. 142 (2018) 70–82. doi:10.1016/j.buildenv.2018.06.014.

[210] S. Zhang, Z. Zhang, J. Pei, R. Li, J. Zhang, J. Cai, J. Cui, A novel TiO2-SiO2 aerogel nanocomposite absorbent: preparation, characterization and photocatalytic degradation effects on automobile exhaust, Mater. Res. Express. 5 (2018) 25036. doi:10.1088/2053-1591/aaaf10.

[211] H.-L. Wang, H.-P. Qi, X.-N. Wei, X.-Y. Liu, W.-F. Jiang, Photocatalytic activity of TiO_2 supported SiO_2-Al_2O_3 aerogels prepared from industrial fly ash, Chinese J. Catal. 37 (2016) 2025–2033. doi:https://doi.org/10.1016/S1872-2067(16)62546-9.

[212] J. Liu, X. Wang, F. Shi, L. Yu, S. Liu, S. Hu, D. Liu, Synthesis of mesoporous SiO_2 aerogel/W$xTiO_2$ nanocomposites with high adsorptivity and photocatalytic activity, Adv. Powder Technol. 27 (2016) 1781–1789. doi:https://doi.org/10.1016/j.apt.2016.06.009.

[213] G. Zu, J. Shen, W. Wang, L. Zou, Y. Lian, Z. Zhang, Silica–Titania Composite Aerogel Photocatalysts by Chemical Liquid Deposition of Titania onto Nanoporous Silica Scaffolds, ACS Appl. Mater. Interfaces. 7 (2015) 5400–5409. doi:10.1021/am5089132.

[214] S. Cheng, X. Liu, S. Yun, H. Luo, Y. Gao, SiO_2/TiO_2 composite aerogels: Preparation via ambient pressure drying and photocatalytic performance, Ceram. Int. 40 (2014) 13781–13786. doi:https://doi.org/10.1016/j.ceramint.2014.05.093.

[215] C.J. Brinker, G.W. Scherer, Sol-Gel Science: The Physics and Chemistry of Sol-Gel Processing, 2013. doi:10.1016/C2009-0-22386-5.

[216] M. Thommes, K. Kaneko, A. V. Neimark, J.P. Olivier, F. Rodriguez-Reinoso, J. Rouquerol, K.S.W. Sing, Physisorption of gases, with special reference to the evaluation of surface area and pore size distribution (IUPAC Technical Report), Pure Appl. Chem. 87 (2015) 1051–1069. doi:10.1515/pac-2014-1117.

[217] S. He, Y. Huang, G. Chen, M. Feng, H. Dai, B. Yuan, X. Chen, Effect of heat treatment on hydrophobic silica aerogel, J. Hazard. Mater. 362 (2019) 294–302. doi:https://doi.org/10.1016/j.jhazmat.2018.08.087.

[218] M. Gordienko, D. Belous, A. Tyrtyshnikov, I. Mitrofanov, N. Menshutina, E. Lebedev, Prediction of structure changes of organic-silica aerogels during pyrolysis, in: A. Espuña, M. Graells, L. Puigjaner (Eds.), Comput. Aided Chem. Eng., Elsevier, 2017: pp. 181–186. doi:https://doi.org/10.1016/B978-0-444-63965-3.50032-5.

[219] M. Dowson, M. Grogan, T. Birks, D. Harrison, S. Craig, Streamlined life cycle assessment of transparent silica aerogel made by supercritical drying, Appl. Energy. 97 (2012) 396–404. doi:10.1016/j.apenergy.2011.11.047.

[220] L.K. Turner, F.G. Collins, Carbon dioxide equivalent (CO_2-e) emissions: A comparison between geopolymer and OPC cement concrete, Constr. Build. Mater. 43 (2013) 125–130. doi:10.1016/j.conbuildmat.2013.01.023.

[221] Z. Yao, W. Li, Microstructure and thermal analysis of APS nano PYSZ coated aluminum alloy piston, J. Alloys Compd. 812 (2020). doi:10.1016/j.jallcom.2019.152162.

[222] A.C. Pierre, Chemistry of Aerogels and Their Applications, Chem. Rev. 102 (2002) 4243.

[223] N. Husing, U. Schubert, Aerogel Airy Materials: Chemistry, Structure, and Properties, Chem. Int. Ed. 37 (1998) 22–45.

[224] J. Fricke, Aerogels-Recent progress in production techniques and novel applications, J. Sol-Gel Sci. Technol. 13 (1998) 299.

[225] L.W. Hrubesh, Aerogel applications, J. Non. Cryst. Solids. 225 (1998) 335–342.

[226] C.E. Carraher, General Topics: silica aerogel-Properties and uses, Polym. News. 30 (2005) 386–388. doi:10.1080/00323910500402961.

[227] J.L. Gurav, I.-K. Jung, H.-H. Park, E.S. Kang, D.Y. Nadargi, Silica Aerogel: Synthesis and Applications, J. Nanomater. 2010 (2010) 1–11. doi:10.1155/2010/409310.

[228] S. Liu, T. Yu, N. Hu, R. Liu, X. Liu, High strength cellulose aerogels prepared by spatially confined synthesis of silica in bioscaffolds, Colloids Surfaces A Physicochem. Eng. Asp. 439 (2013) 159–166. doi:10.1016/j.colsurfa.2012.11.020.

[229] J.T. Korhonen, M. Kettunen, R.H. Ras, O. Ikkala, Hydrophobic nanocellulose aerogels as floating, sustainable, reusable, and recyclable oil absorbents, ACS Appl Mater Interfaces. 3 (2011) 1813–1816.

doi:10.1021/am200475b.

[230] M. Koebel, A. Rigacci, P. Achard, Aerogel-based thermal superinsulation: an overview, J. Sol-Gel Sci. Technol. 63 (2012) 315–339. doi:10.1007/s10971-012-2792-9.

[231] L.F. Su, L. Miao, S. Tanemura, G. Xu, Low-cost and fast synthesis of nanoporous silica cryogels for thermal insulation applications, Sci Technol Adv Mater. 13 (2012) 35003. doi:10.1088/1468-6996/13/3/035003.

[232] R. Ciriminna, A. Fidalgo, V. Pandarus, F. Beland, L.M. Ilharco, M. Pagliaro, The sol-gel route to advanced silica-based materials and recent applications, Chem. Rev. 113 (2013) 6592–6620. doi:10.1021/cr300399c.

[233] M.A. Aegerter, N. Leventis, M.M. Koebel, Aerogel handbooks, Springer, NewYork, 2011.

[234] Z. Tang, W. Li, V.W.Y. Tam, C. Xue, Advanced progress in recycling municipal and construction solid wastes for manufacturing sustainable construction materials, Resour. Conserv. Recycl. X. 6 (2020). doi:10.1016/j.rcrx.2020.100036.

[235] A. Lazaro, N. Vilanova, L.D.B. Torres, G. Resoort, I.K. Voets, H.J.H. Brouwers, Synthesis, polymerization, and assembly of nanosilica particles below the isoelectric point, Langmuir. 33 (2017) 14618–14626. doi:10.1021/acs.lagmuir.7b01498.

[236] X. Gao, Q.L. Yu, A. Lazaro, H.J.H. Brouwers, Investigation on a green olivine nano-silica source based activator in alkali activated slag-fly ash blends: Reaction kinetics, gel structure and carbon footprint, Cem. Concr. Res. 100 (2017) 129–139. doi:10.1016/j.cemconres.2017.06.007.

[237] Z. Luo, W. Li, Y. Gan, X. He, A. Castel, D. Sheng, Nanoindentation on micromechanical properties and microstructure of geopolymer with nano-SiO_2 and nano-TiO_2, Cem. Concr. Compos. 117 (2021). doi:10.1016/j.cemconcomp.2020.103883.

[238] A. Demilecamps, C. Beauger, C. Hildenbrand, A. Rigacci, T. Budtova, Cellulose-silica aerogels, Carbohydr Polym. 122 (2015) 293–300. doi:10.1016/j.carbpol.2015.01.022.

[239] S. Zhao, Z. Zhang, G. Sèbe, R. Wu, R. V Rivera Virtudazo, P. Tingaut, M.M. Koebel, Multiscale Assembly of Superinsulating Silica Aerogels Within Silylated Nanocellulosic Scaffolds: Improved Mechanical Properties Promoted by Nanoscale Chemical Compatibilization, Adv. Funct. Mater. 25 (2015) 2326–2334. doi:10.1002/adfm.201404368.

[240] A. Demilecamps, G. Reichenauer, A. Rigacci, T. Budtova, Cellulose–silica composite aerogels from "one-pot" synthesis, Cellulose. 21 (2014) 2625–2636. doi:10.1007/s10570-014-0314-3.

[241] H. Sai, L. Xing, J. Xiang, L. Cui, J. Jiao, C. Zhao, Z. Li, F. Li, T. Zhang, Flexible aerogels with interpenetrating network structure of bacterial cellulose-silica composite from sodium silicate precursor via freeze drying process, RSC Adv. 4 (2014) 30453–30461. doi:10.1039/c4ra02752c.

[242] A. Lazaro, Nano-silica production at low temperatures from the dissolution of olivine: Synthesis, tailoring and modeling, Eindhoven University of Technology, 2013.

[243] F. Rafieian, M. Hosseini, M. Jonoobi, Q. Yu, Development of hydrophobic nanocellulose-based aerogel via chemical vapor deposition for oil separation for water treatment, Cellulose. 25 (2018) 4695–4710. doi:10.1007/s10570-018-1867-3.

[244] S. Sepahvand, M. Jonoobi, A. Ashori, F. Gauvin, H.J.H. Brouwers, K. Oksman, Q. Yu, A promising process to modify cellulose nanofibers for carbon dioxide (CO_2) adsorption, Carbohydr. Polym. (2020). doi:10.1016/j.carbpol.2019.115571.

[245] A. Demilecamps, G. Reichenauer, A. Rigacci, T. Budtova, Cellulose-silica composite aerogels from "one-pot" synthesis, Cellulose. 21 (2014) 2625–2636. doi:10.1007/s10570-014-0314-3.

[246] J.C.H. Wong, H. Kaymak, S. Brunner, M.M. Koebel, Mechanical properties of monolithic silica aerogels made from polyethoxydisiloxanes, Microporous Mesoporous Mater. 183 (2014) 23–29. doi:10.1016/j.micromeso.2013.08.029.

[247] S. He, X. Chen, Flexible silica aerogel based on methyltrimethoxysilane with improved mechanical property, J. Non. Cryst. Solids. 463 (2017) 6–11. doi:10.1016/j.jnoncrysol.2017.02.014.

[248] S. Cui, Y. Liu, M. Fan, A.T. Cooper, B. Lin, X. Liu, G. Han, X. Shen, Temperature dependent microstructure of MTES modified hydrophobic silica aerogels, Mater. Lett. 65 (2011) 606–609. doi:10.1016/j.matlet.2010.11.026.

[249] G. Hayase, K. Kanamori, K. Kazuki, T. Hanada, Synthesis of New Flexible Aerogels from MTMS/DMDMS via Ambient Pressure Drying, IOP Conf. Ser. Mater. Sci. Eng. 18 (2011) 32013. doi:10.1088/1757-899x/18/3/032013.

[250] A. Venkateswara Rao, M.M. Kulkarni, D.P. Amalnerkar, T. Seth, Superhydrophobic silica aerogels based on methyltrimethoxysilane precursor, J. Non. Cryst. Solids. 330 (2003) 187–195. doi:https://doi.org/10.1016/j.jnoncrysol.2003.08.048.

[251] B. Xu, J.Y. Cai, Z. Xie, L. Wang, I. Burgar, N. Finn, Z. Cai, L. Wong, An improved method for preparing monolithic aerogels based on methyltrimethoxysilane at ambient pressure Part II: Microstructure and performance of the aerogels, Microporous Mesoporous Mater. 148 (2012) 152–158. doi:https://doi.org/10.1016/j.micromeso.2011.08.015.

[252] B. Xu, J.Y. Cai, N. Finn, Z. Cai, An improved method for preparing monolithic aerogels based on methyltrimethoxysilane at ambient pressure Part I: Process development and macrostructures of the aerogels, Microporous Mesoporous Mater. 148 (2012) 145–151. doi:https://doi.org/10.1016/j.micromeso.2011.08.012.

[253] A. Örn, Degradation studies on polydimethylsiloxane, Åbo Akademi University, Finland (2019).

[254] L. Zhou, H. He, M. Li, S. Huang, C. Mei, Q. Wu, Enhancing mechanical properties of poly (lactic acid) through its in-situ crosslinking with maleic anhydride-modified cellulose nanocrystals from cottonseed hulls, Ind. Crops Prod. 112 (2018) 449–459.

[255] J.C.H. Wong, H. Kaymak, P. Tingaut, S. Brunner, M.M. Koebel, Mechanical and thermal properties of nanofibrillated cellulose reinforced silica aerogel composites, Microporous Mesoporous Mater. 217 (2015) 150–158.

[256] Y. Luo, Z. Li, W. Zhang, H. Yan, Y. Wang, M. Li, Q. Liu, Rapid synthesis and characterization of ambient pressure dried monolithic silica aerogels in ethanol/water co-solvent system, J. Non. Cryst. Solids. 503 (2019) 214–223.

[257] B.P. Jelle, Traditional, state-of-the-art and future thermal building insulation materials and solutions – Properties, requirements and possibilities, Energy Build. 43 (2011) 2549–2563. doi:10.1016/j.enbuild.2011.05.015.

[258] P. Nejat, F. Jomehzadeh, M.M. Taheri, M. Gohari, M.Z. Muhd, A global review of energy consumption, CO_2 emissions and policy in the residential sector (with an overview of the top ten CO_2 emitting countries), Renew. Sustain. Energy Rev. 43 (2015) 843–862. doi:10.1016/J.RSER.2014.11.066.

[259] C.A. Ikutegbe, M.M. Farid, Application of phase change material foam composites in the built environment: A critical review, Renew. Sustain. Energy Rev. 131 (2020) 110008. doi:10.1016/J.RSER.2020.110008.

[260] G. Wei, Y. Liu, X. Zhang, F. Yu, X. Du, Thermal conductivities study on silica aerogel and its composite insulation materials, Int. J. Heat Mass Transf. 54 (2011) 2355–2366. doi:10.1016/j.ijheatmasstransfer.2011.02.026.

[261] A. Lamy-Mendes, A.D.R. Pontinha, P. Alves, P. Santos, L. Durães, Progress in silica aerogel-containing materials for buildings' thermal insulation, Constr. Build. Mater. 286 (2021) 122815. doi:10.1016/j.conbuildmat.2021.122815.

[262] S. Ng, B.P. Jelle, L.I.C. Sandberg, T. Gao, Ó.H. Wallevik, Experimental investigations of aerogel-incorporated ultra-high performance concrete, Constr. Build. Mater. 77 (2015) 307–316. doi:10.1016/j.conbuildmat.2014.12.064.

[263] T. Gao, B.P. Jelle, A. Gustavsen, S. Jacobsen, Aerogel-incorporated concrete: An experimental study, Constr. Build. Mater. 52 (2014) 130–136. doi:10.1016/j.conbuildmat.2013.10.100.

[264] M. de Fátima Júlio, L.M. Ilharco, A. Soares, I. Flores-Colen, J. de Brito, Silica-based aerogels as aggregates for cement-based thermal renders, Cem. Concr. Compos. 72 (2016) 309–318. doi:10.1016/j.cemconcomp.2016.06.013.

[265] P. Zhu, X. Xu, H. Liu, S. Liu, C. Chen, Z. Jia, Tunnel fire resistance of self-compacting concrete coated with SiO2 aerogel cement paste under 2.5 h HC fire loading, Constr. Build. Mater. 239 (2020) 117857. doi:10.1016/j.conbuildmat.2019.117857.

[266] S. Ng, B.P. Jelle, Y. Zhen, Ó.H. Wallevik, Effect of storage and curing conditions at elevated temperatures on aerogel-incorporated mortar samples based on UHPC recipe, Constr. Build. Mater. 106 (2016) 640–

649. doi:10.1016/j.conbuildmat.2015.12.162.

[267] M. Pedroso, I. Flores-Colen, J.D. Silvestre, M.G. Gomes, L. Silva, L. Ilharco, Physical, mechanical, and microstructural characterisation of an innovative thermal insulating render incorporating silica aerogel, Energy Build. 211 (2020) 109793. doi:10.1016/j.enbuild.2020.109793.

[268] C.Y. Zhang, R. Han, B. Yu, Y.M. Wei, Accounting process-related CO_2 emissions from global cement production under Shared Socioeconomic Pathways, J. Clean. Prod. 184 (2018) 451–465. doi:10.1016/j.jclepro.2018.02.284.

[269] M. Lahoti, S.F. Wijaya, K.H. Tan, E.H. Yang, Tailoring sodium-based fly ash geopolymers with variegated thermal performance, Cem. Concr. Compos. (2020). doi:10.1016/j.cemconcomp.2019.103507.

[270] P. Duxson, J.L. Provis, G.C. Lukey, J.S.J. Van Deventer, The role of inorganic polymer technology in the development of 'green concrete,' Cem. Concr. Res. 37 (2007) 1590–1597.

[271] M.T. Marvila, A.R.G. Azevedo, G.C.G. Delaqua, B.C. Mendes, L.G. Pedroti, C.M.F. Vieira, Performance of geopolymer tiles in high temperature and saturation conditions, Constr. Build. Mater. 286 (2021) 122994. doi:10.1016/j.conbuildmat.2021.122994.

[272] T. Bakharev, Thermal behaviour of geopolymers prepared using class F fly ash and elevated temperature curing, Cem. Concr. Res. 36 (2006) 1134–1147. doi:10.1016/j.cemconres.2006.03.022.

[273] J. Zhao, L. Tong, B. Li, T. Chen, C. Wang, G. Yang, Y. Zheng, Eco-friendly geopolymer materials: A review of performance improvement, potential application and sustainability assessment, J. Clean. Prod. 307 (2021) 127085. doi:10.1016/j.jclepro.2021.127085.

[274] C. Liu, J. Luo, Q. Li, S. Gao, D. Su, J. Zhang, S. Chen, Calcination of green high-belite sulphoaluminate cement (GHSC) and performance optimizations of GHSC-based foamed concrete, Mater. Des. 182 (2019) 107986. doi:10.1016/j.matdes.2019.107986.

[275] X. Wang, L. Liu, H. Zhou, T. Song, Q. Qiao, H. Zhang, Improving the compressive performance of foam concrete with ceramsite: Experimental and meso-scale numerical investigation, Mater. Des. 208 (2021) 109938. doi:10.1016/j.matdes.2021.109938.

[276] G. Samson, M. Cyr, X.X. Gao, Thermomechanical performance of blended metakaolin-GGBS alkali-activated foam concrete, Constr. Build. Mater. 157 (2017) 982–993. doi:10.1016/j.conbuildmat.2017.09.146.

[277] P. Hlaváček, V. Šmilauer, F. Škvára, L. Kopecký, R. Šulc, Inorganic foams made from alkali-activated fly ash: Mechanical, chemical and physical properties, J. Eur. Ceram. Soc. 35 (2015) 703–709. doi:10.1016/j.jeurceramsoc.2014.08.024.

[278] G. Masi, W.D.A. Rickard, L. Vickers, M.C. Bignozzi, A. Van Riessen, A comparison between different foaming methods for the synthesis of light weight geopolymers, Ceram. Int. 40 (2014) 13891–13902. doi:10.1016/j.ceramint.2014.05.108.

[279] J.G. Sanjayan, A. Nazari, L. Chen, G.H. Nguyen, Physical and mechanical properties of lightweight aerated geopolymer, Constr. Build. Mater. 79 (2015) 236–244. doi:10.1016/j.conbuildmat.2015.01.043.

[280] J. Maia, M. Pedroso, N.M.M. Ramos, P.F. Pereira, I. Flores-Colen, M.G. Gomes, L. Silva, Hygrothermal performance of a new thermal aerogel-based render under distinct climatic conditions, Energy Build. 243 (2021) 111001. doi:10.1016/j.enbuild.2021.111001.

[281] T. Alioua, B. Agoudjil, A. Boudenne, K. Benzarti, Sensitivity analysis of transient heat and moisture transfer in a bio-based date palm concrete wall, Build. Environ. 202 (2021) 108019. doi:10.1016/j.buildenv.2021.108019.

[282] C. Zhao, Y. Li, W. Ye, X. Shen, X. Yuan, C. Ma, Y. Cao, Performance regulation of silica aerogel powder synthesized by a two-step Sol-gel process with a fast ambient pressure drying route, J. Non. Cryst. Solids. 567 (2021) 120923. doi:10.1016/j.jnoncrysol.2021.120923.

[283] W.D.A. Rickard, R. Williams, J. Temuujin, A. van Riessen, Assessing the suitability of three Australian fly ashes as an aluminosilicate source for geopolymers in high temperature applications, Mater. Sci. Eng. A. 528 (2011) 3390–3397. doi:10.1016/J.MSEA.2011.01.005.

[284] BS EN 12350-1:2009, Testing fresh concrete Part6: density, Eur. Norms. (2009) 5–8. https://www.en-standard.eu/din-en-12350-2-testing-fresh-concrete-part-2-slump-test/%0Ahttps://bsol.bsigroup.com/Home.

[285] BS EN 12390-7, Testing hardened concrete Part 7: Density of hardened concrete, J. Chem. Inf. Model. 53 (2009) 1689–1699.

[286] EN1097-7, Test for mechanical and physical properties of aggregates-Part 7: Determination of the particle density of filler-phcnometer method, (1999).

[287] BS EN 196-1, Methods of testing cement, Part 1 Determ. Strength. (2005).

[288] BS EN 12390-3, Testing hardened concrete Part 3: Compressive strength of test specimens, Aberdeen's Concr. Constr. (2009).

[289] ASTM C 597-02, Pulse Velocity Through Concrete, United States Am. Soc. Test. Mater. 04 (2003) 3–6.

[290] Y.X. Chen, S. Sepahvand, F. Gauvin, K. Schollbach, H.J.H. Brouwers, Q. Yu, One-pot synthesis of monolithic silica-cellulose aerogel applying a sustainable sodium silicate precursor, Constr. Build. Mater. 293 (2021) 123289. doi:10.1016/ j.conbuildmat.2021.123289.

[291] Z. Zhang, J.L. Provis, A. Reid, H. Wang, Mechanical, thermal insulation, thermal resistance and acoustic absorption properties of geopolymer foam concrete, Cem. Concr. Compos. 62 (2015) 97–105. doi:10.1016/j.cemconcomp.2015.03.013.

[292] J.W. N. Neithalath and J. Olek, Acoustically Efficient Concretes Through Engineered Pore Structure, ACI Symp. Publ. 226 (n.d.). doi:10.14359/14395.

[293] E.N. Landis, D.J. Corr, Three dimensional analysis of air void systems in concrete, in: Meas. Monit. Model. Concr. Prop., Springer, 2006: pp. 517–524.

[294] L. Korat, V. Ducman, A. Legat, B. Mirtič, Characterisation of the pore-forming process in lightweight aggregate based on silica sludge by means of X-ray micro-tomography (micro-CT) and mercury intrusion porosimetry (MIP), Ceram. Int. 39 (2013) 6997–7005.

[295] R. Sharma, D. Varade, P. Bahadur, Mixed Micelles of Triton X-100 and Sodium Dodecyl Sulfate and Their Interaction with Polymers, J. Dispers. Sci. Technol. 24 (2003) 53–61. doi:10.1081/DIS-120017943.

[296] H.J.Y. El-Aila, Interaction of nonionic surfactant Triton-X-100 with ionic surfactants, J. Dispers. Sci. Technol. 30 (2009) 1277–1280.

[297] F. Attar, Hamed, M. Zoveidavianpoor, The Foaming Behavior and Synergistic Effect in Aqueous CO_2 Foam by In Situ Physisorption of Alpha Olefin Sulfonate and Triton X-100 Surfactants and Their Mixture, Pet. Sci. Technol. 32 (2014) 2376–2386. doi:10.1080/10916466.2013.831874.

[298] K. Thakkar, B. Bharatiya, D. Ray, V.K. Aswal, P. Bahadur, Molecular interactions involving aqueous Triton X-100 micelles and anionic surfactants: Investigations on surface activity and morphological transitions, J. Mol. Liq. 223 (2016) 611–620. doi:https://doi.org/10.1016/j.molliq.2016.08.086.

[299] Q. Huo, D.I. Margolese, U. Ciesla, P. Feng, T.E. Gier, P. Sieger, R. Leon, P.M. Petroff, Generalized synthesis of periodic surfactant/inorganic composite materials, Nature. 368 (1994) 317.

[300] C.T. Kresge, M.E. Leonowicz, W.J. Roth, J.C. Vartuli, J.S. Beck, Ordered mesoporous molecular sieves synthesized by a liquid-crystal template mechanism, Nature. (1992). doi:10.1038/359710a0.

[301] M. Vallet-Regí, F. Balas, D. Arcos, Mesoporous materials for drug delivery, Angew. Chemie Int. Ed. 46 (2007) 7548–7558.

[302] F. Liu, K. Huang, S. Ding, S. Dai, One-step synthesis of nitrogen-doped graphene-like meso-macroporous carbons as highly efficient and selective adsorbents for CO_2 capture, J. Mater. Chem. A. 4 (2016) 14567–14571. doi:10.1039/c6ta06583j.

[303] F. Liu, S. Zuo, X. Xia, J. Sun, Y. Zou, L. Wang, C. Li, C. Qi, Generalized and high temperature synthesis of a series of crystalline mesoporous metal oxides based nanocomposites with enhanced catalytic activities for benzene combustion, J. Mater. Chem. A. (2013). doi:10.1039/c3ta01505j.

[304] Y. Wan, D. Zhao, On the controllable soft-templating approach to mesoporous silicates, Chem. Rev. 107 (2007) 2821–2860. doi:10.1021/cr068020s.

[305] Y. Liu, Y. Guo, Y. Zhu, D. An, W. Gao, Z. Wang, Y. Ma, Z. Wang, A sustainable route for the preparation of activated carbon and silica from rice husk ash, J. Hazard. Mater. (2011). doi:10.1016/j.jhazmat.2010.12.007.

[306] F. Liu, K. Huang, Q. Wu, S. Dai, Solvent-Free Self-Assembly to the Synthesis of Nitrogen-Doped Ordered

Mesoporous Polymers for Highly Selective Capture and Conversion of CO_2, Adv. Mater. 29 (2017) 1–8. doi:10.1002/adma.201700445.

[307] K.S. Hui, C.Y.H. Chao, Synthesis of MCM-41 from coal fly ash by a green approach: Influence of synthesis pH, J. Hazard. Mater. 137 (2006) 1135–1148. doi:10.1016/j.jhazmat.2006.03.050.

[308] M. Bhagiyalakshmi, L.J. Yun, R. Anuradha, H.T. Jang, Utilization of rice husk ash as silica source for the synthesis of mesoporous silicas and their application to CO_2 adsorption through TREN/TEPA grafting, J. Hazard. Mater. 175 (2010) 928–938. doi:10.1016/j.jhazmat.2009.10.097.

[309] Z.S. Liu, W.K. Li, C.Y. Huang, Synthesis of mesoporous silica materials from municipal solid waste incinerator bottom ash, Waste Manag. 34 (2014) 893–900. doi:10.1016/j.wasman.2014.02.016.

[310] J.L. Blin, C. Otjacques, G. Herrier, B.-L. Su, Pore Size Engineering of Mesoporous Silicas Using Decane as Expander, Langmuir. 16 (2000) 4229–4236. doi:10.1021/la9914615.

[311] M. Kruk, M. Jaroniec, Y. Sakamoto, O. Terasaki, R. Ryoo, C.H. Ko, Determination of Pore Size and Pore Wall Structure of MCM-41 by Using Nitrogen Adsorption, Transmission Electron Microscopy, and X-ray Diffraction, J. Phys. Chem. B. 104 (2000) 292–301. doi:10.1021/jp992718a.

[312] K. Cassiers, T. Linssen, M. Mathieu, M. Benjelloun, K. Schrijnemakers, P. Van Der Voort, P. Cool, E.F. Vansant, A detailed study of thermal, hydrothermal, and mechanical stabilities of a wide range of surfactant assembled mesoporous silicas, Chem. Mater. 14 (2002) 2317–2324. doi:10.1021/cm0112892.

[313] Q. Huo, D.I. Margolese, G.D. Stucky, Surfactant Control of Phases in the Synthesis of Mesoporous Silica-Based Materials, Chem. Mater. 8 (1996) 1147–1160. doi:10.1021/cm960137h.

[314] H.T. Jang, Y.K. Park, Y.S. Ko, J.Y. Lee, B. Margandan, Highly siliceous MCM-48 from rice husk ash for CO_2 adsorption, Int. J. Greenh. Gas Control. 3 (2009) 545–549. doi:10.1016/j.ijggc.2009.02.008.

[315] L. Chen, T. Horiuchi, T. Mori, K. Maeda, Postsynthesis Hydrothermal Restructuring of M41S Mesoporous Molecular Sieves in Water, J. Phys. Chem. B. 103 (1999) 1216–1222. doi:10.1021/jp983100o.

[316] M. Anpo, H. Yamashita, K. Ikeue, Y. Fujii, S.G. Zhang, Y. Ichihashi, D.R. Park, Y. Suzuki, K. Koyano, T. Tatsumi, Photocatalytic reduction of CO_2 with H_2O on Ti-MCM-41 and Ti-MCM-48 mesoporous zeolite catalysts, Catal. Today. 44 (1998) 327–332. doi:10.1016/S0920-5861(98)00206-5.

[317] M.S. Morey, S. O'Brien, S. Schwarz, G.D. Stucky, Hydrothermal and postsynthesis surface modification of cubic, MCM-48, and ultralarge pore SBA-15 mesoporous silica with titanium, Chem. Mater. 12 (2000) 898–911. doi:10.1021/cm9901663.

[318] H. Van Damme, Concrete material science : Past , present , and future innovations, Cem. Concr. Res. 112 (2018) 5–24. doi:10.1016/j.cemconres.2018.05.002.

[319] E. Fehling, M. Schmidt, J. Walraven, T. Leutbecher, S. Fröhlich, Ultra-High Performance Concrete UHPC: Fundamentals, Design, Examples, 2015. doi:10.1002/9783433604076.

[320] R. Jing, Y. Liu, P. Yan, Uncovering the effect of fly ash cenospheres on the macroscopic properties and microstructure of ultra high-performance concrete (UHPC), Constr. Build. Mater. 286 (2021) 122977. doi:10.1016/j.conbuildmat.2021.122977.

[321] Z. Mo, R. Wang, X. Gao, Hydration and mechanical properties of UHPC matrix containing limestone and different levels of metakaolin, Constr. Build. Mater. 256 (2020) 119454. doi:10.1016/j.conbuildmat.2020.119454.

[322] Ç. Yalçınkaya, O. Çopuroğlu, Hydration heat, strength and microstructure characteristics of UHPC containing blast furnace slag, J. Build. Eng. 34 (2021). doi:10.1016/j.jobe.2020.101915.

[323] Y. Ma, J. Bai, C. Shi, S. Sha, B. Zhou, Effect of PCEs with different structures on hydration and properties of cementitious materials with low water-to-binder ratio, Cem. Concr. Res. 142 (2021) 106343. doi:10.1016/j.cemconres.2020.106343.

[324] L. Wang, N. Ur Rehman, I. Curosu, Z. Zhu, M.A.B. Beigh, M. Liebscher, L. Chen, D.C.W. Tsang, S. Hempel, V. Mechtcherine, On the use of limestone calcined clay cement (LC3) in high-strength strain-hardening cement-based composites (HS-SHCC), Cem. Concr. Res. 144 (2021) 106421. doi:10.1016/j.cemconres.2021.106421.

[325] M. Aly, M.S.J. Hashmi, A.G. Olabi, M. Messeiry, E.F. Abadir, A.I. Hussain, Effect of colloidal nano-silica on the mechanical and physical behaviour of waste-glass cement mortar, Mater. Des. 33 (2012) 127–

135. doi:10.1016/j.matdes.2011.07.008.

[326] B. Bose, C.R. Davis, K.A. Erk, Microstructural Refinement of Cement Paste Internally Cured by Polyacrylamide Composite Hydrogel Particles Containing Silica Fume and Nanosilica, Cem. Concr. Res. 143 (2021).

[327] N.K. Lee, K.T. Koh, M.O. Kim, G.S. Ryu, Uncovering the role of micro silica in hydration of ultra-high performance concrete (UHPC), Cem. Concr. Res. 104 (2018) 68–79. doi:10.1016/j.cemconres.2017.11.002.

[328] Z. Wu, K.H. Khayat, C. Shi, Effect of nano-SiO_2 particles and curing time on development of fiber-matrix bond properties and microstructure of ultra-high strength concrete, Cem. Concr. Res. 95 (2017) 247–256. doi:https://doi.org/10.1016/j.cemconres.2017.02.031.

[329] N.M. Azmee, N. Shafiq, Ultra-high performance concrete: From fundamental to applications, Case Stud. Constr. Mater. 9 (2018). doi:10.1016/j.cscm.2018.e00197.

[330] Y. Sargam, K. Wang, A. Tsyrenova, S. Jiang, F. Liu, Effects of anionic and nonionic surfactants on the dispersion and stability of nanoSiO_2 in aqueous and cement pore solutions, Cem. Concr. Res. v1 (2020) 106417. doi:10.1016/j.cemconres.2021.106417.

[331] A. Vandenberg, H. Bessaies-Bey, K. Wille, N. Roussel, Influence of mixing on the generation of nanoparticles in cement systems, Cem. Concr. Res. 143 (2021) 106379. doi:10.1016/j.cemconres.2021.106379.

[332] N. Ye, J. Zheng, X. Ye, J. Xue, D. Han, H. Xu, Z. Wang, L. Zhang, Performance enhancement of rubber composites using VOC-Free interfacial silica coupling agent, Compos. Part B Eng. 202 (2020) 108301. doi:10.1016/j.compositesb.2020.108301.

[333] X. Wu, J. Zheng, B. Han, L. Zhang, J. Lu, X. Ye, Designing novel epoxy-terminated polybutadiene to construct chemical interface between nanosilica and rubbers with green nature, Compos. Part B Eng. 178 (2019) 107451. doi:10.1016/j.compositesb.2019.107451.

[334] K. Kolman, O. Nechyporchuk, M. Persson, K. Holmberg, R. Bordes, Combined Nanocellulose/Nanosilica Approach for Multiscale Consolidation of Painting Canvases, ACS Appl. Nano Mater. 1 (2018) 2036–2040. doi:10.1021/acsanm.8b00262.

[335] S. Kongparakul, S. Kornprasert, P. Suriya, D. Le, C. Samart, N. Chantarasiri, P. Prasassarakich, G. Guan, Self-healing hybrid nanocomposite anticorrosive coating from epoxy/modified nanosilica/perfluorooctyl triethoxysilane, Prog. Org. Coatings. 104 (2017) 173–179. doi:10.1016/j.porgcoat.2016.12.020.

[336] Z. Asadi, R. Norouzbeigi, Synthesis of colloidal nanosilica from waste glass powder as a low cost precursor, Ceram. Int. 44 (2018) 22692–22697. doi:10.1016/j.ceramint.2018.09.050.

[337] E.D.E.R. Hyde, A. Seyfaee, F. Neville, R. Moreno-Atanasio, Colloidal Silica Particle Synthesis and Future Industrial Manufacturing Pathways: A Review, Ind. Eng. Chem. Res. 55 (2016) 8891–8913. doi:10.1021/acs.iecr.6b01839.

[338] K. Tadanaga, K. Morita, K. Mori, M. Tatsumisago, Synthesis of monodispersed silica nanoparticles with high concentration by the Stöber process, J. Sol-Gel Sci. Technol. 68 (2013) 341–345. doi:10.1007/s10971-013-3175-6.

[339] D. Schuiling, A method for neutralizing waste sulfuric acid by adding a silicate, WO/1986/000288, 1986.

[340] A. Lazaro, K. Sato, H.J.H. Brouwers, J.W. Geus, Pore structure development of silica particles below the isoelectric point, Microporous Mesoporous Mater. 267 (2018) 257–264. doi:10.1016/j.micromeso.2018.03.031.

[341] H. Van Damme, Concrete material science: Past, present, and future innovations, Cem. Concr. Res. 112 (2018) 5–24. doi:https://doi.org/10.1016/j.cemconres.2018.05.002.

[342] A. Lázaro García, Nano-silica production at low temperatures from the dissolution of olivine, PhD Thesis, Eindhoven University of Technology, Eindhoven, 2014.

[343] R. Yang, R. Yu, Z. Shui, C. Guo, S. Wu, X. Gao, S. Peng, The physical and chemical impact of manufactured sand as a partial replacement material in Ultra-High Performance Concrete (UHPC), Cem. Concr. Compos. 99 (2019) 203–213. doi:10.1016/j.cemconcomp.2019.03.020.

[344] X. Wang, R. Yu, Z. Shui, Q. Song, Z. Liu, M. Bao, Z. Liu, S. Wu, Optimized treatment of recycled

construction and demolition waste in developing sustainable ultra-high performance concrete, J. Clean. Prod. 221 (2019) 805–816. doi:10.1016/j.jclepro.2019.02.201.

[345] A.H.M. Andreasen and J. Andersen, Über die Beziehung zwischen Kornabstufung und Zwischenraum in Produkten aus losen Körnern (mit einigen Experimenten), Kolloid-Zeitschrift. 50 (1930) 217–228.

[346] R. Yu, P. Spiesz, H.J.H. Brouwers, Mix design and properties assessment of ultra-high performance fibre reinforced concrete (UHPFRC), Cem. Concr. Res. 56 (2014) 29–39.

[347] G. Hüsken, A multifunctional design approach for sustainable concrete: with application to concrete mass products, PhD thesis, Einhoven Univeristy of Technology, Eindhoven, (2010).

[348] R. Yu, P. Spiesz, H.J.H. Brouwers, Development of Ultra-High Performance Fibre Reinforced Concrete (UHPFRC): Towards an efficient utilization of binders and fibres, Constr. Build. Mater. 79 (2015) 273–282.

[349] X. Wang, R. Yu, Q. Song, Z. Shui, Z. Liu, S. Wu, D. Hou, Optimized design of ultra-high performance concrete (UHPC) with a high wet packing density, Cem. Concr. Res. 126 (2019) 105921. doi:10.1016/j.cemconres.2019.105921.

[350] A. Mendes, W.P. Gates, J.G. Sanjayan, F. Collins, NMR, XRD, IR and synchrotron NEXAFS spectroscopic studies of OPC and OPC/slag cement paste hydrates, Mater. Struct. Constr. 44 (2011) 1773–1791. doi:10.1617/s11527-011-9737-6.

[351] B. Walkley, J.L. Provis, Solid-state nuclear magnetic resonance spectroscopy of cements, Mater. Today Adv. 1 (2019) 100007. doi:10.1016/j.mtadv.2019.100007.

[352] K. Johansson, C. Larsson, O.N. Antzutkin, W. Forsling, H.R. Kota, V. Ronin, Kinetics of the hydration reactions in the cement paste with mechanochemically modified cement29Si magic-angle-spinning NMR study, Cem. Concr. Res. 29 (1999) 1575–1581. doi:10.1016/S0008-8846(99)00135-0.

[353] L.T. Zhuravlev, V. V. Potapov, Density of silanol groups on the surface of silica precipitated from a hydrothermal solution, Russ. J. Phys. Chem. A. 80 (2006) 1119–1128. doi:10.1134/S0036024406070211.

[354] M.D. Andersen, H.J. Jakobsen, J. Skibsted, Characterization of white Portland cement hydration and the C-S-H structure in the presence of sodium aluminate by ^{27}Al and ^{29}Si MAS NMR spectroscopy, Cem. Concr. Res. 34 (2004) 857–868. doi:10.1016/j.cemconres.2003.10.009.

[355] A.S. Brykov, A.S. Vasil'Ev, M. V. Mokeev, Hydration of Portland cement in the presence of high activity aluminum hydroxides, Russ. J. Appl. Chem. 85 (2012) 1793–1799. doi:10.1134/S1070427212120014.

[356] M.R. Jones, D.E. Macphee, J.A. Chudek, G. Hunter, R. Lannegrand, R. Talero, S.N. Scrimgeour, Studies using ^{27}Al MAS NMR of AFm and AFt phases and the formation of Friedel's salt, Cem. Concr. Res. 33 (2003) 177–182. doi:10.1016/S0008-8846(02)00901-8.

[357] T. Isobe, T. Watanabe, J.B. D'Espinose De La Caillerie, A.P. Legrand, D. Massiot, Solid-state 1H and ^{27}Al NMR studies of amorphous aluminum hydroxides, J. Colloid Interface Sci. 261 (2003) 320–324. doi:10.1016/S0021-9797(03)00144-9.

[358] ASTMC 1856, Standard Practice for Fabricating and Testing Specimens of Ultra-High Performance Concrete, 2017.

[359] A. Spyrogianni, I.K. Herrmann, K. Keevend, S.E. Pratsinis, K. Wegner, The silanol content and in vitro cytolytic activity of flame-made silica, J. Colloid Interface Sci. 507 (2017) 95–106. doi:10.1016/j.jcis.2017.07.096.

[360] Q. Alam, Valorization of municipal solid waste incineration bottom ash: chemical nature, leachability and treatments of hazardous elements, PhD thesis, Eindhoven university of technology, Eindhoven, 2019.

List of notations

Abbreviations

A&A	Andreasen and Andersen model
AE	Air entraining agent
AG	Aerogel
APD	Ambient pressure drying
BCBLWAs	Bio-based cold-bonded lightweight aggregates
BD	Bulk density
BET	Brunauer-Emmett-Teller
BJH	Barrett-Joyner-Halenda
C_2S	Dicalcium silicate
C_3A	Tricalcium aluminate
C_3S	Tricalcium silicate
C_4AF	Calcium aluminoferrite
CEM	Cement
CH	Calcium hydroxide
CSH	Calcium silicate hydrate
CSS	Converter steel slag
DTG	Differential thermogravimetry
DSC	Differential scanning calorimetry
EWG	Expanded waste glass
FA	Fly ash
FTIR	Fourier transform infrared
GFAR	Geopolymer foam aerogel render
GGBS	Ground Granulated Blast Furnace Slag
GM	Grinding media
HPLC	High performance liquid chromatography
ITR	Interfacial thermal resistance
ITZ	Interfacial transition zone
LCA	Life cycle assessment
LECA	Lightweight expanded clay aggregate
LLS	Laser light scattering
LOI	Loss of ignition
LP	Limestone powder
LWC	Lightweight concrete
MA	Maleic anhydrite
MF	Miscanthus fiber
MIP	Mercury intrusion porosimetry
MLC	Miscanthus lightweight concrete
MP	Miscanthus powder
MTMS	Methyltrimethoxysilane
NCA	Nanocellulose aerogel

NFC	Nano-fibrillated cellulose
NIM	Nano insulation materials
NMR	Nuclear magnetic resonance
NO_x	Nitrogen oxides
NO	Nitric oxide
NO_2	Nitrogen dioxide
NRC	Noise reduction coefficient
OMS	Olivine mesoporous silica
OnS	Olivine nano-silica
OPC	Ordinary Portland cement
OSA	Olivine silica aerogel
PCO	Photocatalytic oxidation
PDMS	Polydimethylsiloxane
PEG-PPG-PEG	Poly(propylene glycol)-poly(ethylene glycol)-poly(propylene glycol)
PSD	Particle size distribution
PoSD	Pore size distribution
SAA	Sound absorption average
SCA	Silica-cellulose aerogel
SCD	Supercritical drying
SCMs	Supplementary cementitious materials
SDS	Sodium dodecyl sulfate
SEM	Scanning electron microscopy
SF	Silica fume
SP	Superplasticizer
SS	Steel slag
SSA	Specific surface area
TC	Thermal conductivity
TEM	Transmission electron microscopy
TGA	Thermal gravimetry analysis
TMCS	Trimethylsilyl chloride
TP	Titanium isopropoxide
TS	Titanium-silica catalyst
μCT	Micro computed tomography
UHPC	Ultrahigh performance concrete
ULMC	Ultralightweight miscanthus concrete
UPV	Ultrasonic pulse velocity
UV	Ultraviolet
W	Water
WCA	Water contact angle
WG	Water glass
WU	Water uptake
XRD	X-ray powder diffraction
XRF	X-ray fluorescence

Nomenclature		SI unit
a_0	Constant parameters in Eq. 3.3	W/m·K
A	Contact area for crushing resistance	m^2
b_0	Constant parameters in Eq. 3.3	m^3/kg
C	Crushing resistance	Pa
C_1	Parameter in Chapter 7 Eq. 7-38	N/m
D_{max}	Maximum particle size	m
D_{min}	Minimum particle size	m
F	Compression force	N
L	Force generated by the load cell	N
L	Crystal size in Chapter 5	nm
m_s	Mass of saturated sample in dry condition	g
m_d	Mass of oven dry sample	g
m_w	Mass of water saturated sample	g
h	Height of the individual aggregate	m
R	Ideal gas constant	-
r	Radius of curvature	m
s_0	Solubility of a flat surface of the solid phase	g/L
s	Solubility of silica	g/L
S	Strain of aerogel	%
v_0	Volume fraction of phase 0	%
v_1	Volume fraction of phase 1	%
v_2	Volume fraction of phase 2	%

Greek letters		SI unit
α	Crushing strength of each artificial pellets tested	Pa
α^*	Fracture stress of silica-cellulose aerogel	Pa
α	Thermal diffusivity of in Chapter 8	mm^2/s
β	Width of a peak at half the maximum intensity in radians	-
γ	Solid-liquid interfacial tension	N
E	Young's modulus	Pa
Φ_{inter}	Inter-particle porosity	%
Φ_{intra}	Intra-particle porosity	%
φ_w	Water permeable porosity	%
θ	corresponding peak angle	^{o}
K	Effective thermal conductivity	W/m·K
K	Particle shape factor	-
k_0	Thermal conductivity of cement matrix	W/m·K
k_1	Thermal conductivity of EWG	W/m·K
k_2	Thermal conductivity of MF	W/m·K
λ	Thermal conductivity	W/m·K
λ_s	Solid thermal conductivity	W/m·K
λ_g	Gaseous thermal conductivity	W/m·K
λ_r	Radiative thermal conductivity	W/m·K
λ	Wavelength of the used X-ray	Å
ρ	Density	g/cm^3
ρ_b	Bulk density	g/cm^3
ρ_p	Particle density	g/cm^3

List of publications

Peer-reviewed journal papers

[1] **Y.X. Chen**, Q.L. Yu, H.J.H. Brouwers, Acoustic performance and microstructural analysis of bio-based lightweight concrete containing miscanthus, Construction and Building Materials 157 (2017) 839-851.

[2] **Y.X. Chen**, F. Wu, Q.L. Yu, H.J.H. Brouwers, Bio-based ultra-lightweight concrete applying miscanthus fibers: Acoustic absorption and thermal insulation, Cement and Concrete Composites 114 (2020) 103829.

[3] **Y.X. Chen,** G. Liu, K. Schollbach, H.J.H. Brouwers, Development of cement-free bio-based cold-bonded lightweight aggregates (BCBLWAs) using steel slag and miscanthus powder via CO_2 curing, Journal of Cleaner Production 322 (2021) 129105.

[4] **Y.X. Chen**, Y. Hendrix, K. Schollbach, H.J.H. Brouwers, A silica aerogel synthesized from olivine and its application as a photocatalytic support, Construction and Building Materials 248 (2020) 118709.

[5] **Y.X. Chen,** S. Sepahvand, F. Gauvin, K. Schollbach, H.J.H. Brouwers, Q.L. Yu, One-pot synthesis of monolithic silica-cellulose aerogel applying a sustainable sodium silicate precursor, Construction and Building Materials 293 (2021) 123289.

[6] **Y.X. Chen**, R.M.L.M. Dalessi, H.J.H. Brouwers, The development of co-precursor silica-cellulose aerogel via ambient pressure drying (in preparation).

[7] **Y.X. Chen**, K. Klima, K. Schollbach, Q.L. Yu, H.J.H. Brouwers, Effect of silica aerogel on thermal insulation and acoustic absorption of geopolymer foam render: Towards the role of different particle sizes (in preparation).

[8] A. Lazaro, **Y.X. Chen**, C. Verhoeven, Y. Hendrix, One-step synthesis of ordered mesoporous silica from olivine and its pore size tailoring, Journal of Cleaner Production 238 (2019) 117951.

[9] **Y.X. Chen**, S. Li, R. Yu, B. Mezari, E.J.M. Hensen, K. Schollbach, Q.L. Yu, H.J.H. Brouwers, Highly dispersed colloidal nano-silica from olivine and its effect on the rheology and hydration of ultrahigh performance concrete (submitted).

Conferences

[1] **Y.X. Chen**, Y. Hendrix, K. Schollbach, H.J.H Brouwers. A silica aerogel synthesized from olivine and its application as a photocatalytic support. The 2nd International Conference of Sustainable Building Materials (ICSBM 2019), 12-15 August, Eindhoven, The Netherlands, 2019.

[2] **Y.X. Chen**, Y. Hendrix, K. Schollbach, A. Lazaro, H.J.H Brouwers, Development and characterization of silica aerogel using olivine silica as a sustainable precursor, 5th international seminar of aerogel: Properties-Manufacture-Applications, TU Hamburg, Germany, 2020. (Poster)

Curriculum vitae

Yuxuan Chen was born in Wuhan, Hubei Province, China on January 19th, 1990. After finishing his primary, middle and high school educations in Wuhan, he started to study at Wuhan University of Technology (WUT) in September 2008. In June 2012, he received his bachelor's degree majored in Materials Chemistry. In September 2012, he started to study at the School of Materials Science and Engineering (WUT) as a master student supervised by Prof. Zhonghe Shui and Prof. Wei Chen, majoring in advanced cement-based materials and gaining his master's degree in June 2015. His research interests include the chloride resistance of concrete by using layered double hydroxides (LDHs) and ultrahigh performance concrete. In February 2016, he joined the Building materials group of TU/e as a guest researcher. His research topic was bio-based lightweight concrete. In November 2016, he started a PhD study in WUT majoring in building materials. In November 2017, he got the CSC scholarship and began his PhD study under the supervision of Prof. H.J.H. (Jos) Brouwers, Prof. Qingliang Yu. and Dr. K. (Katrin) Schollbach at Eindhoven University of Technology (TU/e), Eindhoven, the Netherlands. His PhD research includes application of miscanthus fibers in sustainable building materials for thermal insulation and acoustic absorption, and sustainable development of silica aerogel and its application in building materials, and mesoporous and colloidal silica from olivine and its utilization in functional and high-strength concrete.

The energy consumption in the building sector accounts for a significant part of the world's total energy use and greenhouse gas emissions. It is of great interests to design sustainable and high-performance insulation materials for energy saving. Meanwhile, the healthy living environment is also an important aspect in today's building design, especially acoustic and air pollutions. Owing to the widely availability and porous structure of miscanthus fibers, it can be used as bio-lightweight aggregates in concrete, improving acoustic absorption and thermal insulation. Furthermore, silica aerogel, a super-insulating inorganic material, can be applied in building's fabric to improve the conditions inside. The high embedded energy of aerogel is compensated with the use of olivine as a precursor. Lastly, mesoporous silica is developed from olivine to at low temperatures and applied as photocatalytic support and accelerator in concrete. Therefore, this thesis aims to provide new insights of green bio-concrete, sustainable silica aerogel and olivine nano-silica for insulation and functionalization of building materials.

DEPARTMENT OF THE BUILT ENVIRONMENT

TU/e EINDHOVEN UNIVERSITY OF TECHNOLOGY